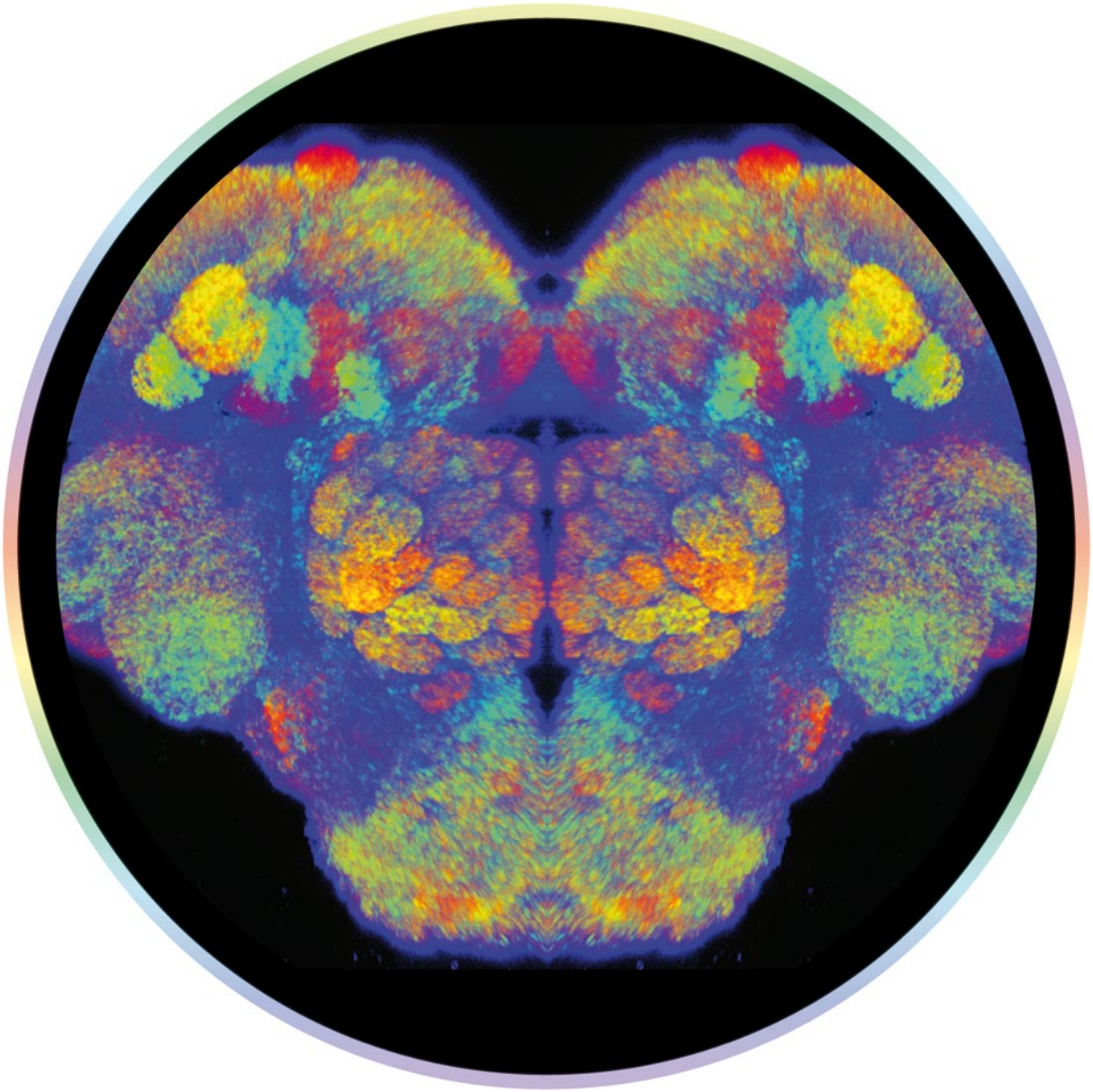

Structural and Functional Diversity of Synapses in the *Drosophila* CNS

submitted by
Till Andlauer

Würzburg, 2013

CC BY NC ND

Structural and Functional Diversity of Synapses in the *Drosophila* CNS

Strukturelle und funktionale Diversität von Synapsen im ZNS von *Drosophila*

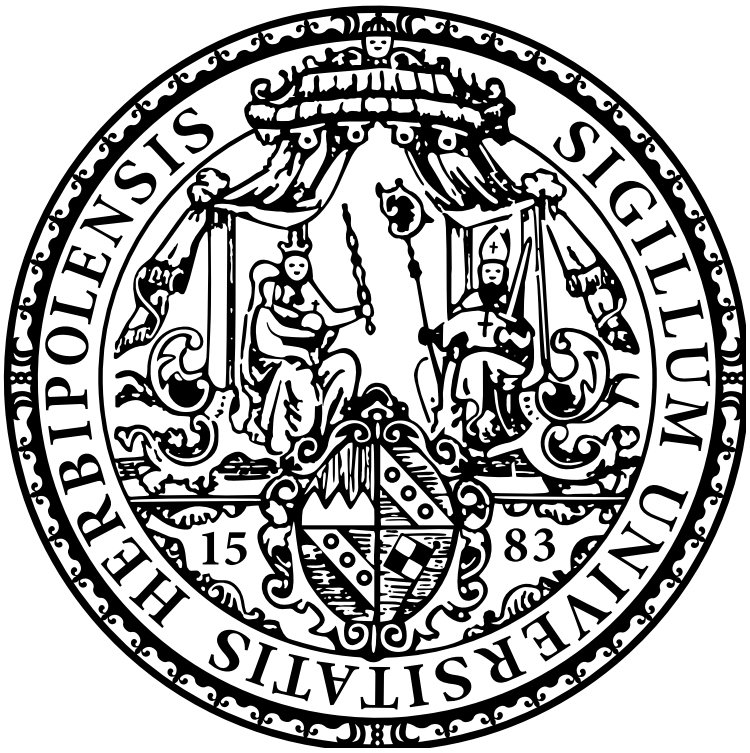

Doctoral thesis for a doctoral degree
at the Graduate School of Life Sciences,
Julius-Maximilians-Universität Würzburg,
Section Biomedicine

submitted by
Till Felix Malte Andlauer

from
Freiburg im Breisgau

Würzburg, 2013

Submitted on: 19th September 2013

Members of the *Promotionskomitee*:

Chairperson:	Prof. Dr. Caroline Kisker
Primary Supervisor:	Prof. Dr. Stephan Sigrist
Supervisor (Second):	Prof. Dr. Erich Buchner
Supervisor (Third):	Prof. Dr. Thomas Raabe

Date of Public Defence: 19th December 2013

Date of Receipt of Certificates:

Affidavit

I hereby confirm that my thesis entitled *Structural and Functional Diversity of Synapses in the Drosophila CNS* is the result of my own work. I did not receive any help or support from commercial consultants. All sources and/or materials applied are listed and specified in the thesis.

Furthermore, I confirm that this thesis has not yet been submitted as part of another examination process neither in identical nor in similar form.

Till Andlauer

Eidesstattliche Erklärung

Hiermit erkläre ich an Eides statt, die Dissertation *Strukturelle und funktionale Diversität von Synapsen im ZNS von Drosophila* eigenständig, das heißt inbesondere selbständig und ohne Hilfe eines kommerziellen Promotionsberaters, angefertigt und keine anderen als die von mir angegebenen Quellen und Hilfsmittel verwendet zu haben.

Ich erkläre außerdem, dass die Dissertation weder in gleicher noch in ähnlicher Form bereits in einem anderen Prüfungsverfahren vorgelegen hat.

Till Andlauer

TABLE OF CONTENTS

This thesis can be downloaded in electronic form at http://biologie.andlauer.net/thesis.pdf

SUMMARY

Large-scale anatomical and functional analyses of the connectivity in both invertebrate and mammalian brains have gained intense attention in recent years. At the same time, the understanding of synapses on a molecular level still lacks behind. We have only begun to unravel the basic mechanisms of how the most important synaptic proteins regulate release and reception of neurotransmitter molecules, as well as changes of synaptic strength. Furthermore, little is known regarding the stoichiometry of presynaptic proteins at different synapses within an organism. An assessment of these characteristics would certainly promote our comprehension of the properties of different synapse types. Presynaptic proteins directly influence, for example, the probability of neurotransmitter release as well as mechanisms for short-term plasticity.

We have examined the strength of expression of several presynaptic proteins at different synapse types in the central nervous system of *Drosophila melanogaster* using immunohistochemistry. Clear differences in the relative abundances of the proteins were obvious on different levels: variations in staining intensities appeared from the neuropil to the synaptic level. In order to quantify these differences, we have developed a ratiometric analysis of antibody stainings.

By application of this ratiometric method, we could assign average ratios of presynaptic proteins to different synapse populations in two central relays of the olfactory pathway. In this manner, synapse types could be characterized by distinct fingerprints of presynaptic protein ratios. Subsequently, we used the method for the analysis of aberrant situations: we reduced levels of Bruchpilot, a major presynaptic protein, and ablated different synapse or cell types. Evoked changes of ratio fingerprints were proportional to the modifications we had induced in the system. Thus, such ratio signatures are well suited for the characterization of synapses.

In order to contribute to our understanding of both the molecular composition and the function of synapses, we also characterized a novel synaptic protein. This protein, Drep-2, is a member of the Dff family of regulators of apoptosis. We generated *drep-2* mutants, which did not show an obvious misregulation of apoptosis. By contrast, Drep-2 was found to be a neuronal protein, highly enriched for example at postsynaptic receptor fields of the input synapses of the major learning centre of insects, the mushroom bodies.

Flies mutant for *drep-2* were viable but lived shorter than wildtypes. Basic synaptic transmission at both peripheral and central synapses was in normal ranges. However, *drep-2* mutants showed a number of deficiencies in adaptive behaviours: adult flies were locomotor hyperactive and hypersensitive towards ethanol-induced sedation. Moreover, the mutant animals were heavily impaired in associative learning. In aversive olfactory conditioning, *drep-2* mutants formed neither short-term nor anaesthesia-sensitive memories. We could demonstrate that Drep-2 is required in mushroom body intrinsic neurons for normal olfactory learning. Furthermore, odour-evoked calcium transients in these neurons, a prerequisite for learning, were reduced in *drep-2* mutants. The impairment of the mutants in olfactory learning could be fully rescued by pharmacological application of an agonist to metabotropic glutamate receptors (mGluRs).

Quantitative mass spectrometry of Drep-2 complexes revealed that the protein is associated with a large number of translational repressors, among them the fragile X mental retardation protein FMRP. FMRP inhibits mGluR-mediated protein synthesis. Lack of this protein causes the fragile X syndrome, which constitutes the most frequent monogenic cause of autism. Examination of the performance of *drep-2* mutants in courtship conditioning showed that the animals were deficient in both short- and long-term memory. *Drep-2* mutants share these phenotypes with *fmrp* and *mGluR* mutants. Interestingly, *drep-2*; *fmrp* double mutants exhibited normal memory. Thus, we propose a model in which Drep-2 antagonizes FMRP in the regulation of mGluR-dependent protein synthesis. Our hypothesis is supported by the observation that impairments in synaptic plasticity can arise if mGluR signalling is imbalanced in either direction. We suggest that Drep-2 helps in establishing this balance.

ZUSAMMENFASSUNG

Umfangreiche anatomische und funktionelle Analysen der Konnektivität in Gehirnen von Wirbellosen und Säugern haben in den letzten Jahren große Aufmerksamkeit erhalten. Gleichzeitig ist unser Verständnis von Synapsen auf molekularer Ebene jedoch noch unvollständig. Wir haben erst damit begonnen, die grundlegenden Mechanismen zu entschlüsseln, nach denen die wichtigsten synaptischen Proteine die Ausschüttung und Erkennung von Neurotransmittern sowie Veränderungen der Stärke von Synapsen regulieren. Darüber hinaus ist auch über die Stöchiometrie präsynaptischer Proteine an verschiedenen Synapsen noch wenig bekannt. Eine Untersuchung dieser Eigenschaften würde zum besseren Verständnis der Merkmale verschiedener Synapsentypen beitragen. Präsynaptische Proteine beeinflussen zum Beispiel die Wahrscheinlichkeit der Ausschüttung von Neurotransmittern sowie Mechanismen zur Erzeugung von Kurzzeit-Plastizität.

Wir haben die Expressionsstärke mehrerer präsynaptischer Proteine an verschiedenen Synapsentypen des Zentralnervensystems von *Drosophila melanogaster* mittels Immunhistochemie untersucht. Auf mehreren Ebenen waren deutliche Unterschiede in der relativen Anreicherung der Proteine offensichtlich: Färbungsintensitäten variierten von der Neuropilebene bis zum einzelnen Synapsentyp. Um diese Unterschiede zu quantifizieren, haben wir eine ratiometrische Analyse von Antikörperfärbungen entwickelt.

Mit dieser Methode war es möglich, verschiedenen Synapsenpopulationen zweier Schaltstellen der Riechbahn durchschnittliche Ratios präsynaptischer Proteine zuzuweisen. Synapsentypen konnten durch eindeutige Fingerabdrücke präsynaptischer Proteinratios charakterisiert werden. So gelang es uns, die Auswirkungen einer Verringerung der Menge des wichtigen präsynaptischen Proteins Bruchpilot sowie der Entfernung verschiedener Synapsen- und Zelltypen zu untersuchen. Die in diesen Situationen hervorgerufenen Veränderungen der Ratio-Fingerabdrücke entsprachen den von uns im System erzeugten Abweichungen. Ratios präsynaptischer Proteine eignen sich daher gut dafür, Synapsentypen zu charakterisieren.

Um unser Verständnis von sowohl der molekularen Zusammensetzung als auch der Funktion von Synapsen zu verbessern, haben wir außerdem das neue synaptische Protein Drep-2 charakterisiert. Drep-2 gehört zu den Dff-Proteinen, einer Familie von Apoptoseregulatoren. Wir haben *drep-2* Mutanten erzeugt, bei denen Zelltod jedoch nicht fehlreguliert erschien. Stattdessen stellte sich Drep-2 als neuronales Protein heraus, angereichert zum Beispiel postsynaptisch an Eingangssynapsen der Pilzkörper, den Lernzentren von Insekten.

Fliegen, denen das Gen *drep-2* fehlte, waren lebensfähig, lebten jedoch kürzer. Die basale Übertragung an peripheren und zentralen Synapsen erschien unverändert. Die Mutanten zeigten jedoch Ausfälle in verschiedenen adaptiven Verhaltensweisen: Die Fliegen waren hyperaktiv in ihrer Bewegung sowie hypersensibel gegenüber Ethanol. Zudem zeigten die Tiere ein stark eingeschränktes assoziatives Lernvermögen. In aversivem Geruchslernen konnten die Mutanten weder Kurz- noch Mittelzeiterinnerungen bilden. Wir konnten nachweisen, dass Drep-2 für normales Geruchslernen in Pilzköper-intrinsischen Neuronen benötigt wird. Außerdem waren bei den Mutanten in diesen Neuronen durch Gerüche hervorgerufene Kalziumsignale, eine Voraussetzung für Lernen, reduziert. Die Lerneinschränkungen der Mutanten konnten durch Gabe eines pharmakologischen Agonisten metabotroper Glutamatrezeptoren (mGluR) vollständig behoben werden.

Quantitative Massenspektrometrie von Drep-2-Komplexen zeigte, dass das Protein mit einer großen Anzahl von Translationsrepressoren assoziiert ist. Unter diesen befand sich das Fragile X Protein FMRP. FMRP inhibiert mGluR-vermittelte Proteinsynthese. Ein Mangel an FMRP erzeugt das Fragile X Syndrom, die häufigste monogenetische Ursache für Autismus. Bei Balzkonditionierung konnten *drep-2* Mutanten weder Kurz- noch Langzeiterinnerungen speichern. Diesen Phänotyp haben sie mit *fmrp*- und *mGluR*-Mutanten gemeinsam. *Drep-2*; *fmrp* Doppelmutanten hatten jedoch ein normales Gedächtnis. Wir gehen daher davon aus, dass Drep-2 FMRP bei der Regulierung von mGluR-abhängiger Translation entgegenwirkt. Die Beobachtung, dass synaptische Plastizität gestört sein kann, wenn mGluR-Signalwege unausgewogen sind, stärkt diese Hypothese. Wir nehmen an, dass Drep-2 dazu beiträgt, von mGluR erzeugte Signale zu balancieren.

LYRICAL ABSTRACT

A cell must die, eventually,
It is the saddest fact:
The fate of every entity
Is merely to be wrecked.

In apoptosis things take place
You could tell to your nieces:
The DNA, transformed to haze,
Gets chopped to little pieces.

The protein that here degrades,
As you will surely see,
In its importance never fades
Through all our history.

This Fragmentation Factor Forty,
Which is its legal name,
Is not a fellow very sporty,
But that's part of the game:

It's tightly being regulated
Through proteïns close by,
Yet cleavage gets it stimulated
To turn to wild from shy.

Drosophila, our flying friend,
Contains a group of four
Such peptides and we comprehend
They share a common core.

We focused on a single one,
It's name is D-rep-2,
Which, finally, when hopes were gone,
Made our dreams come true:

It locates, as it is expressed,
Not to a random site,
The synapse is, as we assessed,
where D-rep-2 shines bright.

In Kenyon cells it does appear
to label PSDs –
and D-rep-2 is common here
as doves in times of peace.

When D-rep-2 is missing, though,
Things are not as they should:
Experiments in learning show
Performance isn't good.

If flies receive a punishment
Paired with a poignant smell
The odour causes some lament
Right in the Kenyon cell.

Conditioning, that's how it's called,
Is heavily disturbed:
The learning process is quite stalled,
The memory perturbed.

And to the mutants utter grief
They cannot have some drinks:
They're really hypersensitive
To alcoholic things.

What is the cause of all this fuss,
Say, what is going on,
Why do the mutants act so cross?
Replies begin to dawn:

Metabotropic pathways do
Appear to play a role,
Which regulate, I'm telling you,
Translation as a whole.

And furthermore, oh what a bliss,
There is another link
To Fragile X that really is
A peptide quite distinct:

We need it in our brains so that
Plasticity works swell
And if we lack it we get mad –
life won't be quite as well.

To counteract the Fragile X,
We'll see if this is true,
Is probably, so say the facts,
A job of D-rep-2.

Introduction

Seht ihr den Mond dort stehen?
Er ist nur halb zu sehen,
Und ist doch rund und schön.
So sind wohl manche Sachen,
Die wir getrost belachen,
Weil unsre Augen sie nicht sehn.

Matthias Claudius, Abendlied

RARELY HAS A DISCIPLINE OF Biology received as much attention as Neurosciences have since the 1990s (Abbott, 2013; Albus et al., 2007; Alivisatos et al., 2012; *Celebrating a decade of progress*, 1999; Markoff and Gorman, 2013; Van Essen et al., 2012). In an aging society, disorders of the nervous system, for example Alzheimer's or Parkinson's disease, to name but two, have become widespread (Dorsey et al., 2007; Hebert et al., 2003). Efforts to find treatments for such complex disorders have gained momentum: progress in sequencing and non-invasive imaging technologies, together with the identification of specific biomarkers, have brought us closer to the discovery of efficient therapies (Holtzman et al., 2012).

However, an understanding of multicausal neuronal disorders requires for a better model of the brain in general (Bardin, 2012; Castellanos et al., 2013; Jiang, 2013; Van Essen and Ugurbil, 2012). Also here, enormous efforts are being undertaken. A project of a scope surpassing the decipherment of the human genome is the establishment of the connectome (Morgan and Lichtman, 2013; Sporns, 2013; *The benefits of brain mapping*, 2013): the map of all neurons and, eventually, all synapses in a brain. Work in *C. elegans* has demonstrated that a mere anatomical map of the central nervous system (CNS) is clearly not sufficient for comprehending computation within it (Morgan and Lichtman, 2013; White et al., 1986). Therefore, attempts to map the activity of neurons have gained importance as well (Alivisatos et al., 2012; Assaf et al., 2013; Briggman et al., 2011; Hutchison et al., 2013; Van Essen et al., 2012).

The different layers of information required to gain substantial insights into the nervous system can be described with an analogy: If the anatomical map of the brain corresponded to the road map of a large city, neuronal activity would tell us how many cars actually drive on which streets. Yet in order to truly understand such traffic, a third layer of information is required: knowledge about road traffic regulations, as well as information regarding traffic lights and signs. This layer corresponds to the molecular composition of synapses: numbers of transmitter vesicles and their respective release probabilities, the composition of neurotransmitter receptors as well as the presence of additional proteins influencing plasticity. Here, efforts lack behind (Eisenstein, 2009; O'Rourke et al., 2012), although synaptic proteins are constantly being identified and characterized, in invertebrate as well as in mammalian model systems (Gundelfinger and Fejtova, 2012; Haucke et al., 2011; Iasevoli et al., 2013; Proctor et al., 2011; Südhof, 2012; Vessey and Karra, 2007).

The aim of this thesis is to promote our understanding of the molecular composition of synapses. To this end, a method for the characterization of synapse populations, based on presynaptic molecular markers, has been developed and applied. In addition, a novel synaptic protein was investigated in detail in the CNS of the vinegar fly *D. melanogaster.* Before describing and interpreting the results of these projects, a brief introduction to the essential background will be provided.

1. Chemical synapses

Neurons were first described as distinct units by Wilhelm Waldeyer 120 years ago (Cowan and Kandel, 2001; Waldeyer, 1891)[1]; connections between neurons became known under the term "synapses" shortly after (Sherrington, 1897). Although electrical synapses (gap junctions) between neurons exist (first identified in crayfish by Furshpan and Potter, 1957), allowing for rapid transmission of signals, this introduction is focused on the description of chemical synapses. The slower chemical synapse is a specialized structure that is highly adapted for the transmission, modification and integration of signals. To this end, chemical compounds are used as intermediates (first discovered by Henry H. Dale, 1914).

In brief, the chemical synapse is the junction between a presynaptic neuron, which transmits information, and a postsynaptic cell, which receives the signal in form of a chemical neurotransmitter (Fig. 1). Electrical signals are propagated within neurons as changes in membrane polarization. If a depolarization surpasses a certain threshold at the presynaptic specialization, fusion of neurotransmitter-containing vesicles with the presynaptic membrane is triggered (Haucke et al., 2011). This process is called exocytosis and involves a large number of specialized proteins. A key factor leading to the release of neurotransmitter is the influx of calcium ions. The protein scaffold that helps bringing synaptic vesicles into the vicinity of voltage-gated calcium channels is called the cytomatrix at the active zone (CAZ) (Südhof, 2012). The active zone (AZ) is the stretch of presynaptic membrane at which transmitter vesicle fusion takes place.

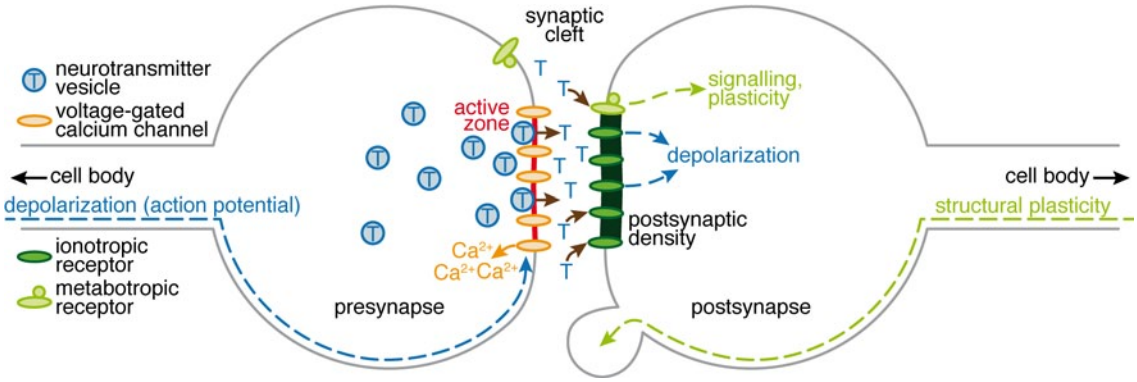

Fig. 1: Highly simplified, schematic illustration of an excitatory chemical synapse.
Compiled with information from Haucke et al., 2011 and Sheng, 2001. A more accurate description of plasticity processes and the roles of ionotropic and metabotropic receptors therein is provided in the sections 1.2 and 2.

On the postsynaptic side, released neurotransmitter molecules are detected by specialized receptors. These receptors cluster at the postsynaptic density (PSD) (Sheng, 2001). One class of receptors, called ionotropic, constitutes an ion channel that directly allows for the influx of ions. Influx of ions alters the polarization of the membrane of the postsynaptic cell. Activation of another class of receptors, called metabotropic, triggers an intracellular signalling cascade, typically mediated by small

[1] All historical information in this paragraph was summarized from Cowan and Kandel, 2001.

GTP-binding proteins (G-protein signalling). Chemical synapses can be excitatory or inhibitory, depending on whether transmission of the signal leads to a de- or a hyperpolarization of the postsynaptic cell. Postsynaptic neurons can integrate both excitatory and inhibitory input, an action potential will be triggered if the summed signal exceeds a certain depolarization threshold. In the following paragraphs, several selected synaptic proteins will be described that are of special importance in the context of this thesis.

1.1. Selected proteins at the presynaptic active zone

The fusion of synaptic vesicles with the presynaptic membrane leads to exocytosis of neurotransmitter molecules. Many different proteins tightly regulate the steps ranging from docking of vesicles at the membrane to their fusion (Haucke et al., 2011). These proteins are either attached to the synaptic vesicles, e.g. Synaptobrevin, or to the AZ, e.g. Syntaxin. The relatively small number of vesicles docked at each AZ are part of the readily-releasable pool of vesicles. Additional pools of vesicles exist, recycling and reserve pools, which can be mobilized to the AZ during periods of sustained stimulation (Rizzoli and Betz, 2005).

After docking to the AZ, vesicles are made competent for fusion with the synaptic membrane. This process, called priming, involves proteins forming the SNAP/SNARE complex. Following stimulation by Ca^{2+}, primed vesicles release their content into the synaptic cleft. A local increase in Ca^{2+} concentrations is detected by synaptotagmin proteins. After release of neurotransmitters, vesicles are recycled, a process called endocytosis.

A characteristic element of presynaptic AZs is an electron-dense proteinaceous matrix in the adjacent cytosol, decorated with synaptic vesicles (Fig. 2B; Zhai and Bellen, 2004). Core components of this T-shaped scaffold in *Drosophila* are the proteins Bruchpilot (Brp) and RIM binding protein (RBP) (Kittel et al., 2006; Liu et al., 2011).

1.1.1. Bruchpilot/ELKS, Bassoon and Piccolo

Filaments formed by the two Bruchpilot isoforms Brp^{170kDa} and Brp^{190kDa} cluster at AZs (Fig. 2) and form a structure visible in electron microscopy as a T-bar (Fig. 2B; Wichmann and Sigrist, 2010). However, botanists might rather associate the respective model with a bouquet of flowers (Fig. 2C). *Brp* null mutants completely lack T-bars (Kttel et al., 2006). The N- and C-termini of Brp have two separate functions: the N-terminus clusters voltage-gated Ca^{2+} channels, while the C-terminus tethers synaptic vesicles (Hallermann et al., 2010; Kittel et al., 2006; Wagh et al., 2006). In addition, the amount of Brp influences the size of the pool of readily-releasable neurotransmitter vesicles docked at the membrane (Matkovic et al., 2013). Thus, Brp establishes close proximity of synaptic vesicles and Ca^{2+} channels. In consequence, animals mutant for *brp* release less vesicles per action potential and show disturbed synaptic short-term plasticity.

The N-terminal half of Brp is homologous to mammalian ELKS/ERC/CAST proteins (Wagh et al., 2006). However, these mammalian counterparts appear to play a less important role at excitatory synapses than Brp does in flies: here, synapses of

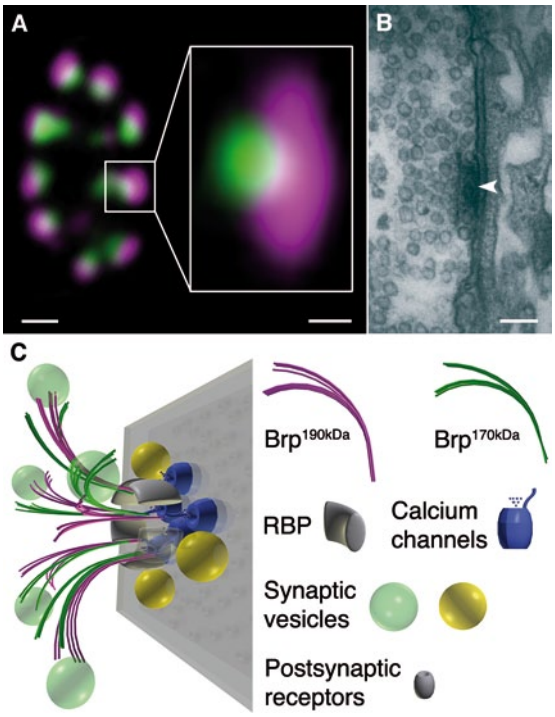

Fig. 2: Brp is part of the cytomatrix at the active zone.
A: Immunohistochemical staining of a bouton of a larval neuromuscular junction (comprising several synapses, left box) and an individual synapse in lateral view (right box). Green: anti-Brp^{Nc82} (recognizing both the 170kDa and the 190kDa isoform), magenta: anti-DGluR^{IID} (postsynaptic ionotropic glutamate receptor subunit). Scale bars: bouton: 1 µm; synapse: 100 nm.
B: Ultrastructure of an AZ. The arrowhead points at the T-bar, synaptic vesicles cluster next to it. Scale bar: 100 nm.
A-B: Adapted, with permission, from Andlauer and Sigrist, 2012.
C: Simplified model of AZ organization. Brp filaments consist of both Brp isoforms in an alternating pattern, which create release slots for synaptic vesicles. Postsynaptic receptors are dimly visible behind the gray membrane.
C: Adapted, with permission of the authors, from Matkovic et al., 2013 (Copyright 2013 by Matkovic et al., published by Rockefeller University Press).

elks mutants do not show severe defects in (excitatory) transmission, Ca^{2+} channels remain clustered, and synaptic vesicle densities are in a normal range (Kaeser et al., 2009; tom Dieck et al., 2012). Interestingly, high frequency release of neurotransmitters is supported by the protein in both flies and mammals (Kittel et al., 2006; tom Dieck et al., 2012).

A reason for the limited effect of a lack of ELKS in mammals could be that functions executed by Brp in flies might, in mammals, be performed by two separate proteins (Südhof, 2012). The mammalian CAZ contains two large coiled-coil proteins, Piccolo and Bassoon, which show structural similarity to the Plectin-related C-terminus of Brp. The genome of *Drosophila* codes for a Piccolo homologue, Fife, but a Bassoon homologue has not yet been discovered (Bruckner et al., 2012). Hence, it is probable that Brp combines functions of both mammalian ELKS and Bassoon in one protein. In accordance with this hypothesis, *bassoon* mutants do show stronger deficits than *elks* mutants, e.g. a reduction in the number of Ca^{2+} channels and of tethered vesicles at synapses, as well as loss of attachment of electron-dense ribbons (Frank et al., 2010; tom Dieck et al., 2005).

1.1.2. RIM, RIM-binding protein and Munc13

While Brp could be designated as the master organizer of the CAZ in flies, RIM proteins are candidates for a similar title in mammals (Südhof, 2012). RIM proteins interact, among others, with synaptic vesicle proteins (hence the name, Rab3-interacting module/molecule (RIM)), voltage-gated Ca^{2+} channels, and the RIM-binding protein (RBP) (Südhof, 2012). Accordingly, RIM is important for vital functions, such as docking and priming of synaptic vesicles to the presynaptic membrane as well as

for recruitment of calcium channels (summarized in Südhof, 2012). In *Drosophila*, major RIM functions are conserved (Graf et al., 2012; Müller et al., 2012).

However, RIM depends on the associated RBP for its function in concentrating Ca^{2+} channels at AZs (Kaeser et al., 2011; Liu et al., 2011). Furthermore, *Drosophila* RBP is, together with Brp, essential for the formation of properly shaped electron-dense T-bars (Liu et al., 2011). Accordingly, RBP is required for normal release of neurotransmitters, as well as for synaptic short-term plasticity. Thus, RBP is a core component of the CAZ (Fig. 2C).

RIM also interacts with UNC-13/Munc13, a protein important for vesicle priming (reviewed in Südhof, 2012). *C. elegans* UNC mutants were discovered in a screen for uncoordinated movement, hence the name. RIM influences priming of vesicles via activation of Munc13. Through regulation of vesicle priming, Munc13 proteins also influence short-term plasticity.

1.1.3. Liprin-α and Syd-1

During the maturation of synapses, Brp is a protein arriving rather late (Fig. 3; Fouquet et al., 2009). In fact, T-bars formed by Brp constitute the characteristic element of mature presynapses. By contrast, Liprin-α and Syd-1 are two important players in early CAZ assembly (Fouquet et al., 2009; Owald et al., 2010; 2012). Liprin-α binds to RIM, Brp, and Syd-1, and has, like Syd-1, mainly been studied in invertebrates (Südhof, 2012). Liprin-α is a factor mediating CAZ assembly and hence controls the size of the AZ as well as the accumulation of synaptic vesicles (Kaufmann et al., 2002; Patel et al., 2006; Spangler et al., 2013). Interestingly, Liprin-α might also regulate transport of CAZ components to the synapse (Miller et al., 2005).

Syd-1, only recently identified to be present also at vertebrates synapses (Wentzel et al., 2013), interacts with Liprin-α during early AZ formation (Owald et al., 2010; 2012). The RhoGAP-like protein synchronizes pre- with postsynaptic assembly via an interaction with the cell adhesion molecule Neurexin (Fig. 3; Owald et al., 2012). At the AZ, Syd-1 mediates appropriate localization of both Liprin-α and Brp. Hence, *Drosophila syd-1* and *liprin-α* mutants show a reduced number of synapses (Owald et al., 2010). Remaining T-bars in *syd-1* mutants are often of irregular size and shape. Moreover, ectopic Brp accumulates in *syd-1* mutants at sites distant from AZs. In mice mutant for the homologue *mSyd1A*, synapse numbers are unaltered, but less synaptic vesicles are docked at the AZ membrane (Wentzel et al., 2013).

1.2. Receptors at the postsynaptic density

The postsynaptic specialization contains an electron-dense protein scaffold attached to the synaptic membrane as well, called the postsynaptic density (PSD) (Sheng, 2001). Specialized receptors for each type of chemical transmitter used at a synapse, as well as additional ion channels, reside in the postsynaptic membrane. These receptors are embedded in a scaffold that anchors them at appropriate locations (Iasevoli et al., 2013). The perhaps best known postsynaptic scaffolding protein is PSD-95, its *Drosophila* homologue is called Discs large (Dlg). PSD-95 and Dlg cluster predominantly on the postsynaptic side. However, both PSD-95 and Dlg, as well as a number

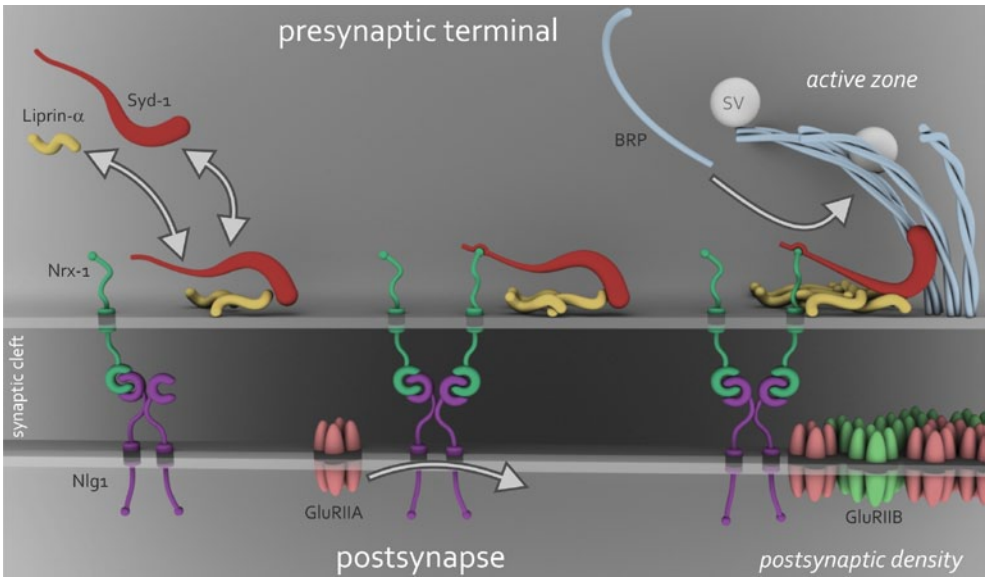

Fig. 3: Model of early synapse assembly at *Drosophila* NMJs, involving Liprin-α and Syd-1.
Left: Clusters of Liprin-α and Syd-1 undergo rounds of assembly and disassembly.
Centre: Interaction with Neurexin (Nrx-1) defines the sites where novel synapses form. On the postsynaptic side, Neuroligin (Nlg1) is instructive for early rapid incorporation of ionotropic glutamate receptor complexes containing the subunit GluRIIA.
Right: As the synapse matures, Syd-1 regulates the incorporation of Brp into the presynaptic CAZ. Postsynaptic glutamate receptors mature accordingly, by incorporation of receptors containing the subunit GluRIIB. Image taken, with permission, from Owald et al., 2012.

of additional proteins, among them Liprin-α, can be present on both sides of the synapse (Cho et al., 1992; Kistner et al., 1993; Lahey et al., 1994; Spangler and Hoogenraad, 2007).

1.2.1. Ionotropic neurotransmitter receptors

A major component of PSDs in the mammalian CNS are ionotropic, NMDA-type glutamate receptors (Sheng, 2001).[2] These receptors are stimulated, in addition to L-glutamate, by the compound N-methyl-D-aspartate (NMDA). PSD-95 anchors NMDA receptors in the postsynaptic membrane. Ionotropic glutamate receptors are ligand-gated ion channels: stimulation of NMDA receptors leads to an influx of cations, causing a depolarization of the postsynaptic cell. Importantly, also divalent cations, like Ca^{2+}, can pass NMDA receptor channels under certain conditions.

All other kinds of ionotropic glutamate receptors can be summarized as non-NMDA receptors, one of these is the AMPA receptor. It was named after the agonist α-amino-3-hydroxy-5-methyl-4-isoxazole propionic acid (AMPA), which selectively stimulates this receptor type, in addition to glutamate. Unlike NMDA receptors, AMPA receptors are ion channels that allow influx only of monovalent cations (e.g., Na^+, K^+).

Ionotropic glutamate receptors are tetramers, i.e. they consist of four subunits. A large number of different subunits exists. For example, five different subunits, GluRIIA-GluRIIE, compose non-NMDA receptors at the *Drosophila* larval neuromuscular

[2] All information in this section not designated with a specific reference was compiled from Sheng, 2001.

junction (NMJ) (Qin et al., 2005). These subunits modify the properties of the receptors. At the NMJ, young receptors mainly contain GluRIIA subunits, which are partly replaced by complexes containing GluRIIB subunits during maturation of the synapse (Fig. 3; Schmid et al., 2008). The number of available subunits is especially large for NMDA receptors.

L-glutamate is the dominant excitatory transmitter at synapses in the mammalian CNS, as well as at *Drosophila* NMJs. In the CNS of flies, by contrast, acetylcholine (ACh) constitutes the major excitatory transmitter (Gundelfinger and Hess, 1992; Yasuyama and Salvaterra, 1999). Different classes of ACh receptors have been characterized; nicotinic ACh receptors are ionotropic cation channels, typically activated by the ligand ACh, and named after the specific agonist nicotine. Each ACh receptor is composed of five subunits; however, the available pool of subunits is larger. The subunit α7 can form homomeric receptors (Couturier et al., 1990; Fayyazuddin et al., 2006; Grauso et al., 2002). It was thus used for the generation of transgenic markers of ACh receptors (Leiss et al., 2009b, Palma et al., 2002).

Moreover, inhibitory ionotropic receptors exist, activated by the ligands γ-aminobutyric acid (GABA) or glycine. These ion channels mediate the influx of Cl^- ions and thus hyperpolarize the cell.

1.2.2. Metabotropic receptors

Metabotropic receptors are, in contrast to ionotropic ones, no ion channels. Instead, ligand-mediated activation of metabotropic receptors triggers second-messenger signalling cascades (Nicholls et al., 2001). Metabotropic receptors can, for example, be activated by glutamate (mGluRs), ACh (muscarinic ACh receptors), biogenic amines (mainly adrenaline, noradrenaline, dopamine, serotonin, histamine, and octopamine), or by neuropeptides. Furthermore, specific metabotropic receptors exist for the inhibitory transmitters GABA and glycine.

Typically, metabotropic receptors are coupled to G-proteins (Nicholls et al., 2001). A large variety of G-proteins is known, some directly activate ion channels, others stimulate signalling pathways. Activation of G-protein-coupled receptors causes the dissociation of a G-protein trimer into its subunits, mediated via the exchange of the eponymous GTP for GDP. Two important classes of G-proteins are G_s, which stimulates adenylyl cyclase, and G_i, which inhibits the same enzyme. Adenylyl cyclases, in turn, catalyse synthesis of the second messenger cAMP. An important adenylyl cyclase in *Drosophila* is the protein Rutabaga (Aceves-Piña et al., 1983; Dudai et al., 1983). G-proteins can also activate other pathways: for example, G_q couples to Phospholipase C (PLC) (Nicholls et al., 2001). Increased cAMP-levels can have widespread effects, up to an activation of the transcription factor CREB via the intermediate Protein kinase A (PKA).

While several metabotropic glutamate receptors have been identified in mammals, *Drosophila* contains only one functional mGluR, DmGluRA, a homologue of mammalian mGluR2 and mGluR3 (Parmentier et al., 1996). DmGluRA is coupled to G_i, and thus inhibits synthesis of cAMP. Of note, there is evidence that DmGluRA can also stimulate the G_q pathway (Pan and Broadie, 2007). Two functional metabotropic

$GABA_B$ receptor subtypes are known in *Drosophila*, which form heterodimers and are related to DmGluRA (Mezler et al., 2001). *Drosophila* $GABA_B$ receptors are coupled to G_i and inhibit adenylyl cyclases, just as DmGluRA does.

2. Synaptic plasticity

Neuronal activity can trigger changes in synaptic efficacy, ranging from a temporary buildup of Ca^{2+} levels, over the modification of neurotransmitter receptor subunits, to the formation of novel synapses between cells. Such synaptic plasticity also mediates information storage during memory formation.

2.1. Short-term plasticity

Short-term plasticity takes place on a milliseconds to minutes time scale and is typically presynaptic (Zucker and Regehr, 2002). Synaptic enhancement is normally caused by elevated intracellular Ca^{2+} levels, leading, for example, to a facilitation of the fusion of additional synaptic vesicles. Short trains of stimulation cause such accumulation of Ca^{2+} and thus presynaptic facilitation; for example in *dmGluRA* mutants, facilitation is enhanced, apparently due to a misregulation of synaptic components during development (Bogdanik et al., 2004).

Short-term depression, by contrast, is usually caused by the depletion of vesicles that are ready for release (Zucker and Regehr, 2002). Depletion of readily releasable vesicles can, for example, occur during high-frequency stimulation. This vesicle pool is diminished in certain *brp* mutants (Matkovic et al., 2013). Moreover, in other *brp* mutants impaired in vesicle tethering, a reservoir pool of synaptic vesicles is disturbed, causing synaptic depression (Hallermann et al., 2010).

2.2. Long-term plasticity

Plasticity of the postsynaptic cell, i.e. changes in the sensitivity of neurotransmitter recognition, can cause long-term potentiation (LTP) and depression (LTD) of a synapse (Malenka and Siegelbaum, 2001). Long-term plasticity has primarily been studied in mammals, where it was established that it constitutes a prerequisite for memory formation and thus for adaptive behaviours. Mechanisms for the establishment of LTP and LTD are mainly changes in the composition and physical properties of ionotropic neurotransmitter receptors at the synapse. For example, the phosphorylation of receptor subunits can lead to an increase in the rate of receptor desensitization and thus to a decrease in receptor activity (Malenka and Siegelbaum, 2001).

2.2.1. Long-term potentiation

An important mechanism for the induction of LTP is the influx of Ca^{2+} ions through NMDA receptors, while the postsynaptic cell is already depolarized. This influx of Ca^{2+} activates the Ca^{2+}/Calmodulin-dependent kinase II (CaMKII) (Malenka and Siegelbaum, 2001; Molnár, 2011). As a result, CaMKII phosphorylates AMPA receptors and also stimulates the incorporation of additional AMPA receptors. Thus, NMDA receptors can, similarly to adenylyl cyclases, act as coincidence detectors of

two stimuli. In case of NMDA receptors, this coincidence constitutes simultaneous glutamate release and postsynaptic depolarization and, therefore, coincident pre- and postsynaptic activity. Such classical Hebbian plasticity has also been described in *Drosophila* and other invertebrates (Cassenaer and Laurent, 2007; Hebb, 1949; Ljaschenko et al., 2013; Xia et al., 2005). However, not only AMPA receptors, but also NMDA receptors themselves can undergo activity-dependent modifications and are regulated in the context of long-term plasticity (reviewed in Hunt and Castillo, 2012).

Long-term plasticity can be mediated by metabotropic receptors as well. For example, mGluRs induce LTP via changes of NMDA or AMPA receptors (reviewed in Anwyl, 2009). Here, again a rise of intracellular Ca^{2+} levels is the key factor: activation of mGluRs can, for example, cause the opening of voltage-gated Ca^{2+} channels or of TRP channels, as well as the release of Ca^{2+} from intracellular stores. Moreover, induction of LTP via mGluRs typically involves the activation of additional pathways, for example via PLC, PKA, or Protein kinase C (PKC) (Anwyl, 2009). These pathways can, in turn, also stimulate synthesis of novel proteins.

2.2.2. Additional mechanisms for long-term plasticity

The formation of memories not only requires for mechanisms that strengthen synapses, but also for the possibility to weaken connections, i.e. long-term depression (Collingridge et al., 2010). LTD of synapses can, for example, be triggered by prolonged low-frequency stimulation and its induction typically involves either NMDA or mGluR receptors (or both), just as LTP does. One mechanism for the establishment of LTD is, similarly to LTP, the alteration of AMPA receptor numbers at the postsynapse. However, LTD also often includes changes at the presynapse (e.g., a decrease of the transmitter release probability), mediated via retrograde messengers, for example nitric oxide.

Long-term plasticity not only involves the modification of receptors and of receptor numbers at existing synapses; in addition, structural plasticity takes place, for example the formation of novel dendritic spines. Such structural changes are induced by activation of NMDA receptors, CaMKII, and G-proteins as well (Bosch and Hayashi, 2012). For the establishment of structural plasticity, modification of actin filaments, part of the cytoskeleton, is of pivotal importance. While structural plasticity at mammalian CNS synapses has been investigated since the 1970s (Harreveld and Fifkova, 1975), it has only been observed recently in the CNS of *Drosophila* (Kremer et al., 2010). Of note, structural plasticity in the peripheral nervous system has already been described earlier (Sigrist et al., 2003).

2.2.2.1. Caspases and long-term plasticity

Caspases constitute an unusual group of proteins that can influence long-term plasticity. These proteases, typically activated during apoptosis, have recently been implicated in the regulation of both LTP and LTD (reviewed in Li and Sheng, 2012). Caspase-3 is, together with Caspase-7, the major effector protease during programmed cell death (Crawford and Wells, 2011; Kumar, 2007). Of note, the respective *Drosophila* homologues are the principal effector caspase DrICE, as well as the partly redundant

Dcp-1 (Hay and Guo 2006; Kumar, 2007). In recent years, an increasing number of non-apoptotic roles of caspases have been described, including regulation of synaptic plasticity (D'Amelio et al., 2010; Feinstein-Rotkopf and Arama, 2009; Kumar, 2004; Li and Sheng, 2012).

Interestingly, NMDA-receptor-dependent LTD in the murine hippocampus was shown to depend on activation of Caspase-3 (Jiao and Li, 2011; Li et al, 2010). In contrast to apoptosis, Caspase-3 is here only transiently activated to a low level, via a mitochondrial pathway. When activated in this manner, Caspase-3 mediates internalization of AMPA receptors. In addition, it has also been demonstrated that caspases can inhibit the formation of LTP (see Li and Sheng, 2012).

Moreover, Caspase-3, as well as the initiator Caspase-9, have been implicated in the pathogenesis of dementia, including Alzheimer's disease (D'Amelio et al., 2011; Tamayev et al., 2012). In the context of Alzheimer's, Caspase-3 triggers the removal of AMPA receptors, leading to a deficit in hippocampus-dependent memory (D'Amelio et al., 2011). Additional non-apoptotic neuronal roles of caspases lie in the regulation of long-term song-response habituation in birds, of dendrite arbour morphology in *Drosophila*, as well as of long-term sensitization in snails (summarized in D'Amelio et al., 2010). Thus, caspases also mediate long-term plasticity in invertebrates.

2.2.2.2. Local synaptic translation

The list of processes involved in mediating synaptic long-term plasticity can easily be extended further. Additional mechanisms are, for example, the regulation of the transport of both mRNA and of proteins (e.g., receptor subunits), as well as the regulation of protein synthesis, locally at the synapse.

The probably best known pathway for the establishment of long-term memory is cAMP-mediated activation of the transcription factor CREB (reviewed in Benito and Barco, 2010). However, long-term plasticity can also be mediated by the translation of already existing mRNA transcripts. In fact, local translation of synaptic proteins is a key factor for making both maintenance and adaptations at individual and independent synapses within a neuron feasible. Synthesis of proteins occurring directly at synapses has been observed in both mammals and invertebrates (Bramham, 2008; Dubnau et al., 2003; Iacoangeli and Tiedge, 2013; Kang and Schumann, 1996; Sigrist et al., 2000; Sinnamon and Czaplinski, 2011). The mRNAs employed for local translation are trafficked to and distributed at synapses in granules, called ribonucleoprotein (RNP) particles, containing both RNA and associated proteins (Sinnamon and Czaplinski, 2011).

Metabotropic glutamate receptors are principal regulators of local translation. Their activation stimulates protein synthesis at the synapse via ERK1/2 and mTOR signalling (Bhakar et al., 2012). Thus stimulated translation leads, for example, to LTD (Bear et al., 2004; Huber et al., 2000). MGluR-dependent protein synthesis is antagonized by the fragile X mental retardation protein (FMRP) (Fig. 4). Lack of FMRP causes the fragile X syndrome (FXS), the most frequent form of monogenic, inherited intellectual disability in humans (Bhakar et al., 2012). FXS is characterized by altered neuronal development, autism-like behaviour, and hyperactivity. FMRP, encoded by

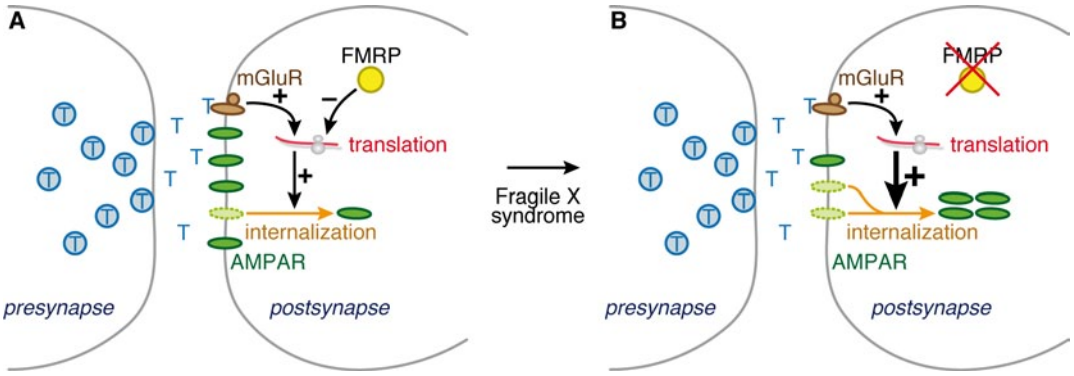

Fig. 4: Simplified illustration of the mGluR theory of the fragile X syndrome.
Activation of mGluRs stimulates synthesis of proteins that promote AMPA receptor (AMPAR) internalization. This process is inhibited by FMRP (A: normal/healthy situation). In the absence of FMRP (fragile X syndrome), mGluR-mediated translation is unbalanced, leading to excess internalization of AMPA receptors and thus to LTD (B: FXS). Both mGluRs and FMRP have more functions than shown here. For example, both mGluRs and FMRP are also involved in LTP.
This scheme is based on information from Oostra and Willemsen, 2009.

the *fmr1* locus, is part of RNP granules, binds mRNA and represses local translation (Bhakar et al., 2012; Iacoagneli and Tiedge, 2013). Loss of FMRP thus leads to excessive mGluR-induced translation of synaptic proteins (Fig. 4)[3]. Accordingly, FMRP is necessary for both LTD and LTP (Sidorov et al., 2013). In flies, FMRP is required for normal synaptic transmission, brain morphology, and activity levels, as well as for different forms of memory (summarized in Bhakar et al., 2012). According to current models, FMRP represses translation by activation of repressive regulatory RNAs and the mRNA silencing complex, as well as by blocking translocation of polyribosomes during the elongation phase (Bhakar et al., 2012; Iacoangeli and Tiedge, 2013; Willemsen et al., 2011).

While many aspects of memory formation could be understood by studying isolated pathways in mammals, this system is still too complex for a systematic examination of the integration of learning processes into behavioural responses. The tools developed for the invertebrate *Drosophila*, however, offer the possibility to examine learning mechanisms during adaptive behaviours *in vivo*.

3. Anatomy of the *Drosophila* CNS

The adult central brain of *Drosophila* is composed of the supraesophageal ganglion, located above the oesophagus, and the ventral subesophageal ganglion, which is attached to the peripheral ventral nerve cord (Fig. 5B; Strausfeld, 1976). The supraesophageal ganglion can be divided into the central cerebrum and the paired lateral optic lobes. The central cerebrum is a bilateral symmetric structure containing about 30,000 neurons (Ito et al., 2013). Alternatively, the supraesophageal is subdivided into three fused neuromeres: protocerebrum, deuterocerebrum, and the ventral tritocerebrum. In *Drosophila*, the tritocerebrum is fused to the subesophageal ganglion (Rajashekhar and Singh, 1994). The antennal lobe (AL) is part of the deu-

[3] Fig. 82, on page 149, illustrates the typical mechanism for loss of FMRP in FXS patients. The corresponding section 2.3 of the discussion contains a more detailed explanation of FMRP.

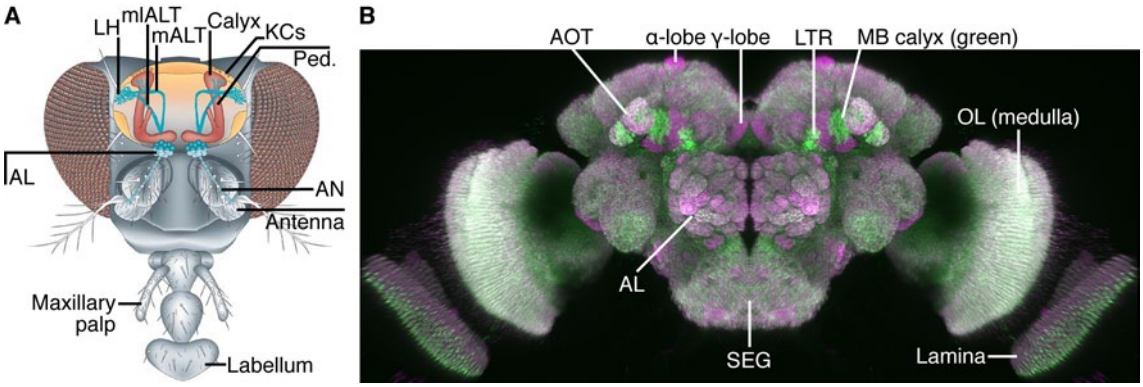

Fig. 5: The central nervous system of *D. melanogaster*.
A: Selected structures of the olfactory pathway, embedded into a cartoon head. See Fig. 6 and Fig. 7 for additional explanations. LH: Lateral horn; mlALT: mediolateral AL tract; mALT: medial AL tract; Calyx: mushroom body (red) calyx. KCs: cell bodies of Kenyon cells; Ped.: MB peduncle; AL: antennal lobe (blue); AN: antennal nerve. Adapted, with permission, from Keene and Waddell, 2007.
B: Neuropil staining of the adult brain. Frontal 3D reconstruction of a confocal stack; immunohistochemical staining; green: Anti-Drep-$2^{C\text{-}Term}$, magenta: Brp^{Nc82}. To simplify the model, the left half of the brain was mirrored to the right side, the right hemisphere was removed. AOT: anterior optic tubercle; α-lobe: tip of the mushroom body α-lobe; γ-lobe: medial end of the MB γ-lobe; LTR: lateral triangle at the central complex; OL: optic lobe; lamina: part of the OL; SEG: subesophageal ganglion.
Of note, both the lateral triangle and the posterior calyx are usually not recognizable in a frontal section showing anterior neuropils like the ALs. However, since anti-Drep-$2^{C\text{-}Term}$ (green) intensely stains these two structures, they are visible in this 3D reconstruction nonetheless.

terocerebrum, most other prominent neuropils belong to the protocerebrum (e.g., optic lobes, mushroom bodies (MBs), and the central complex).

3.1. The olfactory pathway

Flies sense odours via bipolar olfactory receptor neurons (ORNs), which are located in the two external structures called antennae and maxillary palp (Fig. 5A; Vosshall and Stocker, 2007). From there, ORNs project bilaterally to discrete glomeruli of the paired antennal lobes of the brain. There are about 1200 ORNs per antenna, each expressing a combination of odourant receptors (ORs) (Vosshall and Stocker, 2007). About 50 types of ORNs have been described in adult flies, as well as 50-60 different odourant receptors (Wilson, 2013). Each OR is expressed in 10-100 ORNs per antenna. Typically, Or83b, acting as a coreceptor, is expressed together with a second OR (Vosshall and Stocker, 2007). However, also combinations of 2-3 receptors exist, again in combination with Or83b. Thus, most ORNs respond to several molecules and most molecules activate several types of ORNs (Wilson, 2013). The tuning range of ORNs is variable, reaching from narrow to broad or anything in between.

3.1.1. The antennal lobes

At the AL, each ORN expressing the same OR projects to the same glomerulus (Wilson, 2013). Typically, each glomerulus is specific for one OR, an organization similar to the olfactory bulb of mammals. However, some glomeruli receive input from several ORs. The ALs constitute the first relay of the olfactory pathway. Here, information is processed, before it is transmitted further by projection neurons (PNs) to the

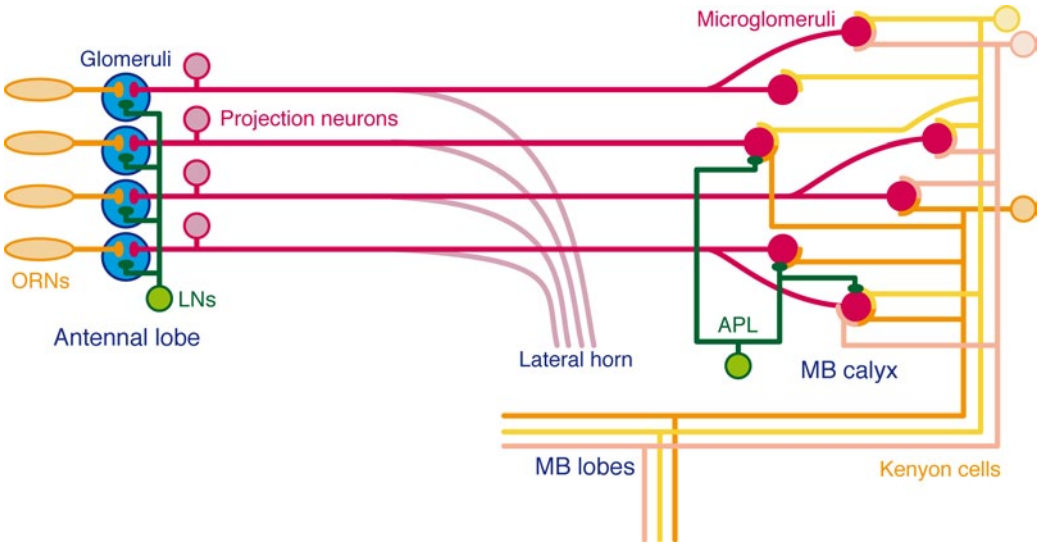

Fig. 6: Simplified wiring diagram of the olfactory pathway in *Drosophila*.
Highly simplified model with arbitrary scales and positions of elements. Not all cells and synapses involved have been included in the diagram. LNs: both inhibitory and excitatory local interneurons. APL: inhibitory anterior paired lateral neuron. The scheme is based on information from Butcher et al., 2012 and Wilson, 2013.

calyx of the mushroom body (MB), as well as to the lateral horn (Fig. 5A; Fig. 6; Fig. 7). Procession of information in the AL involves both excitatory (eLNs) and inhibitory local interneurons (iLNs).

In AL glomeruli, a complex connectivity pattern was unravelled (Yaksi and Wilson, 2010): ORNs synapse onto PNs and iLNs; iLNs onto ORNs, eLNs, and PNs; eLNs onto iLNs and PNs; PNs, in turn, synapse back onto both eLNs and iLNs and also form reciprocal synapses with other PNs in the same glomerulus. PNs typically receive direct input only from a single type of ORN and form groups of cells that carry highly correlated signals (Wilson, 2013). Local interneurons convey lateral inhibition or excitation between glomeruli (Fig. 6). Typically, they innervate most or even all glomeruli. Lateral inhibition renders PN responses more transient and decreases their sensitivity. Thus higher odour concentrations are required for saturation of PN firing rates. The function of eLNs, however, remains unclear.

3.1.2. The mushroom bodies

About 150 projection neurons per hemisphere convey olfactory information from the AL to higher-order centres, i.e. to the lateral horn and the mushroom body calyx (Fig. 5A; Fig. 6; Fig. 7; Vosshall and Stocker, 2007). At the calyx, a substructure of MBs on the posterior-dorsal side of the brain, PNs synapse onto about 2500 Kenyon cells (KCs). Of note, these neurons received their name from a Golgi analysis of the brain of the honeybee, conducted by Frederick C. Kenyon (Kenyon, 1896)[4]. The MB-intrinsic KCs project along the peduncle into the MB lobes, which lie on the anterior side of the brain, close to the ALs.

[4] Unfortunately, F.C. Kenyon was committed to an insane asylum only three years later, "on account of his eccentricities", which put an end to his scientific career (*A Washington Doctor Insane*, The New York Times, November, 25th, 1899).

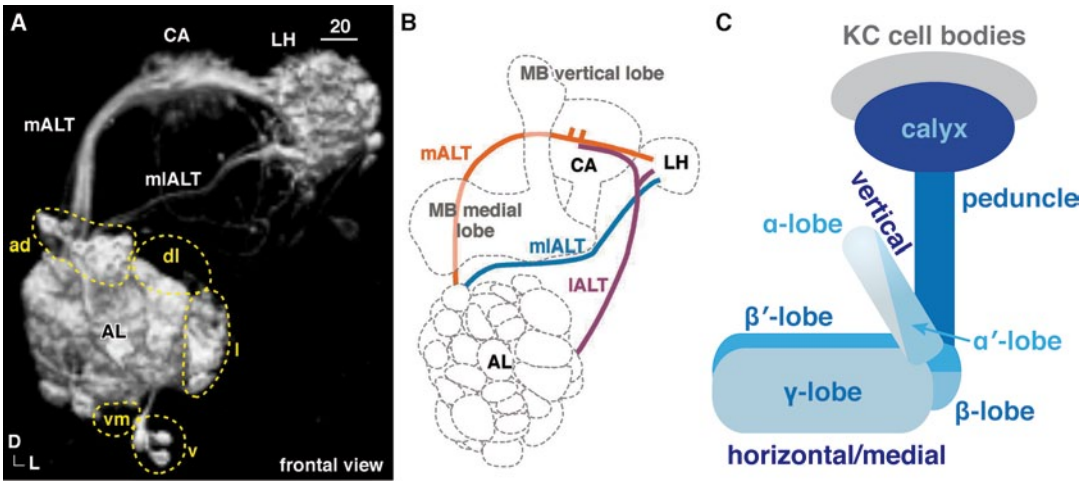

Fig. 7: Projection neurons connect the antennal lobe to the mushroom body.
A: Two major tracts of PNs, connecting the AL to the MB calyx (CA) and the lateral horn (LH): the medial AL tract (mALT) and the mediolateral AL tract (mlALT). D: dorsal; L: lateral; yellow dashed circles: major PN cell body clusters surrounding the AL. Scale bar: 20 µm.
B: Schematic diagram of all three classical AL tracts. Abbreviations as in A, plus lALT: lateral AL tract.
A-B: Adapted, with permission, from Tanaka et al., 2012.
C: Simplified scheme of the mushroom body. Based on information from Tanaka et al., 2008.

MBs are crucial neuropils in insects for several higher brain functions, especially for olfactory associative learning (Dubnau and Chiang, 2013; Heisenberg, 2003). Interestingly, Félix Dujardin suggested already 160 years ago that MBs might be the structures providing insects with a degree of intelligent control over their actions (Dujardin, 1850; Strausfeld et al., 1998).

The synapses of PNs with KCs in the calyx have an easily distinguishable shape in the adult brain, they are thus called microglomeruli (Fig. 8; Butcher et al., 2012; Leiss et al., 2009a; Yasuyama et al., 2002). PNs form large, mainly cholinergic presynaptic boutons, which are tightly surrounded by dendritic claws of KCs (Yasuyama et al., 2002); accordingly, KCs express ACh receptors (Gu and O'Dowd, 2006). The stereotypic arrangement of microglomeruli allows for a comparably easy identification of pre- and postsynaptic compartments, already on the level of light microscopy.

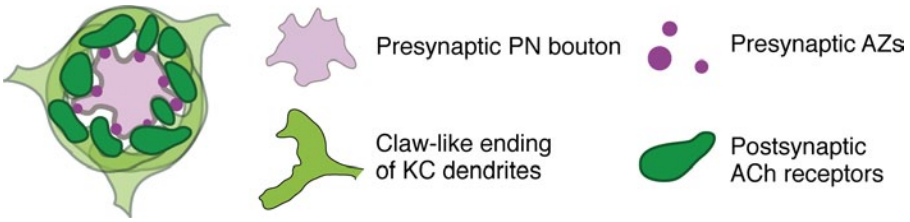

Fig. 8: Scheme of a microglomerulus in the calyx.
The GABAergic APL neuron has not been included. Adapted, with permission, from Kremer et al., 2010.

Naturally, the complexity of synaptic connections in the calyx is higher than outlined so far (and in Fig. 6). Moreover, the exact connectivity still remains unclear, especially regarding extrinsic neurons. It has been demonstrated that several types

of MB-extrinsic cells form synapses in the calyx, for example cells releasing biogenic amines like dopamine or octopamine (Aso et al., 2012; Butcher et al., 2012; Pech et al., 2013). Furthermore, the GABAergic, inhibitory anterior-paired lateral (APL) neuron broadly innervates the calyx (Fig. 6; Liu and Davis, 2009). Moreover, we could recently show that KCs themselves also form presynapses in the calyx (Christiansen et al., 2011). Thus, KCs are not purely postsynaptic here, as previously assumed. However, the postsynaptic partners of these KC presynapses have not been identified yet.

KCs can be broadly distinguished into three classes: αβ, α'β', and γ neurons, which project into the MB lobes of the same names (Fig. 7C; Tanaka et al., 2008)[5]. The peduncle connects the posterior calyx to the anterior lobes. At its anterior end, αβ and α'β' axons branch to form vertical and horizontal (also called: medial) lobes. The vertical lobe is shaped by α and α' axons, the horizontal lobe by β, β', and γ projections. Of note, γ KCs do not bifurcate. Due to this peculiar anatomy of MB lobes, these paired neuropils are easily recognizable in insect brains. In the lobes, KC receive additional input, for example from dopaminergic cells (Aso et al., 2012; Qin et al., 2012). They synapse onto various, largely unknown MB-extrinsic cells; for example, KCs are connected to ring cell neurons of the central complex (Wu et al., 2007; Zhang et al., 2013).

3.2. The central complex

The central complex is an additional, anatomically distinct structure of the protocerebrum. It is located on the midline of the brain and can be further subdivided into four substructures: the protocerebral bridge, situated in between the calyces, the fan-shaped body, the ellipsoid body, as well as the noduli (Fig. 9; Young and Armstrong, 2010). While all of these structures are bilaterally symmetric, only the noduli are paired neuropils. The lateral triangle and the ventral bodies are two additional neuropils associated with the central complex. The central complex is important for several higher brain functions, for example locomotor control and visual learning (Kong et al., 2010; Neuser et al., 2008; Strauss, 2002).

Ring cells are the major class of large-field ellipsoid body neurons, their arborizations form the eponymous ellipsoid ring. Their cell bodies lie further lateral and are thus not visible in Fig. 9 (compare Fig. 67C, page 114); most ring cells are postsynaptic in the lateral triangle and then project to the ellipsoid body, where all ring cells are presynaptic (Hanesch et al., 1989; Renn et al., 1999; Young and Armstrong, 2010).

In the lateral triangle, ring cells express both ionotropic (NMDA) and metabotropic glutamate receptors (Kahsai et al., 2012; Wu et al., 2007), as well as nicotinic ACh receptors (Schuster et al., 1993). In addition, they express metabotropic but not ionotropic (Rdl) GABA receptors (Enell et al., 2007; Kahsai et al., 2012; Liu et al., 2007). Moreover, ring cells express metabotropic dopamine and serotonin receptors (Kahsai et al., 2012; Kong et al., 2010). Of note, most of these receptors were attributed to ring cells due to an intense antibody staining in the lateral triangle, overlapping with ring

[5] The anatomy of the mushroom body can also be well recognized in Fig. 81A on page 147, a 3D reconstruction of αβ- and γ-KCs.

cell postsynapses; only NMDA receptors were demonstrated to be expressed in ring cells by more elaborate experiments (Wu et al., 2007).

In turn, different types of ring cells also release a wide range of transmitters at their synapses in the ellipsoid body: ACh, glutamate, dopamine, serotonin, and GABA (Kahsai et al., 2012; Wu et al, 2007). This high variability of both the input into ring cells, as well as of neurotransmitters released by different types of ring cells (and other neurons of the central complex, not discussed here), underlines the importance of the central complex as a higher integration centre.

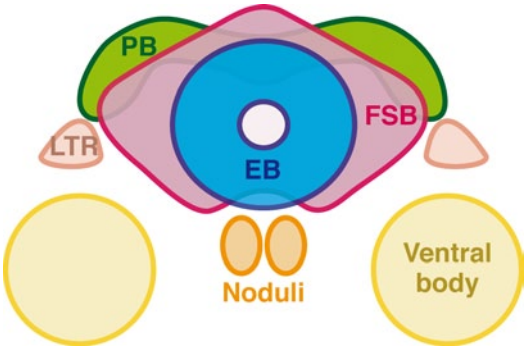

Fig. 9: Scheme of the central complex in *Drosophila*.
EB: Ellipsoid body; FSB: Fan-shaped body; PB: protocerebral bridge; LTR: Lateral triangle. Within this scheme, EB is anterior and medial, PB posterior and dorsal. Based on information from Kahsai et al., 2012 and Young and Armstrong, 2010.

3.3. Genetic tools for the analysis of the *Drosophila* CNS

A major strength of *Drosophila* as a model system is the availability of an extensive array of genetic tools. These tools have been developed since decades, ranging from balancer chromosomes and p-elements (Muller, 1927; Rubin and Spradling, 1982; Thompson, 1977), over the Gal4/UAS system and mosaic analysis with a repressible cell marker (MARCM) (Brand and Perrimon, 1993; Lee and Luo, 1999), to P[acman] artificial chromosomes and the brainbow fly (Hampel et al., 2011; Venken et al., 2006) – to name just a few examples. However, among these, development of the Gal4/UAS system (Brand and Perrimon, 1993) was of exceptional importance, for both the invention of many subsequent tools and the realization of this thesis. Therefore, it will be briefly introduced.

The *gal* family of genes enables various organisms to use galactose as a carbon source. Gal4 is a potent transcription factor from the budding yeast *S. cerevisiae*, binding to a sequence called UAS (galactose upstream activating sequence). Thereby, it recruits DNA polymerase to trigger transcription of any downstream gene (elaborately explained in Ptashne and Gann, 2002). This pair of sequences was adapted for use in *D. melanogaster*, where it is employed as an exogenous binary expression system (Brand and Perrimon, 1993; Fischer et al., 1988).

To this end, both components are typically integrated in the coding sequence of p-element transposons, which can be used for stable transformation of *Drosophila* (Rubin and Spradling, 1982). With the help of these transposons, the *gal4* coding sequence can be inserted pseudo-randomly within the *Drosophila* genome. This mechanism has been employed for an enhancer-trap approach: if the *gal4* sequence is inserted close to an endogenous promoter or enhancer, Gal4-dependent expression

mirrors this element's temporal and spatial expression pattern (Brand and Perrimon, 1993; Kaiser 1993). During the last twenty years, large Gal4-line libraries have been generated using this method, driving expression in a great variety of cells and tissues.

S. cerevisiae also codes for an inhibitor of Gal4, Gal80, which is widely used in *Drosophila* as well: prominent applications are a variant of the inhibitor, Gal80^{ts}, expressed in a temperature-sensitive manner, as well as the MARCM system (Lee and Luo, 1999; McGuire et al., 2003). Both allow for a restriction of Gal4-mediated expression, in one case to defined time spans, in the other to single cells.

4. Selected adaptive behaviours of *Drosophila*

In 1905, Frederic W. Carpenter observed that when he placed flies in glass vessels close to a window, they "accumulated in the greatest numbers on the upper part of the side of the vessel" (Carpenter, 1905). This prompted him to make a more detailed assessment of the behaviour of *Drosophila*, and others followed in his footsteps. Over 60 years later, Seymour Benzer began systematically generating *Drosophila* mutants deficient for specific behaviours, by EMS mutagenesis (Benzer, 1967). Thereby, he established the field of *Drosophila* neurogenetics. At the beginning, he used phototactic responses, just as Carpenter did.

4.1. Aversive olfactory learning and memory

Over the years, mutants defective for more complex behaviours were characterized. In 1974, William Quinn, in Seymour Benzer's lab, devised a method for efficiently assaying aversive olfactory operant conditioning in large numbers of flies (Quinn et al., 1974). First learning mutants were isolated quickly, e.g. *dunce* in 1976, *amnesiac* in 1979, and *rutabaga* in 1982 (Aceves-Piña et al., 1983; Dudai et al., 1976; Quinn et al., 1979). Ten years later, Tim Tully and William Quinn modified the original assay and developed a paradigm for classical conditioning (Tully and Quinn, 1985). To this end, they designed a significantly improved apparatus, which is still being used (Krashes and Waddell, 2011).

In operant conditioning an animal associates the consequences of its own behaviour with a reward or punishment (Siwicki and Ladewski, 2003). The animal learns that it can control occurrence of the reinforcing stimulus by its own actions. By contrast, in classical conditioning two external stimuli of the outside world are being associated. The animal learns that the occurrence of one stimulus likely entails the incidence of a distinct, second stimulus.

In aversive olfactory (classical) conditioning, flies are trained to avoid an odour paired with electric foot shock. Successful learning is tested in a T-maze, in which the two trained odours are presented simultaneously, within the two arms of the machine. Thus, in this form of associative learning, a distinct odour is associated with negative reinforcement, and is subsequently avoided. It was demonstrated much later that sensation of the electric foot shock, the unconditioned stimulus, leads to release of dopamine onto Kenyon cells, which activates adenylyl cyclases (compare section 1.2.2; Fig. 10A; Kim et al., 2007; Schwaerzel et al., 2003).

By contrast, sensation of an odour, the conditioned stimulus, causes increased Ca^{2+} levels in KCs. This increase is likely mediated via Ca^{2+} influx through nicotinic ACh receptors in the calyx (Chorna and Hasan, 2012; Gu and O'Dowd, 2006) and, subsequently, through voltage-gated Ca^{2+} channels (Fig. 10A; Busto et al., 2010). Ca^{2+}, in turn, activates the messenger protein Calmodulin. The detection of coincidence between both stimuli, electric shock and odour, is mediated by the Ca^{2+}/Calmodulin-dependent adenylyl cyclase Rutabaga in the γ-lobes of the mushroom body (Aso et al., 2012; Dudai et al., 1983; Qin et al., 2012; Zars et al., 2000).

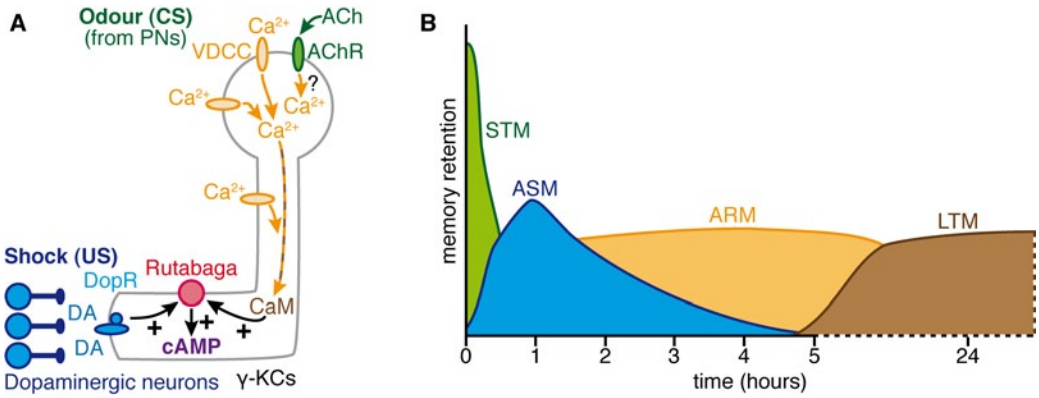

Fig. 10: Associative olfactory learning in *Drosophila*.
A: Coincidence detection in MB Kenyon cells via the adenylyl cyclase Rutabaga.
CS: conditioned stimulus; US: unconditioned stimulus; AChR: nicotinic acetylcholine receptor; VDCC: voltage-dependent calcium channel; CaM: Calmodulin; DopR: dopamine receptor; DA: dopamine. Based on information from Busto et al., 2010 and Gu and O'Dowd, 2006.
B: Illustration of the four major memory phases after aversive conditioning. LTM extends beyond the time shown. Adapted, with permission, from Heisenberg, 2003.

Many of the proteins found to be important for memory formation, both in *Drosophila* and other model systems, are associated with cAMP-dependent signalling. Examples are the cAMP-specific phosphodiesterase Dunce (Dudai et al., 1976; Kauvar, 1982), the cAMP-dependent adenylyl cyclase Rutabaga (Aceves-Piña et al., 1983; Dudai et al., 1988; Isabel et al., 2004), the cAMP-stimulating neuropeptide Amnesiac (Quinn et al., 1979; Waddell et al., 2000), the cAMP-dependent Protein kinase A (Schwaerzel et al., 2007; Skoulakis et al., 1993), as well as the cAMP/PKA-dependent transcription factor CREB (Chen et al., 2012; Yin et al., 1994).

Several forms of memory can be distinguished, which rely on different cells and different proteins: short-term memory (STM), intermediate-term memory (ITM), and long-term memory (LTM) (Fig. 10B; Davis, 2011; Dubnau and Chiang, 2013). ITM can be further subdivided into the entirely distinct forms anaesthesia-sensitive (ASM) and anaesthesia-resistant memory (ARM) (Folkers et al., 1993; Quinn and Dudai, 1976; Scheunemann et al., 2012; Tully et al., 1994). Protein-synthesis-dependent LTM can be separated into an early and a late phase.

Following coincidence detection in γ-neurons, activity in other types of KCs, as well as in MB-extrinsic neurons, is necessary for different aspects of memory formation, consolidation, storage, and retrieval (reviewed in Dubnau and Chiang, 2013). In brief,

for the stabilization of memories, a recurrent loop of activity is established between α'β'-KCs and the electrically coupled GABAerigc APL and serotonergic DPM neurons (Pitman et al., 2011; Wang et al., 2008; Wu et al., 2011). Of note, DPM neurons also release the neuropeptide Amnesiac, which is specifically required for ASM (Quinn et al., 1979; Waddell et al., 2000).

Eventually, long-term memory is consolidated in αβ- and γ-type KCs, as well as in MB-extrinsic cells, likely involving another recurrent activity loop (Akalal et al., 2010; Blum et al., 2009; Chen et al., 2012; Dubnau and Chiang, 2012; Pen et al., 2013). Of note, formation of LTM requires for spaced training protocols, unlike the shorter forms of memory. For memory retrieval, transmission from αβ-KCs is necessary (Krashes et al., 2007). Interestingly, also ring cells of the central complex have been implicated in formation of both olfactory ASM and LTM (Wu et al., 2007; Zhang et al., 2013).

4.2. Courtship conditioning

Courtship conditioning constitutes a different paradigm for associative learning. In this assay, male flies learn from unsuccessful courtship attempts (Siegel and Hall, 1979). Courtship is a complex behaviour, involving the perception of various sensory stimuli and the execution of diverse locomotor actions (for detailed descriptions see Spieth, 1974 and Siwicki and Ladewski, 2003). Moreover, during courtship, males need to adapt their behaviour according to the reactions of the female.

Naïve male flies, which have never encountered a female before, court female virgins persistently (Siegel and Hall, 1979). By contrast, experienced males are defined as flies that were previously in contact with a recently fertilized, and thus unreceptive female. Such males hardly court for several hours afterwards; this reluctance includes courting of receptive virgins for a reduced, and courting of mated females for a longer period of time (Kamyshev et al., 1999).

In conditioned courtship suppression, mated females are employed to train naïve males. Afterwards, the behaviour of the then experienced males towards receptive virgins is assayed. Alternatively, behaviour of the males towards another pre-mated female can be examined (the latter was done in this thesis). As in olfactory conditioning, formation of LTM is triggered by spaced training (McBride et al., 1999). This paradigm is a form of classical conditioning (Siwicki and Ladewski, 2003). The unconditioned stimulus is a combination of aversive behaviour and unattractive pheromones, by which recently mated females repel additional philanderers (Ejima et al., 2007). The conditioned stimulus is represented by positive, aphrodisiac, and thus courtship-stimulating cues.

Many proteins involved in olfactory conditioning also play a role in courtship learning, including the classical factors Dunce, Amnesiac, and Rutabaga (Gailey et al., 1984; Siegel and Hall, 1979). Indeed, as in olfactory learning, dopaminergic input onto γ-type KCs transmits the unconditioned stimulus (Keleman et al., 2012). CaMKII activity in mushroom bodies is essential for consolidation of courtship memory beyond STM (Joiner and Griffith, 2000). Interestingly, also metabotropic glutamate receptors are required for both courtship behaviour and conditioning (Schoenfeld et al., 2013).

4.3. Ethanol-mediated behaviours

The study of ethanol-related behaviours of fruit flies – or, of wine-drinking cellar flies – is, apparently, one of the oldest disciplines of *Drosophila* ethology: Kirby and Spence remarked in their *Introduction to entomology*: "The larva of a little fly (*Musca cellaris*, L[innaeus]; *Oinopota cellaris*, Kirby), whose economy, as I can witness from my own observations, is admirably described by Mentzelius[6]: [it] disdains to feed on anything but wine or beer, which, like Boniface[7] in the play, it may be said both to eat and drink. Though, unlike its toping counterpart, [it is] indifferent to the age of its liquor, which, whether sweet or sour, is equally acceptable." (Kirby and Spence, 1816; with adaptations in punctuation to improve readability). It appears that this little fly, which tempted Kirby and Spence to employ such a peculiar comparison, is indeed *Drosophila melanogaster* (Endersby, 2007).

In recent years, *Drosophila* has been established as a model system for studying the effects of ethanol on the nervous system (reviewed in Devineni and Heberlein, 2013). Ethanol occurs in the natural environment of fruit flies, for example in ripe fruits. Thus, evolution of resistance towards the adverse effects of alcohol-induced intoxication was beneficiary. Moreover, ethanol constitutes an energy source that can be utilized by flies.

Ethanol intake produces similar effects in *Drosophila* as in other animals: low doses stimulate various behaviours, e.g. locomotor activity, high doses act as a depressant (Pohorecky, 1977). Ethanol sensitivity of flies can be measured through an assessment of alcohol-induced locomotion impairment and sedation. To this end, different methods have been established (Cohan and Graf, 1985; Maples and Rothenfluh, 2011; Wolf et al., 2002).

Flies that are exposed to ethanol develop tolerance towards the sedative effects of alcohol. Brief, high-concentration exposure causes rapid, but transient tolerance; prolonged exposure to low doses leads to the establishment of long-term (chronic) tolerance (Berger et al, 2004). Of note, fruit flies can also become addicted to ethanol and show withdrawal symptoms when abstinent (Devineni and Heberlein, 2009; Ghezzi et al., 2012; Robinson et al., 2012). In fact, flies interpret, despite initial aversion, moderate ethanol intoxication as a rewarding stimulus (Kaun et al., 2011).

Interestingly, a large number of genes involved in olfactory learning also mediates ethanol sensitivity and/or tolerance (Berger et al., 2008; LaFerriere et al., 2008; Morozova et al., 2011). This list includes several members of the cAMP pathway: *amnesiac*, *rutabaga*, and genes coding for PKA subunits (Lane and Kalderon, 1993; Moore et al., 1998; Park et al., 2000). Interestingly, flies mutant for the phosphodiesterase *dunce*, which show abnormally high cAMP levels, do not exhibit an altered sensitivity to

[6] A reference to a publication of the 17th century physician Christian Mentzel.

[7] It can be safely assumed that this does neither constitute a reference to medieval Saint Boniface, nor to any pope or antipope of that name, but rather to the heavily drinking innkeeper in George Farquhar's 1707 play "The Beaux' Stratagem": "Boniface: *I have fed purely upon ale; I have eat my ale, drank my ale, and I always sleep upon ale.*" (Act I, Scene I). Of note, Christian Mentzel was not alive anymore when this play premiered in London.

ethanol (Moore et al., 1998). Thus, for normal sensitivity, flies need to be able to increase cAMP levels (Amnesiac, Rutabaga) and to sense such increased levels (PKA).

In general, ethanol affects a large number of proteins and pathways (reviewed in Harris et al., 2008). Primary molecular targets are NMDA receptors, inhibited by ethanol, as well as ionotropic GABA and glycine receptors, enhanced by the compound. Other receptors are involved as well, for example mGluRs (Bird et al., 2005).

Within the fly brain, several neuropils were reported to play a role in mediating ethanol sensitivity or tolerance. Neurons in the pars intercerebralis and the ventral subesophageal ganglion, known to release neuropeptides, are required for normal ethanol sensitivity (Corl et al., 2005; Rodan et al., 2002). By contrast, mushroom bodies are not (Moore et al., 1998). Ring cells (and, in case of tolerance, small-field neurons) of the central complex are essential for both sensitivity and tolerance (Scholz et al., 2000; Urizar et al., 2007). Interestingly, the mGluR-associated protein Homer is required in ring cells for normal ethanol-induced behaviours (Urizar et al., 2007). Moreover, ring cells also mediate ethanol-induced locomotor activity (Kong et al., 2010).

Within this introduction, a brief insight into the complexity of the nervous system of animals in general, and of *Drosophila* in particular was provided. As described in the following chapters, we have strived to slightly increase our understanding of the nervous system by two approaches. In the first study, a method for the characterization of synapse types in the *Drosophila* CNS was developed and applied. In a second study, a novel synaptic protein was examined and described. This protein, Drep-2, was found to be essential for several adaptive behaviours. Moreover, we found evidence that Drep-2 antagonizes FMRP-mediated synaptic protein synthesis.

Materials & Methods

Better to take pleasure in a rose
than to put its root under a microscope.

Oscar Wilde, Intentions

1. Animal rearing and fly strains

ALL FLY STRAINS WERE REARED under standard laboratory conditions (Sigrist et al., 2003) at 25°C, 65-70% humidity and a constant 12/12 hours light/dark regimen. Flies were fed standard semi-defined cornmeal/molasses medium. Bloomington stock collection strain 5905, w^{1118}, was used as background for both the generation of transgenic animals (Bestgene, Inc.) and for behavioural assays.

1.1. Fly strains generated in the context of this thesis

Drep-2^{ex13} mutants were generated by Rui Tian using FLP-FRT recombination between the two stocks *drep-2*^{d00223} and *drep-2*^{e04659}, as previously described (Tian, 2011).

In short, one of the elements containing a FRT site was combined with a line expressing the FLP recombinase under a heat shock promoter. These flies were crossed with the strain containing the second element, to place both FRT sites *in trans*. Expression of FLP recombinase was triggered by a heat shock to 37°C. Offspring was collected; mutant candidates were validated by genomic single-fly PCR:
forward primer: 5'-GCT GCT TGA GTA TGG GTG CA-3'
reverse primer: 5'-GGA GAC ATC CTC TCA AAG C-3'

Other transgenic stocks that were generated (in alphabetical order):

Drep-3^{Donor} (for homologous recombination according to Huang et al., 2009);
P[acman] Drep-2^{GFP}; P[acman] Drep-3^{GFP};

UAS-Drep-2 (not identical with UAS-Drep-2 generated by Rui Tian);

UAS-Drep-3^{Caspase}; UAS-Drep-3^{GFP}.

For details on the generation of these transgenic flies see section 4.1.

For generation of *drep-2*; *fmr1* double mutants, two stable lines were established: *drep-2*^{ex13}/*CyO* ; *fmr1*^{B55}/*MKRS* and *drep-2*^{ex13}/*CyO* ; *fmr1*$^{\Delta 50M}$/*MKRS*

Lack of *fmr1* was validated by single-fly PCR:
Control PCR: forward primer: 5'-AGC GCC CCT TTG CGT CAA CT-3'
reverse primer: 5'-ATG CGG GTG AGT GTG GCG TG-3'
Test PCR: forward primer: 5'-CCG CCG AGG GCA AAC GAA GT-3'
reverse primer: 5'-TCG CCG CCG AAA TGC TTC GT-3'

Lack of *drep-2* was validated by immunostainings.

DmGluRA mutants (*112b*) were validated by single-fly PCR:
forward primer: 5'-GGT GCC CCT TGC GGA CCA AA-3'
reverse primer: 5'-TTG TCG TCT GCG GCA CTG GG-3'

All flies used for behavioural experiments were outcrossed to w^{1118} for more than five generations, in order to generate an isogenic genetic background. W^{1118} flies are mutant for the *white* gene and thus have white instead of red eyes. In some assays, flies with an intact *white* gene (*white*$^{+}$) were required as controls. To this end, red-eyed *Canton-S* (*Canton, Ohio Standard wild strain*) control flies with an intact *white* gene were outcrossed to w^{1118}, while selecting for red eye colour. Thus, these *Canton-S* flies are isogenic to w^{1118}, except for the *white* locus, which they retained from *Canton-S*.

1.2. Previously published fly strains used in this thesis

Gal4 drivers: 121y-Gal4 (Zars et al., 2000), 17d-Gal4 (Melzig et al., 1998), 30y-Gal4 (Yang et al., 1995), appl-Gal4 (Torroja et al., 1999), c232-Gal4 (O'Dell et al., 1995), c305a-Gal4 (Krashes et al., 2007), c42-Gal4 (Renn et al., 1999), c81-Gal4 (Manseau et al., 1997), c819-Gal4 (Renn et al., 1999), d42-Gal4 (Yeh et al., 1995), elav^{c155}-Gal4 (Lin and Goodman, 1994), elav^{L3}-Gal4 (Luo et al., 1994), gad1-Gal4 (Ng et al., 2002), gbr2-Gal4 (Root et al., 2008, received from Dick Nässel), gh146-Gal4 (Stocker et al., 1997), LN1^{NP1227}-Gal4 (Das et al., 2008, received from Silke Sachse), mb247-Gal4 (Zars et al., 2000), krasavietz-Gal4 (Dubnau et al., 2003, received from Silke Sachse), mz19-Gal4 (Ito et al., 1998), ok107-Gal4 (Connolly et al., 1996), ok6-Gal4 (Aberle et al., 2002), or83b-Gal4 (Wang et al., 2003, received from Silke Sachse).

Brp lines: Brp$^{170kDa\text{-}eGFP}$ and Brp$^{190kDa\text{-}mCherry}$ (Matkovic et al., 2013), mb247::brp$^{short\text{-}GFP}$ (Christiansen et al., 2011), UAS-brp^{RNAi} (Wagh et al., 2006), UAS-Brp$^{short\text{-}GFP}$ (Schmid et al., 2008).

Other tagged proteins: mb247::Dα7^{GFP} (Kremer et al., 2010), mb247::Gal80 (Krashes et al., 2007), UAS-ANF^{Emerald} (Burke et al., 1997; Rao et al., 2001), UAS-Dα7^{GFP} (Leiss et al., 2009b), UAS-DmGluRA^{HA} (received from Marie-Laure Parmentier), UAS-Homer^{Myc} (Diagana et al., 2002, received from John B. Thomas), UAS-Liprin-α^{GFP} (Fouquet et al., 2009), UAS-Mito^{GFP} (Pilling et al., 2006), UAS-Synaptotagmin^{GFP} (Zhang et al., 2002).

Mutants: *ark* (several alleles, provided by Thomas Hummel), *DmGluRA^{112b}* and its control *DmGluRA^{2b}* (Bogdanik et al., 2004, provided by Marie-Laure Parmentier), *fmr1^{B55}* (Inoue et al., 2002, received from Bassem Hassan's lab), *fmr1$^{\Delta 50M}$* (Zhang et al., 2001, received from Bassem Hassan's lab), *homer^{R102}* (Diagana et al., 2002, received from John B. Thomas), *p(dICAD)* (*drep-1*, Mukae et al., 2002, reiceived from Shigekazu Nagata), *shakb^{2}* (Phelan et al., 1996; Thomas and Wyman, 1984).

Miscellaneous strains: *Canton-S* (Benzer, 1967), Gal80^{ts} (on IIIrd chromosome, McGuire et al., 2003), UAS-mCD8-GFP (on IIIrd chomosome, stock collection Biozentrum Würzburg), UAS-GCaMP3 (on IIIrd chomosome, provided by Gero Miesenböck's lab; Tian et al., 2009), UAS-p35 (Hay et al., 1994, Zhou et al., 1997), *w^{1118}* (Hazelrigg et al., 1984).

If no other source is stated, flies were either taken from our own stock collection or obtained from the Bloomington stock collection.

2. Imaging

2.1. Immunohistochemistry

2.1.1. Solutions

HL3 (500 mL): NaCl 70 mM, KCl 5 mM, $MgCl_2$ 20 mM, $NaHCO_3$ 10 mM, Trehalose 5 mM, Sucrose 115 mM, Hepes 5 mM, H_2O *ad* 500 mL. Adjust pH to 7.2.

10x **PBS** (1000 mL): 80g NaCl, 2g KCl, 2g KH2PO4, 11.5g $Na_2HPO_4{\cdot}2H_2O$, H_2O *ad* 1000 mL. Adjust pH of 1x PBS to 7.4.

Ringer's solution: 5 mM Hepes-NaOH (pH 7.3), 130 mM NaCl, 5 mM KCl, 2 mM $MgCl_2$, 2 mM $CaCl_2$.

2.1.2. Antibodies

Primary antibodies: rabbit anti-$Brp^{Last200}$ (Depner, 2013) 1:500; mouse Brp^{Nc82} (Wagh et al., 2006, a gift from Erich Buchner) 1:100; guinea pig anti-$Brp^{N\text{-}Term}$ (8GP41, Sigrist lab) 1:800; rabbit anti-$Brp^{N\text{-}Term}$ (5232, Fouquet et al., 2009) 1:350; mouse anti-ChAT (4B1, Yasuyama and Salvaterra, 1999) 1:1000; mouse anti-CSP (ab49, Zinsmaier et al., 1994), 1:40; rat anti-Dα7 (Fayyazuddin et al., 2006, a gift from Hugo Bellen) 1:2000; mouse anti-Dlg (4F3, Parnas et al., 2001) 1:500; guinea pig anti-DmGluRA (GPmG21), 1:500; mouse $DmGluRA^{7G11}$ (Panneels et al., 2003, a gift from Irmgard Sinning's lab) 1:100; rabbit anti-Drep-1 (1098) 1:250 (IHC), 1:1000 (WB); rabbit anti-$Drep\text{-}2^{C\text{-}Term}$ (1783) 1:500; rabbit anti-$Drep\text{-}2^{N\text{-}Term}$ 1:500; rabbit anti-$Drep\text{-}2^{N+C\text{-}Term}$ 1:500; rabbit anti-$Drep\text{-}3^{N\text{-}Term}$ (1093) 1:250 (IHC), 1:1000 (WB); anti-Drep-4 (J173, Yokoyama et al., 2000, a gift from Shigekazu Nagata), 1:400; mouse anti-Fasciclin II (1D4, Lin and Goodman, 1994), 1:50; mouse anti-FMRP (5A11, Okamura et al., 2004, a gift from Mikiko Siomi) 1:10; mouse anti-GFP (3E6, Invitrogen) 1:500; rabbit anti-GFP (A11122, Invitrogen) 1:500; rabbit anti-$GluR^{IID}$ (Qin et al., 2005), 1:500; mouse anti-HA (16B12, Abcam), 1:200; guinea pig anti-Homer (DHNG2, Diagana et al., 2002, a gift from Uli Thomas) 1:200; HRP-Cy5 (Dianova); rabbit anti-Liprin-α (8111, Sigrist lab), 1:100; mouse anti-Myc (9E10, Sigma-Aldrich) 1:500; rabbit anti-$RBP^{C\text{-}Term}$ (9171, Liu et al., 2011) 1:800; rabbit anti-Syd-1 (2850, Owald et al., 2010) 1:500.

Secondary antibodies: goat anti-mouse Alexa 488 (A11001, Invitrogen) 1:500; goat anti-rabbit Alexa 488 (A11034, Invitrogen) 1:500; goat anti-guinea pig Alexa 555 (A21435, Invitrogen), goat anti-rabbit Cy3 (111-167-003, Dianova) 1:500; goat anti-guinea pig Cy3 (106-166-003, Dianova), 1:500; donkey anti-rat Cy3 (712-165-153, Dianova) 1:250; goat anti-mouse Atto 647N (50185, Sigma) 1:200; goat anti-rabbit Atto 647N (40839, Sigma) 1:200.

2.1.3. Staining protocols

2.1.3.1. Wholemount adult brains

Adult brains were dissected in ice-cold hemolymph-like saline (HL3) solution (Stewart et al., 1994), fixed for 20 min in 4% paraformaldehyde (PFA) in phosphate-buffered saline (1x PBS), pH 7.2, and then blocked in 5% normal goat serum (NGS) in PBS with 0.3% Triton X-100 (PBT) for 30 min. The brains were incubated with primary antibodies together with 5% NGS for 48h at room temperature and then washed in PBT for 3h, followed by overnight incubation with secondary antibodies at room temperature. The brains were then washed for 3h with PBT and mounted in VectaShield (Vector Laboratories) on slides. 3-7d old female flies were used for dissections. Of note, in case of donkey secondary antibodies, normal donkey (instead of goat) serum was used for blocking and staining steps.

2.1.3.2. Larval body wall muscle preparations

Stage 3 larvae were dissected in ice-cold HL3 (Stewart et al., 1994) and fixed for 10 min in 4% PFA. For blocking and staining, 0.05% Triton X-100 in PBS was used (plus 5% NGS). Primary antibodies were incubated over night, secondaries for four hours. All other steps as for wholemount brains.

2.1.3.3. Cryostat sections (STED)

12 µm slices were used. Slices were encircled with liquid blocker pen. Incubation with solution containing primary antibodies in PBS with 0.05% Triton X-100 (PBT) and 5% NGS, for 24h at 4°C. Slices were rinsed and washed with PBS for 60 min. Incubation with secondary antibodies for 2h at room temperature. Rinsing and washing for 60 min. Complete removal of liquid blocker with tissues. Mounting with small amount (20 µl) of VectaShield or Mowiol.

2.1.4. Image acquisition

Conventional confocal images were acquired at 21°C with a Leica Microsystems TCS SP5 confocal microscope using a 63x, 1.4 NA oil objective for detailed scans and a 20x, 0.7 NA oil objective for overview scans. All images were acquired using Leica LCS AF software. For detailed scans, lateral pixel size was set to values around 90 nm. Exact values varied, depending on the situation. Typically, 1024x1024 images were scanned at 100 Hz using 4x line averaging.

STED microscopy was performed using a Leica TCS STED setup equipped with a 100x, 1.4 NA oil immersion STED objective, as previously described (Waites et al., 2011). The depletion laser (Mai Tai Ti:Sapphire; Newport/Spectra Physics) was set to 760 nm. 1024x1024 STED images were scanned at 10 Hz using 2x line averaging.

2.2. *In vivo* imaging

Intravital *in vivo* imaging of *Drosophila* larvae was conducted as described in Andlauer and Sigrist, 2010. Typically, 512x512 images were scanned at 400 Hz without averaging.

2.3. Image post-processing and analysis

Confocal stacks were processed using ImageJ software (http://rsbweb.nih.gov/ij). Deconvolution of conventional images was done using MediaCybernetics AutoQuant X2.1.1. STED images were processed using linear deconvolution software integrated into the Imspector software bundle (Max Planck Innovation GmbH). For visualization, contrast was adapted using the levels tool in Adobe Photoshop CS4, where necessary. Images shown in a comparison or quantified were processed with exactly the same parameters. Of note, images were not post-processed before quantification, but exclusively afterwards and only for visualization.

Cell body counts were quantified similarly as described previously (Christiansen et al., 2011; Kremer et al., 2010). The area of interest was segmented in ImageJ and after-

wards analysed in Bitplane Imaris v6.23 using the surface tool. Other analyses were conducted in ImageJ, as outlined in Andlauer and Sigrist, 2010.

2.4. Functional calcium imaging

For Ca^{2+} imaging, GCaMP3.0 (Tian et al., 2009) was expressed in MBs under control of mb247-Gal4. 3-5d old female flies were briefly anaesthetized on ice and immobilized in a small chamber under thin adhesive tape. A small window was cut through the adhesive tape and the cuticle of the head capsule using a splint of a razor blade. Tracheae were carefully removed and 2% low-melting agarose was applied to reduce the movement of the brain. The exposed brain was then covered with Ringer's solution.

Odours (4-methyl-cyclohexanol and 3-octanol, diluted in mineral oil 1:100 and 1:150, respectively) were applied to the flies' antennae for 2s each, using a custom-built olfactometer at an air flow rate of 1 l/min. Three consecutive odour stimulations were applied to each individual fly.

Optical imaging was performed using a two-photon microscope (Zeiss LSM 7 MP) equipped with a Ti-sapphire Chameleon Vision II laser (Coherent) tuned to 680–1080 nm, a Zeiss band-pass filter for GFP emission and a Zeiss W Plan-Apochromat, 20× / 1.0 NA DIC VIS-IR water immersion objective. Images were acquired at a frame rate of 5 Hz with an excitation wavelength of 920 nm using the Zeiss ZEN software.

Images were aligned using the ImageJ plugin TurboReg (Thévenaz et al., 1998) to reduce slight movements. Fluorescence emission was determined within a region of interest (ROI) covering the tip of the α lobe of one mushroom body per fly. Changes in fluorescence emission were calculated as $\Delta F/F_0$, where F is the fluorescence measured at each time point and F_0 the baseline fluorescence before odour stimulation. F_0 is calculated as the average of five frames before odour onset. For the analysis, the $\Delta F/F_0$ values of the three consecutive odour stimulations were averaged. For creating false-colour coded images, three frames of baseline fluorescence before odour onset were averaged, subtracted from the average of three frames covering the peak of the increase in fluorescence, and divided by the averaged baseline fluorescence.

2.5. Immunoelectron microscopy

Immunoelectron microscopy was performed by Christine Quentin. Brains where dissected in HL3 solution and fixed for 20 min at room temperature with 4% paraformaldehyde and 0.2% glutaraldehyde in a buffer containing 50 mM sodium cacodylate and 50 mM NaCl at pH 7.5. Afterwards, brains were washed twice in the buffer and dehydrated through a series of increasing alcohol concentrations. Samples were embedded in LR-Gold resin by incubation in ethanol / LR-Gold 1:1 solution over night at 4°C, followed by ethanol / LR-Gold 1:5 solution for 4h at room temperature and, finally, 3x with LR-Gold / 0.2% benzil once over night, then for 4h and again over night. Thereafter the brains were placed in BEEM capsules covered with LR-Gold / 0.2% benzil resin and placed under a UV-lamp at 4°C for five days to allow for polymerization of the resin.

Following embedding, 70-80 nm sections were cut using a Leica Ultracut E ultramicrotome equipped with a 2 mm diamond knife. Sections were collected on 100 mesh nickel grids (Plano GmbH, Germany) coated with 0.1% Pioloform resin and transferred to a buffer solution (20 mM Tris-HCl, 0.9% NaCl, pH 8.0). Prior to staining, sections were blocked for 10 min with 0.04% BSA in buffer. Sections were incubated with the primary antibody in blocking solution over night at 4°C. After washing 4x in buffer, sections were incubated in buffer containing the secondary antibody (goat anti-rabbit 10 nm colloidal gold, British Biocell, 1:100) for 2-3h at room temperature. Finally, the sections were washed 4x in buffer and 3x in distilled water. Contrast was enhanced by placing the grids in 2% uranyl acetate for 30 min, followed by 3x washing with water and, afterwards, incubation in lead citrate for 2 min. Afterwards the grids were washed 3x with water and dried.

Images were acquired on a FEI Tecnai Spirit, 120kV transmission electron microscope equipped with a FEI 2K Eagle CCD camera.

3. Ratiometric analysis of presynaptic proteins

We quantified ratios of antibody stainings of presynaptic proteins. To this end, we calculated the ratio between two antibody signal intensities for each pixel of an image stack. The method is outlined in section 1.2 of the results chapter. Here, some additional details will be provided.

The analysis was conducted with help of the related applications Fiji (http://fiji.sc) and ImageJ (http://rsbweb.nih.gov/ij). For semi-automated analysis, a collection of plugins was generated. These plugins can be downloaded, along with their source code and documentation at http://ratios.andlauer.net. Thus, the complete analysis can be reproduced by examination of the published source code. The last *commit* to the GIT repository at http://ratios.andlauer.net used for analysis of data displayed in this thesis is *ec2ff55*, August, 15th, 2013. However, the basic algorithms have not been significantly altered since the initial *commit* to the repository in September, 2012.

3.1. Segmentation and Thresholding

The neuropil of interested was segmented using the Fiji plugin *Segmentation Editor* (Schindelin et al., 2012; Schmid, 2010). This approach was equivalent to previously published segmentations (Christiansen et al., 2011; Kremer et al., 2010). Masks for segmentation were saved in the Amira file format.

To retain only the relatively brightest (synaptic) signal, segmented neuropils were thresholded in the following manner (plugin *Mask Generator*, class *Mask_Generator.java*):

1. *Segmentation*
   1.1. Generation of segmentation masks using *Segmentation Editor*.
   1.2. RGB merge of the individual channels of the original image stack.
   1.3. Conversion of the RGB image into a single 8 bit grayscale channel. Thus, all channels of the stack contribute equally to finding the threshold.

1.4. All pixels in the image stack generated in step 1.3 that are not part of the segmentation mask from step 1.1, are set to an intensity of 0 (*Mask_Generator* function *createMask*).

2. *Percentile thresholding*

2.1. In order to find a threshold that preserves only the brightest pixels in the masked image stack generated in step 1.4, percentile thresholding is used (Doyle, 1962).

To understand the basic approach, consider an example were only the 20% of pixels that are the brightest should be kept. If all pixels that are among the brightest 20% were part of group *A*, all dimmer pixels would be in group *B*.

To separate *A* from *B*, intensities of all pixels within the masked stack are counted and the threshold is set to the value separating pixels into the two desired populations *A* and *B*.

2.2. If the image stack contains more than 30 slices (i.e. 30 single image planes), the stack is divided into substacks prior to computing the threshold. Each substack has a size of at least 30 slices.

This is required, since absolute intensities within a stack vary: the deeper one penetrates into neuronal tissue, the lower the absolute intensity.

The number of pixels per masked image plane is not constant. In the centre of the stack, masks typically cover a large portion of the image plane. By contrast, towards the upper and lower ends of the stack, often only a small area of the slice is included in the mask.

Moreover, the pixels at each end of the stack are likely brighter or dimmer than the average intensity of the complete stack. For these two reasons, the outcome of percentile thresholding is dependent on the number of pixels included in the calculation of the optimal threshold.

Accordingly, if thresholds are calculated for a substack that is too large, thresholds are not optimally representative for the absolute intensities of pixels in all slices. If, however, substacks are too small (1 substack = 1 slice, in an extreme case), calculated thresholds differ strongly between stacks and no homogenous population of pixels is acquired. A threshold calculated from 1000×1000 = 1,000,000 pixels is likely more reliable than one calculated from 10×10 = 100 pixels.

Thus, a compromise regarding the size of substacks is required: substacks containing a minimum of 30 slices each were found to produce reliable thresholds. Comparisons with manually chosen values confirmed that these thresholds were suited for proper separation of bright, synaptic signal from dim, non-synaptic background staining.

2.3. Substacks are determined in the following manner:

2.3.1. n = number of slices contained in the image stack.
If n>30, substacks are generated.

2.3.2. Empty slices not containing any masked pixels are temporarily removed;
e = number of empty slices.

2.3.3. *s* = number of substacks = (*n*-*e*) / 30. *s* is rounded down.
For example, if *n*=90 and *e*=7, *s*=83/30=2.

2.3.4. The last substack can be smaller or larger than the others, to compensate for rounding errors. In the example shown above, the first substack contains 42 slices, the second 41.

2.4. Calculation of the actual thresholds was adapted from Gabriel Landini's *AutoThresholder* class, part of the ImageJ code. In brief, histograms for each substack are calculated, followed by determination of the threshold value according to the *percentile* algorithm (Doyle, 1962), ported to MATLAB by Antti Niemisto in 2004 (GPL license). The percentage of pixels to be retained can be chosen by the user. Computation of thresholds was implemented in the *Mask_Generator* function *execThresh*.

2.5. Next, thresholds calculated for substacks are interpolated, in order to assign an individual threshold to each slice. This had the following reason: if thresholds varied between substacks, neighbouring slices at the ends of substacks could receive vastly different thresholds.

For example, slice *A* is the last slice of substack *S1*, slice *B* the first slice of substack *S2*. Slice *B* follows directly after slice *A* and the signal in both is probably highly similar. The threshold found for substack *S1* is 50, the one for substack *S2* is 60. Thus, without interpolation, the threshold for slice *A* is 50 and for slice *B* 60. By contrast, if thresholds are interpolated, both slices *A* and *B* receive the threshold value 55. At the same time, the centre slices of substacks *S1* and *S2* retain the values 50 and 60, respectively.

2.5.1. The percentile threshold determined in 2.4 is assigned to the centre slice of each substack.

2.5.2. Individual thresholds are interpolated for each single slice, so that a smooth transition from one threshold/slice to the next is achieved, spanning the borders of substacks. The thresholds calculated in 2.4 and assigned to the centre slices thus merely constitute the minimum/maximum values of the threshold distribution.

2.5.3. The average threshold of all slices is shown to the user as an indication.

2.6. Finally, the individual thresholds are applied to each slice, substacks are recombined into one stack and empty slices that were temporarily removed from the ends of the stack (step 2.3.2) are added again.

2.7. The final product of *Mask_Generator* is a 3D mask, indicating the positions of the pixels to be included in the calculation of ratios.

The thresholds were determined from a signal combining all channels of the recording (steps 1.2, 1.3).

3. For masks of antibody stainings containing two channels, *Mask Generator* was used with the percentile threshold 0.8.
For masks of the GFP signal, *Mask Generator* was used with the percentile threshold 0.95.

3.2. Calculation of ratio values

Ratios were calculated in the following manner (plugin *Ratio Calculator*, class *Ratio_Calculator.java*):

1. *Generation of ranks (function rankGenerator, called by calcRatio)*

1.1. Ratio values are calculated for every pixel of an image stack. A typical image stack contains over 150 million pixels in total (1024×1024×150). The most precise data type for storage of floating point values (real numbers) in the programming language *Java* is *double*. Each *double* value requires 64 bit of memory, thus more than 1.2 Gigabyte per image stack. Therefore, storage of and calculations with data in this format are impractical.

Since, in the case of 8 bit images as input, only 39641 different ratio values can occur (for an explanation see results, section 1.2.2), each real ratio number is mapped in ascending order to an integer, ranging from 1 to 39641. Accordingly, the ratio 1/1 corresponds to 19821 and 255/0 to 39641. Ratio values can thus be stored in a smaller data type, *short*, requiring only 16 bit per value. These uniformly distributed ratio values can be saved for each pixel in the format of a 16 bit TIFF stack.

To save more memory during execution of the plugin, individual ratio values are not stored at all, unless requested by the user. Instead, merely the frequency with which each ratio value occurs is counted. However, the original ratio values can easily be reconstructed for each pixel, if the ratio image stack is saved in 16 bit format (this constitutes an optional decision of the user).

1.2. Handling of the value 0

- Raw ratio values range from 0 (0/255) over 1 (1/1) to infinity (255/0). However, the value 0 has to be handled especially. First, divisions by zero (e.g., $x/0$) do not produce a real number. Second, a ratio of 0/0 has to be considered as 1, because in such a case the signal of both stainings is equally low. Third, it is desired that ratios show a smooth, uniform distribution, without large steps at the end of the distribution.
- In order to create a relatively uniform sequence of ratios, any ratio $0/n$, $1 \leq n \geq 255$, was defined as $1/(255 \times 4) = 0.000928$ instead of 0; any ratio $n/0$ was defined as $255 \times 4 = 1020$ instead of *infinity*.
- To avoid divisions by 0, an alternative calculation of ratios is possible: the ratio r of two values a and b can also be calculated by the formula $r = (a\text{-}b)/(|a|+|b|)$ instead of $r = a/b$. This is implemented as an optional choice for the user.

  For the data presented in this thesis, the ratio $r = a/b$ was used. The formula $r = (a\text{-}b)/(|a|+|b|)$ produces a uniformly distributed ratio, ranging from -1 to +1. However, information is lost: the calculation yields, in the case of a=4 and b=1, r=0.6. By contrast, the formula $r = a/b$ produces, in the same case, the result r=4. In the latter case, it is directly recognizable that a is enriched 4-fold over b.

1.3. A ratio/rank table is generated containing all possible 8 bit intensity values for pixels *a* and *b*, the value *r* of the ratio *a*/*b*, as well as the corresponding, uniformly distributed rank (see step 1.1).
A random example from this matrix is: $a = 1$, $b = 2$, $ratio = 0.5$, $rank = 9911$.
The complete table can be displayed by executing the plugin *Show ratio table*.

2. *Calculation of ratios (function calcRatio)*

2.1. For each pixel (voxel) of the 3D image stack, the algorithm checks whether the pixel is part of the mask calculated by *Mask_Generator* (explained previously, in section 3.1). If the pixel is not part of the mask, the pixel is ignored.

2.2. If the pixel is part of the mask, absolute intensity values for both channels are determined. Corresponding ratios and ranks are looked up in the matrix generated by *rankGenerator* and thus do not need to be calculated again.

2.3. In the analysis presented in this thesis, ratios were ignored if one of the two channels was saturated for the respective pixel (i.e. had a value of 255). Otherwise, statistics would have potentially been skewed.

2.4. If the user chooses to save ratios as an image, all ratio values are stored as 16 bit values in form of an image stack.

2.5. For calculation of ratio statistics and histograms, ratio values are not stored. Instead, frequencies of ratios are directly counted for all possible 39641 bins. This approach saves a large amount of memory. In this manner, statistics and histograms can be calculated even for huge stacks, without running out of memory. Thus, in case of large image stacks, the option to generate a ratio image should be deselected.

2.6. The ratio image is displayed with a special colour code (lookup table), shown in Fig. 19. Ratios close to 1:1 are shown in black, negative values, in descending order, in magenta-blue-cyan, positive values, in ascending order, in green-yellow-red.
This lookup table can be downloaded as the file *Ratio Spectrum.lut*.

3. *Calculation of statistics and histograms*

3.1. To summarize ratios of an image stack, rank-based statistics are calculated: minimum, lower quartile, median, upper quartile, and maximum values (function *calcStats*).

3.2. Histograms are computed and normalized by the total amount of data, to ease comparisons between image stacks containing different amounts of slices and different masks (function *calcHisto*).

3.3. Statistics, as well as normalized and original histogram values, are saved and can be used for additional analyses (see section 3.3).

4. *Generation of scatter plots*

Scatter plots of the intensity values of both channels can be displayed (function *generate_Scatter*). However, scatter plots were not used in the analyses conducted here.

3.3. Analysis of ratiometric results and statistics

The following analyses of ratio data can be (and were) conducted using the plugin *Ratio Analysis* (class *Ratio_Analysis.java*). In each analysis, text files containing the output and scripts that can be used for plotting the data with GnuPlot are generated.

1. *Calculation of mean statistics (function basicAnalysis)*
   - *Ratio Calculator* computes the following values for each image stack (see section 3.2, item 3.1): minimum, lower quartile, median, upper quartile, and maximum ratio value.

     For the calculation of mean statistics, a data set consists of a number of such values. For example, the median ratios of ten different image stacks, all belonging to the same genotype. Each image stack is one sample.
   - *Ratio Analysis*, as used in the analysis presented here, calculates mean values and standard errors of the mean (SEMs) of these parameters, for a number of image stacks. If s is the standard deviation of a data set and n is the number of samples, the SEM e is $e = s/\sqrt{n}$.
   - Alternatively, median values and standard errors of the median can be calculated, according to Sachs, 2003:
     standard error of the median = $e = (a\text{-}b) / 3.4641$,
     where a is the $a = (n/2 + \sqrt{(3\times n)}/2)$th observation
     and b is the $b = (n/2 - \sqrt{(3\times n)}/2)$th observation,
     each rounded up to the next integer; n = number of samples.
   - As a third possibility, median values and median absolute deviations can be calculated. The median absolute deviation corresponds to the median of the differences of the individual values to the median. Thus, first, each value is subtracted from the median. Second, the median of these values is the median absolute deviation.

2. *Calculation of mean histograms (function basicAnalysis)*
   - Either mean or median values for the frequency bins of several histograms are calculated. Each individual histograms is generated by *Ratio Calculator* from one image stack and constitutes one sample of a data set.
   - The available options for calculation of errors are as described for *mean statistics* (SEM, standard error of the median, median absolute deviation). In the analysis presented here, mean frequencies plus SEMs were used.
   - In addition, the function generates an image similar to a contact sheet, which shows a comparison of all individual histograms.

3. *Calculation of mean scatter plots (function basicAnalysis)*

   This calculation is done in an analogous manner to the previous ones.

4. *Comparison of several data sets (groups) (function compAnalysis)*
   - This module uses data generated by module 1, *mean statistics*.
   - It generates scripts that allow GnuPlot to plot combined graphs for several data sets (e.g., for several genotypes).

- In addition, the data sets are being compared in groups of two, by either Mann-Whitney U-tests or T-tests. For these tests, the Apache Commons Library *Math* v3.3.0 is employed, classes *MannWhitneyUTest* and *TestUtils*, respectively.

5. *Normalization of a data set to a reference data set (module "Ratio of two groups", function normAnalysis)*

   The module was not used in the analysis presented in this thesis.

   - Both data sets need to be dependent on each other. A possible application is the normalization of a subset of a neuropil to the complete neuropil. For example, a GFP-labelled subset is compared to the complete neuropil surrounding it. Thus, the first sample of data set 1 is derived from a subset of pixels used for calculation of the first sample in data set 2.
   - For each sample, values of the first set (e.g. the median ratio of the GFP label, first brain) are divided by the corresponding values of the second set (e.g. the median ratio of the entire neuropil, first brain).
   - Options for uncertainties (SEM, standard error of the median, median absolute deviation) are analogous to the ones in module 1, *mean statistics*.
   - Two data sets are compared, each carrying an uncertainty of its own. Thus, final uncertainties are calculated using Gaussian error propagation (Papula, 2008). Calculation of the uncertainty e in case of division of two values x,y with corresponding uncertainties s_x,s_y: $e = \sqrt{((s_x/x)^2 + (s_y/y)^2)}$.

6. *Generation of fingerprints (function fingerAnalysis)*

   This module uses data generated by module 4, *compAnalysis*.

   Ranks are calculated in a similar manner as the one used for determining ranks in *Ratio Calculator* (see section 3.2, item 1). However, here, 8 bit ranks are computed, ranging from 0-255. Moreover, a different type of ratio is used, as explained in the next items.

   6.1. The input file contains pairs of samples that are to be compared:
   e.g., line 1: *a*, statistics of complete neuropil, genotype 1;
   line 2: *b*, statistics of pixels labelled by GFP, genotype 1.

   6.2. Median values are used to calculate the ratio $r = (|b|-|a|)/(|a|+|b|)$.

   6.3. The corresponding 8 bit rank is looked up in the rank matrix.

   6.4. Calculated ratios are saved as text files and ranks are displayed/saved as images, with the same colour code (lookup table) used for display of ratio values in *Ratio Calculator* (see Fig. 19). Ratios close to 1:1 are shown in black, negative values in magenta-blue-cyan, positive values in green-yellow-red.
   These images constitute a signature for each analysed situation and are thus called *fingerprints*.

7. *Calculation of relative distributions (function propAnalysis)*

   This modules determines the relative distribution of ratio values, i.e. the relative proportions of low, balanced, and high ratio values in a data set.

7.1. Here, ratio values between 0.95 and 1.05 are considered as balanced, ratios <0.95 as low, and ratios >1.05 as high.

7.2. Frequencies of ratios are counted for each of these three bins, final frequencies are relative to the total amount of data.

7.3. In addition, this module calculates the number of pixels that were used for the calculation of ratios in each sample, as well as the mean number of pixels included in a complete data set.

7.4. Data generated by this module was used for calculating the Bayesian conditional probability that a single, random spot with a certain property r (e.g. a high ratio a/b) is part of a certain population t of pixels: $p(t|r) = p(r|t) \times p(t)/p(r)$.

- $p(t)$ is the probability that any pixel in the neuropil is part of the population t. For example, this can constitute the relative amount of pixels labelled by GFP within a neuropil. This value can thus be computed by dividing the numbers of pixels positive for GFP by the total number of pixels covering this neuropil.
- $p(r)$ is the probability that any random pixel in the neuropil has the distinct ratio r. This corresponds to the proportion of all pixels with this property r in the complete neuropil (e.g., a high ratio a/b).
- Finally, $p(r|t)$ is the probability that any pixel positive for GFP (and thus part of t) has the distinct ratio r, which corresponds to the proportion of all pixels with this property r in the GFP-labelled subset t.
- Thus, all three probabilities required for the calculation of conditional probabilities are estimated by this module.

8. *Subtraction of two histograms (function subtractHistos)*

This module uses data generated by module 2, *mean histograms*.

- Two histograms are subtracted, e.g., frequencies of ratios of pixels labelled by GFP from the frequencies calculated for the complete, surrounding neuropil.
- Frequencies are subtracted for each bin.
- Two data sets are compared, each carrying an uncertainty of its own. Thus, final uncertainties are calculated using Gaussian error propagation (Papula, 2008). Calculation of the uncertainty e in case of subtraction of two values x,y with corresponding uncertainties s_x,s_y: $e = \sqrt{((s_x/2)^2 + (s_y/2)^2)}$.

3.4. Additional modules

1. For masks of antibody stainings containing three channels (plus the segmentation mask), *4-Channel Mask Generator* (class *Mask_Generator_Triple.java*) was used, percentile threshold 0.8. This plugin functions analogously to the standard *Mask Generator*.
2. For the calculation of intensity statistics, *Intensity Calculator* was used (class *Intensity_Calculator.java*), which functions analogously to *Ratio Calculator*.
3. For the analysis of intensity data, *Intensity Analysis* was used (class *Intensity_Analysis.java*), which functions analogously to *Ratio Analysis*.

4. Molecular cloning

Molecular cloning was done according to standard protocols (Sambrook and Russell, 2000). T4 Ligase was purchased from Roche, restriction enzymes from Fermentas (now part of Thermo Scientific). Elongase (Invitrogen), Vent (New England Biolabs) or AccuStar (Eurogentec) polymerases with proofreading activity were used for polymerase chain reactions (PCRs). Oligonucleotides were obtained from Eurofins MWG Operon; the same company was used for DNA sequencing services.

4.1. Constructs for the generation of transgenic flies

4.1.1. UAS constructs

***Drep-2*:** Rui Tian generated transgenic flies expressing either plain *drep-2* cDNA or eGFP-/mStrawberry-tagged *drep-2* constructs, all under the UAS enhancer (Tian, 2011). In the context of this thesis, the following of her constructs were used: UAS-^{eGFP}Drep2 (N-terminal eGFP tag, vector *pTGW*); UAS-^{mStrawberry}Drep2 (N-terminal mStrawberry tag, *pTSW*); UAS-Drep2^{mStrawberry} (C-terminal mStrawberry tag, *pTWS*). Invitrogen gateway cloning was used to create the eGFP and mStrawberry constructs from *pEnter*. For eGFP, *pTWG* and *pTGW* vectors were used (Carnegie Institution of Washington); for mStrawberry constructs, eGFP was replaced with mStrawberry by PCR to create *pTWS* and *pTSW* plasmids (plasmids were previously used in Banovic et al., 2010). All three tagged versions of Drep-2 worked equally well.

***pEnter drep-2*:** New pEnter-drep2 and UAS-drep2 (*pTW*) constructs were generated. To this end, the *drep-2* cDNA *LD32009* was amplified using:
forward primer: 5'-CAT GCC ATG GCA ATG GCC AGA GAG GAG TCT CGC-3'
reverse primer: 5'-CGG GGT ACC AAT TCT GTC CTC CTC ATC CTC TTCC-3'

The amplicon was inserted into the *pEnter* vector using *Nco*I and *Kpn*I restriction sites. *pEnter* is the *pENTR4* vector (Invitrogen) without the *chloramphenicol resistance* and *ccdB* genes but with additional restriction enzyme sites. w^{1118} was used as a background for generation of transgenes (BestGene, Inc, CA).

***pEnter drep-3*:** pEnter-drep3 was generated from the cDNA *RH09855* (DGRC) using the following primers:
forw. primer: 5'-CAT GCC ATG GCA ATG ACA GCA ATG AAT GCG GAT GAG AC-3'
rev. primer: 5'-CGG GGT ACC GCA AGA CAA TTC CGT TGA TAG CCG T-3'

The amplicon was inserted into the *pEnter* vector using *Nco*I and *Kpn*I.
pEnter-drep3 was used for the generation of UAS-^{eGFP}Drep3 (N-terminal eGFP tag, *pTGW*) and UAS-Drep3^{eGFP} constructs (C-terminal eGFP tag, *pTWG*) by Gateway cloning.

***pEnter drep-3^{Caspase}*:** pEnter-drep3^{Caspase} codes for Drep-3 with mutated putative caspase cleavage sites. Drep-3 is predicted to be cleaved by caspases. The stretch of sequence that is predicted to contain several cleavage sites is shown in Fig. 79. The core amino acid sequences of the respective cleavage sites are: DADD, DGLD, GLDD, and DAAD. To generate a mutated *drep-3*, a new, altered cDNA was synthesized (Eurofins MWG Operon), using the sequence of the *drep3-RA* transcript as a base:

CATGCCATGGCAATGACAGCAATGAATGCGGATGAGACAAAGCTGGCT-
GGAATGCCTCAAGGAGCTGAGGAGGAGCAGGAACCGGAGAGGGAGCAGAA-
GAAGGAGAGCGATGGAGCAGCAGCTGCAGCAGGAGTACAGTGTGATCCT-
GATAGCAGAATAGTGGCTCCGCCGCCCAGGCAGCGGACTCTGACAAGGACG-
GCCGAACTGGACGCGGACTGCGAGGACATCGAGTTAGATGCCGAC**TC**TGGTTT-
GG**G**C**TC**TGCGGCGG**G**TAGCATCACCTTGGAGTTGGCCCTATCGCCGCACAG-
CAGCGCCACGCCCACGCCCTCGCCCACCACCGCCGACGAGGATTTCGCCCAGCT-
GGACAACAGCAAGCCCTTCAAGATCAAGGACATCACGAGGAACATCCGCAAG-
GCAGTTGTGGCCACAACGCTGTCGGAGCTGCGGACGAAGGTGTCGCTGAAATTT-
GAGCGGGCTCAGCCGGCGATACACCTGGATTGCGATGGCACCGAGGTCGAC-
GATGAGGAGTACTTCAGCACTCTGGAGCCAAATGCCGAATTGATTGCCGTCTT-
TCCTGGCGAGCAGTGGCGCGATCCCAGTGACTACAATGCCAATCTGCGTCGCA-
CATCGCTGGATGCACAGCGTCTGCGGAGTCTGGTGAGCAAACTGCAGCCGAAC-
TATATGAACGATGATGATTTGGATAAGCTGTCGAACATGGATCCCAACTC-
CCTGGTGGATATCACGGGTCGGGAGCCCAAGGACAACGAATACTCAGCCA-
GAAGCGATGCCGCACGGCTATCAACGGAATTGTCTTGCGGTACCCCG.

The six mutated bases are indicated in bold font. The alterations were: GA→TC, A→G, GA→TC, A→G. This sequence contains an *Nco*I site at the 5' end and a *Kpn*I site at the 3' end. Malou Mampell was so friendly to subclone the sequence into *pEnter*, using these two restriction sites. UAS-drep3^{Caspase} (*pTW*) was generated via Gateway.

4.1.2. P[acman] constructs

***Drep-2* constructs:** Drep-2^{GFP} flies expressing Drep-2^{GFP} under the endogenous *drep-2* promoter were generated by recombineering from the P[acman] BAC clone *CH322-103H19* (Venken et al., 2008). The vector *PL452 C-EGFP* was used for adding a C-terminal eGFP tag to Drep-2. The recombineering followed the reaction described in Venken et al., 2006 and Matkovic et al., 2013 and was conducted by Tanja Matkovic.

PCR reaction:
forward primer: 5'-ACG GCG AGG AGG TCG AGG AGG AGG AGG AAG AGG ATG AGG AGG ACA GAA TTG CAG CCC AAT TCC GAT CAT ATT C-3'
reverse primer: 5'-TGG GAC AGT CAT GAA CCT GTG GGT TTG CCC GTC TGC CTG TCA TTG GCA CTT TAC TTG TAC AGC TCG TCC ATG-3'

Verification of recombination by PCR:
5' arm: forward primer: 5'-GAC CGG CGA GCA TAT ACC ATC-3'
reverse primer: 5'-TAA AGC GCA TGC TCC AGA CTG-3'
3' arm: forward primer: 5'-TTG TGG GCA TGG GTG TAT GTG-3'
reverse primer: 5'-GGT GGG CTC TAT GGC TTC TGA-3'

ΦC31-integrase-mediated site-specific transgenesis was done using the Bloomington stock center fly strain 9732, carrying the insertion site *attP-9A*^{VK00013} on chromosome IIIL (BestGene, Inc, CA). Target site: 9732, cytosite: 76A2 (*fz2* gene, intronic).

***Drep-3* P[acman] constructs:** Drep-3^{GFP} flies expressing Drep-3^{GFP} under the endogenous *drep-3* promoter were generated by recombineering from the P[acman] BAC clone *CH322-86P21*. Recombineering was conducted in an analogous manner to Drep-2^{GFP}, but with the following primers:

forward primer: 5'-CGA ATA CTC AGC CAG AAG CGA TGC CGC ACG GCT ATC AAC GGA ATT GTC TTG CGC AGC CCA ATT CCG ATC ATA TTC-3'
reverse primer: 5'-CTT AAG CTA ACA TAT GTA CGT TAA TTC GTT GAG GGA AAA ATG CAT TCC CTT ACT TGT ACA GCT CGT CCA TG-3'.

Verification of recombination by PCR:
5' arm: forward primer: 5'-CGC CTC CAT TCC AGA TCA AGG-3'
reverse primer: 5'-TAA AGC GCA TGC TCC AGA CTG-3'
3' arm: forward primer: 5'-ACG ACA ATG TGG GCT CGA AAA-3'
reverse primer: 5'-GGT GGG CTC TAT GGC TTC TGA-3'

The construct was inserted into the same site as Drep-2^{GFP} was.

4.1.3. Miscellaneous constructs

We undertook several unsuccessful attempts to create *drep-2* **RNAi**. Details of the strategies that were used are available on request.

Drep-2, -3, and -4 were subcloned into the vector ***pESC-HIS*** for expression in yeast. Primers included a Kozak sequence.

Drep-2 (first forward primer without STOP codon):
forward primer: 5'-GCA TCG ATG CAA TTC TGT CCT CCT CAT CCT CTT CC-3'
reverse primer: 5'-TTT GAA TTC AAA ATG GCC AGA GAG GAG TCT CGC-3'
forward (STOP): 5'-TAA TCG ATT AAA TTC TGT CCT CCT CAT CCT CTT CC-3'
The PCR product was inserted into the vector using *Cla*I and *Eco*RI sites.

Drep-3 (first forward primer without STOP codon):
forward primer: 5'-GCA TCG ATG CGC AAG ACA ATT CCG TTG ATA GCC GT-3'
reverse primer: 5'-TTT GAA TTC AAA ATG ACT GCA ATG AAT GCG GAT GAG AC-3'
forward (STOP): 5'-TAA TCG ATT AGC AAG ACA ATT CCG TTG ATA GCC GT-3'
The PCR product was inserted into the vector using *Cla*I and *Eco*RI sites.

Drep-4 (only without STOP codon):
forward primer: 5'-GCA TCG ATG CAG TGG CTA GAC TGT CCA CCT-3'
reverse primer: 5'-ATA AGA ATG CGG CCG CAA AAA TGA TTA GCT ACA TTA GAG ATG C-3'
The PCR product was inserted into the vector using *Cla*I and *Not*I sites.

pGX-Drep3^{Donor}: For ends-out homologous recombination according to Huang et al., 2009, the construct pGX-Drep-3^{Donor} was generated. To this end, two homologous arms were amplified from the P[acman] BAC clone *CH322-86P21* and inserted into the vector *pGX*. Primers were:

5'-HA: forward primer: 5'-GTA GCT AGC TAC GCT TTG ACT GCT TTT GAT GTG T-3'
reverse primer: 5'-CCG GTA CCG GAG ACC ATG GAA TGT TAT TGC-3'
3'-HA: forward primer: 5'-GTC GGC GCG CCG ACT GGG GCT TCT ACG AAT-3'
reverse primer: 5'-AAG GCC TTC ATC TTA CAG GTT TCG GCT TCG-3'

The construct for recombination of the 5'-arm was inserted into *pGX* via *Nhe*I and *Kpn*I, the one for the 3'-arm using *Asc*I and *Stu*I.

This construct was used for p-element-based transformation of flies. Homologous recombination was attempted as outlined in Huang et al., 2008 and Huang et al., 2009. Based on PCR-based analyses, none of the candidate recombinants had underwent recombination at both arms. Details are available on request.

Additional pGX constructs were generated for homologous recombination of the *brp* locus. Details are available on request.

4.2. Antibodies

Anti-Drep-2: A rabbit serum against a 6xHis-tagged C-terminal Drep-2 construct was produced by Rui Tian (Seqlab GmbH, Germany; Tian 2011). Serum was affinity purified with the same peptide. The peptide comprised amino acids 252-483 of Drep-2. To create the peptide, the *drep-2* cDNA *LD32009* was amplified using the forward primer 5'-GAC CGT CGA CGT GGG TGT GGG AGC TGT CCA-3' and the reverse primer 5'-GAC CCT CGA GTG AAT TCT GTC CTC CTC ATC CTC-3'. The amplicon was inserted into the *pENTR4* vector (Invitrogen) using *Sal*I and *Xho*I restriction sites. Invitrogen gateway cloning was used to create a 6xHis-tagged construct in *pDEST17* (Invitrogen). For additional anti-Drep-2 antibodies see Tian 2011.

Anti-Drep-1: Antibodies directed against the peptide GRPLCAKRNAEDRLN were raised in rabbit (Seqlab, #1097 and #1098). The antisera were affinity purified with the same peptide. #1097 did not show a recognizable staining in brains or at NMJs.

Anti-Drep-3: Antibodies were raised in rabbit (Seqlab). In one case directed against the N-terminal peptide AAGVQCDPDSRIVAPP (#1093 and #1094), in the other directed against the C-terminal peptide YSARSDAARLSTELSC (#1095 and #1096). The antisera were affinity purified with the same peptides. #1094, #1095, and #1096 did not show a recognizable staining in brains or at NMJs.

Anti-DmGluRA: Antibodies directed against the peptide SESVWYRKIS were raised in guinea pig (Seqlab, #12Gp20 and #12Gp21). The antisera were affinity-purified using the same peptide. #12Gp20 did not show a recognizable staining in brains or at NMJs. The staining pattern of #12Gp21 did not correspond to the one produced by the monoclonal antibody DmGluRA^{7G11}, directed against the same peptide (Panneels, et al., 2003).

4.3. Single-fly PCR

For genotyping, DNA from single flies was analysed. Individual flies were immobilized in reaction tubes by short incubation at -20°C. Fly homogenate was generated by squashing flies for 10s using a pipette filled with squashing buffer. 500 mL buffer contained: 0.6g TRIS, 0.185g EDTA, 0.73g NaCl, H_2O *ad* 500 mL (pH was adjusted to 8.2). 990 µl buffer were mixed with 10 µl Proteinase K. After squashing, flies were incubated in buffer for 30 min at 37°C. Subsequently, Proteinase K was inactivated by heating the solution to 95°C for 2 min. 1 µl of the homogenate was used as template for the PCR. The single-fly PCRs were conducted using the Qiagen HotStarTaq master mix (30 cycles, 1 min elongation at 55°C).

4.4. *In situ* hybridization

In situ hybridizations of wholemount embryos were performed by Rui Tian, as described by the Berkeley Drosophila Genome Project (http://www.fruitfly.org) and in Tian, 2011. For preparing antisense RNA probes, the plasmid *LD32009* was cut using *Bam*HI and *in vitro* transcribed using Sp6 RNA polymerase. For sense probes, the plasmid was cut with *Sma*I and transcribed with T7 RNA polymerase.

5. Biochemistry

5.1. Ethanol absorption

Ethanol absorption was analysed by Dana Robertson. Whole flies (20 per tube) were exposed to ethanol (100:50 E:A) for 0, 2, 5, or 10 minutes, then immediately frozen on dry ice and homogenized in 200 µl of ice-cold 50 mM Tris, pH 7.5, and centrifuged for 20 min at 4°C to remove particulates. Homogenate (10 µl) was then added to 500 µl of reagent from an ethanol detection kit (Sigma, St. Louis, MO), and concentration was determined according to the instructions of the manufacturer, as described previously (Moore et al., 1998). Values are standardized to the average weight of a fly as determined from the weight of 100 frozen flies.

5.2. *In vitro* experiments using purified Drep-2 and -3

The purification of Drep-2 and Drep-3 and subsequent experiments were conducted by Nicole Holton, Jennifer Lardong, and Bernhard Loll.

5.2.1. Protein expression and protein purification

The gene coding for Drep-2 was fused to an N-terminal His-tagged maltose binding protein. *Drep-2* was transformed in *Escherichia coli* BL21 Rosetta2 (DE3) pLys cells (NEB). Drep-2 was cultured in TB medium at 37 C until an OD of ~1.0 was reached and subsequently cooled down to 20°C. Protein expression was induced by addition of 0.5 mM IPTG. Cells grew overnight and were harvested by centrifugation (6 min, 6000 rpm at 4°C). The pellet of Drep-2 was resuspended in 20 mM Tris/HCl pH 7.4, 250 mM NaCl, 8 mM imidazol, 1 mM DTT. Cells were lysed by sonication at 4°C and the supernatant was cleared by 45 min centrifugation (21500 rpm at 4°C). A Ni^{2+}-NTA (cv ~1 ml; GE Healthcare) was equilibrated with 20 mM Tris/HCl pH 7.4, 250 mM NaCl, 1 mM $MgCl_2$, 8 mM imidazole and 1 mM DTT. Drep-2 was loaded on the column and washed with 3 cv of equilibration buffer. Drep-2 was eluted in a linear gradient to 20 mM Tris/HCl pH 7.5, 250 mM NaCl, 400 mM imidazol, 1 mM DTT a. The maltose binding protein was cleaved by TEV proteases yielding untagged Drep-2 protein, during dialysis into 20 mM Tris/HCl pH 7.4, 100 mM NaCl, 1 mM DTT and loaded on a MonoQ 10/100 column (GE Healthcare) equilibrated with 20 mM Tris/HCl pH 7.4 and 1 mM DTT. Drep-2 was eluted in a linear gradient from 100 to 1000 mM NaCl. Size exclusion chromatography was performed with a HighLoad Superdex S200 16/60 column (GE Healthcare), equilibrated with 20 mM Tris/HCl pH 7.5, 250 mM NaCl, and 1 mM DTT. Purification of Drep-3 was conducted analogously.

5.2.2. Nuclease activity assay

In limited digestion experiments, 10 µg of Drep-2 were incubated with 0.3 µg linearized *pUC19* plasmid DNA in 15 µl reaction buffer (20 mM Hepes-NaOH pH 7.4, 50 mM NaCl, 5 mM $MgCl_2$) at 37°C. Aliquots were taken at different time intervals and the reaction was stopped by DNA loading dye containing 10 mM EDTA. Samples were electrophoretically separated over a 1% (w/v) agarose gel containing ethidium bromide.

5.2.3. Caspase cleavage assays

Purified Drep-2 or Drep-3 were incubated with recombinant, active rat Caspase-3 (Abcam, ab52072) for 1h at 37°C. Subsequently, proteins were analysed by western blotting. No cleavage of either Drep-2 or Drep-3 was observed.

In a separate experiment, Sabrina Büttner expressed flag-tagged *drep-2* or *drep-3* constructs in yeast (*pESC-HIS* vector). Proteins were pulled down using Anti-FLAG-coupled agarose beads and incubated with active rat Caspase-3 for 1h or 2h at 37°C. Proteins were analysed by western blotting, no cleavage of either Drep-2 or Drep-3 was observed. In a third attempt, apoptosis was triggered in *drep-2/-3*-expressing yeast cells using either acetic acid, hydrogen peroxide, DDT, or Cisplatin. Although induction of apoptosis was confirmed, by quantification of accumulation of reactive oxygen species, no cleavage of either Drep-2 or Drep-3 was observed.

5.3. Pulldown experiments

Fly heads were sheared mechanically, using a motor-driven homogenizer, in 900 µl homogenization buffer containing 25 mM Hepes (pH 8.3), 150 mM NaCl, 1 mM $MgCl_2$, 1 mM EGTA, 10% glycerol, 0.8% DOC, 1% Triton X-100, and protease inhibitors (Complete Mini, Roche). After incubation on ice for 30 min, the homogenate was centrifuged several times at 14'000g for 15 min at 4°C to remove insoluble material. The recovered supernatant was used as protein extract. This extract was incubated for 12h at 4°C with antibodies coupled to Protein A Sepharose-beads (Bio-Rad). After washing of the beads, elution of the protein was done using 70 µl of 2x SDS-PAGE sample buffer. Of note, the pulldown experiments in the context of quantitative mass spectrometry were done using a different protocol (described in section 5.7.2).

5.4. Fly head extracts for western blotting

For fly head protein extraction, 20 heads per genotype were sheared manually in 40 µL of 2% SDS aqueous solution, using a micropistil fitting tightly into a 1.5 mL cup. 40 µL of 2x sample buffer (Laemmli, 1970) were added and samples were heated to 95°C for 5 min. After centrifugation for 5 min at 16'000g, in order to pellet fly head debris, 8 or 20 µL of each sample (equivalent to 2 or 5 heads) were subjected to denaturing SDS-PAGE using a 12% Tris-HCl gel. Of note, both the amounts of sample and the type of gel are typical values that were adapted, depending on the experiment.

5.5. Western blotting

Protein samples were fractionated by standard SDS-PAGE, transferred to nitrocellulose membranes in cold western blot transfer buffer (25 mM TRIS (pH 8.0), 150 mM glycine, 20% methanol) and incubated for 60 min at 100V, 4°C. The membrane was blocked with 5% milkpowder in PBS. For detection, a horseradish-peroxidase–conjugated secondary antibody and an enhanced chemoluminescence substrate (GE Healthcare) were used. Signal was captured on autoradiography films (Hyperfilm ECL, GE Healthcare). Films were scanned in transmission mode (Epson V700).

For the confirmation of results from mass spectrometry, eluates of pulldowns with GFP-Trap or plain (control) beads were ethanol-precipitated and proteins were dissolved in 50 µl Laemmli sample buffer (Laemmli, 1970). Both the input control and the eluates were subjected to denaturing SDS-PAGE using Tris-HCl gels. Subsequently, proteins were transferred onto nitrocellulose membranes and probed with the primary antibody.

5.6. Synaptosome preparations

Synaptosome preparations were prepared by Harald Depner, as explained in Depner, 2013.

5.7. Quantitative mass spectrometry

Quantitative mass spectrometry was performed by Marieluise Kirchner and will be explained in the following paragraphs.

5.7.1. Quantitative affinity purification and mass spectrometry

Drep-2 *in vivo* interaction partners were identified using quantitative affinity purification and mass spectrometry. The major challenge in such experiments is to distinguish true interaction partners from nonspecific contaminants. Quantitative affinity purification and mass spectrometry can solve this problem by comparing the abundance of identified proteins with a control (Paul et al., 2011; Vermeulen et al., 2008).

Drep-2^{GFP} was expressed using $elav^{c155}$-Gal4. We purified Drep-2^{GFP} from fly heads using a single chain anti-GFP antibody coupled to agarose beads. To control for unspecific binding, we performed parallel pulldowns on the same lysates using control agarose beads. As an additional control, GFP-negative lysate from wildtype flies was included into the experiment. In total, we identified 3284 proteins in the pulldown experiments. 202 proteins were significantly enriched in GFP pulldowns compared to plain bead controls. 35 of these proteins could be confirmed in comparative analysis with GFP pulldowns of wildtype lysates and were therefore defined as robust interactors/core proteins (permutation-based FDR = 1%; S_0=1).

5.7.2. Pulldown experiments

500 µl fly heads were immersed in liquid nitrogen and pulverized mechanically with a BioPulverizer (Biospec Products, OK). Powdered tissue was homogenized in cold 500 µl lysis buffer (50 mM Tris-HCl (pH 7.6), 150 mM NaCl, 1 mM $MgCl_2$, 1 mM EDTA, 10% glycerol, 0.4% DOC and protease inhibitors (Complete Mini, Roche)). After incubation on ice for 30 min, 500 µl lysis buffer without DOC and Triton were added to a final concentration of 1%. Samples were centrifuged at 14'000g for 15 min at 4°C to remove insoluble material. The supernatant was transferred to a fresh tube for pull-down experiments.

For the tandem mass spectrometry (MS/MS) analysis, immunoprecipitations of GFP-tagged bait proteins were performed in triplicates using GFP-Trap agarose beads (Chromotek GmbH, Germany) according to the manufacturer's instructions. Soluble protein fractions were incubated with either 25 µl of GFP-Trap or plain control beads for 60 min at 4°C under constant rotation. The beads were washed two times with washing buffer (50 mM Tris-HCl (pH 7.6), 150 mM NaCl, 1 mM $MgCl_2$, 1 mM EDTA, 10% glycerol) and once with PBS. Proteins bound to the beads were eluted by applying two times 50 µl elution buffer (6M urea / 2M thiourea) and proceeded to in-solution digestion followed by liquid chromatography (LC) MS/MS analysis.

5.7.3. Liquid chromatography MS/MS analysis

Protein eluates were reduced for 30 min at room temperature (RT) in 10 mM dithiothreitol solution followed by alkylation for 20 min by 55 mM iodacetamide in the dark at RT. The endoproteinase LysC (Wako, Japan) was added following a protein:enzyme ratio of 50:1 and incubated for 4h at RT. After dilution of the sample with 4x digestion buffer (50 mM ammonium bicarbonate in water (pH 8.0)), sequence grade modified trypsin (Promega) was added (same protein:enzyme ratio as for LysC) and digested over night. Finally, trypsin and LysC activity were quenched by acidification of the reaction mixtures with TFA to pH ~2. Afterwards, peptides were extracted and desalted using StageTips (Rappsilber et al., 2003).

Peptide mixtures were separated by reversed phase chromatography using the EASY-nLC system (Thermo Scientific) on in-house manufactured 20 cm fretless silica microcolumns with an inner diameter of 75 µm. Columns were packed with ReproSil-Pur C18-AQ 3 µm resin (Dr. Maisch GmbH). Peptides were separated on a 8-60% acetonitrile gradient (214 min) with 0.5% formic acid at a nanoflow rate of 200 nl/min. Eluting peptides were directly ionized by electrospray ionization and transferred into a Q Exactive mass spectrometer (Thermo Scientific). Mass spectrometry was performed in the data dependent positive mode with one full scan (m/z range = 300-1,700; R = 70,000; target value: 3 x 106; maximum injection time = 120 ms). The 10 most intense ions with a charge state greater than one were selected (R = 35,000, target value = 5 x 105; isolation window = 4 m/z; maximum injection time = 120 ms). Dynamic exclusion for selected precursor ions was set to 30s.

MS/MS data were analysed by MaxQuant software v1.2.2.5, as described (Cox et al., 2011). The internal Andromeda search engine was used to search MS/MS spectra against a decoy *D. melanogaster* UniProt database (DROME.2016-06) containing for-

ward and reverse sequences. The search included variable modifications of methionine oxidation and N-terminal acetylation, and fixed modification of carbamidomethyl cysteine. Minimal peptide length was set to six amino acids and a maximum of two missed cleavages was allowed. The false discovery rate (FDR) was set to 0.01 for peptide and protein identifications. If the identified peptide sequence set of one protein was equal to or contained another protein's peptide set, these two proteins were grouped together and the proteins were not counted as independent hits.

Label-free quantification (LFQ) was performed in MaxQuant as described (Hubner et al., 2010). Unique and razor peptides were considered for quantification with a minimum ratio count of 1. Retention times were recalibrated based on the built-in nonlinear time-rescaling algorithm. MS/MS identifications were transferred between LC-MS/MS runs with the *Match between runs* option, in which the maximal retention time window was set to 2 min. For every peptide, corresponding total signals from multiple runs were compared to determine peptide ratios. Median values of all peptide ratios of one protein then represent a robust estimate of the protein ratio. LFQ intensity values were logarithmized and missing values were imputed with random numbers from a normal distribution, whose mean and standard deviation were chosen to best simulate low abundance values below the noise level (width = 0.3; shift = 1.8). GFP pull-down samples and plain-beads control samples were selected as individual groups of 3 technical replicates each; significantly enriched proteins were determined by a volcano plot-based strategy, combining standard two-sample t-test p-values with ratio information. Significance corresponding to an FDR of 1, 5 or 10% was determined by a permutation-based method (Tusher et al., 2001).

5.7.4. Generation of the network of interactors

The network of biochemical interactions (Fig. 72) was created using Microsoft Excel 2011, Cytoscape v2.8.3 / v3.0.0 and Adobe Illustrator CS4.
Proteins that DroID, Flybase or other literature lists as (putative) interactors of any of the highly enriched proteins (FDR 1%) were added (white circles), if they fit the following three conditions:

- Enriched in the pulldowns (*elav^{c155};UAS-drep-2^{GFP}* flies, GFP beads vs. plain beads) at a 10% FDR
- Not enriched in the control experiment (GFP beads, wildtype flies vs. *elav^{c155};UAS-drep-2^{GFP}* flies) at a 10% FDR (to eliminate false-positives)
- A (predicted) interaction with at least two of the 35 core proteins

The circle (node) and font size correspond to the rank within the results (indicated in Table 7, Table 9). The line (edge) width and shade correspond to the number of interactions each of the significantly enriched proteins has with others. The line/edge length is arbitrary. A more detailed protocol is published online at:
http://protocols.andlauer.net/cytoscape.pdf

6. Behavioural analyses

6.1. Olfactory conditioning

Olfactory conditioning experiments were conducted by Sabrina-Scholz-Kornehl. Flies were raised at 24°C and 60% relative humidity at a 14/10h light/dark cycle, on cornmeal-based food prepared according to the Würzburg recipe (Guo et al., 1996). Flies were transferred to fresh food vials for up to 48h before behavioural experiments. All experiments were conducted with 3-5d old animals and carried out in a w^{1118} genetic background; flies were outcrossed for at least five generations. Behavioural experiments were performed in dim red light at 70% relative humidity with 3-octanol (1:150 dilution in mineral oil presented in a 14 mm cup) and 4-methylcyclohexanol (1:100 dilution in mineral oil presented in a 14 mm cup), serving as olfactory cues. 120V AC current served as behavioural reinforcer.

Associative training was done following the single-cycle training procedure previously described (Tully and Quinn, 1985). Electric foot shock was applied after 10s of odour presentation, afterwards twelve shock/odour pairings were conducted within 50s. STM was tested immediately after the end of the training session, 3 min after training onset. Performance of ITM and ARM was determined 3h after training; flies were transferred to neutral containers without food for the resting period. For separation of consolidated ARM and labile ASM, two groups of flies were separately trained and one group was cooled in an ice-bath (0°C) for 90s, 2.5h after training. Odour memory of this group was tested after a 30 min recovery period, i.e. 3h after training onset. Since labile ASM is erased by this procedure, performance of the cooled group is solely due to ARM. Pharmaceutical components (MPEP (ab120008, Abcam) and 1S,3R-ACPD (#0284, Tocris Bioscience, UK)) were supplemented to fly food as previously described (McBride et al., 2005; Tauber et al., 2011). 1S,3R-ACPD was used at a concentration of 72.2 µM, MPEP at 9.7 µM (McBride et al., 2005; McBride et al., 2010; Parmentier et al., 1996).

Calculation of behavioural indices was done as originally introduced (Tully and Quinn, 1985). ASM can be calculated by subtracting performance of the cooled group from an uncooled group (Knapek et al., 2011).

6.2. Courtship conditioning

Courtship conditioning was done by Cornelia Oppitz. Flies were raised on semi-defined medium at 25°C at a 12/12h light/dark cycle. *Drep-2*^{ex13} and *CantonS* flies were outcrossed to w^{1118} for more than five generations. Virgin males were collected at eclosion and aged individually for 5 days before training. *CantonS*^{w1118} pre-mated females were aged for 4 days in groups of 50-100 with *CantonS*^{w1118} males collected at the same time.

Males were assayed for courtship conditioning as described (Siwicki and Ladewski, 2003). For training, individual males were placed in food chambers either with (trained) or without (naïve) a single pre-mated female. After training, each male was recovered, transferred to a fresh food chamber and kept in isolation until testing. For short-term memory, the training period was 1h and the test was performed within

30 min. For long-term memory, males were trained for 7h and tested after 24h. Tests were performed in 10 mm diameter courtship chambers and videotaped for 10 min.

Videos were scored with automated software (C. Schusterreiter, C. Machacek, B. Dickson, *unpublished*) for courtship index (CI). CI is the percentage of time each male spent courting during the test. Median CIs were used to calculate the learning index (LI): $(CI_{naïve}\text{-}CI_{trained})/CI_{naïve} \times 100$ (Kamyshev et al., 1999). LI=0 thus implies that the flies did not learn.

LIs were analysed by a non-parametric permutation (randomization) test using a MATLAB script (according to the algorithm described in Kamyshev et al., 1999). Briefly, the entire set of courtship indices for both the naïve and trained flies was pooled and then randomly assorted into simulated naïve and trained sets of the same size as in the original data. The general approach was here to calculate a large amount of permuted data sets and then to assay the probability of observing the statistic determined for the experiment by chance. Hypothetical LI_P was calculated for each of 100,000 randomly permuted data sets, and p-values were estimated as the fraction for which $LI_P > LI$ (to test H_0, LI=0).

6.3. Ethanol sedation

Flies were maintained at 25°C and 65-70% relative humidity on a 12/12h light/dark cycle and fed standard cornmeal/molasses medium. Flies were subjected to brief CO_2 anaesthesia, no less than 24h before behavioural assays. In the rescue experiments, flies were briefly cooled down to 4°C to allow for transfer to test vials, no less than 2h before experiments. All flies had a w^{1118} genetic background.

Initially, sedation sensitivity was quantified by Dana Robertson with the loss of righting assay as described previously (Corl et al., 2009; Rothenfluh et al., 2006): Flies were acclimated to the *booze-o-mat* for 10 min before being exposed to vaporized ethanol at a concentration of 100:50 (ethanol vapor: humidified air). The tubes were spun at 2.5-min intervals, and the number of flies having lost righting ability was counted at each time point. From these data, we calculated ST50 (time to 50% sedation). Subsequent rescue experiments were conducted using a simpler protocol that did not allow for control over ethanol concentration (Maples and Rothenfluh, 2011).

6.4. Locomotor activity

Locomotor activity was assayed by Dana Robertson. Flies were maintained as described for ethanol sedation experiments. Experiments were carried out in a w^{1118} genetic background, using 20-25 male flies aged 2-4d after eclosion. Motor movement was assessed in the automated locomotor tracking system as described previously (Wolf et al., 2002). Flies were acclimated to a stream of humidified air for 10 min before the start of recordings. Recordings lasted 20 min and motion was measured at 2.5-min intervals.

7. Miscellaneous methods

7.1. Electrophysiology

Electrophysiological recordings at larval NMJs were conducted by Elena Knoche, as published previously (Bogdanik et al., 2004; Kittel et al., 2006; Liu et al., 2011). Electroretinogram recordings in adult animals were done by Christina Hollmann, as previously described (Burg et al., 1993; Heisenberg, 1971; Wagh et al., 2006).

7.2. Adult life span

For the life span assay, male flies were placed in groups of 25 animals in small food vials and transferred to fresh vials at least twice per week. Flies were kept at standard conditions. After each transfer, the numbers of dead and remaining flies were counted. For each vial, the number of days was determined at which 50% of flies were dead.

7.3. General data analysis and statistics

Non-parametric tests (Mann-Whitney U-test or Kruskal-Wallis) were used, unless stated otherwise, due to mostly small sample sizes. The significance level α was set to 5%. Asterisks are used to indicate significance in figures (* = $p < 0.05$; ** = $p < 0.01$; *** = $p < 0.001$; ns = $p \geq 0.05$). If several genotypes were compared, α and * symbols were adjusted by dividing the significance level by the number of comparisons (Bonferroni correction).

In situations were outliers were removed (courtship conditioning and ethanol sedation, as indicated in the text), the fourth spread method was used, as explained in Devore, 2011. The fourth spread f is the difference of the upper quartile q_3 to the lower quartile q_1: $f = q_3 - q_1$. Values v were considered as outliers, if $v<a$ or $v>b$, where $a = median - (1.5 \times f)$ and $b = median + (1.5 \times f)$.

Standard error of the mean (SEM): if s is the standard deviation of a sample set and n is the number of samples, the SEM e is defined as $e = s/\sqrt{n}$.
Standard error of the median can be calculated according to Sachs, 2003:
standard error of the median = $e = (a-b) / 3.4641$,
where a is the $a = (n/2 + \sqrt{(3 \times n)}/2)$th observation
and b is the $b = (n/2 - \sqrt{(3 \times n)}/2)$th observation,
each rounded up to the next integer; n = number of samples.

Experimental data was analysed using Microsoft Office 2011 and OriginLab Origin Pro 9.0, unless stated otherwise. Graphs were created using GnuPlot v4.6 and Adobe Illustrator CS4. Images were processed as described in section 2.3. The protein alignment was created using Geneious v5.3.6.

RESULTS

The scientist is the explorer of beautiful things.

Modified after:
Oscar Wilde, Preface to the Picture of Dorian Gray

1. CHARACTERIZATION OF SYNAPTIC DIVERSITY USING RATIOMETRIC ANALYSES

THE ACTIVE ZONE (AZ) IS defined as the stretch of presynaptic membrane at which neurotransmitter vesicle fusion takes place (Südhof, 2012; Zhai and Bellen, 2004). A typical feature of AZs is an electron-dense structure in the adjacent cytosol, formed by the proteins Bruchpilot (Brp) and RIM Binding Protein (RBP) in *Drosophila* (Kittel et al., 2006; Liu et al., 2011). These two proteins are part of a larger scaffold, the cytomatrix at the AZ (CAZ), a small unit of 200-300 nm in size (Hallermann et al., 2010; Liu et al., 2011; Maglione and Sigrist, 2013; Südhof, 2012). Additional CAZ members are, amongst others, Liprin-α, Syd-1, RIM, and Munc13 (Owald et al., 2010; Südhof, 2012). In an effort to dissect CAZ assembly, Brp, Liprin-α, Syd-1, and RBP were characterized in *Drosophila* during the last years in our lab (Fouquet et al., 2009; Kittel et al., 2006; Liu et al., 2011; Owald et al., 2010; 2012).

1.1. Comparison of expression patterns of presynaptic proteins

Costainings of Brp and Syd-1 in the mushroom body (MB) calyx (Christiansen et al., 2011; Owald et al., 2010) as well as of Brp and RBP in the antennal lobe (AL) (Liu, 2012) of adult fly brains suggested a differential expression pattern of these AZ proteins. We therefore wondered whether presynapses of distinct neuron types could be characterized and identified by the protein composition of their CAZ. In such a case, synapses would, depending on their properties, contain different stoichiometric amounts of individual CAZ proteins. In order to investigate this hypothesis, we examined the distribution of the core AZ protein Brp relative to RBP (Fig. 12) and to Syd-1 (Fig. 13), respectively, in different neuropils of the adult brain.

The *brp* gene codes for several Brp isoforms, including two large proteins of 170 and 190 kDa (Matkovic et al., 2013). We have raised a number of antibodies against Brp (Fouquet et al., 2009). One of these, $Brp^{N\text{-}Term}$, recognizes the 190 but not the 170 kDa isoform (Fig. 11, Matkovic et al., 2013). By contrast, Brp^{Nc82}, binding to the C-terminus, labels both the 170 and the 190 kDa isoforms. To assess whether these two isoforms play functionally different roles at central synapses, we included both antibodies in our analysis (Fig. 14). For an easier distinction of these two antibodies, Brp^{Nc82} will be called $Brp^{C\text{-}Term}$ henceforth in this chapter.

Fig. 11: Binding sites of anti-Brp antibodies.
Concatenation of all known Brp exons.
The 170 kDa isoform is shown in orange, the 190 kDa isoform in blue (Matkovic et al., 2013).
The $Brp^{N\text{-}Term}$ antibody (green) does not recognize the 170 kDa isoform,
$Brp^{C\text{-}Term}$ / Brp^{Nc82} (magenta) labels both.
The Brp^{Nc82} epitope was mapped by Annika Günther and Sara Mertel.

For all three antibody combinations, differences in their relative distribution were apparent (Table 1): While anti-Brp$^{C\text{-}Term}$ and anti-Syd-1 produced stainings of a similar intensity in the MB lobes (Fig. 13A), stainings of both RBP and Brp$^{N\text{-}Term}$ were brighter than Brp$^{C\text{-}Term}$ in this neuropil (Fig. 12A, Fig. 14A). The previously observed differences between Brp$^{C\text{-}Term}$ and Syd-1 in the MB calyx (Christiansen et al., 2011; Owald et al., 2010) could be confirmed as well (Fig. 13C).

In the ellipsoid body and the fan-shaped body of the central complex, RBP and Syd-1 showed an expression pattern that was different from Brp in several layers (Fig. 12D,E, Fig. 13D,E). Differences could also be observed in the optic lobes: for example, the most distal layer of the lamina was more strongly labelled by anti-Syd-1 and anti-Brp$^{N\text{-}Term}$ (Fig. 13G, Fig. 14G) than by anti-Brp$^{C\text{-}Term}$ and anti-RBP (Fig. 12G). In the AL, differences in the staining pattern were especially prominent for RBP and Brp$^{C\text{-}Term}$ (Fig. 12A,B), as we had expected (Liu, 2012). Moreover, also the Brp$^{N\text{-}Term}$ label stuck out in some AL glomeruli (Fig. 14A,B).

	RBP$^{C\text{-}Term}$	**Syd-1**	**Brp$^{C\text{-}Term}$**	**Brp$^{N\text{-}Term}$**
Antennal lobes	strongly differential	slightly differential	differential	differential
Mushroom body: lobes	uniformly high	normal and uniform	normal and uniform	uniformly elevated
Mushroom body: calyx	slightly differential	strongly differential	uniform	slightly differential
Central complex: ellipsoid body	strongly differential	strongly differential	uniform	slightly differential
Central complex: fan-shaped body	differential	uniform	strongly differential	strongly differential
Optic lobe: medulla, lobula, lobula plate	differential	slightly differential	differential	differential
Optic lobe: lamina	uniform	strongly differential	uniform	strongly differential

Table 1: Differential expression of CAZ proteins in selected neuropils.
Summary of the variation of CAZ protein expression (Fig. 12, Fig. 13, Fig. 14).
Columns: antibodies; rows: neuropils.
Normal (blue): no difference in antibody staining intensity to surrounding neuropils.
Uniform (blue): no visible change of staining intensity within the neuropil.
Uniformly elevated / high (green): intensity is uniformly increased, relative to surrounding neuropils.
Differential (slightly / strongly) (green): staining intensity varies within the neuropil.

It might be argued that our observations could, in part, have been caused by less-efficient penetration of some antibodies into dense and deeper-laying tissues. Compared to antibodies without such penetration issues, different relative staining intensities might then have occurred. However, the fact that we observed discrete patterns instead of intensity gradients throughout the brain is a clear indication that we did not face such an issue.

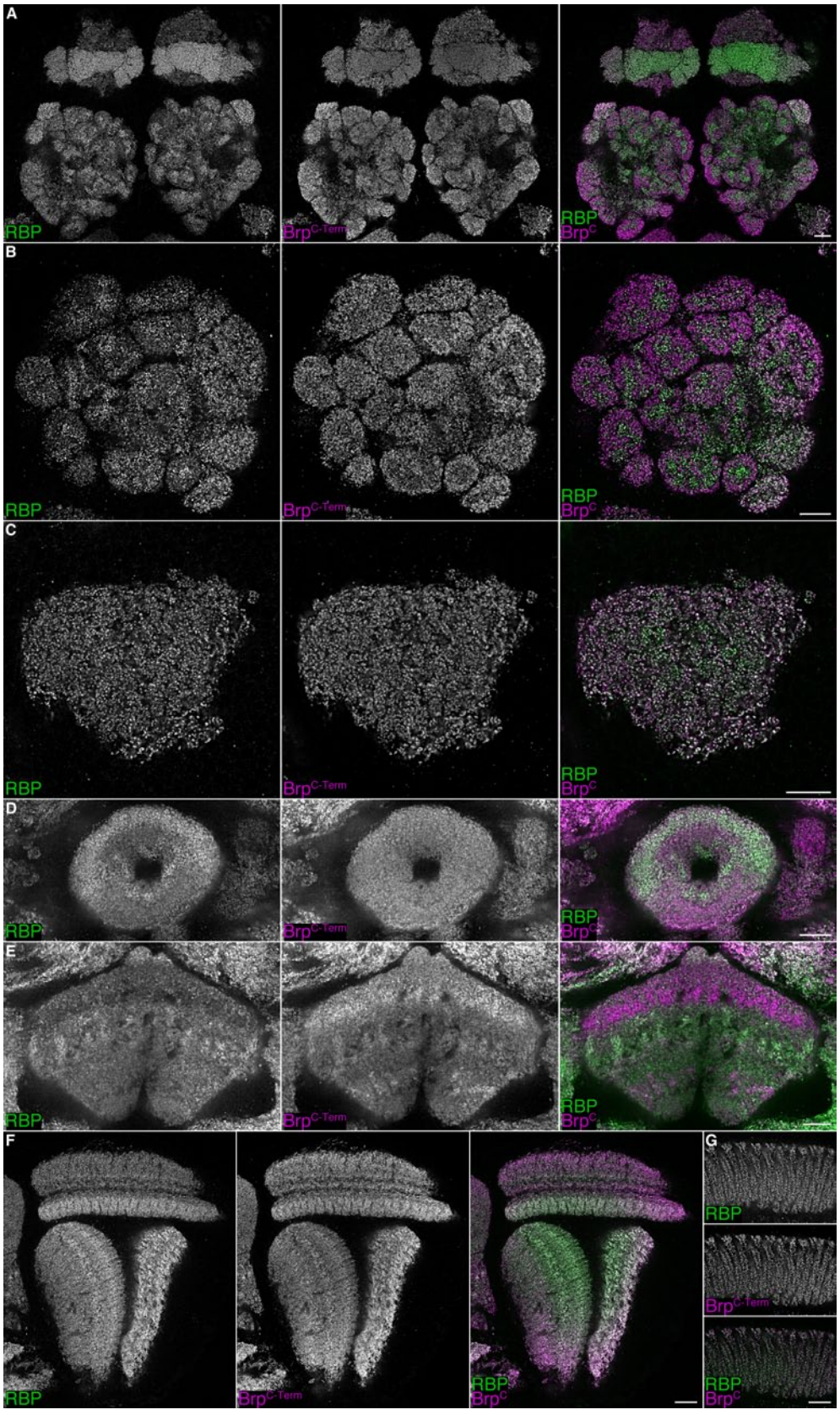

Fig. 12: RBP$^{C\text{-}Term}$ staining compared to Brp$^{C\text{-}Term}$.
Confocal sections of adult *w*^{1118} brains, anti-RBP$^{C\text{-}Term}$ and anti-Brp$^{C\text{-}Term}$ staining.
All scale bars: 10 µm.
A: MB lobes and antennal lobes (AL). **B:** AL. **C:** MB calyx.
D: Ellipsoid body. **E:** Fan-shaped body.
F: Optic lobe (medulla, lobula, lobula plate). **G:** Lamina.

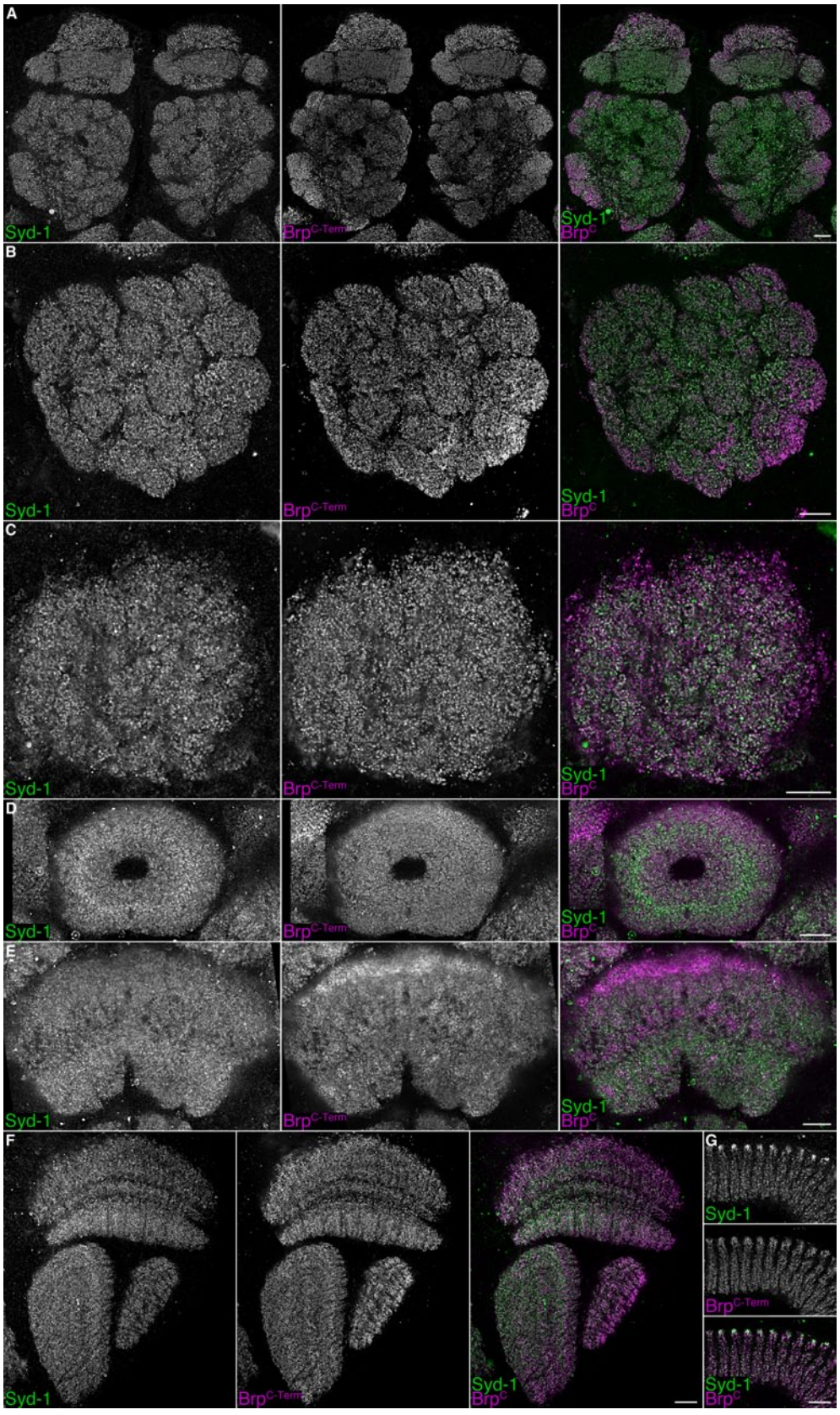

Fig. 13: Syd-1 staining compared to Brp$^{C\text{-}Term}$.
Confocal sections of adult *w*^{1118} brains, anti-Syd-1 and anti-Brp$^{C\text{-}Term}$ staining.
All scale bars: 10 µm.
A: MB lobes and ALs. **B:** AL. **C:** MB calyx. **D:** Ellipsoid body.
E: Fan-shaped body. **F:** Optic lobe. **G:** Lamina.

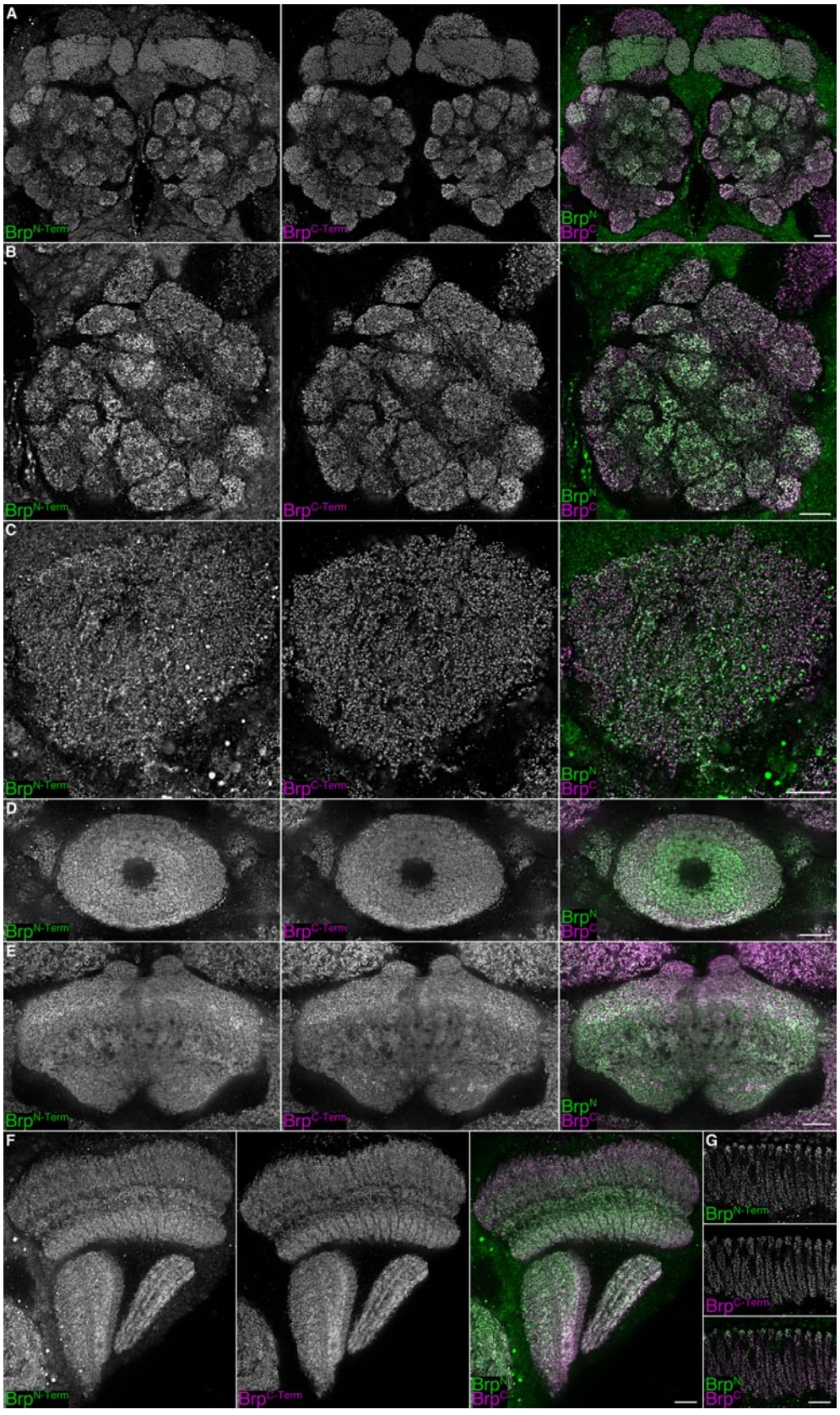

Fig. 14: Brp$^{N\text{-}Term}$ staining compared to Brp$^{C\text{-}Term}$.
Confocal sections of adult *w*^{1118} brains, anti-Brp$^{N\text{-}Term}$ and anti-Brp$^{C\text{-}Term}$ staining.
All scale bars: 10 µm.
A: MB lobes and ALs. **B:** AL. **C:** MB calyx. **D:** Ellipsoid body.
E: Fan-shaped body. **F:** Optic lobe. **G:** Lamina.

In order to validate that the observed patterns are really based on differences in CAZ protein abundance and do not constitute staining artefacts, we sought to validate our results with an approach independent of antibody staining procedures. Thus, we turned to the expression of fluorophore-tagged proteins. To this end, a P[acman] BAC construct of the Brp^{170kDa} isoform was tagged with eGFP, the Brp^{190kDa} isoform with mCherry[8] (Matkovic et al., 2013). These constructs contain the genomic sequence of the complete *brp* gene, including endogenous upstream enhancers (Venken et al., 2009; 2006). Expression of either of the constructs was sufficient to rescue the lethality of $brp^{-/-}$ mutants (Matkovic et al., 2013).

The fluorescent signal of the $Brp^{170kDa\text{-}eGFP}$ and $Brp^{190kDa\text{-}mCherry}$ fusion proteins confirmed the antibody stainings (Fig. 15). Clear differences in the signal intensity of both tagged proteins could be observed, which corresponded to the differential pattern of the antibody stainings (Fig. 14). For example, the 190 kDa isoform was more abundant in the MB lobes. By contrast, the 170 kDa isoform produced a stronger signal in the anterior optic tubercle (*not shown in the antibody staining*). In the AL, both isoforms labelled different glomeruli with varying intensities. Therefore, the differences in the stainings can indeed be attributed to differences in protein abundance at the respective synapses.

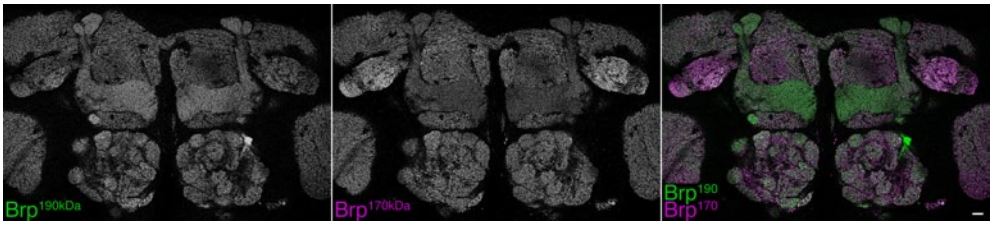

Fig. 15: Brp^{190kDa} signal compared to Brp^{170kDa}.
Adult brains, anti-$Brp^{190kDa\text{-}mCherry}$ (recognized by $Brp^{N\text{-}Term}$) and $Brp^{170kDa\text{-}GFP}$ label (genomic P[acman] BAC constructs). The original fluorophore signal is shown, no counterstaining by antibodies was used. Scale bar: 10 µm. Anterior frontal confocal sections showing MB lobes, ALs and anterior optic tubercles.

1.2. A ratiometric method for the description of differences in CAZ protein expression

The antibody stainings indicated that CAZ proteins do show different expression patterns throughout the adult brain. It seemed improbable that these differences in CAZ protein abundance are caused by differential expression of the proteins at random synapses. By contrast, it appeared likely that presynapses of a certain type (e.g., belonging to a certain type of neuron), could feature a distinct CAZ protein composition. In order to examine this hypothesis, we needed to quantify the differences between antibody stainings. $Brp^{C\text{-}Term}$ showed the most uniform staining of the four antibodies we examined. We therefore decided to use this antibody as a reference and compare the intensity of the other antibody stainings to $Brp^{C\text{-}Term}$. Thus, we expected to be able to determine whether synapses of a certain group of neurons had an equal

[8] The two Brp P[acman] constructs were produced by Tanja Matkovic.

proportion of two CAZ proteins, or whether one of the proteins was present in a larger quantity. In order to reduce the complexity of the task, we began by quantifying the protein distribution within the AL and the MB calyx. Synapse types and the connectivity of neurons have already been described well in these two neuropils (Leiss et al., 2009a; Tanaka et al., 2012; 2008; Yaksi and Wilson, 2010; Yasuyama et al., 2002). Moreover, both structures showed clear differences between CAZ proteins (Table 1).

AZs in *Drosophila* are 200-300 nm in diameter and reach about 100 nm into the cytoplasm (Hallermann et al., 2010; Liu et al., 2011; Maglione and Sigrist, 2013; Südhof, 2012). This corresponds approximately to the resolution limit of conventional light microscopy (Inoué, 2006). We therefore acquired confocal microscopy images with a pixel size adequate for a lateral resolution of up to 200 nm (88 nm). In this manner, we could capture every synapse in a two-dimensional image plane. In order to cover complete, three-dimensional neuropils, we acquired image stacks containing around 150 single image planes. The spacing between these image planes was 296 nm, which constituted a compromise between the desired coverage of all synapses, optimal axial resolution, and the time required for acquisition. Subsequently, we quantified the differences in staining intensity throughout the image stacks. To this end, we calculated the ratio between both antibody signal intensities for each pixel, and thus for each synapse.

1.2.1. Segmentation and thresholding[9]

It is understood that we wanted to quantify stainings at synapses and not weak background signals between synapses or even outside neuropils. We therefore first segmented the respective neuropil of interest from the rest of the brain (Fig. 16), using the Fiji ImageJ plugin *Segmentation Editor* (Schindelin et al., 2012; Schmid, 2010). We used a similar approach for segmentation of the MB calyx previously (Christiansen et al., 2011; Kremer et al., 2010).

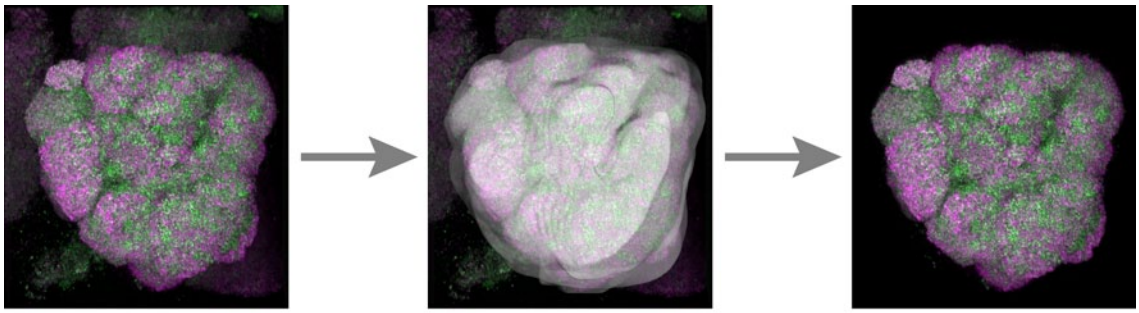

Fig. 16: Illustration of the segmentation of an AL from the surrounding neuropil.

Since all proteins that were examined are mainly synaptic, their expression should be strongest at synapses. Thus, we applied a threshold to each image to keep only pixels with high signal intensities. After considering several methods for finding thresholds, we decided to apply a percentile threshold: in this manner, only pixels that were among the brightest 20% were retained (Fig. 18). Dimmer pixels were set to an inten-

[9] Thresholding is explained in detail in Materials and Methods, section 3.1, pages 37-39.

sity value of zero. This 20% threshold was found to deliver an optimal separation of synaptic from non-synaptic signals, based on manual comparisons. Because intensities vary within image stacks, each stack was divided into substacks for the determination of thresholds. This procedure allowed for the identification of threshold levels suitable for each image plane, even when intensities varied.

The algorithm for merging image stacks with segmentation masks and the subsequent thresholding was implemented into the ImageJ plugin *Mask Generator*. This plugin is, together with all other novel algorithms described here, part of the ImageJ package *Ratio Calculator*. All these plugins are, along with their source code, downloadable from http://ratios.andlauer.net.

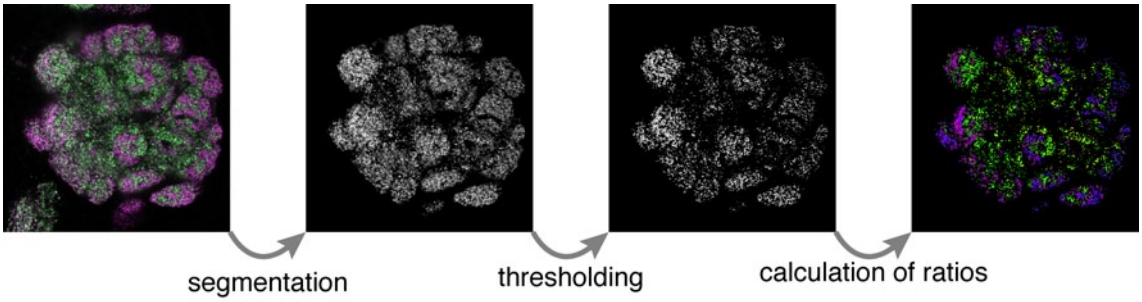

Fig. 18: Illustration of the steps segmentation, thresholding and calculation of ratios.

1.2.2. Calculation of ratios[10]

8-bit images contain 256 (2^8) monochrome intensity values ranging from 0 to 255. Calculating the ratio between two 8-bit values in all 65536 (256×256) possible cases yields only 39641 different values. This is the case because there are, for example, 256 different possibilities for calculating the ratio 1 (1/1, 2/2, 3/3, etc.), 128 different ways of calculating 0.5 (1/2, 2/4, 3/6, etc.), and so forth (Fig. 17).

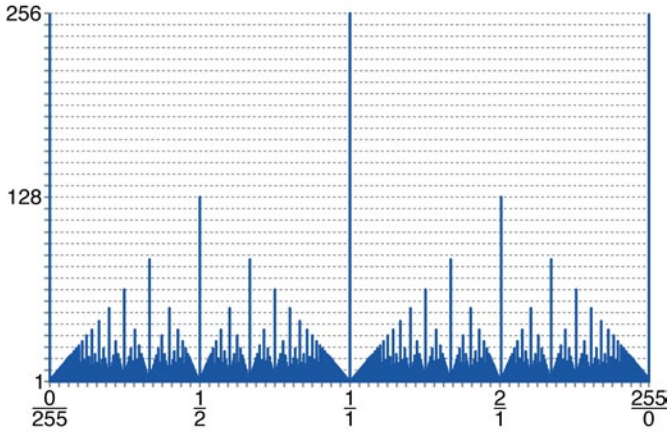

Fig. 17: Frequencies of all possible ratios.
Histogram showing the frequencies (1-256) of all possible ratios *a*/*b* of two values *a* and *b*, each ranging from 0-255.

Ratio values were calculated for every pixel of an image stack. To visualize ratios, each real ratio number was mapped in ascending order to an integer, ranging from 1 to 39641 (because 39641 different ratio values existed). Accordingly, the ratio 1/1

[10] For additional information regarding the calculation of ratios, see Methods 3.2, pages 40-41.

corresponds to 19821 and 255/0 to 39641. The resulting data was displayed as a 16 bit image stack and colours were mapped to the values 1-39641 (Fig. 19). This allowed us to highlight synapse populations with especially strong differences in CAZ protein intensity.

Basic statistics like the median ratio value and a histogram of the ratio distribution were computed for each image stack. Means of medians constitute the average median ratio of a sample set[11]. Errors were calculated as standard error of the mean. More complex analysis of the data, for example a comparison of the area under both halves of the histogram, were considered. However, such computations could neither improve the quality of the analysis further nor facilitate the interpretation of the data. Thus, simple median ratios are shown in all graphs (Fig. 20).

Fig. 19: Colour mapping for the visualisation of ratio values.
Ratio: *other* / Brp$^{C\text{-}Term}$

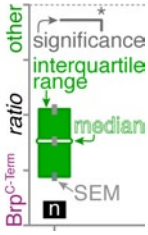

Fig. 20: Scheme of how ratio statistics are presented.
Median = mean of medians. n = sample size. SEM = standard error of the mean. The y-axis showing the ratio values is scaled according to $\log_2$.

Sometimes it could not be avoided that one or both of the channels were oversaturated during image acquisition. All oversaturated pixels have an intensity of 255, irrespective of the original brightness of that spot. This could possibly distort the data and bias the intensity distribution towards the value 255. Therefore, all ratios derived from the value 255 were omitted from the calculation of statistics.

Median ratio values only represent a single data point of an often diverse ratio distribution. Thus, the frequencies of all ratios in an image stack were visualized in histograms. As stacks varied in the amount of image planes, frequencies were normalized for the total amount of data points. Subsequently, all histograms were scaled with the same multiplication factor. To integrate data from the complete sample set containing several image stacks, mean frequencies where calculated for each bin[11].

1.3. Characterization of synapse types

1.3.1. Mushroom body calyx

We began our analysis of ratio distributions with the MB calyx of wildtype animals. Here, ratios of RBP$^{C\text{-}Term}$ to Brp$^{C\text{-}Term}$, Syd-1 to Brp$^{C\text{-}Term}$, and Brp$^{N\text{-}Term}$ to Brp$^{C\text{-}Term}$ were calculated. All three median ratios were slightly below 1/1 and thus showed a trend

[11] Analysis of the data is outlined in more detail in Materials and Methods 3.3, pages 42-44.

towards a stronger presence of Brp$^{C\text{-}Term}$ (Fig. 21). A likely explanation is that Brp$^{C\text{-}Term}$ was generally acquired with a somewhat higher signal intensity than the other three antibodies. A certain variability of the overall signal intensities of antibody stainings can hardly be avoided, preeminently due to differences in their signal-to-noise ratios. This, however, does not constitute a principal issue here, as we were not interested in absolute ratios but in the relative differences between them. We also observed apparent differences in absolute ratios between staining batches and thus always stained and imaged all brains that were to be compared at the same time.

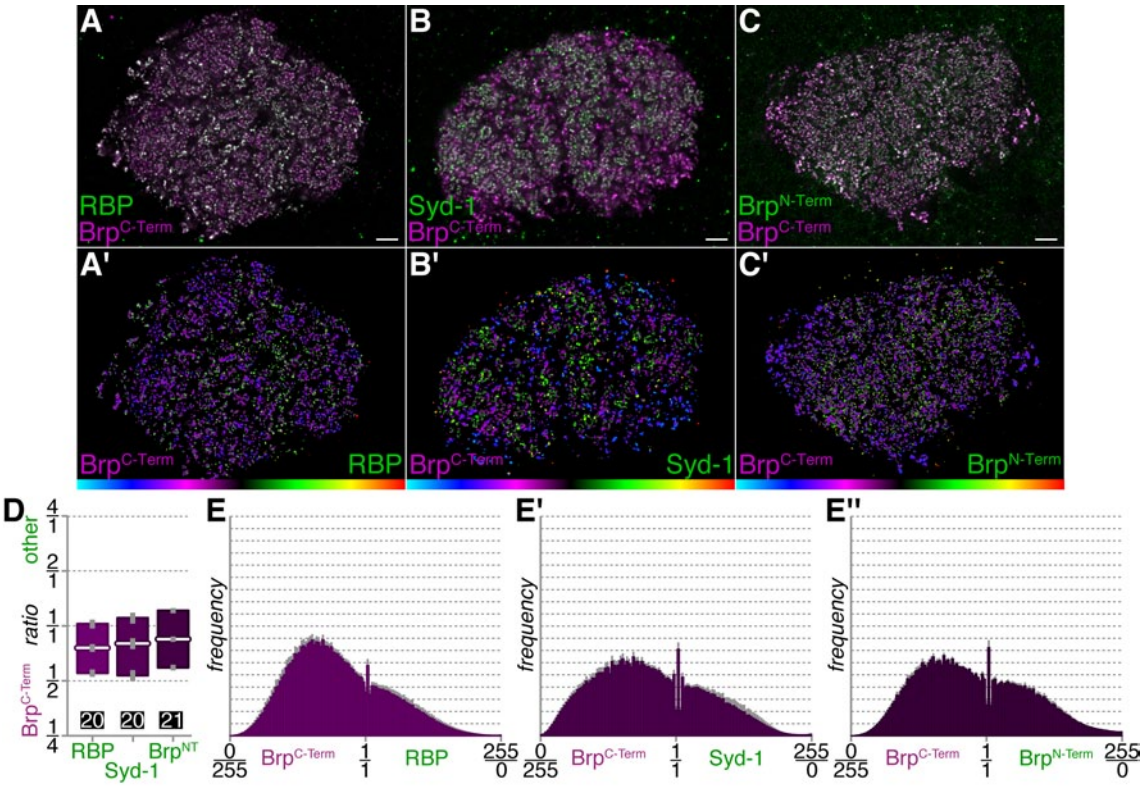

Fig. 21: Ratios in wildtype calyces.
A-C: Antibody stainings, single image planes, scale bars: 5 µm.
A: RBP and Brp$^{C\text{-}Term}$. **B:** Syd-1 and Brp$^{C\text{-}Term}$. **C:** Brp$^{N\text{-}Term}$ and Brp$^{C\text{-}Term}$.
A'-C': Visualisation of ratios in the same image planes.
D,E: The colour code of the graphs corresponds to the respective colour of the median ratio, according to the spectrum shown in Fig. 19 and below the ratio images in A'-C'.
D: Median ratios (see Fig. 20). The y-axis showing the ratio values is scaled according to $\log_2$.
E: Histograms showing the frequency of all ratios throughout the image stacks. To integrate data from the complete sample set, mean frequencies where calculated for each bin. Frequencies were normalized for the total amount of data.

The visualisation of ratio values confirmed the impression that populations of synapses with different relative amounts of CAZ proteins do exist (Fig. 21A'-C'). However, we could not yet allocate individual puncta of a certain ratio to defined neuron types. Therefore, we could not test the hypothesis that distinct CAZ protein ratio classes correspond to certain classes of neuronal cell types. To address this issue, we expressed Brp$^{short\text{-}GFP}$ constructs with cell-specific Gal4 drivers; Brp$^{short\text{-}GFP}$ is a fragment of Brp that depends on endogenous Brp for localization to AZs and accumu-

lates proportionally to full-length Brp isoforms (Fouquet et al., 2009; Kremer et al., 2010; Schmid et al., 2008). Brp$^{short\text{-}GFP}$ therefore labels all presynapses of the cells it is expressed in that contain endogenous Brp. Moreover, expression of the construct does not stimulate the generation of synapses *de novo* (Kremer et al., 2010). Thus, by examining only synapses marked by Brp$^{short\text{-}GFP}$, we were able to observe CAZ protein ratios at identified synapses.

For the GFP-based analysis, first the complete neuropil was segmented, as previously described (Fig. 16). Next, segmentation was refined for GFP-positive synapses; cell bodies and axons strongly labelled by GFP were removed (Fig. 22). Subsequently, a 95% percentile threshold was applied to the segmented GFP signal. Thus, only GFP-positive pixels belonging to the brightest 5% were kept. Thereafter, ratios were calculated once for the complete neuropil and once for the GFP-positive mask.

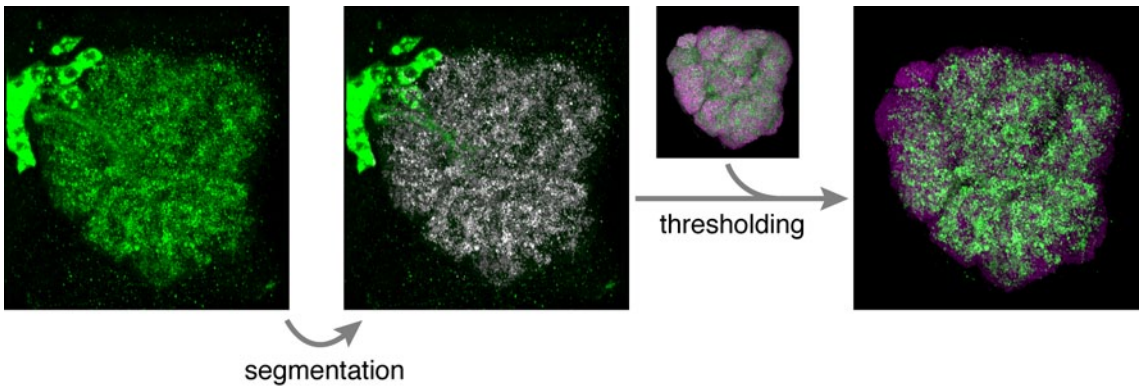

Fig. 22: Illustration of segmentation and thresholding of GFP signals.
Note that the antibody staining of the complete neuropil was just added as a reference here, it does not influence calculation of the threshold for the GFP signal.

We conducted the analysis of ratios at defined synapses with three Gal4 drivers labelling neurons that form presynapses in the MB calyx:

- Mz19-Gal4 drives expression in a subset of projection neurons (PNs), conveying olfactory information from the AL to the MB calyx (Ito et al., 1998; Kremer et al., 2010) (Fig. 23).
- 17D-Gal4 marks a subset of Kenyon cells (KCs), MB-intrinsic neurons and postsynaptic partners of PNs (Aso et al., 2009; Melzig et al., 1998) (Fig. 24). In 2011, we have identified previously unknown synapses in the calyx, at which KCs are presynaptic (Christiansen et al., 2011).
- Gad1-Gal4 is a driver for GABAergic inhibitory neurons (Enell et al., 2010; Ng et al., 2002). Because gad1-Gal4 also shows some expression in KCs, we combined it with the construct *mb247::gal80* that inhibits Gal4 activity in KCs[12] (Fig. 25).

[12] *mb247::gal80* expresses Gal80 (inhibitor of Gal4) under control of the *247* enhancer (upstream of *mef2*) (Schulz et al., 1996). This construct was generated by Frauke Christiansen.

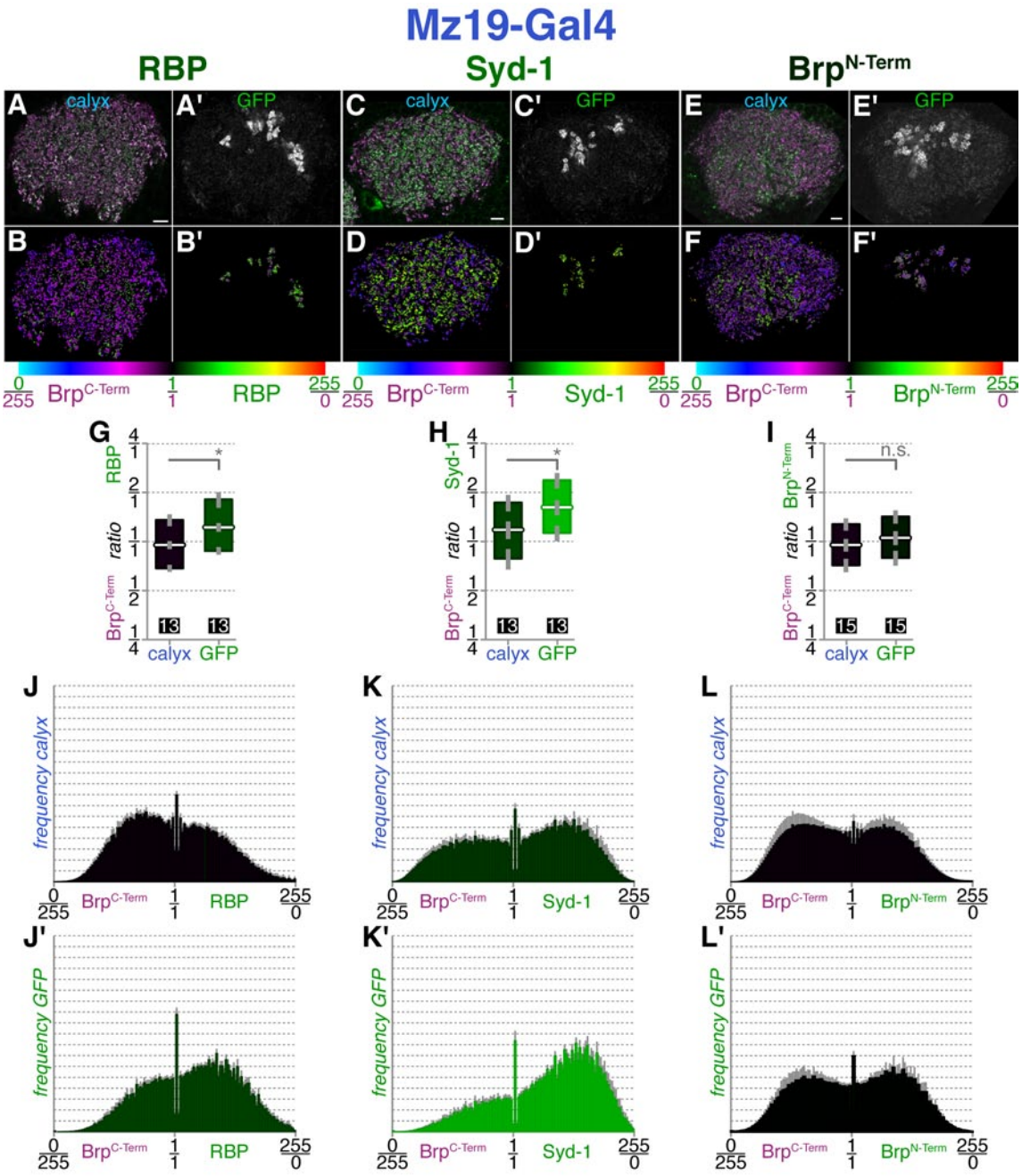

Fig. 23: Ratios at spots labelled by mz19-Gal4 (PNs) in the calyx.
A,C,E: Antibody stainings, single image planes, scale bars: 5 µm. **A:** RBP and Brp$^{C\text{-}Term}$. **B:** Syd-1 and Brp$^{C\text{-}Term}$. **C:** Brp$^{N\text{-}Term}$ and Brp$^{C\text{-}Term}$. **A',C',E':** UAS-brp$^{short\text{-}GFP}$ driven by mz19-Gal4. **B,D,F:** Visualisation of ratios in the same image planes. **G-L:** The colour code of the graphs corresponds to the respective colour of the median ratio, according to the spectrum shown in Fig. 19. **G-I:** Median ratios, signal of the complete calyx vs. signal in GFP-positive spots. Mann-Whitney U-tests (MWU) were used to assay whether median ratios differed significantly. MWU test results: G: p=0.0077, H: p=0.0149, I: p=0.4429; significance level α=0.0167 (Bonferroni-corrected for 3 tests (0.05/3)). **J-L,J'-L':** Histograms of ratio frequencies.
J-L: Ratios within the complete calyx. **J'-L':** Ratios at GFP-positive spots.

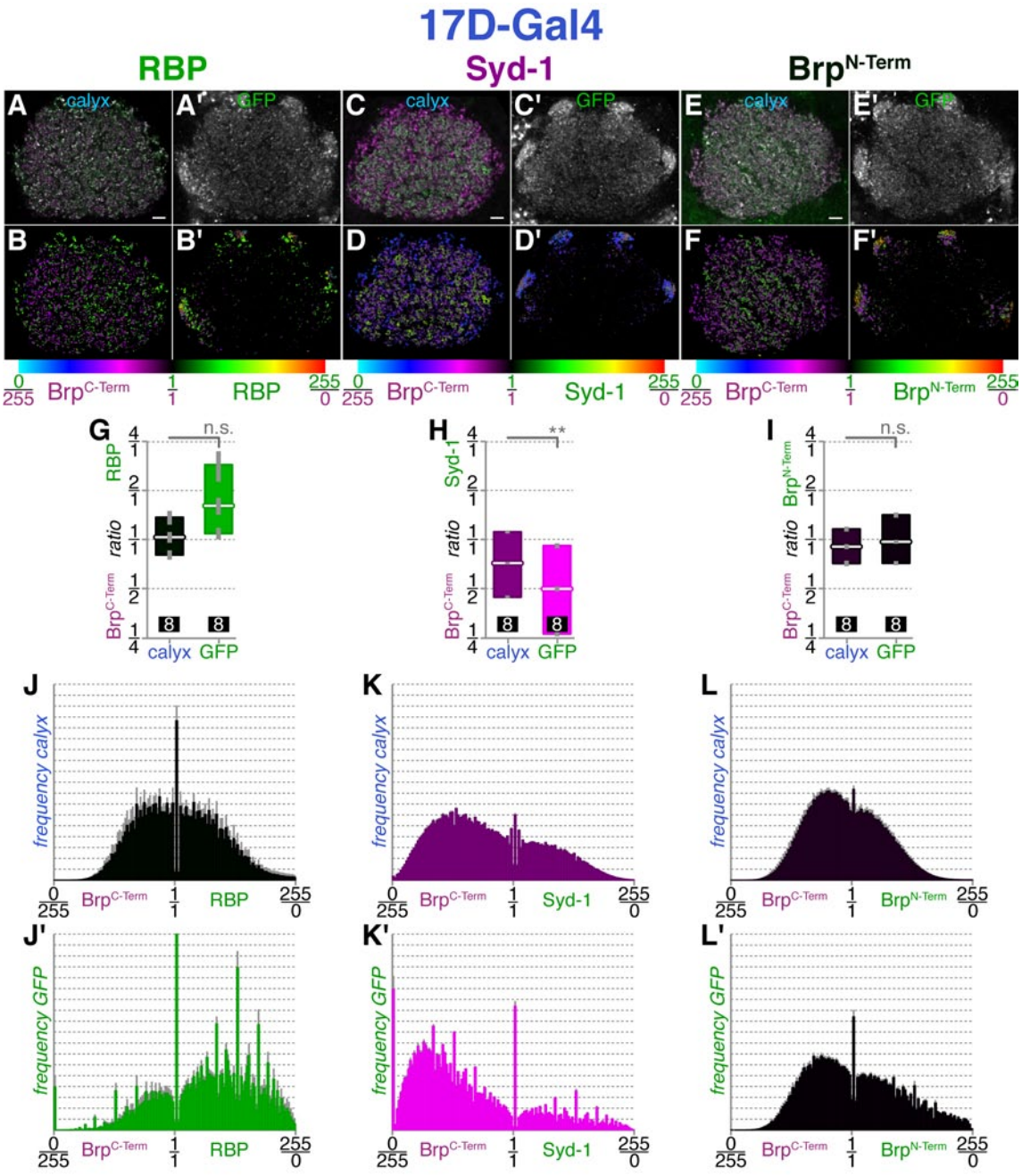

Fig. 24: Ratios at spots labelled by 17D-Gal4 (KCs) in the calyx.
A,C,E: Antibody stainings, single image planes, scale bars: 5 µm.
A: RBP and Brp$^{C\text{-}Term}$. **B:** Syd-1 and Brp$^{C\text{-}Term}$. **C:** Brp$^{N\text{-}Term}$ and Brp$^{C\text{-}Term}$.
A',C',E': UAS-brp$^{short\text{-}GFP}$ driven by 17D-Gal4.
B,D,F: Visualisation of ratios in the same image planes.
G-I: Median ratios, signal of the complete calyx vs. signal in GFP-positive spots.
MWU test results: G: p=0.0313, H: p=0.0008, I: p=0.1722; α=0.0167.
J-L,J'-L': Histograms of ratio frequencies.
J-L: Ratios within the complete calyx. **J'-L':** Ratios at GFP-positive spots.

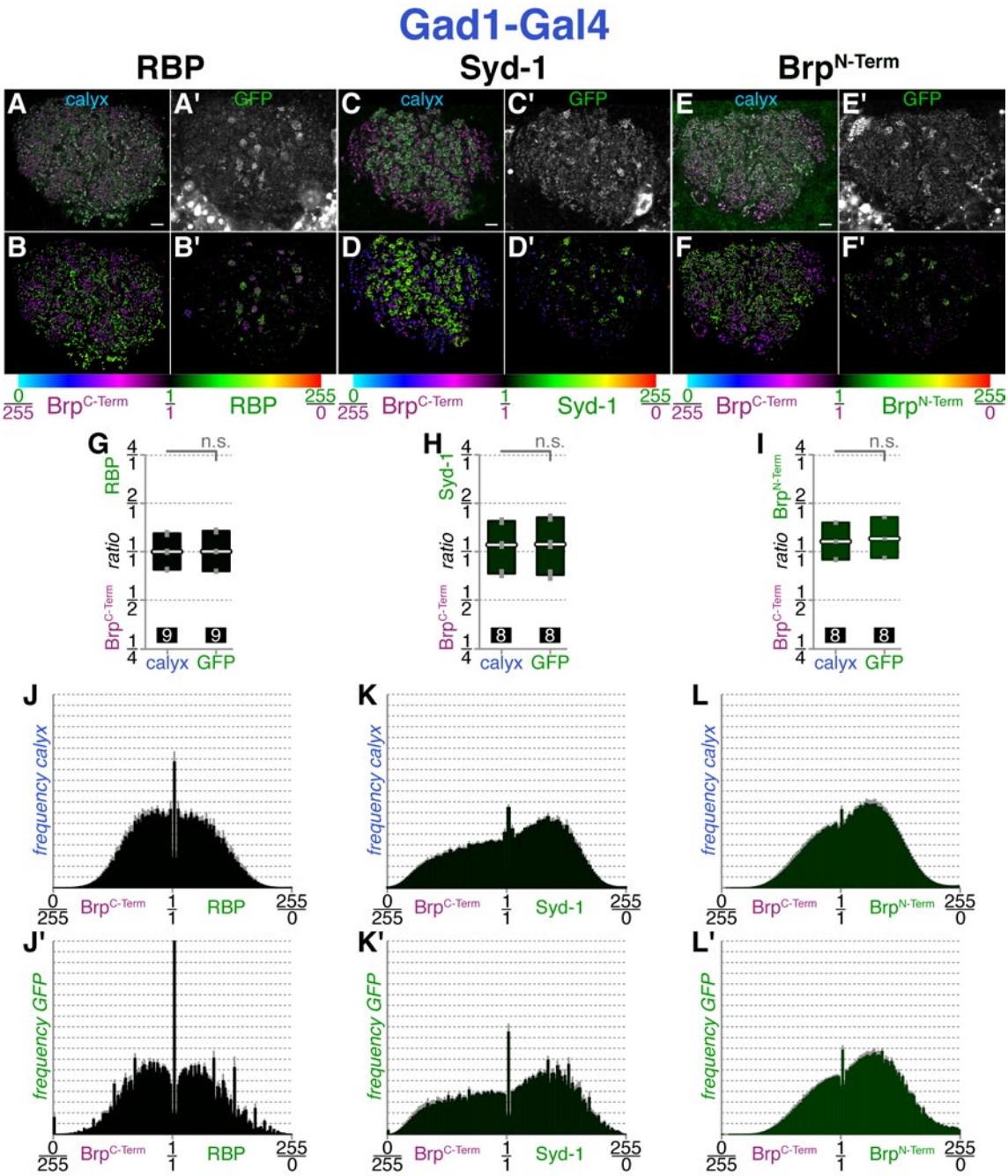

Fig. 25: Ratios at spots labelled by gad1-Gal4 (GABAergic neurons) in the calyx.
A,C,E: Antibody stainings, single image planes, scale bars: 5 µm.
A: RBP and Brp$^{C\text{-}Term}$. **B:** Syd-1 and Brp$^{C\text{-}Term}$. **C:** Brp$^{N\text{-}Term}$ and Brp$^{C\text{-}Term}$.
A',C',E': UAS-brp$^{short\text{-}GFP}$ driven by gad1-Gal4, combined with *mb247::gal80*.
B,D,F: Visualisation of ratios in the same image planes.
G-I: Median ratios, signal of the complete calyx vs. signal in GFP-positive spots.
MWU test results: G: p=0.7911, H: p=0.9164, I: p=0.1722; α=0.0167.
J-L,J'-L': Histograms of ratio frequencies.
J-L: Ratios within the complete calyx. **J'-L':** Ratios at GFP-positive spots.

Only 4.7% of all spots in the calyx were positive for GFP expressed by mz19-Gal4 (Fig. 23, Fig. 26). This is the case because this Gal4 line includes just a rather small subset of PNs. Of note, a previous report stated that about 4% of microglomeruli in the calyx are labelled by mz19-Gal4, a similar proportion (Kremer et al., 2010). We chose this line as a PN driver because it is not contaminated with other cell types at the level of the calyx (Jefferis et al., 2004; Kremer et al., 2010). Accordingly, the share of all PN presynapses in the complete calyx is expected to be much larger than the number including just mz19-positive PNs.

Within this subset of PNs, the two median ratios RBP / $Brp^{C\text{-}Term}$ and Syd-1 / $Brp^{C\text{-}Term}$ were significantly shifted to higher values and thus away from $Brp^{C\text{-}Term}$, when compared to median ratios calculated for the complete calyx (Fig. 23). In other words, mz19-positive PN synapses in the calyx are characterized by elevated RBP / $Brp^{C\text{-}Term}$ and Syd-1 / $Brp^{C\text{-}Term}$ ratios, in combination with a slightly increased $Brp^{N\text{-}Term}$ / $Brp^{C\text{-}Term}$ ratio (merely by 10.6%, see Table 2).

The same two median ratios also showed a shift for GFP-positive puncta when 17D-Gal4 was used as a driver (Fig. 24). For these KC synapses, the median ratio RBP / $Brp^{C\text{-}Term}$ was changed in the direction of RBP (i.e. increased by 56%); when applying Bonferroni correction for three tests (significance level $\alpha = 0.05/3 = 0.0167$), this difference was not significant ($p=0.031$, Mann-Whitney U-test (MWU)). This is probably due to the high variability within the data set (compare error bars in Fig. 24G,H). By contrast, the ratio Syd-1 / $Brp^{C\text{-}Term}$ showed a clear and significant bias towards $Brp^{C\text{-}Term}$ at GFP spots ($p=0.0008$, decrease by 30.5%). $Brp^{N\text{-}Term}$ / $Brp^{C\text{-}Term}$ was unaltered: a ratio was considered as balanced if the difference to the complete neuropil was below 10%; the median ratio of $Brp^{N\text{-}Term}$ / $Brp^{C\text{-}Term}$ was only elevated by 7%.

It can be concluded that KC presynapses in the calyx are distinguished by an increased RBP / $Brp^{C\text{-}Term}$ ratio on the one hand and a decreased Syd-1 / $Brp^{C\text{-}Term}$ ratio on the other hand, while $Brp^{N\text{-}Term}$ / $Brp^{C\text{-}Term}$ is close to the average ratio value of calycal presynapses. 17D-Gal4 labels 20.2% of synapses in the calyx (Fig. 26). Since 17D-Gal4 drives expression only in a subset of KCs, the complete share of KC presynapses in the calyx is larger. In Christiansen et al., 2011, KC presynapses were estimated to constitute 20-30% of the presynapses in the calyx.

In the case of gad1-Gal4, none of the ratios calculated for the GFP signal differed by more than 4.1% from the respective median ratios derived from the complete calyx (Fig. 25). The images suggest that gad1-Gal4 labels a mixed inhibitory synapse population that does not share a preeminent CAZ protein feature (Fig. 25B',D',F').

The results are summarized in Fig. 26 and Table 2. All three synapse types that were examined showed a distinguishable signature in their CAZ protein composition.

	$\frac{RBP^{C\text{-}Term}}{Brp^{C\text{-}Term}}$	$\frac{Syd\text{-}1}{Brp^{C\text{-}Term}}$	$\frac{Brp^{N\text{-}Term}}{Brp^{C\text{-}Term}}$
Projection neurons (mz19, 4.7%)	significantly increased by 28.4% (p=6.9%)	significantly increased by 37.2% (p=6.4%)	slightly increased by 10.6% (p=4.4%)
Kenyon cells (17D, 20.2%)	increased by 56% (not significant) (p=31.2%)	significantly decreased by 30.5% (p=22.9%)	balanced (change: 7%) (p=15.6%)
GABAergic neurons (gad1, 22.3%)	balanced (change: 0.3%) (p=22.6%)	balanced (change: 0.7%) (p=20.9%)	balanced (change: 4.1%) (p=20.8%)

Table 2: Comparison of ratios at presynapses in the MB calyx.
Summary of the differences between ratios at spots marked by Gal4 lines and ratios of the respective complete calyx neuropil (Fig. 23, Fig. 24, Fig. 25).
Columns: antibodies; rows: Gal4 lines.
The share of spots positive for GFP in each case is indicated in the first column.
Ratios are labelled as increased or decreased if the difference in median ratios was at least 10%. This difference is indicated in each cell.
The p-values represent the Bayesian conditional probability that a single, random spot with a certain property (e.g., a high RBP / $Brp^{C\text{-}Term}$ ratio) is part of the synapse population labelled by the respective Gal4 driver: p(Gal4|ratio)=p(ratio|Gal4)×p(Gal4)/p(ratio).
For this calculation, ratios <0.95 were considered as low values and ratios >1.05 as high values.
Additional explanations are provided on page 44, Materials and Methods.

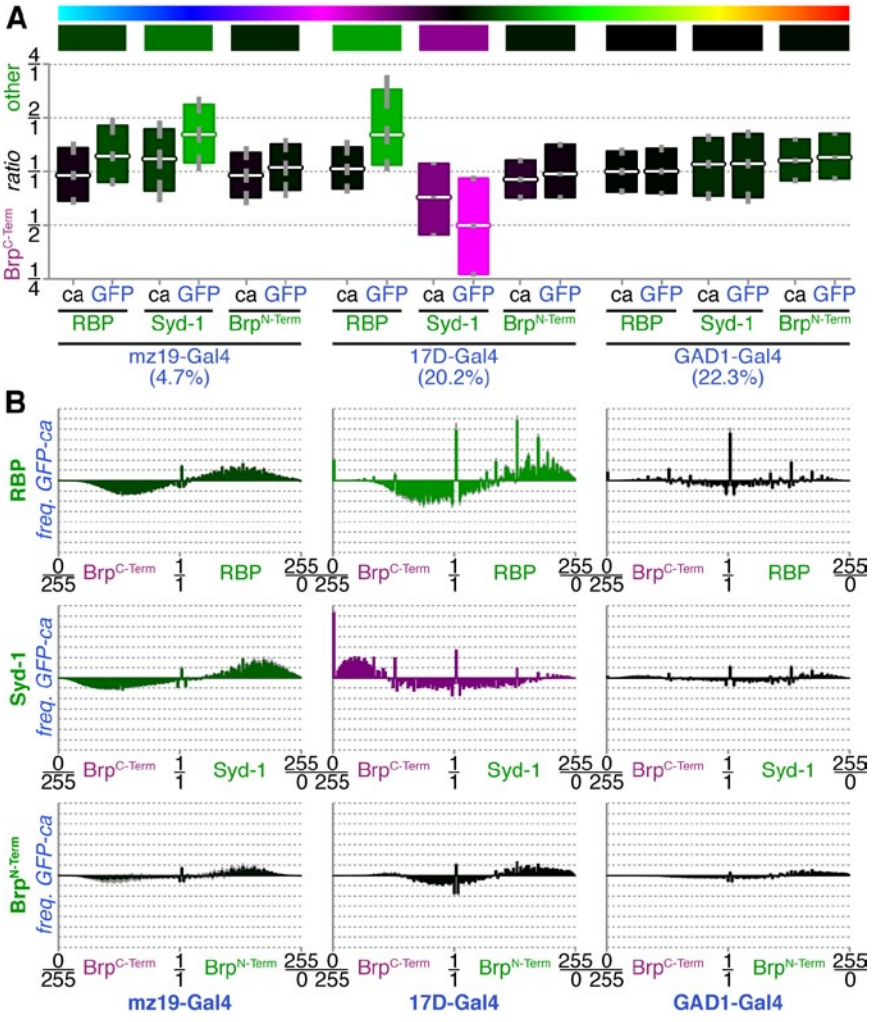

Fig. 26: Summary of ratios in the MB calyx.
Summary from Fig. 23, Fig. 24, Fig. 25; ca=calyx.
A: Median ratios.
The coloured bar above each graph represents the relative difference between the ratio for the GFP-positive area and the ratio of the complete calyx (r_{GFP}/r_{calyx}).
The colour code is visualized at the top of the image, it corresponds to the one shown in Fig. 19.
The percentages at the bottom show the relative share of spots positive for the respective Gal4 line, compared to the complete calyx (n_{GFP}/n_{calyx}).
B: Differences in ratio frequencies between GFP-positive spots and the complete calyx.
The colours correspond to r_{GFP}/r_{calyx}, as in A.
Error bars show cumulative errors (SEMs) from both measurements ($e_{Calyx+GFP} = \sqrt{((e_{Calyx}/2)^2 + (e_{GFP}/2)^2)}$ (Papula, 2008)).

1.3.2. Antennal lobe

After analysis of the MB calyx, we next examined ratios in the AL, where marked differences in CAZ protein compositions were expected from visual inspection of the stainings (Fig. 12B, Fig. 13B, Fig. 14B). In ALs of wildtype animals, the median ratios of all three antibody combinations were close to 1 (Fig. 27). However, the ratio distributions were not restricted to centre values but spread over the complete spectrum. Especially in the case of RBP / Brp$^{C\text{-}Term}$, two peaks appeared, one for low and one for high ratio values, with a dent in the middle of the histogram (Fig. 27E). Thus, it is likely that two distinct ratio values dominate this distribution. In fact, puncta with strong RBP or strong Brp$^{C\text{-}Term}$ intensities appear to be spatially separate in the AL (Fig. 12B, Fig. 27A).

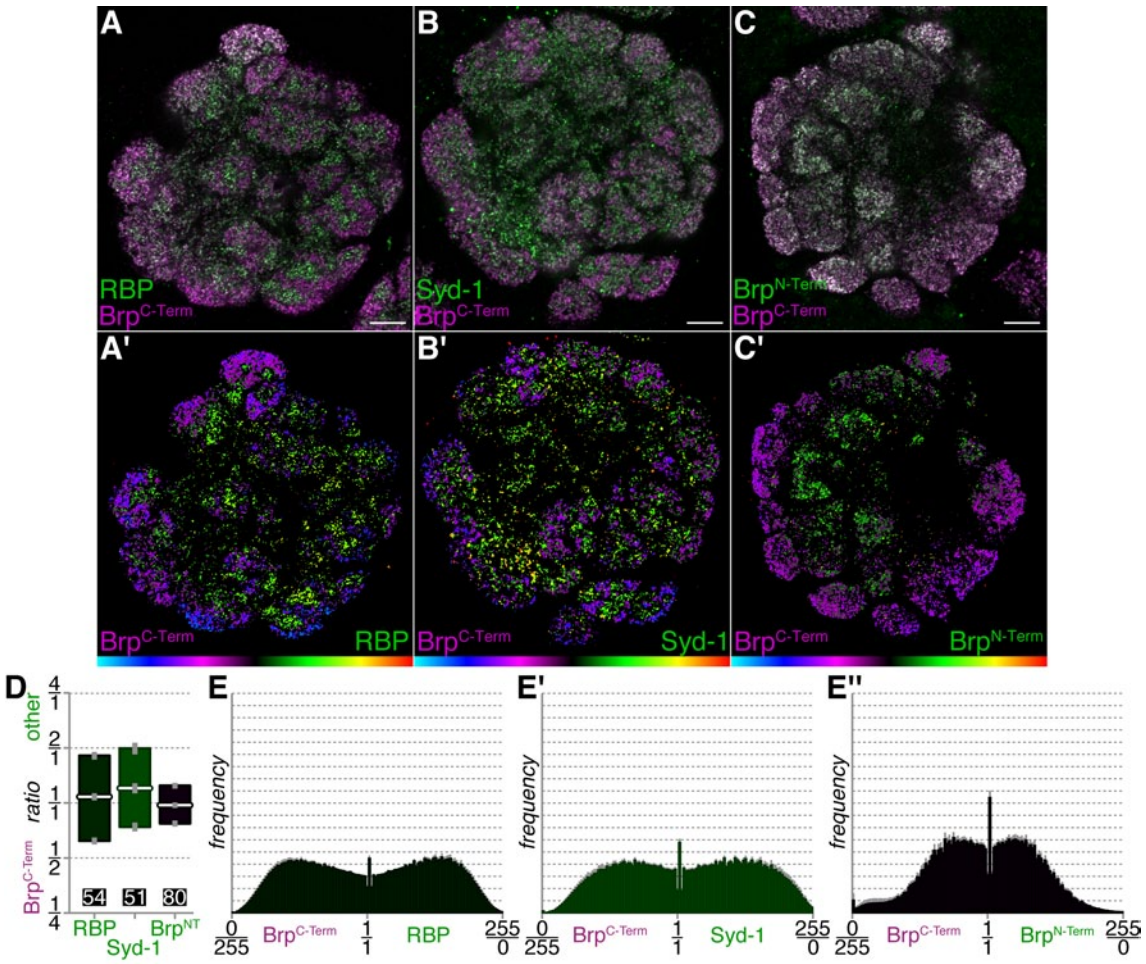

Fig. 27: Ratios in wildtype antennal lobes.
A-C: Antibody stainings, single image planes, scale bars: 10 µm.
A: RBP and Brp$^{C\text{-}Term}$. **B:** Syd-1 and Brp$^{C\text{-}Term}$. **C:** Brp$^{N\text{-}Term}$ and Brp$^{C\text{-}Term}$.
A'-C': Visualisation of ratios in the same image planes.
D,E: The colour code of the graphs corresponds to the respective colour of the median ratio, according to the spectrum shown in Fig. 19.
D: Median ratios. **E:** Histograms of ratio frequencies.

For characterization of ratios at different AL synapse populations, we used four different Gal4 lines:

- Or83b-Gal4 (alias orco-Gal4) is a marker for virtually all olfactory receptor neurons (ORNs), which constitute the main input into the AL (Vosshall et al., 1999; Wang et al., 2003) (Fig. 28).
- LN1-Gal4, also called NP1227-Gal4, drives expression in a population of inhibitory local interneurons (LNs) in the AL (Das et al., 2008) (Fig. 29).
- Krasavietz-Gal4 labels a mixed set of excitatory and inhibitory LNs, reports vary widely in their estimate of the respective percentages (Acebes et al., 2011; Chou et al., 2010; Dubnau et al., 2003; Huang et al., 2010; Seki et al., 2010; Shang et al., 2007; Yaksi and Wilson, 2010) (Fig. 30).
- Mz19-Gal4 is the PN driver also used for analysis of the MB calyx (Ito et al., 1998; Jefferis et al., 2004; Kremer et al., 2010) (Fig. 31).

When $Brp^{short\text{-}GFP}$ was expressed by or83b-Gal4, all three ratios of GFP-positive puncta had a median ratio value that differed significantly from the one calculated from data covering the complete AL (Fig. 28G-I). For both Syd-1 / $Brp^{C\text{-}Term}$ and $Brp^{N\text{-}Term}$ / $Brp^{C\text{-}Term}$, the ratio distribution within the mask for the whole AL was not balanced but shifted to higher or lower values, respectively (Fig. 28K,L). Since we were interested in relative differences of GFP-derived ratios to the surrounding neuropil and not in absolute values, this shift did not matter. Or83b-Gal4 synapses (11.2% of all pixels in the AL) are therefore characterized by a strikingly low RBP / $Brp^{C\text{-}Term}$ ratio, a decreased Syd-1 / $Brp^{C\text{-}Term}$ ratio, as well as an elevated $Brp^{N\text{-}Term}$ / $Brp^{C\text{-}Term}$ ratio.

Synapses positive for expression of LN1-Gal4 (24% of puncta in the AL) feature a CAZ protein composition that is opposite to the one of or83b-Gal4: RBP / $Brp^{C\text{-}Term}$ and Syd-1 / $Brp^{C\text{-}Term}$ ratios were increased, $Brp^{N\text{-}Term}$ / $Brp^{C\text{-}Term}$ decreased for spots marked by GFP (Fig. 29)[13].

By contrast, puncta marked by either krasavietz-Gal4 (23.4%, Fig. 30) or mz19-Gal4 (1.7%, Fig. 31) did not show any significant change of ratios when compared to median ratios computed for the entire AL. GFP-positive median ratios were considered as increased or decreased, if they differed by at least 10% from median ratios of the surrounding neuropil. The change of median ratios positive for krasavietz-Gal4 did not exceed 2.1% in any case. In contrast, ratios at mz19-spots differed by around 20% from ratios derived from the complete AL (increase for RBP / $Brp^{C\text{-}Term}$ and Syd-1 / $Brp^{C\text{-}Term}$; decrease for $Brp^{N\text{-}Term}$ / $Brp^{C\text{-}Term}$), yet this deviation was not significant. Both Gal4 lines include a diverse set of synapse types, which might be the reason for not obtaining a distinct ratio profile for them (see Discussion 1.2.1).

The complete results for the analysis of ALs are summarized in Table 3 and Fig. 32.

[13] An enrichment of RBP at inhibitory LNs was already described in Karen Liu's thesis (Liu, 2012).

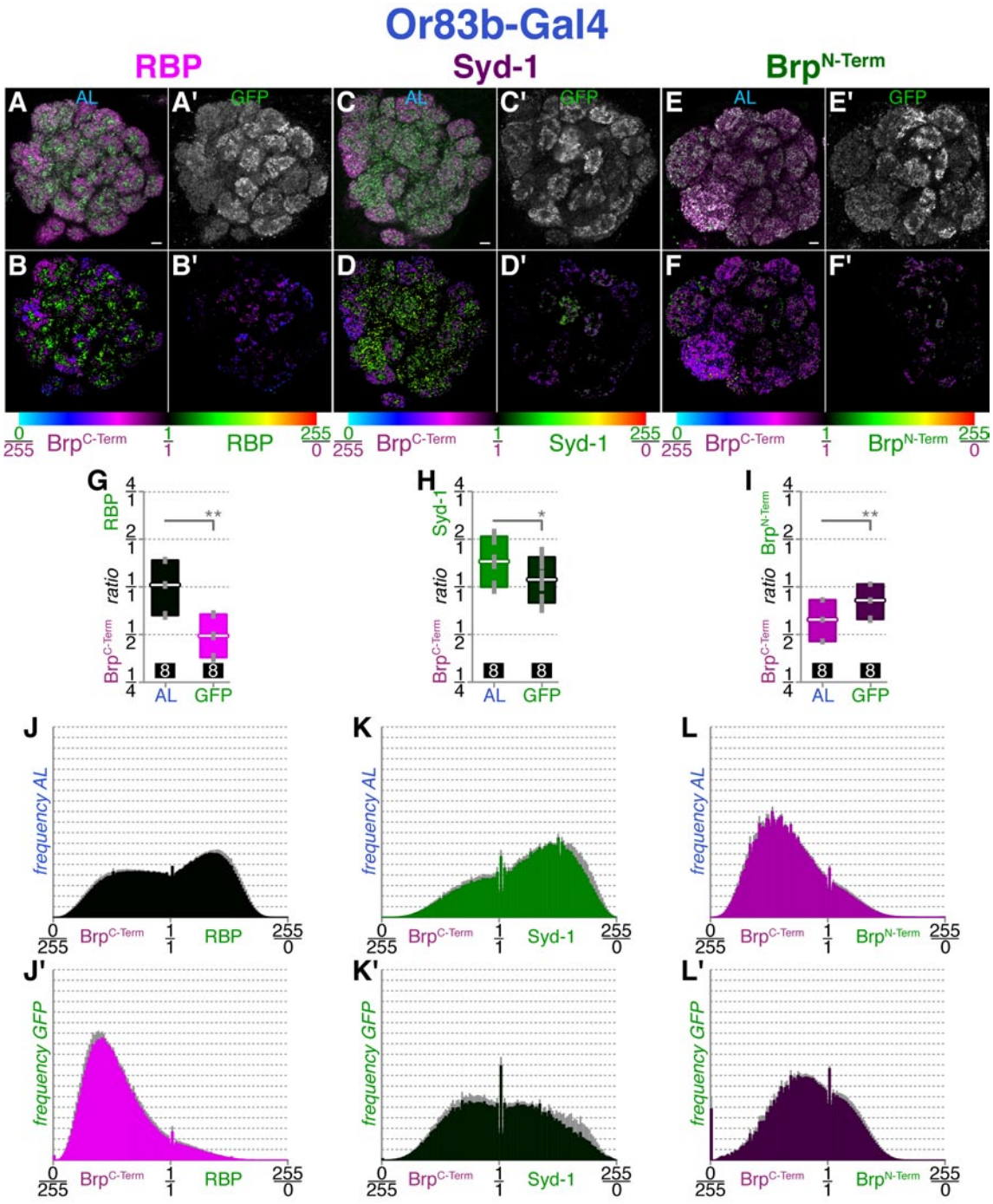

Fig. 28: Ratios at spots labelled by or83b-Gal4 (ORNs) in the antennal lobe.
A,C,E: Antibody stainings, single image planes, scale bars: 5 µm.
A: RBP and Brp$^{C\text{-}Term}$. **B:** Syd-1 and Brp$^{C\text{-}Term}$. **C:** Brp$^{N\text{-}Term}$ and Brp$^{C\text{-}Term}$.
A',C',E': UAS-brp$^{short\text{-}GFP}$ driven by or83b-Gal4.
B,D,F: Visualisation of ratios in the same image planes.
G-I: Median ratios, signal of the complete AL vs. signal in GFP-positive spots.
MWU test results: G: p=0.0008, H: p=0.0117, I: p=0.0016; α=0.0167.
J-L,J'-L': Histograms of ratio frequencies.
J-L: Ratios within the complete AL. **J'-L':** Ratios at GFP-positive spots.

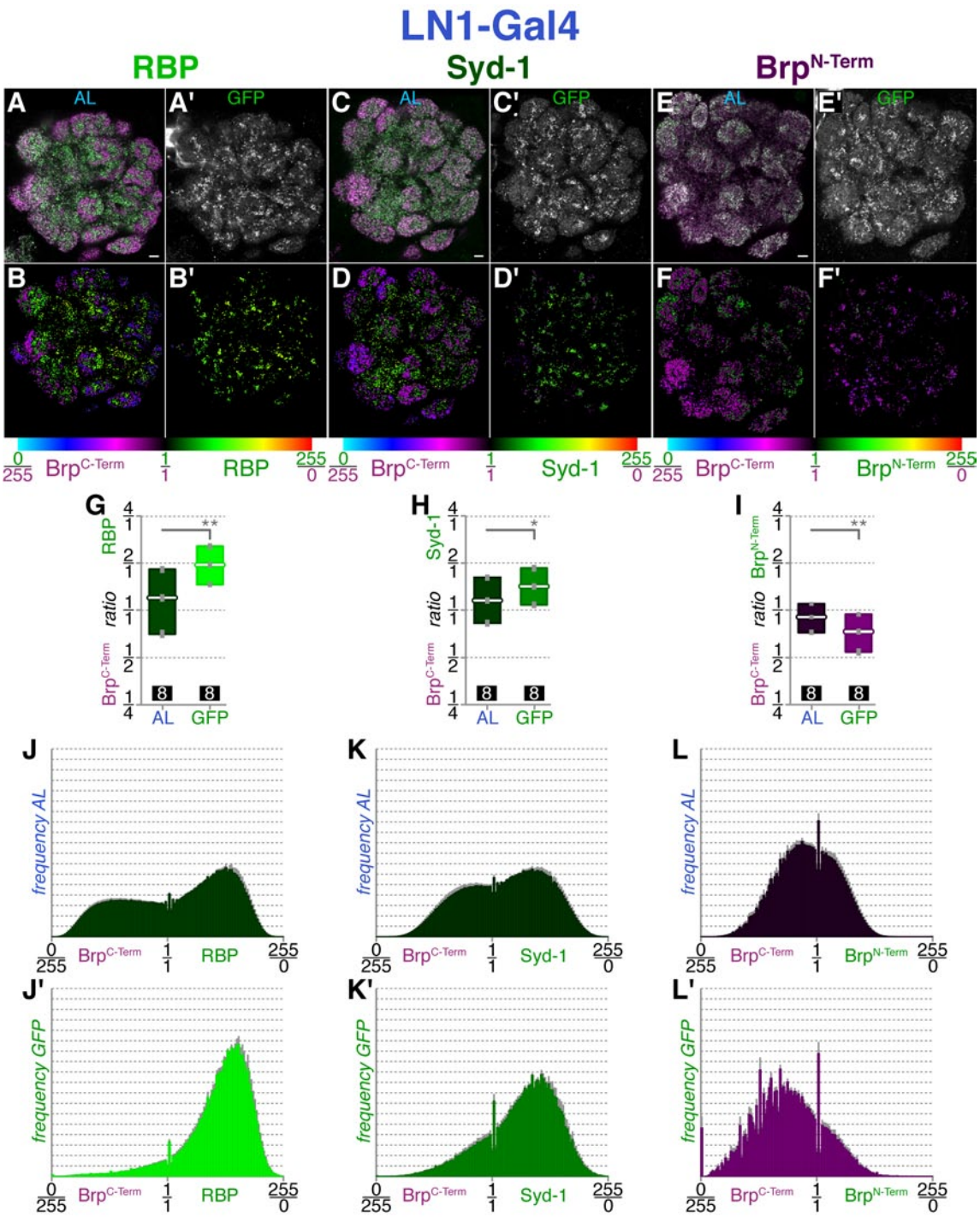

Fig. 29: Ratios at spots labelled by LN1-Gal4 (inhibitory LNs) in the antennal lobe.
A,C,E: Antibody stainings, single image planes, scale bars: 5 µm.
A: RBP and Brp$^{C\text{-}Term}$. **B:** Syd-1 and Brp$^{C\text{-}Term}$. **C:** Brp$^{N\text{-}Term}$ and Brp$^{C\text{-}Term}$.
A',C',E': UAS-brp$^{short\text{-}GFP}$ driven by LN1-Gal4.
B,D,F: Visualisation of ratios in the same image planes.
G-I: Median ratios, signal of the complete AL vs. signal in GFP-positive spots.
MWU test results: G: p=0.0008, H: p=0.0087, I: p=0.00328; α=0.0167.
J-L,J'-L': Histograms of ratio frequencies.
J-L: Ratios within the complete AL. **J'-L':** Ratios at GFP-positive spots.

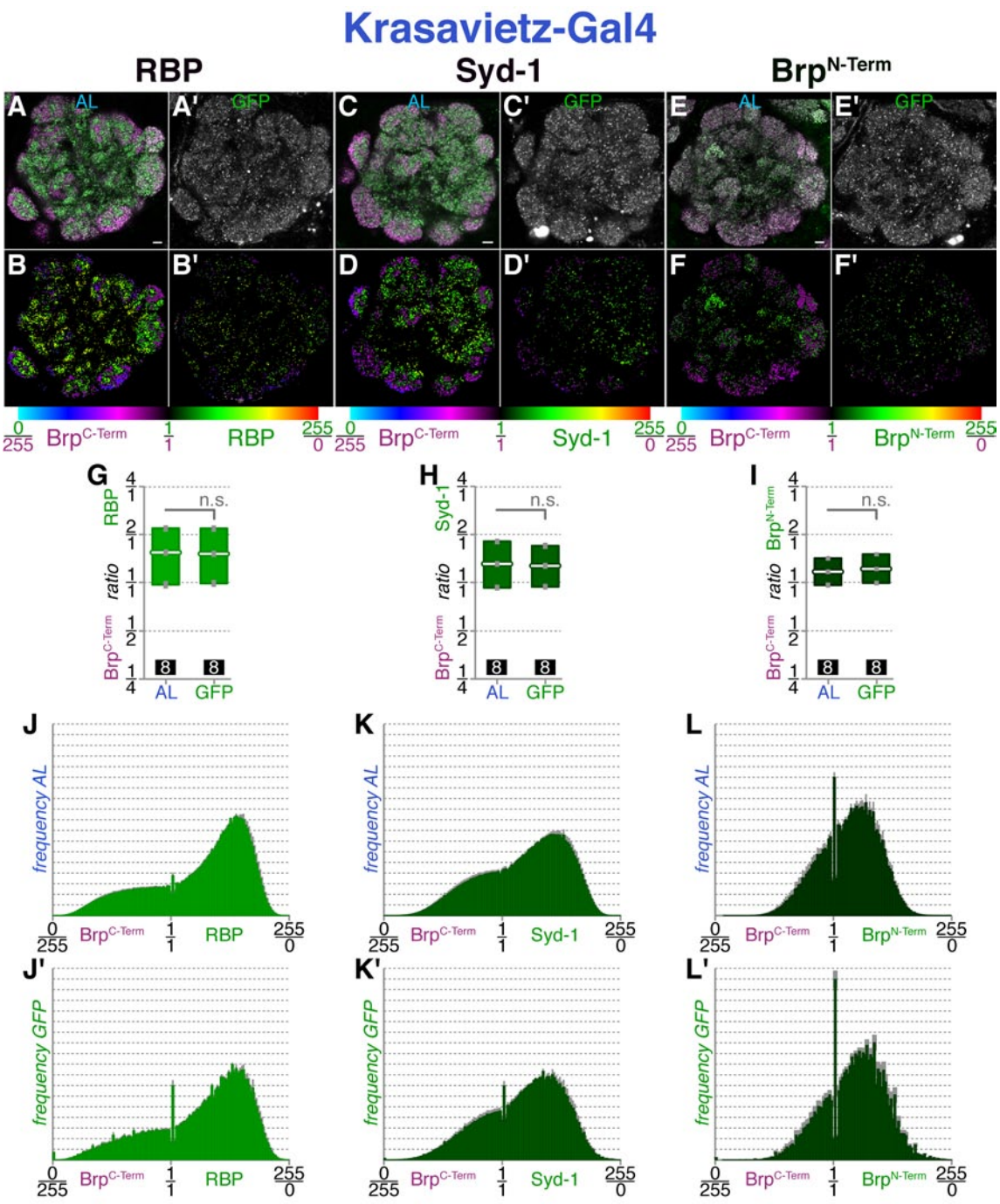

Fig. 30: Ratios at spots labelled by krasavietz-Gal4 (eLNs and iLNs) in the antennal lobe.
A,C,E: Antibody stainings, single image planes, scale bars: 5 µm.
A: RBP and Brp$^{C\text{-}Term}$. **B:** Syd-1 and Brp$^{C\text{-}Term}$. **C:** Brp$^{N\text{-}Term}$ and Brp$^{C\text{-}Term}$.
A',C',E': UAS-brp$^{short\text{-}GFP}$ driven by krasavietz-Gal4.
B,D,F: Visualisation of ratios in the same image planes.
G-I: Median ratios, signal of the complete AL vs. signal in GFP-positive spots.
MWU test results: G: p=0.4948, H: p=0.5286, I: p=0.4948; α=0.0167.
J-L,J'-L': Histograms of ratio frequencies.
J-L: Ratios within the complete AL. **J'-L':** Ratios at GFP-positive spots.

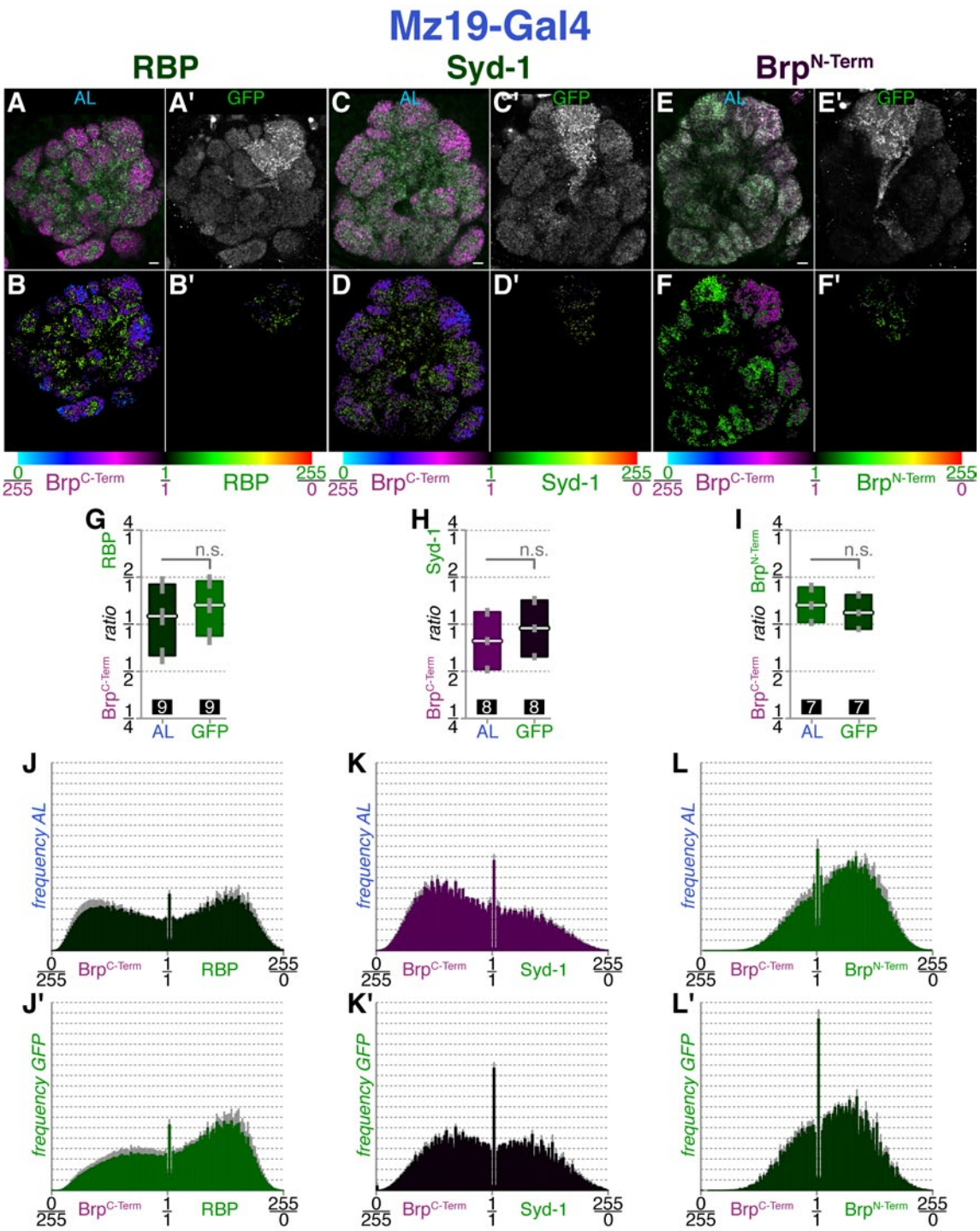

Fig. 31: Ratios at spots labelled by mz19-Gal4 (PNs) in the antennal lobe.
A,C,E: Antibody stainings, single image planes, scale bars: 5 µm.
A: RBP and Brp$^{C\text{-}Term}$. **B:** Syd-1 and Brp$^{C\text{-}Term}$. **C:** Brp$^{N\text{-}Term}$ and Brp$^{C\text{-}Term}$.
A',C',E': UAS-brp$^{short\text{-}GFP}$ driven by mz19-Gal4.
B,D,F: Visualisation of ratios in the same image planes.
G-I: Median ratios, signal of the complete AL vs. signal in GFP-positive spots.
MWU test results: G: p=0.3099, H: p=0.0357, I: p=0.2248; α=0.0167.
J-L,J'-L': Histograms of ratio frequencies.
J-L: Ratios within the complete AL. **J'-L':** Ratios at GFP-positive spots.

	$\frac{RBP^{C\text{-}Term}}{Brp^{C\text{-}Term}}$	$\frac{Syd\text{-}1}{Brp^{C\text{-}Term}}$	$\frac{Brp^{N\text{-}Term}}{Brp^{C\text{-}Term}}$
Olfactory receptor neurons (or83b/orco, 11.2%)	significantly decreased by 52.3% (p=22.5%)	significantly decreased by 23.2% (p=19.7%)	significantly increased by 32.5% (p=26.4%)
Inhibitory local interneurons (LN1/NP1227, 24.0%)	significantly increased by 62.5% (p=38.4%)	significantly increased by 23.2% (p=31.9%)	significantly decreased by 19% (p=32.0%)
Excitatory / inhibitory LNs (krasavietz, 23.4%)	balanced (change: 1.9%) (p=27.2%)	balanced change: 2.8%) (p=26.8%)	balanced (change: 4.1%) (p=21.4%)
Projection neurons (mz19, 1.7%)	increased by 17.7% (p=2.1%)	increased by 20.7% (p=1.9%)	decreased by 20.7% (p=2.0%)

Table 3: Comparison of ratios at presynapses in the AL.
Summary of the differences between ratios at spots marked by Gal4 lines and the respective complete AL neuropils (Fig. 28, Fig. 29, Fig. 30, Fig. 31). Columns: antibodies; rows: Gal4 lines. The share of spots positive for GFP in each case is indicated in the first column. Ratios are labelled as in- or decreased if the difference in median ratios was at least 10%. This difference is indicated in each cell. The p-values represent the Bayesian conditional probability that a single, random spot with a certain property is part of the synapse population labelled by the respective Gal4 driver. For this calculation, ratios <0.95 were considered as low values and ratios >1.05 as high values.

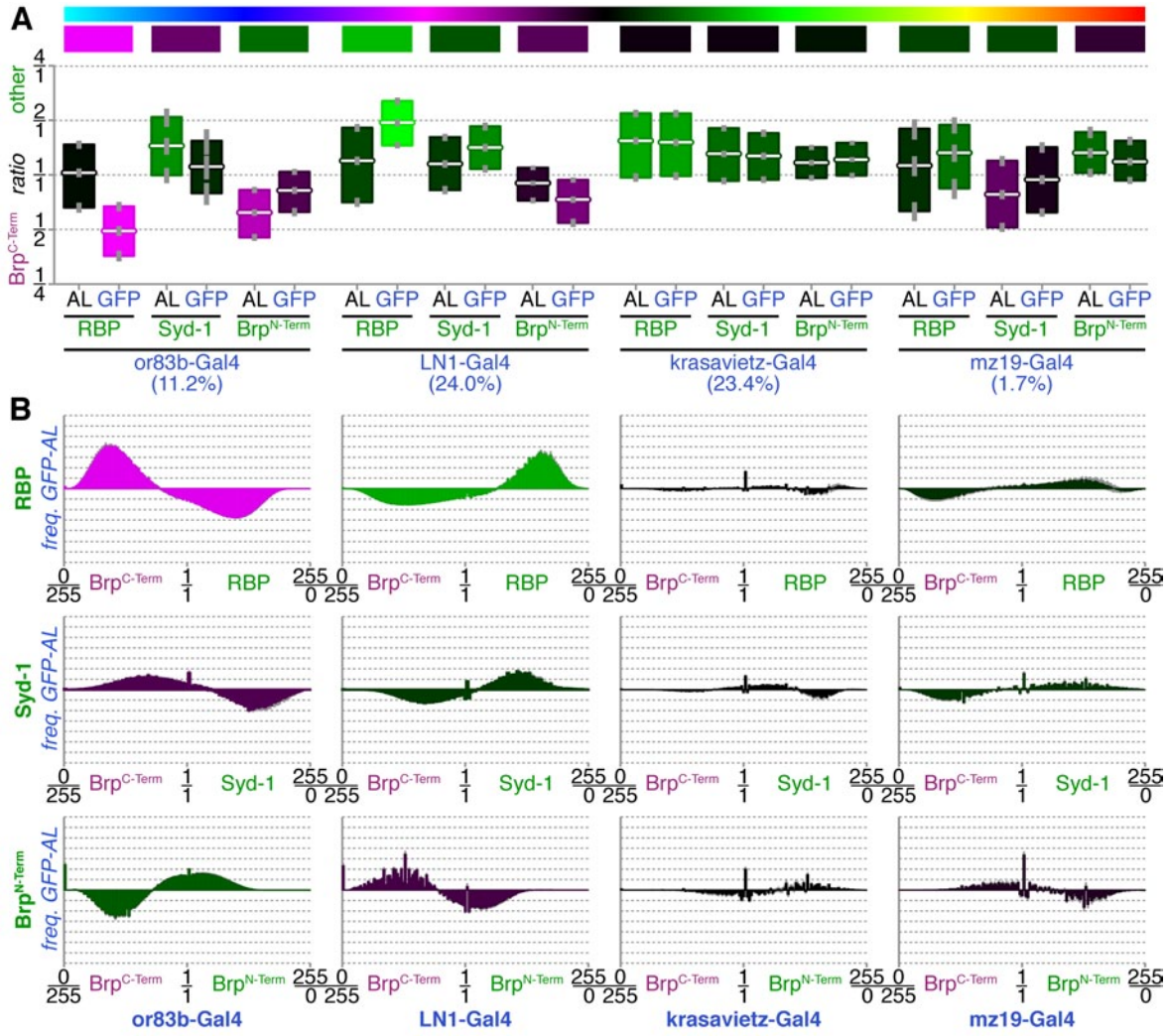

Fig. 32: Summary of ratios in the antennal lobe.
Summarized from Fig. 28, Fig. 29, Fig. 30, Fig. 31. The data is displayed as in Fig. 26.
A: Median ratios. **B:** Difference in ratio frequencies between GFP-positive spots and the complete AL.

1.4. Changes in the CAZ protein composition

We could demonstrate with our analysis of CAZ protein ratios at different synapse types that the ratiometric method is suitable for the illustration and quantification of differences in protein expression. However, we wondered whether it could also be used for the analysis of situations were levels of CAZ proteins were altered.

1.4.1. Analysis of the reduction of Brp levels in Kenyon cells

We have recently established the existence of KC presynapses in the MB calyx (Christiansen et al., 2011). As one approach for verifying the presence of these synapses, Brp levels were reduced in KCs by RNA interference (RNAi). Ok107-Gal4 was used to express the *brp-RNAi* construct, a line that, contrary to 17D-Gal4 used in section 1.3.1, drives expression in all KCs (Aso et al., 2009). Christiansen and colleagues subsequently compared Brp staining intensities in MB calyces between flies expressing *brp-RNAi* and control animals. RNAi-expressing animals showed a marked reduction of Brp levels in the calyx, supporting the notion that KCs feature Brp-positive presynapses in the calyx. The share of KC presynapses in the calyx was estimated to constitute 20-30% of all synapses in the calyx (Christiansen et al., 2011).

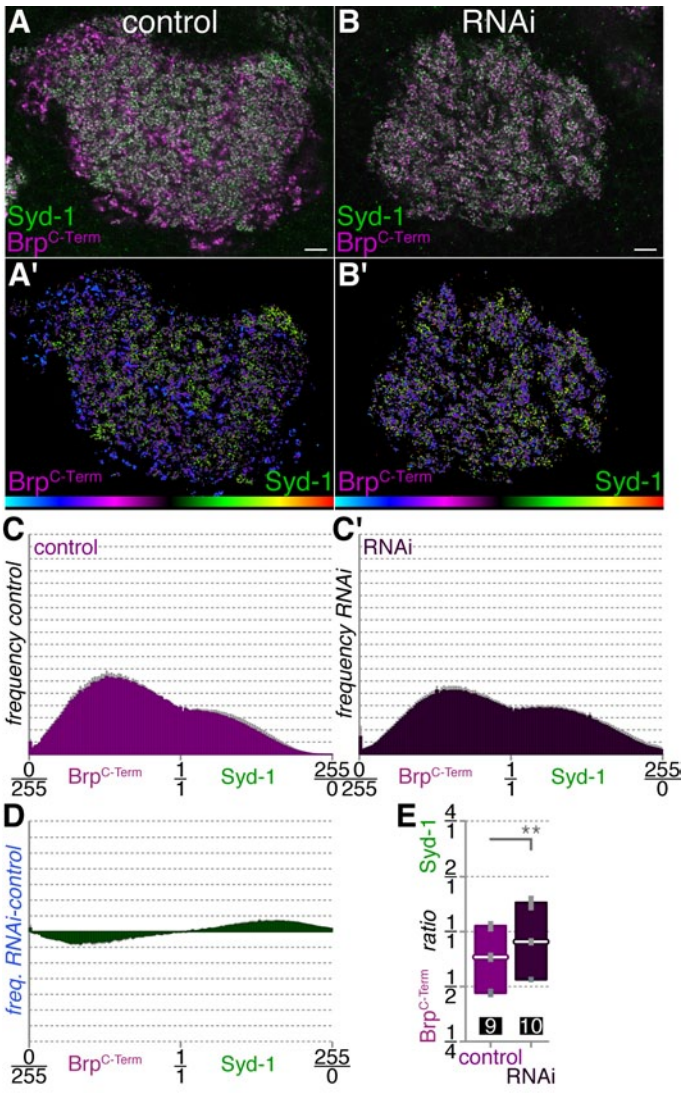

Fig. 33: Quantification of *brp-RNAi* expression in Kenyon cells.
Re-analysis of data from Christiansen et al., 2011.
A,B: Single confocal image planes of MB calyces stained with anti-Brp$^{C\text{-}Term}$ and anti-Syd-1. Scale bars: 5 µm.
A: Control animals not expressing *brp-RNAi*.
B: Animals expressing *UAS-brp-RNAi* by the KC-driver ok107-Gal4.
C,E: The colour code of the graphs corresponds to the respective colour of the median ratio, according to the spectrum shown in Fig. 19, also shown below the ratio images in A' and B'.
C: Histograms showing the frequency of all ratios throughout the image stacks.
D: Difference in ratio frequencies between RNAi and control calyces. The colours correspond to $r_{RNAi}/r_{control}$.
E: Ratios of control and *brp-RNAi* animals. Median ratios are significantly different from each other, MWU test result: p=0.009, α=0.05. The median Syd-1 / Brp$^{C\text{-}Term}$ ratio of *brp-RNAi* animals is 21.5 % higher than the one of control flies.

In order to assess whether our ratiometric analysis was sufficiently sensitive to detect changes in Brp levels, we re-analysed the published data set. When, in *brp-RNAi* flies, Brp was absent from KC presynapses, the overall Syd-1 / $Brp^{C\text{-}Term}$ ratio in calyces was shifted to a higher level, compared to control flies (Fig. 33). The median ratio was significantly different between both genotypes (Fig. 33D), it was increased by 21.5% in *brp-RNAi*-expressing animals. We therefore yielded a comparable result as in the previous quantification (Christiansen et al., 2011: 20-30%). Since less spots with a low Syd-1 / $Brp^{C\text{-}Term}$ ratio could be detected in RNAi-flies, KC presynapses should be characterized by a low Syd-1 / $Brp^{C\text{-}Term}$ ratio. This is exactly what we have found during the analysis of the KC-driver 17D-Gal4 (Fig. 24H,K,K'). Thus, the two experiments mutually confirmed each other. We can conclude that the ratiometric method is sensitive enough for the detection of the deprivation of a single presynaptic protein from a certain type of presynapse within a complex neuropil.

1.4.2. Altered ratio classes in the *shakB²* mutant

The Innexin-family channel proteins coded by the *shaking-B* (*ShakB*) locus are essential components of gap junctions in the AL (Phelan and Starich, 2001; Phelan et al., 1998; Song and Tanouye, 2006; Yaksi and Wilson, 2010) and were originally studied in the giant fibre escape pathway (Phelan et al., 1996; Sun and Wyman, 1996; Thomas and Wyman, 1984). In the AL of *shakB²* mutants, electrical synapses between excitatory LNs and inhibitory LNs, between excitatory LNs and PNs, as well as in between PNs are absent (Yaksi and Wilson, 2010). Moreover, also chemical synapses between excitatory and inhibitory LNs as well as reciprocal chemical synapses between PNs are abolished, probably due to a need of electrical signals for their proper development (Yaksi and Wilson, 2010).

We wondered whether such a loss of several types of presynapses had a specific effect on CAZ protein composition classes. In fact, a distinct change in ratio classes was observed: the RBP / $Brp^{C\text{-}Term}$ ratio in ALs of *shakB²* mutants was strongly and significantly increased (by 124.3%), when compared to wildtype controls (Fig. 34). Thus, synapses with a high RBP / $Brp^{C\text{-}Term}$ ratio remained functional in this mutant, making the synapses that are abolished likely to be poor in RBP. In addition, we also observed a drop in the Syd-1 / $Brp^{C\text{-}Term}$ ratio by 35.7%. However, this change was not significant in case of Bonferroni-correction for three tests (MWU p=0.0223).

Fig. 34: Ratios in ALs of *shakB²* mutants (see page 83).
A,C,E: Antibody stainings, single image planes of ALs, wildtype flies; scale bars: 5 µm. **A:** RBP and $Brp^{C\text{-}Term}$. **B:** Syd-1 and $Brp^{C\text{-}Term}$. **C:** $Brp^{N\text{-}Term}$ and $Brp^{C\text{-}Term}$. **A',C',E':** Single image planes of ALs in *shakB²* mutants. **B,D,F:** Visualisation of ratios in the same image planes.
G-I: Median ratios, signal of wildtype controls (cont.) vs. signal in mutants. MWU test results: G: p=0.0014 (+124.3%), H: p=0.0223 (-35.7%), I: p=0.3971 (-5.2%); α=0.0167. The coloured bar above each graph represents the relative difference of ratios ($r_{shakB}/r_{control}$).
J-L,J'-L': Histograms of ratio frequencies. **J-L:** Ratios within the complete AL. **J'-L':** Ratios at GFP-positive spots. **M-O:** Differences in ratio frequencies between mutant and control ALs.

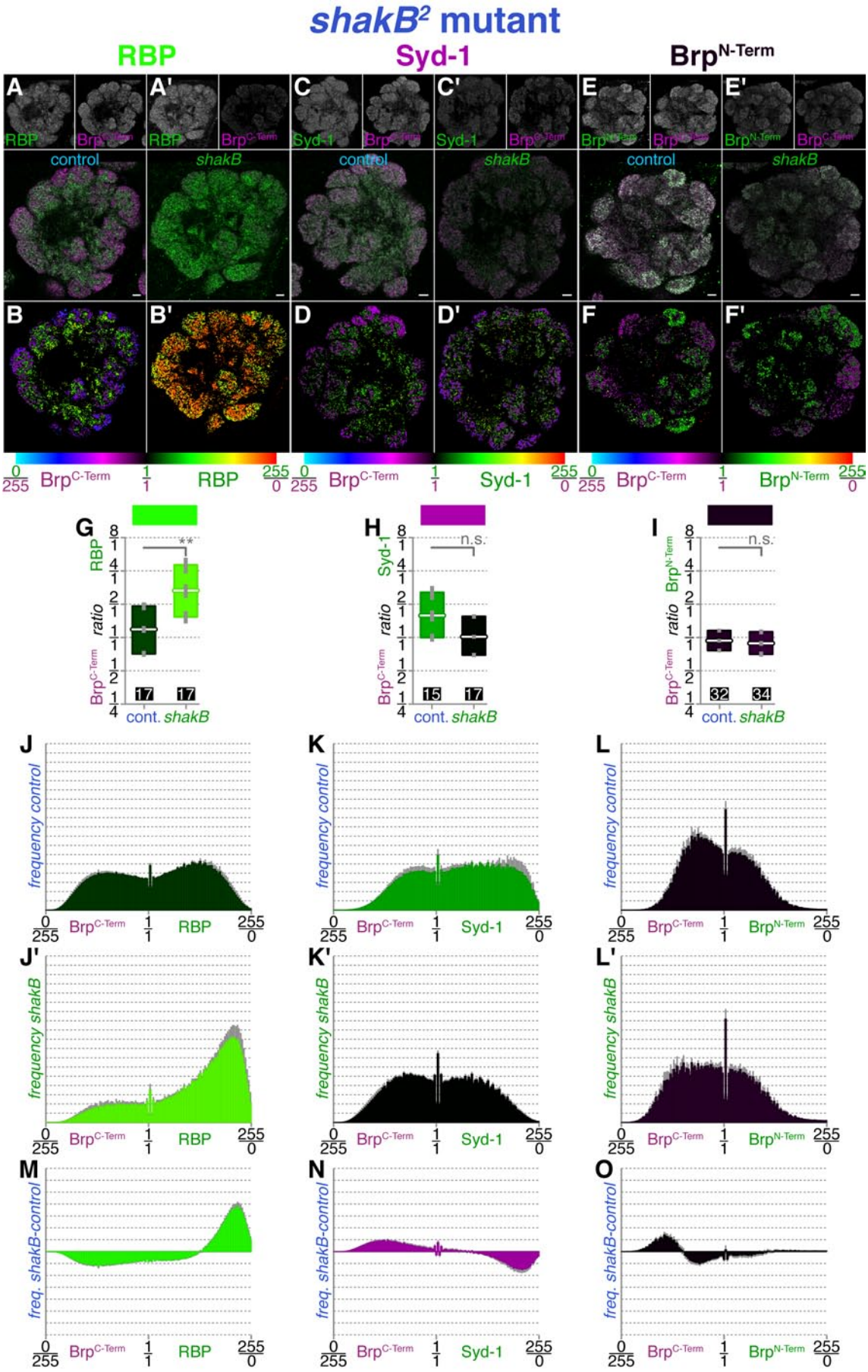

Fig. 34: Ratios in the *shakB*² mutant.
For description see page 82.

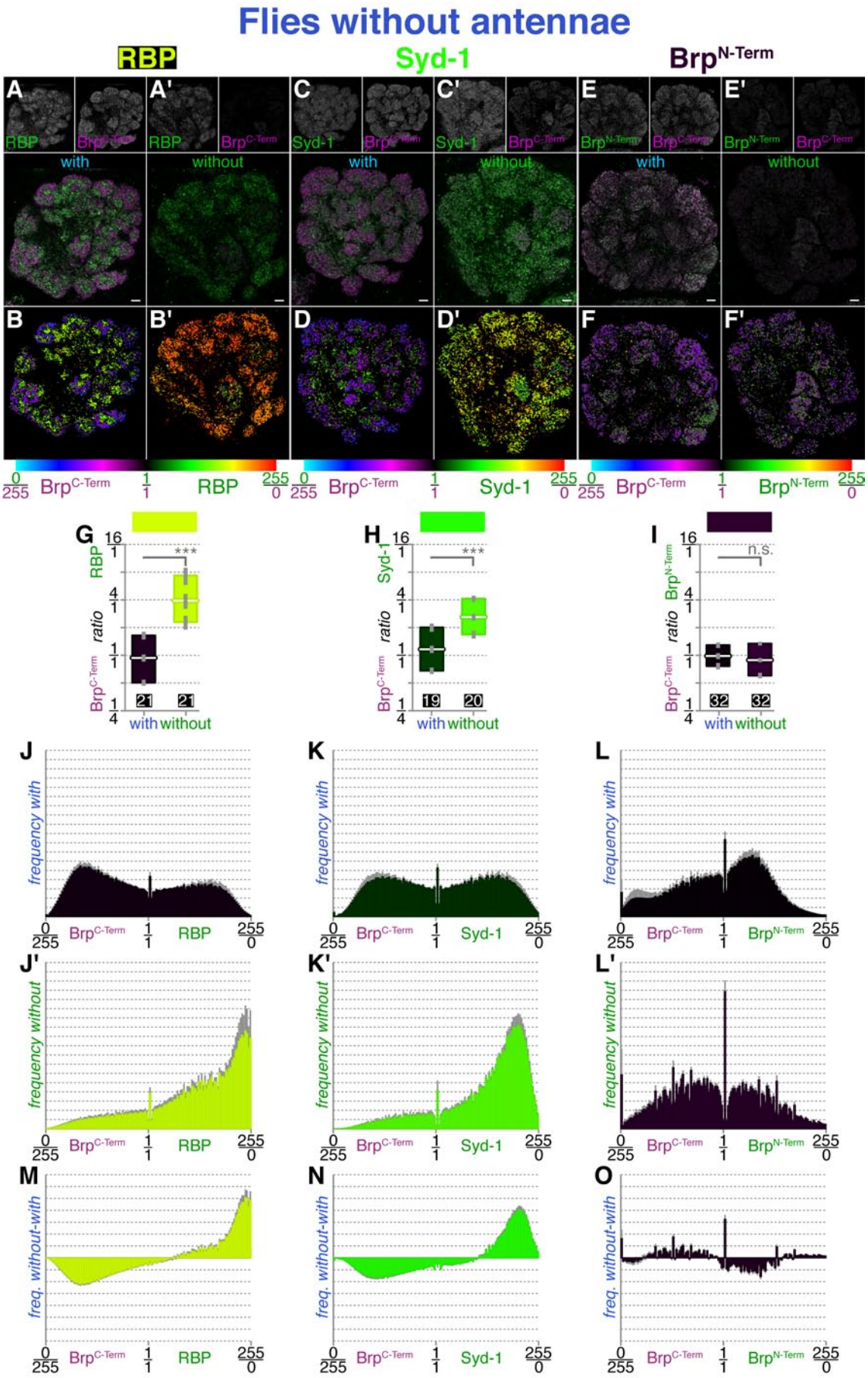

Fig. 35: Ratios in ALs of flies with clipped antennae.
For description see page 85.

From the changes in protein ratios, it seemed as if the signal intensity of all antibodies but anti-RBP had decreased in *shakB²* mutants. To confirm this, we also evaluated absolute signal intensities. In fact, while the intensity of RBP appeared to have increased, intensities of Brp$^{C\text{-}Term}$, Syd-1, and Brp$^{N\text{-}Term}$ decreased (Fig. 36A). Of note, these changes in absolute intensity were all not significant. This constitutes an example for the advantage of the ratiometric approach, which found a significant change in the ratio RBP / Brp$^{C\text{-}Term}$ (Fig. 34G).

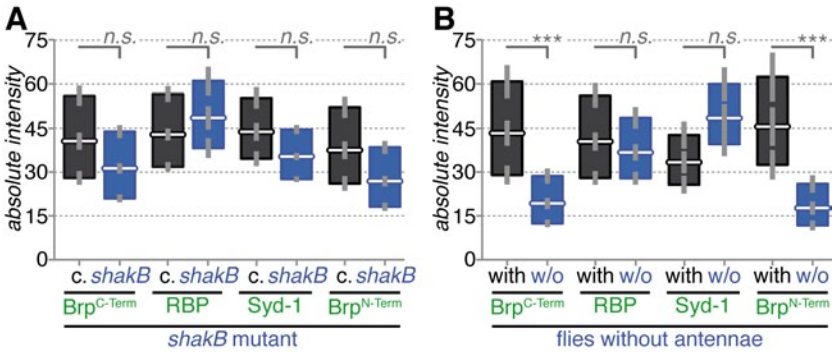

Fig. 36: Quantification of signal intensities.
A: *ShakB²* mutant, median intensities, c. = control. MWU test results: Brp$^{C\text{-}Term}$: p=0.0348, RBP: p=0.1630, Syd-1: p=0.0165, Brp$^{N\text{-}Term}$: p=0.0145, α=0.0125.
B: Flies with clipped antennae, median intensities, w/o = without.
MWU test results: Brp$^{C\text{-}Term}$: p<0.00001, RBP: p=0.2576, Syd-1: p=0.0275, Brp$^{N\text{-}Term}$: p=0.00001, α=0.0125.

1.4.3. Detecting changes in presynapse type abundance after clipping antennae

Because a mixed synapse population was affected in *shakB²* mutants, we wanted to test for the effect of taking just a single synapse type out. We decided against complicated genetic interventions and simply cut off antennae in a group of adult flies, thus ablating ORNs. In flies lacking antennae, both the ratios RBP / Brp$^{C\text{-}Term}$ and Syd-1 / Brp$^{C\text{-}Term}$ increased very strongly (by 318% and by 124%, Fig. 35). Brp$^{N\text{-}Term}$ / Brp$^{C\text{-}Term}$ once again remained unaffected. As for the *shakB* experiment, we also compared this result to changes in absolute signal intensities. As expected from the ratios, Brp$^{C\text{-}Term}$ and Brp$^{N\text{-}Term}$ intensities dropped significantly in flies without antennae (Fig. 36B). The intensity of RBP did not change and Syd-1 was slightly increased.

Fig. 35: Ratios in ALs of flies with clipped antennae (see page 84).
A,C,E: Antibody stainings, single image planes of ALs, wildtype flies; scale bars: 5 µm.
A: RBP and Brp$^{C\text{-}Term}$. **B:** Syd-1 and Brp$^{C\text{-}Term}$. **C:** Brp$^{N\text{-}Term}$ and Brp$^{C\text{-}Term}$.
A',C',E': Single image planes of ALs in flies without antennae.
B,D,F: Visualisation of ratios in the same image planes.
G-I: Median ratios, signal of wildtype controls with antennae vs. signal in flies lacking antennae. MWU test results: G: p=0.00001 (+317.9%), H: p=0.00001 (+124%), I: p=0.2400 (-9.7%); α=0.0167. The coloured bar above each graph represents the relative difference of ratios ($r_{without}/r_{with}$).
J-L,J'-L': Histograms of ratio frequencies.
J-L: Ratios within the complete AL. **J'-L':** Ratios at GFP-positive spots.
M-O: Differences in ratio frequencies between mutant and control ALs.

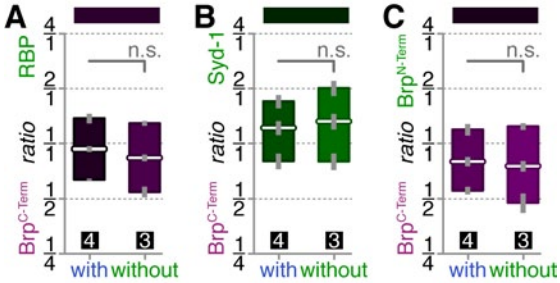

Fig. 37: Ratios in calyces of flies lacking antennae.
Median ratios, signal of wildtype controls with antennae vs. signal in flies with clipped antennae.
MWU test results: G: p=0.1573 (-10.2%), H: p=0.4795 (+8.6%), I: p=0.4795 (-5.6%); α=0.0167.
The coloured bar above each graph represents the relative difference of ratios ($r_{shakB}/r_{control}$).

In 2010, we have demonstrated that changes in activity of PNs can lead to structural plasticity of PN-KC synapses in the MB calyx (Kremer et al., 2010). Since a lack of ORNs should clearly lead to a decrease of activity in PNs, we took a brief look at whether flies without antennae showed an altered CAZ protein composition in the calyx. However, we did not observe significant differences, within the limited number of calyces we examined (Fig. 37).

With the analyses of flies lacking Brp (Fig. 33), *shakB* mutants (Fig. 34), and flies with clipped antennae (Fig. 35), we have illustrated how a quantification of CAZ protein ratios can be employed. We are convinced that, in the future, this straightforward method will proof to be useful for many different types of analyses.

2. NOVEL SYNAPTIC PROTEINS: THE DREP FAMILY

2.1. Characterization of Drep-2

2.1.1. Discovery of Drep-2 as a novel synaptic protein

IN THE PREVIOUS CHAPTER, WE have provided ample evidence for a variegated expression of active zone (AZ) proteins at different synapse types in the *Drosophila* central nervous system (CNS). In this context, we examined proteins that had been discovered and described before. Certainly, a ratiometric characterization of synapses, as shown in the last chapter, would profit from knowledge about additional synaptic proteins. To this end, we not only considered identified synaptic proteins but also strived to discover novel synaptic proteins.

In order to conduct a systematic, unbiased examination of synaptic proteins expressed in the *Drosophila* CNS, a synaptosome-like preparation from adult fly head extracts was established (Depner, 2013; Owald et al., 2012). This material was subjected to immunoprecipitations (IPs) using antibodies against the synaptic protein Bruchpilot (Brp) (Hallermann et al., 2010; Kittel et al., 2006). Pre- and postsynaptic proteins enriched in this manner were subsequently identified by tandem mass spectrometry (MS/MS). Surprisingly, the Dff-family protein Drep-2 was consistently found in these synaptic preparations (Depner, 2013; Owald et al., 2010; Schmidt, 2006; Tian, 2011).

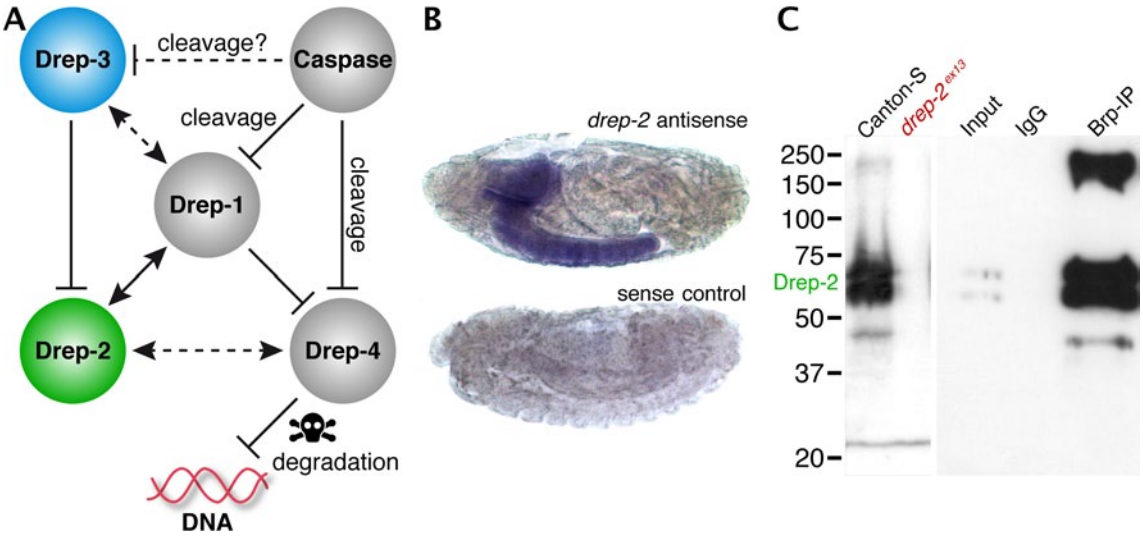

Fig. 38: Drep proteins, *drep-2 in situ* hybridization, and generation of the anti-Drep-2 antibody.
A: Scheme of previously known interactions between and functions of Drep proteins.
B: *In situ* hybridization of *drep-2* reveals a neuronal expression pattern (stage 17) (Tian, 2011).
C: Left: Western blot of adult fly head extracts using the anti-Drep-2$^{C\text{-}Term}$ antibody.
Drep-2 isoforms are predicted to run at 52 and 58 kDa. The signal is absent in the *drep-2*^{ex13} mutant.
Right: Brp^{Last200}-IP on synaptosome preparations, probed with anti-Drep-2$^{C\text{-}Term}$ antibody. Input control: 2%.
Lysed synaptosomes were precleared on Affiprep Rb IgG beads to remove the IgG band running very closely to the anti-Drep-2 bands.

Proteins of the Dff (DNA-fragmentation-factor) family are characterized by the CIDE-N domain, mediating protein-protein interactions (Wu et al., 2008). Dff-related proteins are found throughout the animal kingdom and play roles in the regulation and execution of apoptosis (Wu et al., 2008). The mammalian DNase Dff40/CAD mediates degradation of DNA after caspase-mediated cleavage of its inhibitor Dff45/ICAD (Enari et al., 1998). Four *drep* (dff-related protein) genes have been described in *Drosophila*, including the Dff40-homologue Drep-4 and its repressor Drep-1 (Dff45); both proteins are controlled by caspases (Fig. 38A; Inohara and Nuñez, 1999; Mukae et al., 2000; Yokoyama et al., 2000).

Drep-2, the protein we discovered in the MS/MS, is also related to Dff40/CAD (Fig. 38A, Fig. 39). The fourth Dff protein, Drep-3, binds Drep-2 and is related to Dff45/Drep-1 (Inohara and Nuñez, 1999; Park and Park, 2012). The *drep-1* and *drep-3* genetic loci are arranged in tandem on chromosome IIR and share apparent sequence similarities (Fig. 39). It is therefore probable that they originate from a gene duplication event. Flies might thus not only feature one pair of Dff-family effector plus inhibitor, Drep-4 and Drep-1, but also a second module, Drep-2 and Drep-3 (Park and Park, 2012).

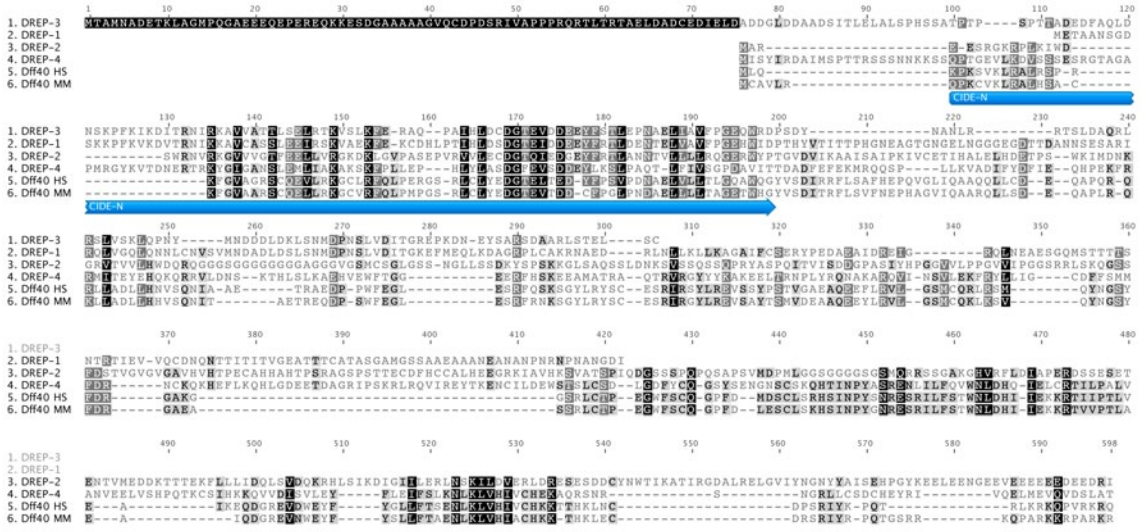

Fig. 39: Drep protein alignment.
Sequence alignment of all four *Drosophila* Dff proteins, as well as human and murine Dff40. Drep-4 has the strongest similarity to Dff40, yet also Drep-2 shows conserved motifs in addition to the CIDE-N domain.

2.1.2. Generation of Drep-2 antibodies and *drep-2* mutants

Interestingly, high-throughput RT-PCR experiments found *drep-2* and *-3* transcripts to be highly enriched within the nervous system, while *drep-1* and *-4* are expressed ubiquitously (Graveley et al., 2011). In fact, we could confirm this restricted expression pattern for *drep-2* by *in situ* hybridization (Fig. 38B; Tian, 2011). To further study the function of Drep-2, polyclonal antibodies against fusion proteins of Drep-2 were produced (Tian, 2011). In the context of this thesis, only the antibody targeted at the fusion protein comprising the C-terminal half of the protein (amino acids 252-483) was used (rabbit #7183, Drep-2$^{C\text{-}Term}$), unless indicated otherwise, since it showed the

best specificity in brain stainings[14]. Four isoforms of Drep-2 have been predicted, differing mainly in the N-terminal exons used (McQuilton et al., 2012). These isoforms are expected to have mass-weights of 52 and 58 kDa. Western blots from wildtype fly head extracts probed with Drep-2$^{C\text{-}Term}$ in fact showed a double band of expected size (Fig. 38C).

Drep-2 mutants were generated by FLP-mediated excision between the FRT-site bearing transposons *P(XP)^{d00223}* and *PBac(RB)^{e04659}* (Tian, 2011). In effect, a chromosome was recovered with a deletion of all known *drep-2* exons but not affecting any other annotated transcription unit (*drep-2^{ex13}*; Fig. 40)[15]. Both bands observed in wildtype flies were absent from western blots on *drep-2^{ex13}* head extracts, mutually confirming the specificity of the antibody and the mutant (Fig. 38C).

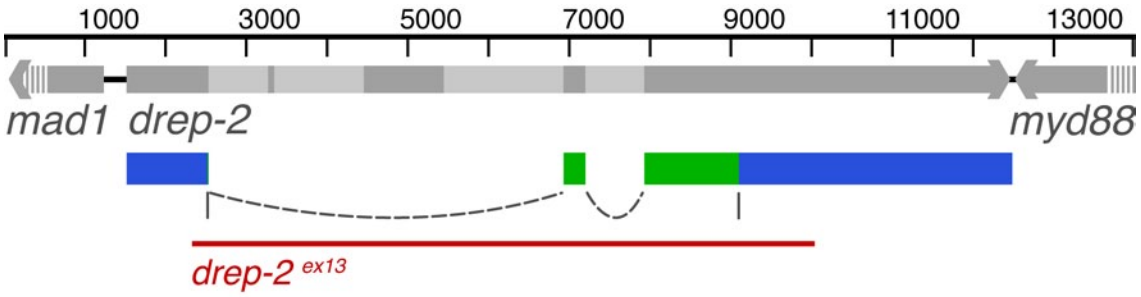

Fig. 40: Genetic scheme of the *drep-2* locus on chromosome IIR.
The neighbouring genes *mad-1* and *myd88* extend beyond the sequence displayed.
The sequence shown in colour was used for rescue experiments.
Blue: untranslated regions; green: exons;
red line: deleted region in the mutant *drep-2^{ex13}* (FLP/FRT excision).

2.1.3. Drep-2 co-precipitates with Bruchpilot

We originally identified Drep-2 by MS/MS in immunoprecipitates of the presynaptic AZ protein Brp (Depner, 2013; Owald et al., 2010; Schmidt, 2006). It was already investigated whether Drep-2 could bind Brp *in vitro* (Tian, 2011): Rui Tian could detect Drep-2 reactivity in Brp precipitates, after co-expression of Brp and Drep-2 in S2R+ cell culture. To confirm this result *in vivo*, we used synaptosome-like preparations of fly head tissue, isolated by differential centrifugation[16]. Brp was immunoprecipated from these preparations with the antibody Brp^{Last200}. Drep-2 was clearly enriched in the precipitate (Fig. 38C)[17]. Thus, Brp and Drep-2 might interact *in vivo*.

[14] In the doctoral thesis Tian, 2011 a different antibody was used, raised against the full-length protein (Drep-2$^{N+C\text{-}Term}$).

[15] In addition, Rui Tian has also created a second mutant, *drep-2^{ex27}*, using the transposon *PBac(RB)^{e02920}* instead of *P(XP)^{d00223}* (Tian, 2011). This second mutant was not used in this thesis; *drep-2^{ex13}* has been used in all experiments.

[16] Husam Babikir and Harald Depner made the synaptosome preparations and did the pull-down experiments.

[17] Note that the IgG-band was removed using Affiprep Rb IgG beads because it ran at a similar height as Drep-2 and thus obscured the result.

2.1.4. Drep-2 at the larval neuromuscular junction

An antibody raised against full-length Drep-2 (Drep-$2^{N+C\text{-}Term}$) showed a signal at the larval neuromuscular junction (NMJ) (Fig. 41A; Tian, 2011). However, this signal remained unaltered in the *drep-2* mutant and is therefore unspecific (*not shown*). The antibody Drep-$2^{C\text{-}Term}$, by contrast, did not produce a staining at wildtype larval NMJs (*not shown*). The possibility remains that Drep-2 is present at NMJs at concentrations below the detection threshold at our imaging conditions. In fact, when four genomic copies of *drep-2* were present (endogenous *drep-2* plus *drep-2*^{GFP} P[acman] BAC construct (see methods, 4.1.2 and Venken et al., 2006; 2009)), the Drep-$2^{C\text{-}Term}$ antibody occasionally yielded a signal at NMJs (Fig. 41B,C). Drep-2 might therefore locate to NMJ boutons at very low levels.

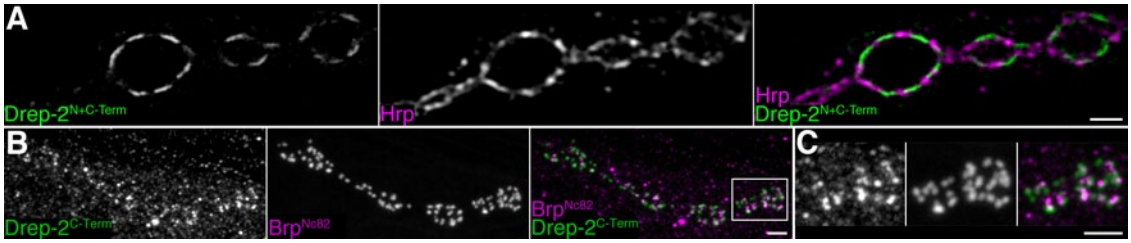

Fig. 41: Drep-2 at the larval NMJ.
Stainings of NMJs at muscle 4 of stage 3 larvae; scale bars: 2 µm. **A:** Anti-Drep-$2^{N+C\text{-}Term}$ (STED) and Hrp (confocal) staining of a w^{1118} wildtype. This signal remained unaltered in *drep-2* mutants.
B-C: Anti-Drep-$2^{C\text{-}Term}$ and Brp^{Nc82} staining of a *drep-2*^{GFP} larva. These animals express a Drep-2^{GFP} fusion protein under the endogenous promoter of *drep-2* (P[acman] clone *CH322-103H19*).
C: Higher resolution image of boxed area in B.

It was already reported that *drep-2* mutants have an increased number of satellite boutons at the NMJ (Tian, 2011). Such a phenotype can have various causes, including faulty upstream signalling in the cell bodies. In order to see whether Drep-2 influences synaptic transmission or plasticity directly at the NMJ, we did electrophysiological measurements[18]: Basic synaptic transmission at NMJs was unaltered in *drep-2* mutants: maximal amplitudes as well as rise and decay times of evoked excitatory junctional currents (eEJCs) were indistinguishable between mutants and controls (Fig. 42A-C). Stimulation at 10 Hz leads to short-term depression of eEJC amplitudes in wildtype animals (Kittel et al., 2006); this form of plasticity was normal in *drep-2* mutants (Fig. 42D).

With the help of paired-pulse protocols, the release probability of synaptic vesicles can be estimated (Hallermann et al., 2010; Kittel et al., 2006; Liu et al., 2011). *Drep-2* mutants showed a slightly lower response to paired-pulse stimulation, at both 10 ms and 30 ms inter-stimulus intervals (ISI) (Fig. 42E,F); this difference was not significant (Mann-Whitney U-test (MWU); 30 ms ISI: p-value = 0.01732; significance level α adapted to five tests by Bonferroni correction, α = 0.05/5=0.01). This result indicates that the readily-releasable pool of synaptic vesicles might be misregulated in *drep-2* mutants (Hallermann et al., 2010). However, further measurements and a larger data set would be necessary to interpret the data in more detail.

[18] Elena Knoche performed the electrophysiological measurements.

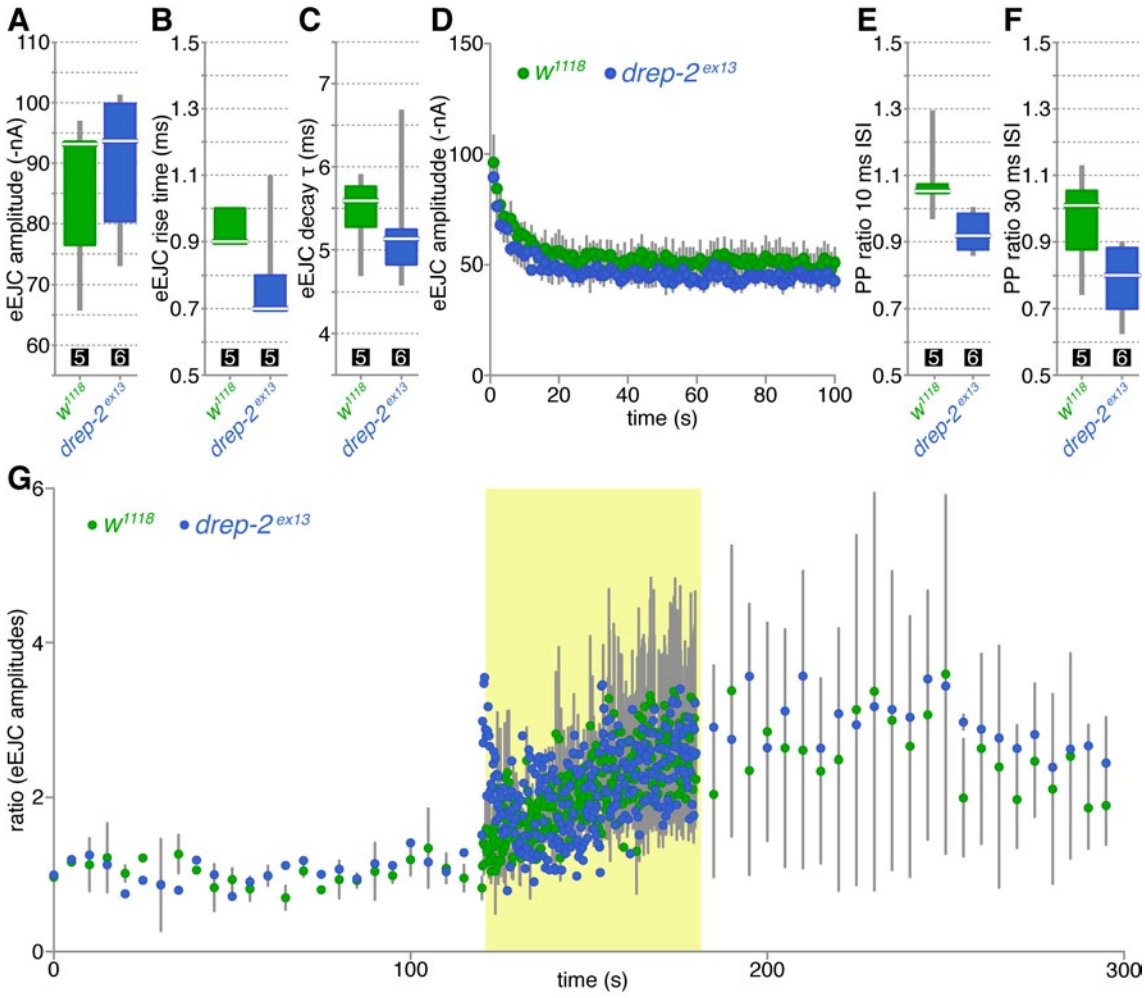

Fig. 42: Synaptic transmission is not significantly altered at larval NMJs of *drep-2* mutants.
Electrophysiological measurements at larval NMJs. N=5/6 except for G, where n=2. Graphs A-C,E,F show median and boxed interquartile range, as well as the maximum data range as whiskers. Graphs D,G show means plus standard error of the mean (SEM).
A-C: *Drep-2* mutants showed normal basic synaptic transmission. **D:** There was no change in short-term depression during stimulation at 10 Hz. **E-F:** Paired-pulse stimulation did not cause a significant facilitation or depression. **G:** 1-minute tetanic stimulation at 5 Hz (during the time highlighted by the yellow box) did not lead to an altered post-tetanic potentiation.

Synaptic transmission at NMJs is not only governed by straightforward ionotropic propagation of signals. Metabotropic signalling and feedback mechanisms also exist (see p. 16; Bogdanik et al., 2004; Koon et al., 2011). A mutant in such a pathway might show normal basal synaptic properties, yet still reveal deficits in more specialized protocols. This is the case for *dmGluRA* mutants. DmGluRA is the only functional metabotropic glutamate receptor (mGluR) in flies (Parmentier et al., 1996). DmGluRA is present at NMJs at very low levels; *dmGluRA* mutants show an abnormal phenotype at larval NMJs during series of high-frequency pulses: tetanic stimulation at 5 Hz causes a higher synaptic facilitation than in controls (Bogdanik et al., 2004). We therefore also tested *drep-2* mutants for altered post-tetanic potentiation, but, at the limited number of trials run, could not observe striking differences (Fig. 42G).

Thus, Drep-2 does not play a major role in basal synaptic transmission at larval NMJs. However, combined data from examination of NMJ morphology and ultrastructure

(Tian, 2011) as well as experiments examining synaptic transmission in *drep-2* mutants suggest that Drep-2 might exhibit a regulatory function at larval NMJs. Clearly, more experiments are required in order to investigate the role of Drep-2 at NMJs further.

2.1.5. Drep-2 is transported bidirectionally along axons

To study the function of Drep-2 in more detail, fusion proteins were generated: the coding sequence for the fluorescent proteins eGFP or mStrawberry was fused to the *drep-2* cDNA (Tian, 2011). When these constructs were overexpressed in larval motoneurons, vivid transport antero- and retrogradely along axons could be observed using non-invasive *in vivo* imaging (Fig. 43; Andlauer and Sigrist, 2010; Tian, 2011). This trafficking took place independently of the tag used (eGFP or mStrawberry) and of the position of the fusion (N- or C-terminally of the cDNA). The constructs shown here carry a C-terminal mStrawberry tag.

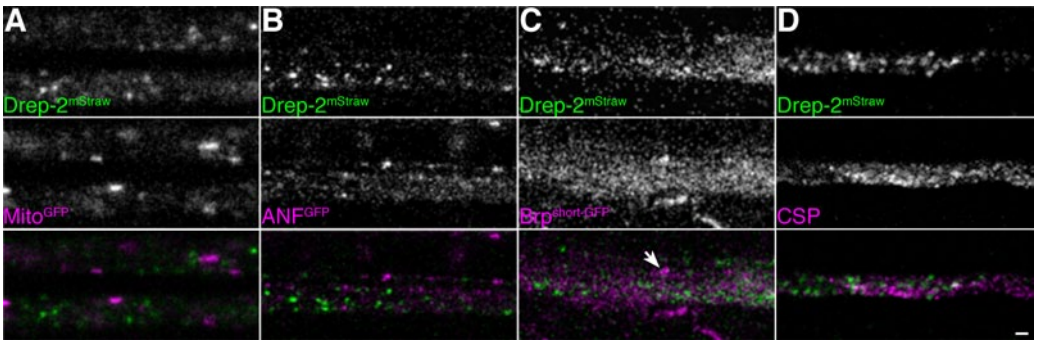

Fig. 43: Drep-2 is actively transported along axons, independently of other constructs.
In vivo imaging of the transport of Drep-2. **A-D:** Scale bar: 1 µm. **A-C:** Drep-2^{mStrawberry} constructs and Mito^{GFP} (A), ANF^{GFP} (B) or Brp$^{short-GFP}$ (C) in larval motoneurons. Constructs were expressed with either ok6- or d42-Gal4. No co-transport was observed. Only few Brp$^{short-GFP}$ spots moved; the arrow highlights an actively transported unit. **D:** Fixed preparation of motoneurons, counterstained with the synaptic vesicle marker CSP.

Drep-2^{mStrawberry} spots were transported along axons and through presynaptic NMJ boutons, yet did not localize to any specific structure at the NMJ (Fig. 44). In an attempt to identify complexes within which Drep-2 is transported, Drep-2^{mStrawberry} was co-expressed with other, GFP-tagged proteins (Fig. 43). However, none of the proteins investigated were clearly co-transported. Drep-2 is thus likely transported independently of mitochondria (Fig. 43A), peptidergic vesicles (Fig. 43B), AZ proteins (Fig. 43C), or synaptic vesicles (Fig. 43D).

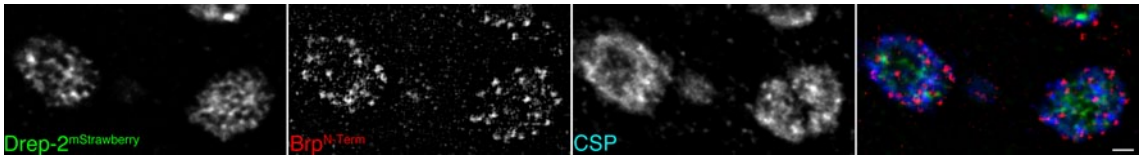

Fig. 44: Drep-2^{mStrawberry} localizes broadly in NMJ boutons.
The overexpressed construct filled the boutons of stage 3 larvae and did not co-cluster with Brp (Brp^{N-Term}, STED) or the synaptic vesicle marker CSP. Scale bar: 1 µm

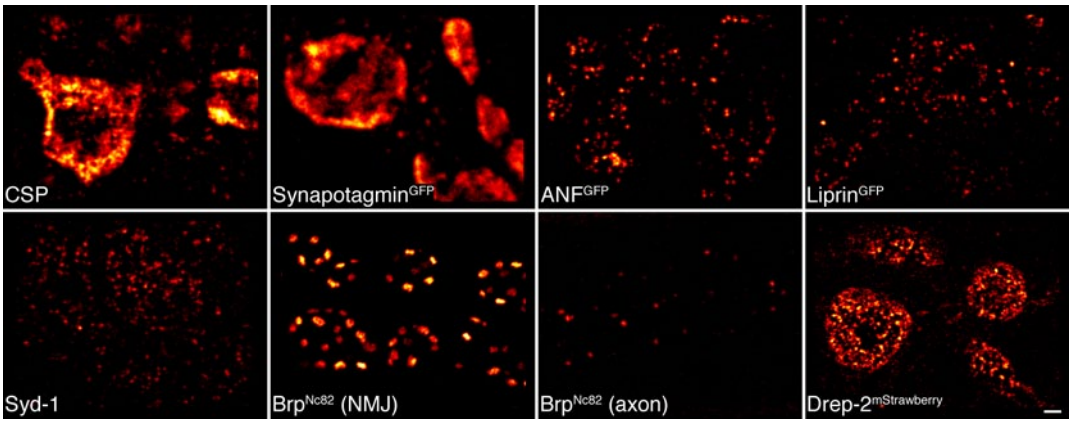

Fig. 45: Drep-2^{Strawberry} clusters are between 40-80 nm in diameter.
STED microscopy of different tagged proteins in NMJ boutons. Stainings of vesicle markers (CSP, Synaptotagmin^{GFP}, ANF^{GFP}), AZ proteins (Liprin-α^{GFP}, Syd-1, Brp), and Drep-2^{mStrawberry}. Fusion proteins were counterstained with anti-GFP antibodies or Anti-Drep-2$^{C\text{-}Term}$. Scale bar: 1 µm

Drep-2^{mStrawberry} spots in NMJ boutons were compared to other proteins at the NMJ using STED microscopy (Fig. 45). Synaptic vesicle markers (CSP and Synaptotagmin^{GFP}) were clearly below the diffraction limit of STED microscopy. Synaptic vesicles are typically about 40 nm in diameter (Jia et al., 1993; Karunanithi et al., 2002; Qu et al., 2009), peptidergic dense-core vesicles (ANF^{GFP}) are above 100 nm in diameter (Atwood et al., 1993; Jia et al., 1993). The resolution limit of the STED microscope used was 80 nm. The AZ proteins Liprin-α and Syd-1 were of a similar size as ANF^{GFP}. Brp clusters at the NMJ were, as expected, larger (Kittel et al., 2006). Drep-2^{mStrawberry} was evenly distributed over boutons, the size of spots was diffraction limited, thus apparently smaller than ANF^{GFP} and larger than CSP.

We have examined the axonal transport of a number of fluorophore-tagged proteins (the ones shown in Fig. 43 and Fig. 45, plus additional synaptic proteins not shown here). Interestingly, of these only Mito^{GFP} and ANF^{GFP} were transported at a similar frequency as Drep-2^{mStrawberry}. Thus, we do not believe that the trafficking of Drep-2 fusion proteins is merely an overexpression artefact. However, the reason for why Drep-2 is transported along axons remains to be uncovered. Of note, the dynein motor cargo adapter cDlc-2 has been identified as a putative interactor of Drep-2 in three yeast-two-hybrid screens (Giot et al., 2003; Murali et al., 2011; Tian, 2011). Dlc-2 mediates localization of both pre- and postsynaptic components in mammals (Fejtova et al., 2009; Fuhrmann et al., 2002). An examination of whether Drep-2 is indeed coupled to cDlc-2 during axonal transport would shed more light on the nature of the trafficking of Drep-2.

2.1.6. Localization of Drep-2 in the central nervous system

We next turned to studying the role of Drep-2 in the central brain (CNS). As a first step in finding a possible function of Drep-2 in the CNS, we examined the expression pattern of Drep-2 in detail. A strong staining of the synaptic neuropil was observed throughout the brains of adult flies (Fig. 46)[19]. This Drep-2$^{C\text{-}Term}$ staining was completely absent in *drep-2* mutants (Fig. 46B). We did not observe Drep-2$^{C\text{-}Term}$ staining in cell bodies or nuclei of neurons. Instead, the protein was detected at synapses throughout the brain, including optic lobes, antennal lobes and central complex (Fig. 47, Fig. 48). The label was particularly prominent at ring cell synapses in the lateral triangle of the central complex (Fig. 48C) and at microglomeruli in the mushroom body (MB) calyx (Fig. 48E).

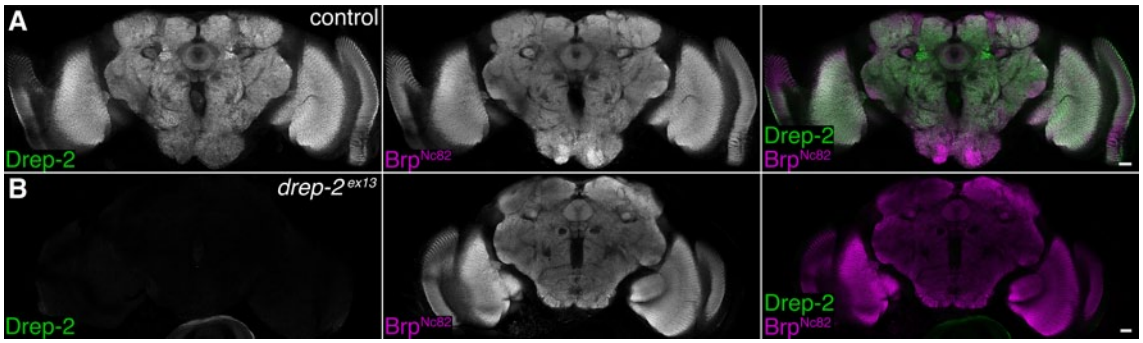

Fig. 46: Drep-2 labels most synapses in adult *Drosophila* brains.
Confocal frontal sections, anti-Drep-2$^{C\text{-}Term}$ and Brp^{Nc82} immunostaining; the latter marks all synaptic AZs. The sections show the central complex (ellipsoid body, strong synaptic Drep-2 staining in the lateral triangle (lateral to the ellipsoid body, see Fig. 9, Fig. 48C, Fig. 67)) and part of the mushroom body. Scale bars: 20 µm.
A: In wildtype flies, synaptic Drep-2$^{C\text{-}Term}$ signal is visible throughout the brain.
B: *Drep-2^{ex13}* mutants show a complete loss of the anti-Drep-2$^{C\text{-}Term}$ staining.

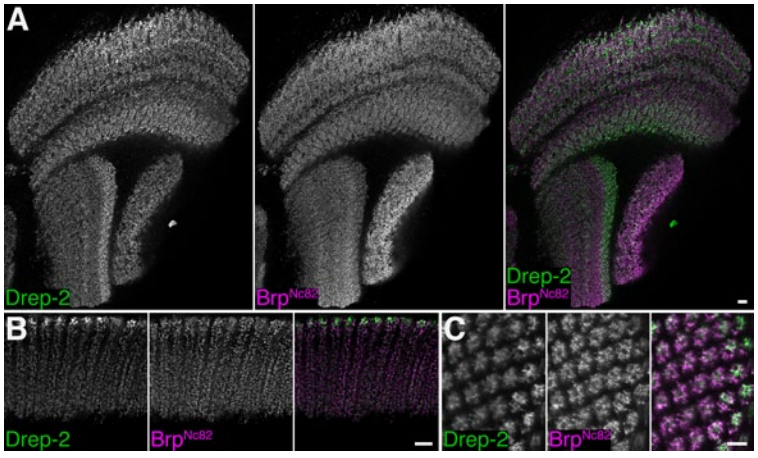

Fig. 47: Drep-2 is present in optic lobes of adult flies.
Confocal sagittal sections. Staining: anti-Drep-2$^{C\text{-}Term}$ and Brp^{Nc82}; all scale bars: 5 µm.
A: Medulla, lobula and lobula plate.
B: In the lamina, Drep-2 labels the most distal synapses strongly.
C: Cross section of optical cartridges in the lamina. Cartridges cut at a distal layer of the lamina (to the right) show the strong Drep-2 staining.

[19] Fig. 5A, page 21, shows a 3D reconstruction of a Drep-2$^{C\text{-}Term}$ CNS staining.

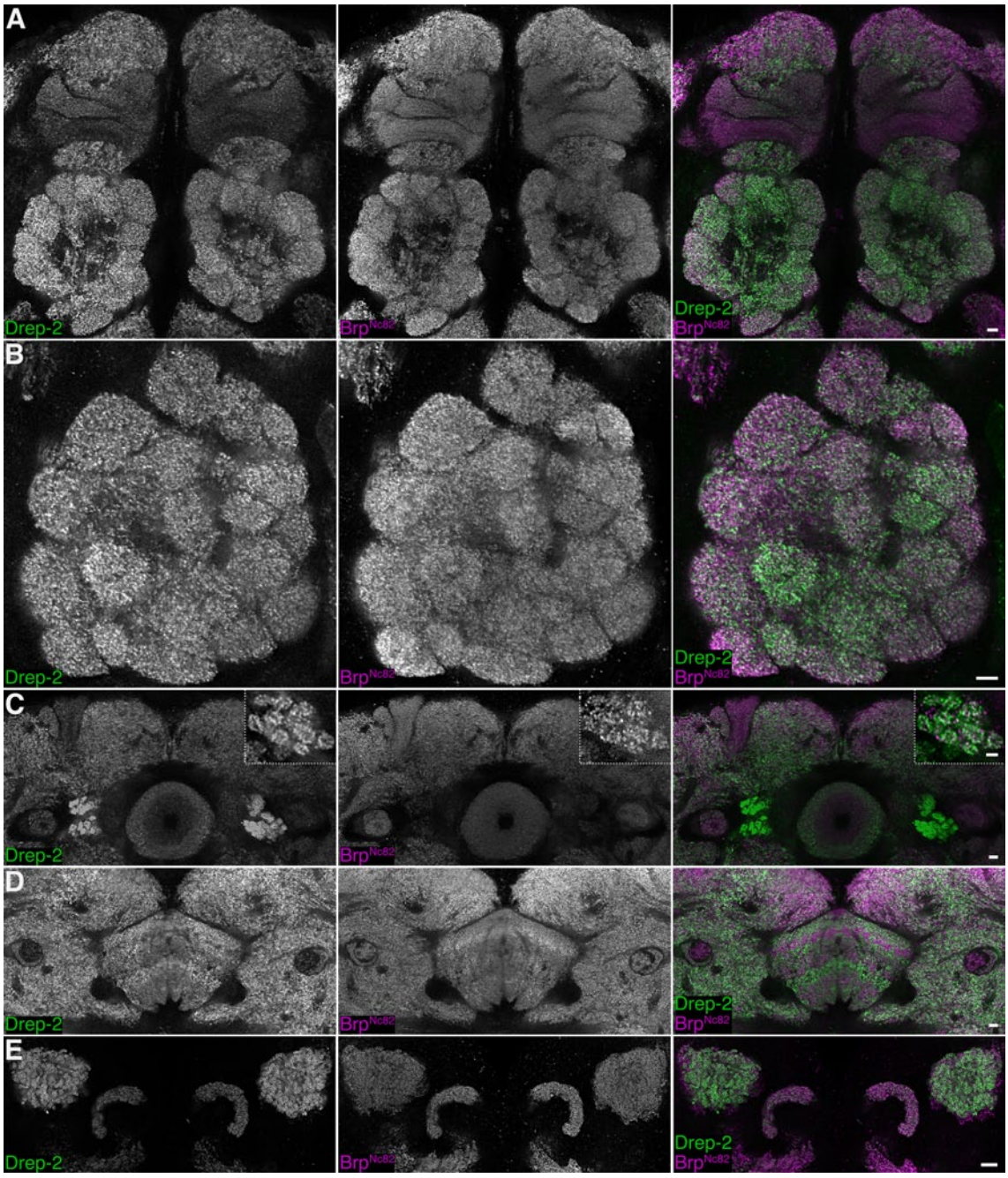

Fig. 48: Drep-2 staining in different neuropils of adult brains.
Confocal frontal sections of adult wildtype brains.
Staining: anti-Drep-2$^{C\text{-}Term}$ and Brp^{Nc82}; all scale bars: 5 µm.
A: Anterior frontal section with antennal lobes and MB lobes.
B: Detail of an antennal lobe.
C: The ellipsoid body in the central complex and the lateral triangle (magnified in inset, strong Drep-2 staining).
D: The fan-shaped body in the central complex and MB peduncles.
E: Posterior-dorsal detail, strong Drep-2 staining in the MB calyces (compare to protocerebral bridge signal in the image centre).

2.1.6.1. Drep-2 localizes to postsynaptic densities at MB calyx microglomeruli

The mushroom bodies showed a very distinct Drep-2 expression: the label was particularly weak in the MB lobes (Fig. 46A, Fig. 48A,C) but especially strong in the calyx (Fig. 48E, Fig. 49A).

MBs are part of the olfactory pathway of insects and crucial neuropils for several higher brain functions, not least olfactory associative learning (see Introduction, section 3.1.2 (pages 22-24), as well as Dubnau and Chiang, 2013). The antennal lobes (ALs) (Fig. 48A,B) form the first relay in olfactory information processing, here receptor neurons synapse onto projection neurons (PNs; Fig. 6). PNs traverse the brain from the anterior to the posterior side, where they arborize in the MB calyx (Fig. 48E) and the lateral horn (Fig. 7). In the calyx, they form synapses with the MB-intrinsic Kenyon cells (KCs). KCs, in turn, project from the calyx along the peduncle (Fig. 48C,D) into the MB lobes (Fig. 48A,C), which lie on the anterior side of the brain.

PNs form large cholinergic presynaptic boutons in the calyx (Yasuyama et al., 2002); dendritic claws of KCs, expressing acetylcholine (ACh) receptors, tightly surround PN presynapses. Thus, the PN-KC synapse features a distinct morphology, called microglomerulus (Butcher et al., 2012; Leiss et al., 2009a; Yasuyama et al., 2002). The anatomy of microglomeruli is easily recognizable, ring-like patches of KC postsynaptic densities (PSDs) encircle the PN presynaptic boutons (Fig. 8). This stereotypic arrangement allows for the identification of pre- and postsynaptic compartments on the level of light microscopy.

The Drep-$2^{C\text{-}Term}$ signal at microglomeruli strikingly overlapped with postsynaptic Dα7 ACh receptor subunits expressed in KCs (Christiansen et al., 2011; Fig. 49A,B,E). Within each microglomerulus, the postsynaptic Dα7/Drep-2 co-clusters surrounded Brp-positive (but Drep-2-negative) PN presynapses (Fig. 49A-C,E). This observation was confirmed by high-resolution STED microscopy (Fig. 49C). Choline acetyltransferase (ChAT), a protein in the presynaptic cytosol, was also always clearly segregated from the Drep-$2^{C\text{-}Term}$ staining at microglomeruli (Fig. 49D). Postsynaptic Discs large (Dlg) scaffolds, on the other hand, colocalized with Drep-2 (Fig. 49F). This gave us reason to believe that, at MB calyx microglomeruli, Drep-2 mainly localizes to postsynapses.

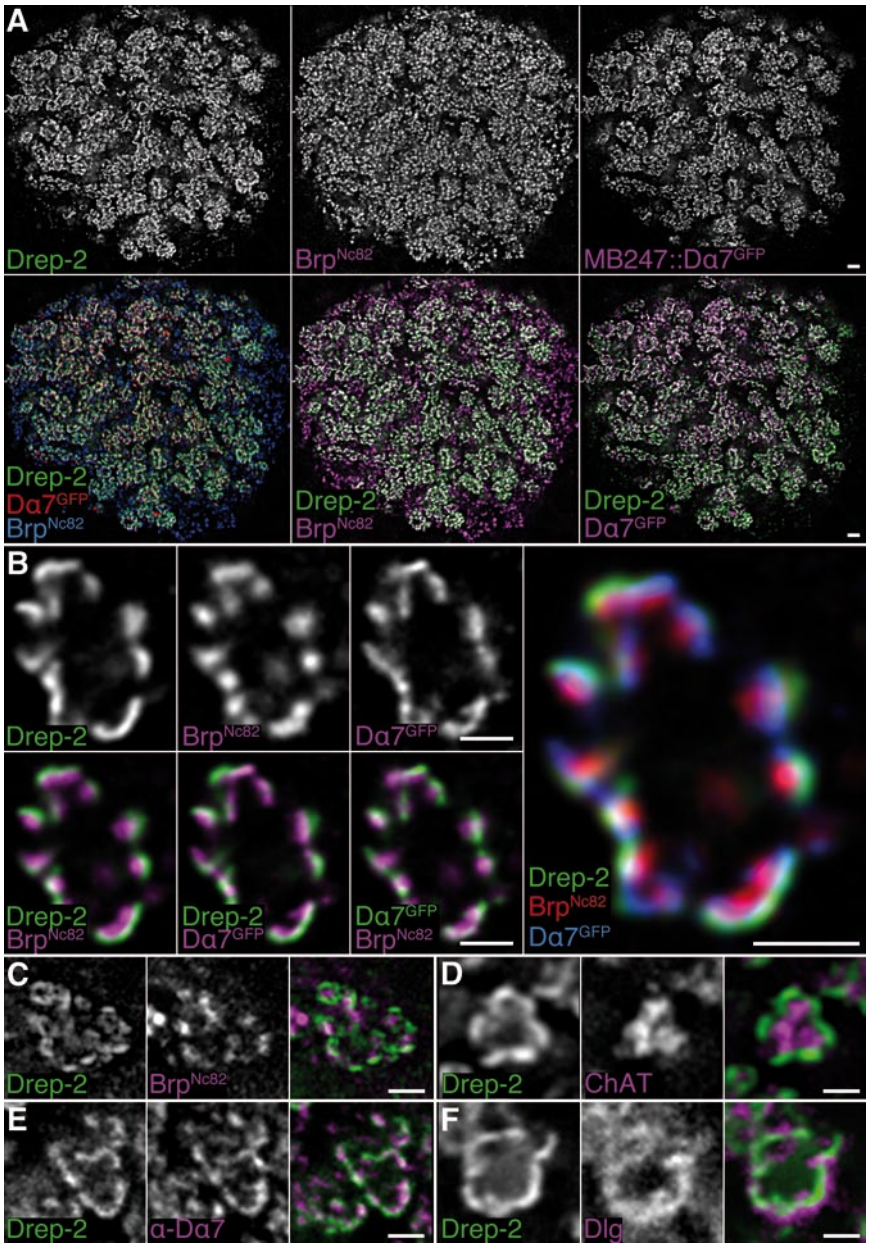

Fig. 49: Drep-2 localizes to the postsynaptic membrane of PN-KC synapses.
A: Detailed image of the MB calyx. The mb247::Dα7^{GFP} channel displays the GFP-tagged Dα7 subunit of ACh receptors, fused to the *mb247* enhancer for expression in KCs. Scale bar: 2 µm.
B-F: Details of a single microglomeruli in the calyx, all scale bars: 1 µm.
B: Dα7^{GFP} is the same construct as shown in A. The Drep-2$^{C\text{-}Term}$ staining overlaps with postsynaptic Dα7^{GFP} and not with presynaptic Brp.
C: STED microscopy superresolution recording of Drep-2$^{C\text{-}Term}$; the Brp^{Nc82} channel is in normal confocal mode. The Drep-2 signal does not overlap with presynaptic Brp.
D-F: Localization of Drep-2$^{C\text{-}Term}$ relative to choline acetyltransferase (ChAT, presynaptic cytosol, D), the postsynaptic ACh receptor subunit Dα7 (antibody staining, E) and the postsynaptic scaffolding protein Discs large (Dlg, F). Drep-2 colocalizes with postsynaptic markers.

2.1.6.1.1. Subcellular distribution of Drep-2 expressed in different neuron types

In order to confirm the postsynaptic localization of Drep-2 in KCs, we expressed fluorophore-tagged *drep-2* constructs using the Gal4/UAS system (see Introduction, section 3.3, page 25). We co-expressed Drep-2^{mStrawberry} with either Brp$^{short-GFP}$ or Dα7^{GFP}, using the PN-driver gh146-Gal4 (Fig. 50). As explained on page 67 (section 1.3.1), Brp-$^{short-GFP}$ is a fragment of Brp that labels presynaptic AZs containing endogenous Brp (Fouquet et al., 2009; Schmid et al., 2008); Dα7^{GFP} labels postsynaptic ACh receptors (Leiss et al., 2009b). The intensity of Drep-2^{mStrawberry} was much higher in ALs, where PNs are postsynaptic, than in the calyx, where they are presynaptic (Fig. 50). It is not surprising that Drep-2^{mStrawberry} is also visible in axons and presynaptic boutons, as the construct is actively transported in neurons (Fig. 43, Fig. 44). Of note, gh146-Gal4 also drives expression in the GABAergic APL neuron within the calyx (Tanaka et al., 2008). Part of the Drep-2^{mStrawberry} signal in the calyx is therefore likely to originate from the APL neuron and not from PNs (see 2.1.6.2).

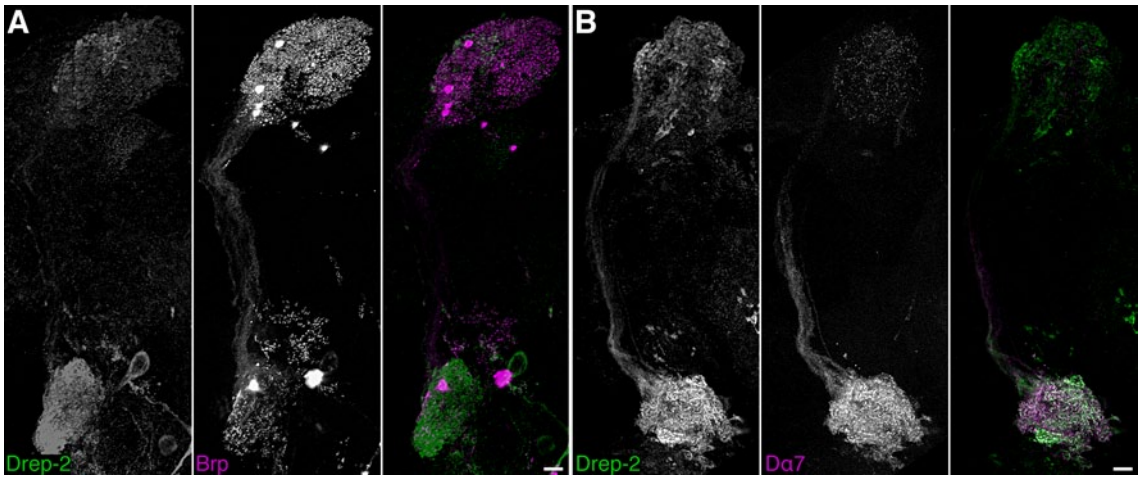

Fig. 50: Drep-2 accumulates in dendrites of projection neurons.
PNs in larval brains, maximum intensity projections. In PNs, Drep-2^{mStrawberry} accumulated mainly in the antennal lobe (lower part of image), where PNs are postsynaptic, and not so much in the calyx (upper structure). Gh146-Gal4, used here, drives expression in PNs and GABAergic APL neurons. Objects interfering with the neurons displayed here were manually removed from the image stacks prior to merging slices.
Scale bars: 5 µm. **A:** Co-expression of Drep-2^{mStraw} with Brp^{GFP}. **B:** Co-expression of Drep-2^{mStraw} with Dα7^{GFP}.

Consequently, a more detailed analysis was necessary to distinguish between overexpression artefacts and Drep-2^{mStrawberry} label representing endogenous Drep-2. In the adult calyx, expression of *drep-2* with either pan-neural (elav^{c155}-Gal4) or KC-specific driver lines (mb247-Gal4 or c305a-Gal4) resulted in a signal equivalent to the Drep-2^{C-Term} antibody staining (Fig. 51). By contrast, expression with the PN driver gh146-Gal4 produced only a weak, diffuse pattern that bore no similarity to the antibody staining of the endogenous Drep-2 protein (Fig. 51). It can thus be concluded that the antibody label at microglomeruli represents Drep-2 in KCs and not in PNs.

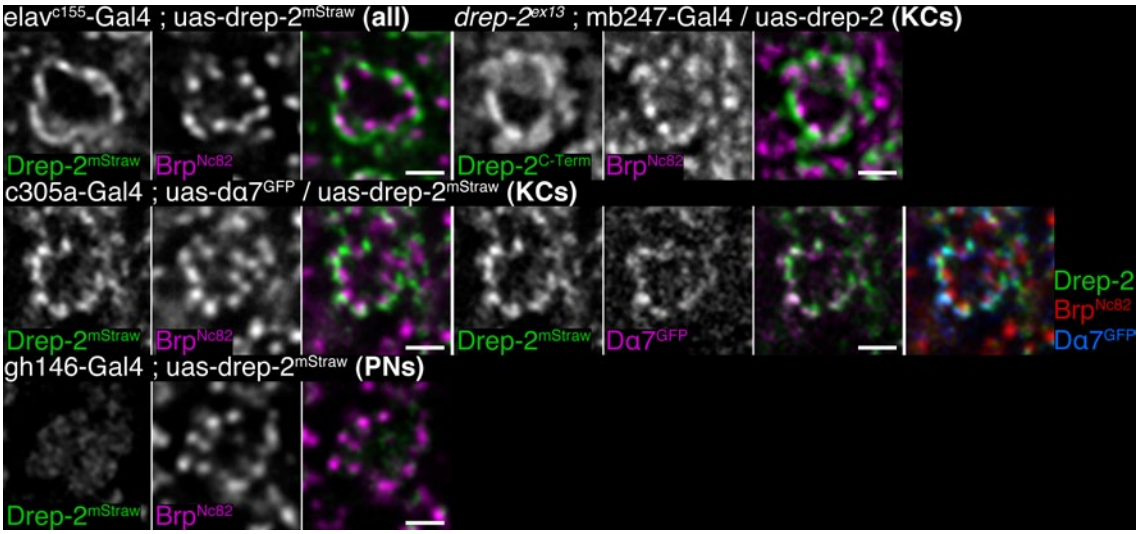

Fig. 51: Expression of *drep-2* constructs from KCs yields a label resembling the antibody staining.
Expression of transgenic *drep-2* constructs in the calyx, using different cell-specific Gal4 drivers.
Drivers: elav^{c155}-Gal4: pan-neural; mb247-Gal4, c305a-Gal4: MB KCs; gh146-Gal4: PNs.
Transgenic constructs: Drep-2^{mStraw}: uas-drep-2^{mStrawberry}, the mStrawberry signal is shown; uas-drep-2: Untagged *drep-2* cDNA in *drep-2^{ex13}* mutant background, Drep-2$^{C\text{-}Term}$ antibody staining is shown; Dα7^{GFP}: uas-dα7^{GFP}, GFP signal. Only expression of drep-2 with a pan-neural or KC driver yielded a pattern similar to the wildtype Drep-2 antibody staining. Thus, Drep-2 localizes to KC postsynapes and not to PN presynapses at microglomeruli. All scale bars: 1 µm.

2.1.6.1.2. Biochemical evidence that Drep-2 localizes to synaptic membranes

Since Drep-2 colocalized with ACh receptors, we wondered whether Drep-2 is associated with synaptic membranes. For this purpose, we produced a synaptosome-like preparation from adult fly head extracts by differential centrifugation[20] (Depner, 2013; Owald et al., 2012). Drep-2 was enriched in the fraction containing synaptic membranes (Fig. 52). Of note, the fractions containing nuclei or presynaptic cytosol did not display larger quantities of Drep-2.

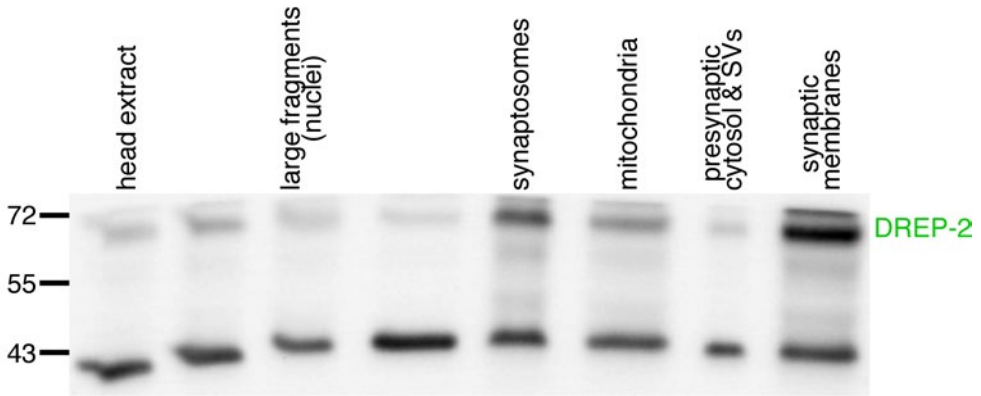

Fig. 52: Drep-2 is enriched at synaptic membranes.
Synaptosome preparation of adult wildtype head extracts, probed with Drep-2$^{C\text{-}Term}$.

[20] Harald Depner established and produced the synaptosome preparation as well as the western blot.

2.1.6.1.3. Immunoelectron microscopy confirms the presence of Drep-2 at postsynaptic membranes

Finally, we examined the localization of Drep-2 in the calyx by post-embedding immunoelectron microscopy[21] (Fig. 53). At PN-KC synapses, Drep-2 localized to postsynaptic membranes (Fig. 53A-C). However, at other, unidentified synapses Drep-2 could also be found presynaptically, close to electron-dense T-bars (Fig. 53D). The latter is consistent with the fact that we found Drep-2 in protein complexes with Brp (Fig. 38C). However, at PN-KC synapses, Drep-2 clustered next to the postsynaptic membrane of KCs.

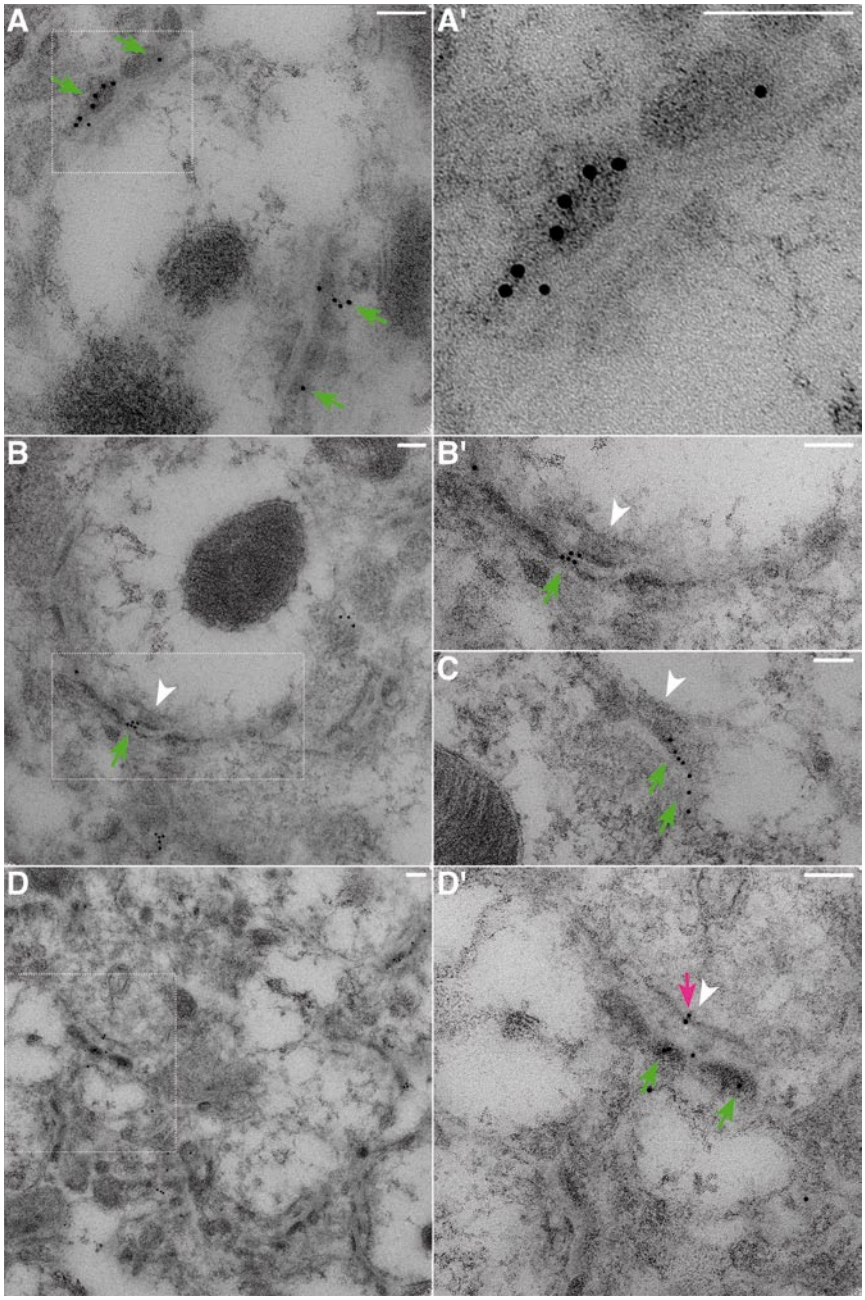

Fig. 53: Post-embedding immunoelectron microscopy of Drep-2 in the MB calyx.
White arrowheads: presynaptic T-bars.
Green arrows: clusters of postsynaptic Drep-2$^{C\text{-}Term}$.
Magenta arrow: presynaptic Drep-2$^{C\text{-}Term}$.
All scale bars: 100 nm.
A-C: Postsynaptic Drep-2 at PN-KC synapses.
D: Pre- and postsynaptic Drep-2 at unidentified synapses.

[21] Christine Quentin did the immunoelectron microscopy.

2.1.6.2. Evidence for Drep-2 at recurrent KC synapses in the calyx

When we expressed Drep-2^{mStrawberry} using gh146-Gal4, we observed Drep-2 signal not only in the antennal lobes but also in the calyx (Fig. 50). While this might be an over-expression artefact, it could also be due to gh146-Gal4 expression in the GABAergic APL neuron (Tanaka et al., 2008).

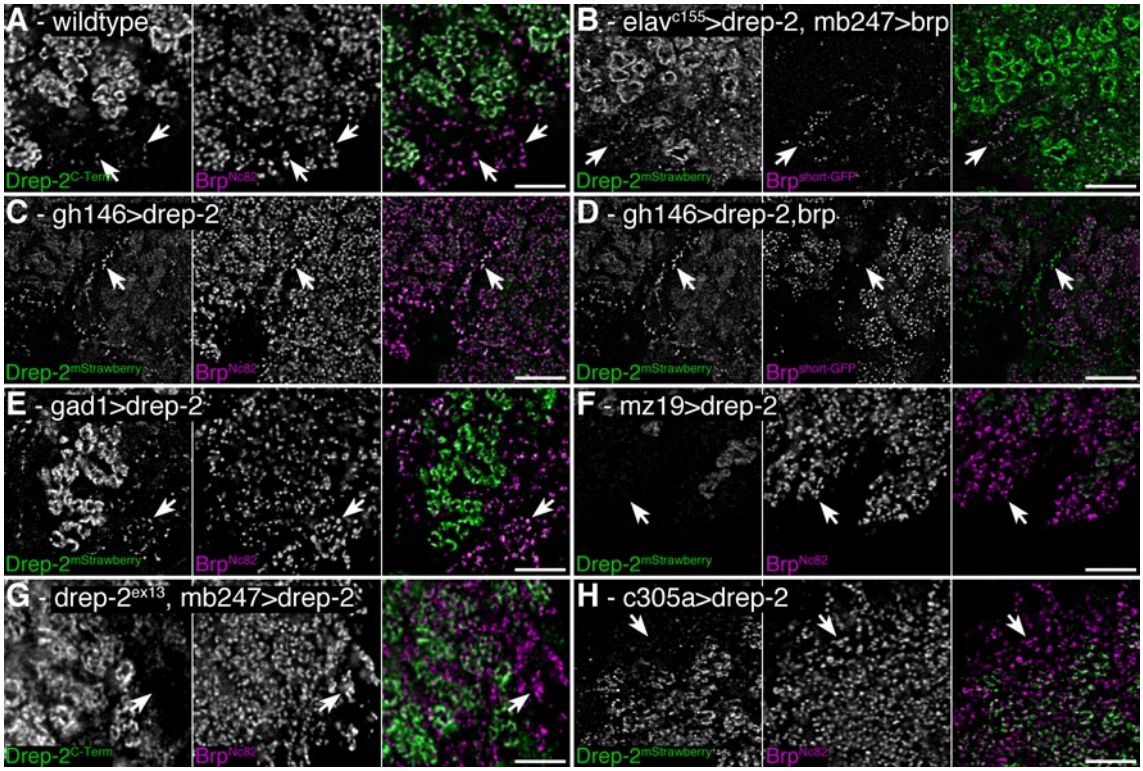

Fig. 54: Drep-2 localizes next to KCACs when expressed in GABAergic cells.
Arrows point at Kenyon cell AZs in the calyx (KCACs). Scale bars: 5 µm.
A: Wildtype. **B:** *elav^{c155}-Gal4 ; uas-drep-2^{mStrawberry} / mb247::brp$^{short-GFP}$*.
C: *gh146-Gal4 ; uas-drep-2^{mStrawberry}*. **D:** *gh146-Gal4 ; uas-drep-2^{mStrawberry} / uas-brp$^{short-GFP}$*.
E: *gad1-Gal4 ; uas-drep-2^{mStrawberry}*. **F:** *mz19-Gal4 ; uas-drep-2^{mStrawberry}*.
G: *drep-2^{ex13} ; mb247-Gal4 / uas-drep-2*, anti-Drep-2$^{C\text{-}Term}$ staining. **H:** *c305a-Gal4 ; uas-drep-2^{mStrawberry}*.

Recently, we have identified presynaptic elements of KCs in the MB calyx (KCACs) (Christiansen et al., 2011). KCs were previously believed to be merely postsynaptic in the calyx and presynaptic in the MB lobes. A *brp$^{short-GFP}$* construct fused to the KC-specific *mb247* enhancer labels KCACs unambiguously; however, a punctate Brp^{Nc82} staining that is not part of microglomeruli also allows for the identification of KCACs (Christiansen et al., 2011). Interestingly, low levels of Drep-2 could be observed next to such Brp label (Fig. 54A,B). Furthermore, Drep-2^{mStrawberry} localized next to KCAC-derived Brp, if expressed by pan-neural elav^{c155}- or PN/APL-expressing gh146-Gal4 (Fig. 54B-D). Gad1-Gal4 drives expression in GABAergic cells, the expression pattern includes some KCs; Drep-2^{mStrawberry} expressed by Gad1-Gal4 is also visible next to KCACs (Fig. 54E). Drep-2 did not mark KCACs if expressed by the pure PN-driver mz19-Gal4 or from KCs (mb247-, c305a-Gal4) (Fig. 54F-H). The Drep-2^{mStrawberry} label close to KCACs is not presynaptic, as Brp$^{short-GFP}$, co-expressed with Drep-2 by gh146-Gal4, did not colocalize with Drep-2^{mStrawberry} (Fig. 54D). Thus, it can be concluded

that, at KCAC-APL synapses, Drep-2 probably localizes to postsynaptic specializations of the APL neuron (Table 4).

Remarkably, this is the first indication that the neurons postsynaptic to KCACs are GABAergic cells and not PNs or KCs.

	elav^{c155}	mz19	gh146	c305a	mb247	gad1	Drep-2 at KCACs
PNs	+	+	+	-	-	-	-
KCs	+	-	-	+	+	+	-
GABAergic	+	-	+	-	-	+	+
Drep-2 at KCACs	+	-	+	-	-	+	

Table 4: Drep-2 localizes next to KCACs when expressed in GABAergic cells.
The table clarifies in which cell types the Gal4 lines drive expression.
Columns: Gal4 drivers; rows: cell types.

2.1.7. Drep-2 expression in relation to the expression of neurotransmitters

2.1.7.1. Colocalization of Drep-2 with acetylcholine receptors

PN-KC synapses, as many excitatory synapses in the *Drosophila* CNS, use ACh as the main neurotransmitter (the transmitter at KCAC synapses is unknown) (Yasuyama et al., 2002; Gu and O'Dowd, 2006). We thus investigated whether the localization of Drep-2 to PSDs is dependent on ACh receptors. In fact, the expression pattern of the postsynaptic ACh receptor subunit Dα7 or the presynaptic choline acetyltransferase (ChAT) is very similar to Drep-2 (Fig. 55). However, some areas showed obvious differences, for example layers in the fan-shaped body (Fig. 55B). We therefore turned to a closer inspection of areas with a striking Drep-2 label.

Drep-2 expression was noticeably stronger in the very distal part of the lamina (Fig. 56). Only two cell types are known to form distinct synapses in this layer, GABAergic C2 neurons and their postsynaptic partner, cholinergic Cha-Tan (La wf1) cells (Fig. 56B; Fischbach and Dittrich, 1989; Kolodziejczyk et al., 2008). Both neuron types contain metabotropic $GABA_BR2$ receptors in the distal lamina (Enell et al., 2007; Kolodziejczyk et al., 2008). Cha-Tan neurons synapse onto unknown cells that contain the nicotinic ACh receptor subunits ARD and Dα3 (Chamaon et al., 2000; Schuster et al., 1993).

Thus, Drep-2 clusters either with $GABA_BR2$ or ARD/Dα3 ACh receptors in the distal lamina. Of note, these two ionotropic ACh receptor subunits are rather weak in the MB calyx (Schuster et al., 1993). Metabotropic $GABA_BR2$ receptors, by contrast, are strongly expressed in the calyx (Enell et al., 2007). However, the ACh receptor subunit Dα7 is distinctly present in the calyx (Fig. 55; Fig. 57A). These mixed observations did not allow for definite conclusions regarding a potential association of Drep-2 with ACh receptors.

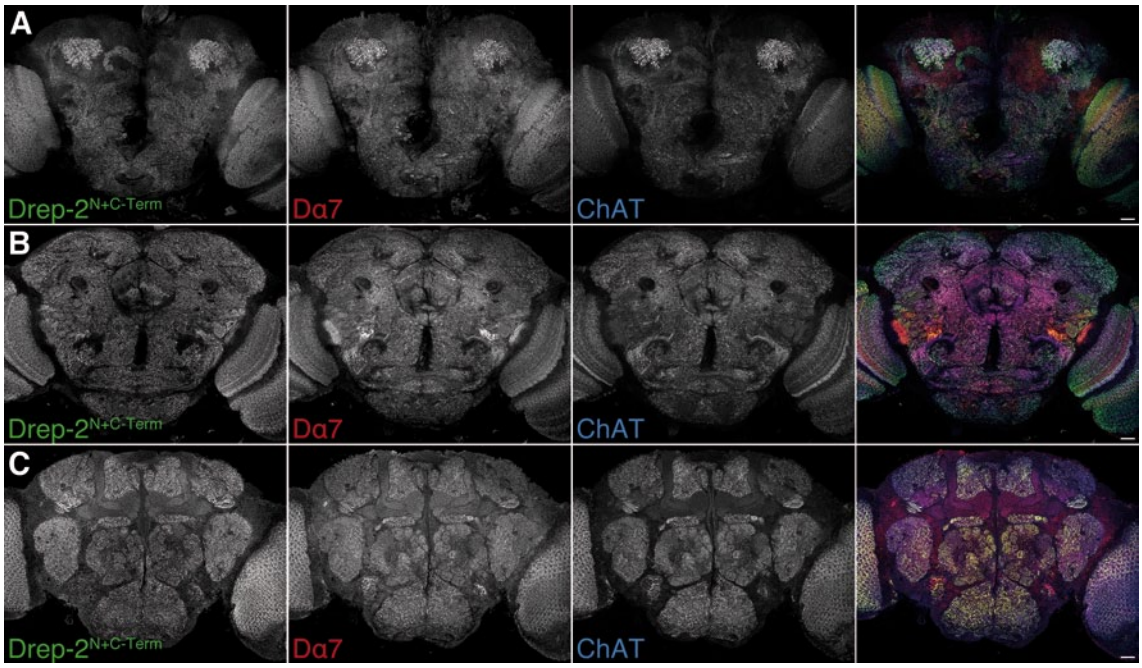

Fig. 55: Drep-2 and ACh receptors.
Confocal frontal sections of an adult wildtype brain stained with anti-Drep-$2^{N+C\text{-}Term}$, anti-Dα7 and anti-ChAT antibodies. Scale bars: 20 µm. In these sections, Drep-$2^{N+C\text{-}Term}$ signal is highly similar to Drep-$2^{C\text{-}Term}$.
A: Posterior section showing the MB calyces. **B:** Central section showing the fan-shaped body.
C: Anterior section showing ALs and MB lobes.

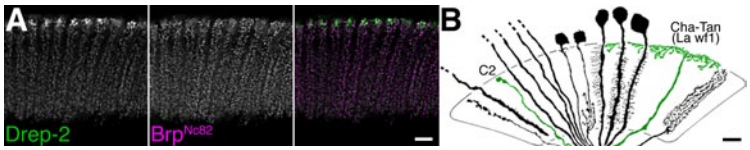

Fig. 56: Drep-2 in the lamina.
The strong Drep-$2^{C\text{-}Term}$ signal in the distal lamina (A) corresponds to synapses of C2 and Cha-Tan neurons (B). Scale bars: 5 µm.
B was taken, with permission, from Fischbach and Dittrich 1989.

2.1.7.2. Expression patterns of different neurotransmitter receptors in the calyx, relative to Drep-2

It remained uncertain whether the colocalization of Drep-2 with ACh receptors throughout the brain was of significance or merely coincidental (due to the broad synaptic expression of both proteins). We therefore continued to investigate other receptor types as well. Since the calyx is such a prominent site of Drep-2 expression, we concentrated on this neuropil. As expected, all microglomeruli displaying anti-Drep-2 signal also showed anti-ChAT and anti-Dα7 labels (Fig. 57A).

We did not have antibodies against GABA receptors at our disposal. Instead, we labelled cells expressing metabotropic $GABA_BR2$ receptors (gbr2-Gal4) with membrane-tagged GFP (Fig. 57B). Furthermore, we marked neurons expressing glutamic acid decarboxylase (gad1-Gal4) with presynaptic $Brp^{short\text{-}GFP}$ (Fig. 57B). Since gad1-Gal4 also drives expression in KCs, we combined this line with a mb247::gal80 construct that inhibits Gal4 expression in KCs. We thus confirmed that KCs do express

$GABA_BR2$ receptors and that GABAergic cells form presynapses in the calyx (as previously shown in Enell et al., 2007).

Widespread expression of metabotropic glutamate receptors (mGluRs) and the associated protein Homer in fly brains has been described (Devaud et al., 2008; Diagana et al., 2002; Hamasaka et al., 2007; Kahsai et al., 2012; Kanellopoulos et al., 2012; Ramaekers, et al., 2001; Urizar et al., 2007). Co-stainings of Drep-$2^{C\text{-}Term}$ and $DmGluRA^{7G11}$, as well as of Drep-$2^{C\text{-}Term}$ and anti-Homer, revealed an exceptional level of colocalization of Drep-2 with these two proteins at calyx microglomeruli (Fig. 57C).

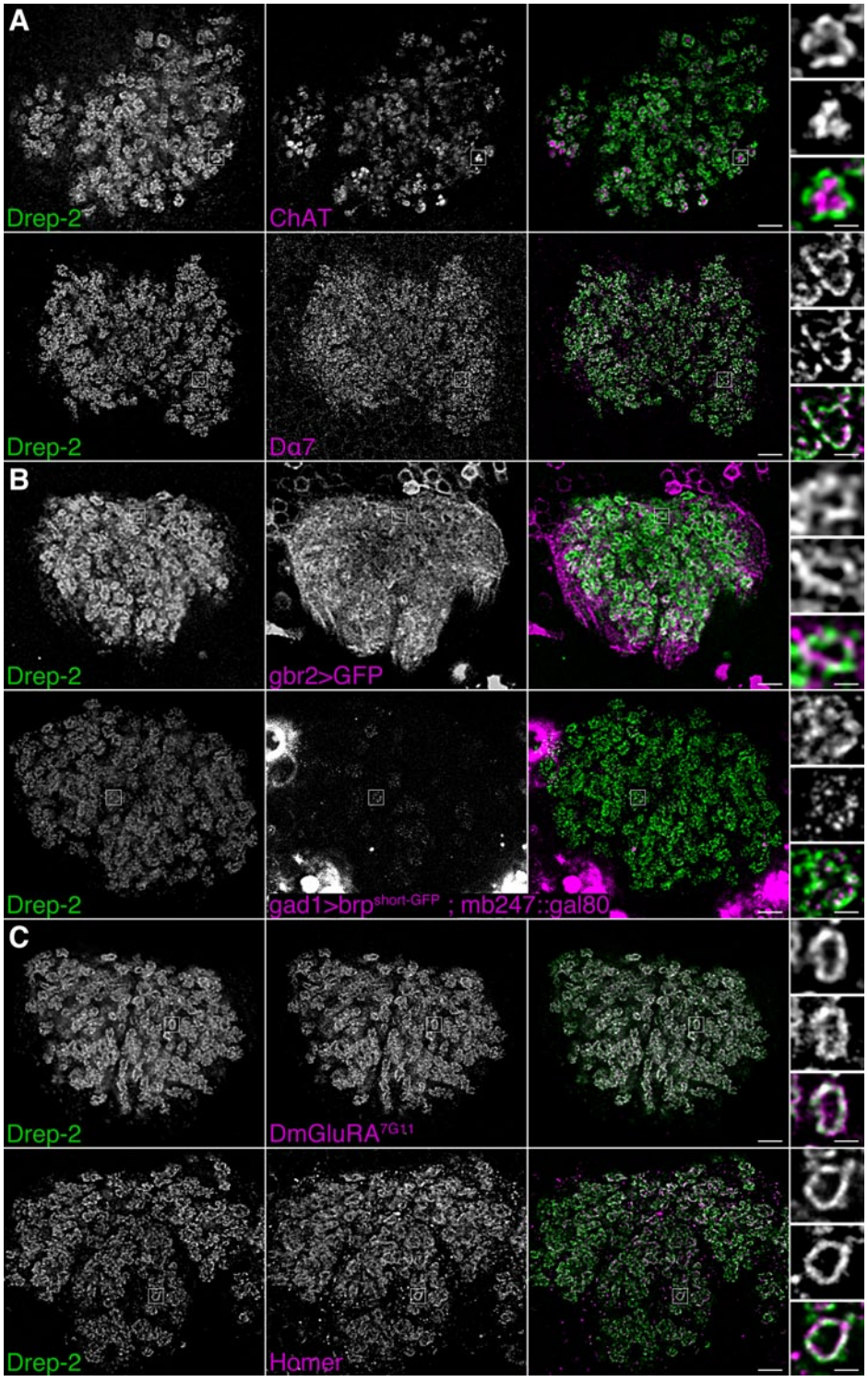

Fig. 57
See page 105.

Fig. 57: Drep-2 and neurotransmitter receptors in the calyx.
See page 104. MB calyces. Scale bars: 5 µm in calyx overviews, 1 µm in details of microglomeruli.
A: Drep-2$^{C\text{-}Term}$ relative to anti-ChAT and anti-Dα7.
B: KCs express $GABA_BR2$ receptors (gbr2-Gal4>GFP), GABAergic cells form synapses in the calyx (gad1-Gal4>brp$^{short\text{-}GFP}$). Gad1 expression in KCs was eliminated by co-expression of mb247::gal80.
C: Drep-2 colocalizes tightly with DmGluRA^{7G11} and anti-Homer.

In fact, co-expression of Drep-2 and DmGluRA was striking throughout the brain (*not shown*). The lamina (Fig. 56), however, constitutes an exception: it does not express DmGluRA receptors (Kolodziejczyk et al., 2008). Of note, DmGluRA is the only functional mGluR in *Drosophila* (Parmentier et al., 1996).

2.1.7.3. Examination of whether Drep-2 can directly interact with metabotropic glutamate receptors

Since Drep-2 and DmGluRA colocalized strongly, we wondered whether the two proteins might interact and thus influence the localization of each other.

We first examined whether Drep-2, DmGluRA, and the mGluR-associated Homer require each other for localization to the membrane. We expressed Drep-2^{mStrawberry}, DmGluRA^{HA}, and Homer^{Myc} constructs in salivary glands of stage 3 larvae (using ok6-Gal4), a non-neuronal tissue. However, each of the constructs localized to the membrane on its own, in absence of the other constructs (*not shown*).

Next, we compared Drep-2 antibody stainings between wildtypes and *dmGluRA* or *homer* mutants. Both the expression pattern and staining intensity of Drep-2 appeared unaltered in the mutants (*not shown*). In addition, we stained *drep-2* mutants with either DmGluRA^{7G11} or anti-Homer and compared the signal to wildtypes. Again, no significant difference in the staining intensity was found (*not shown*).

Thus, the specific distributions of Drep-2 and DmGluRA did not mutually depend on each other. However, we later found evidence for functional interactions between the two proteins (Fig. 65).

2.1.8. Characterization of the *drep-2* mutant

After having established the principle sites of Drep-2 expression in the adult wildtype brain, we examined *drep-2* mutants in detail.

2.1.8.1. The overall morphology of mutant brains appears largely normal

Visual examination of the brains of *drep-2^{ex13}* mutants did not reveal apparent morphological differences from wildtype brains (compare Fig. 46). Brains of mutant animals with mostly normal morphology occasionally show more subtle defects: for example, *fmr1* mutants exhibit fused MB lobe neuropils (Michel et al., 2004). However, such a phenotype was not observed in *drep-2* mutants (Fig. 58). Moreover, *drep-2^{ex13}* mutants did not exhibit significantly up- or downregulated Brp or DmGluRA levels (*not shown*).

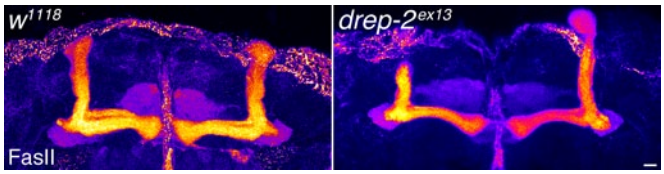

Fig. 58: Absence of major neuroanatomical defects in *drep-2*^{ex13} mutant brains. MB lobes, Fasciclin II (FasII) staining. Scale bar = 10 µm. Max. intensity projections.

2.1.8.2. Apoptosis does not appear to be misregulated in *drep-2* mutants

Drep-2 has been suggested to be a regulator of apoptosis (Inohara and Nuñez, 1999; Park and Park, 2012). Facet eyes of flies are highly ordered structures that are typically affected in apoptosis mutants (Song et al., 2000; Wolff and Ready, 1991). However, eyes of *drep-2* mutants appeared normal and did not show any rough eye phenotype (Fig. 59A). As Drep-2 is strongly expressed in MB Kenyon cells, we examined whether the number of KCs is altered in *drep-2* mutants. To address this question, we expressed GFP in KCs with mb247-Gal4 and counted cell bodies using the software Bitplane Imaris (Fig. 59B). Average cell body counts were in the expected range: control=651, mutant=669, published=700 (Schwaerzel et al., 2002). The difference between the number of cell bodies in control animals and in mutants was not significant (p=0.886, Mann-Whitney U-test (MWU)).

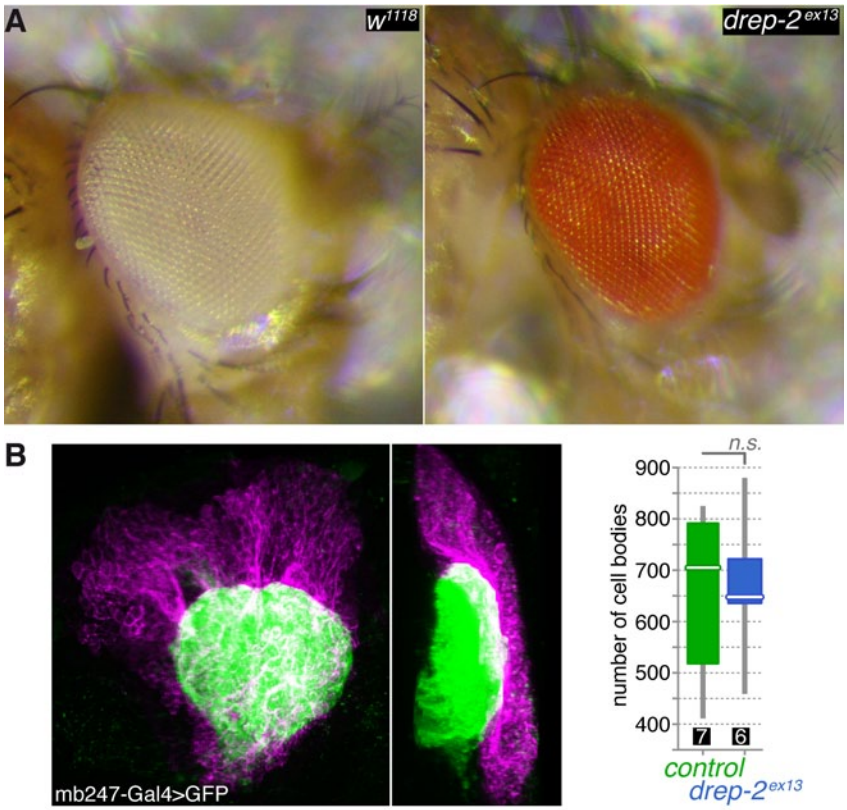

Fig. 59: Apoptosis is not misregulated in *drep-2* mutants.
A: Mutants did not show a rough eye phenotype.
B: Mutants had the same number of KCs as controls. GFP was expressed in MB KCs using mb247-Gal4 (green). GFP-positive cell bodies (magenta) were counted and compared between genotypes. No significant difference was found (Mann-Whitney U-test, p=0.886). The graph on the right shows medians (white bars), interquartile ranges, and min/max values (grey bars). N=7 animals for the control, n=6 for the mutant.

It was reported that Drep-2 degrades linearized plasmid DNA *in vitro* (Park and Park, 2012). However, this is in contrast with results from a previous publication (Inohara and Nuñez, 1999) and with our own experiments (Fig. 60). We rather believe

that Drep-2 precipitates plasmid DNA at high concentrations. Park and Park had incubated purified Drep-2 with DNA at a molar ratio of protein:DNA 80:1. In our experiments[22], part of the plasmid DNA did not enter the agarose gel anymore, if incubated with Drep-2 at equally high concentrations (Fig. 60B). Moreover, Drep-2 is not enriched in nuclei, were one would expect a regulator of apoptosis (Fig. 52). We therefore concluded that the major role of Drep-2 in the CNS does not constitute regulation of apoptosis and continued to investigate putative non-apoptotic functions of synaptic Drep-2.

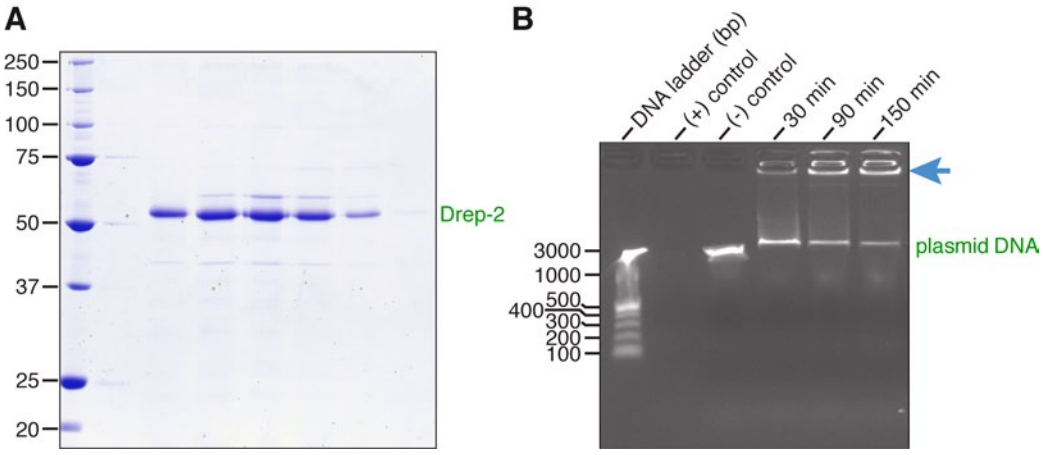

Fig. 60: Purified Drep-2 does not degrade linearized plasmid DNA.
A: SDS-PAGE of the finial elusion profile of purified Drep-2, loaded on a HighLoad Superdex S200 16/60 column. **B:** Nuclease activity assay of purified Drep-2, analysed on a 1% (w/v) agarose gel. Drep-2 was incubated in a time course experiment with linearized plasmid DNA. No nuclease activity could be detected. Instead, Drep-2 seemed to precipitate DNA, as evident by high-molecular DNA not entering into the agarose gel when incubated with Drep-2 (arrow).

2.1.8.3. *Drep-2* mutants live shorter than wildtype flies

In many assays, the performance of mutants is affected by their (often undefined) genetic background outside the locus of interest. Especially in behavioural experiments, controlling for genetic background is of utmost importance, as many subtle genetic modifications can have an influence on behaviour. Therefore, all fly strains used for the analysis of adult *drep-2* phenotypes were outcrossed to w^{1118} for at least six generations to generate an isogenic genetic background. $Drep\text{-}2^{ex13}$ was outcrossed for more than 20 generations. *Drep-2* mutants were homozygously viable, fertile and hatched in expected Mendelian ratios. However, the mutants lived shorter than isogenic w^{1118} control flies (Fig. 61). In lifespan experiments, 50% of mutant flies in each test vial were dead after, on average, 21.5 days. Isogenic control flies did not reach this level within the 45-day observation period.

[22] Expression and purification of Drep-2 as well as nuclease activity assays were conducted by Nicole Holton and Bernhard Loll, lab of Markus Wahl, Freie Universität Berlin.

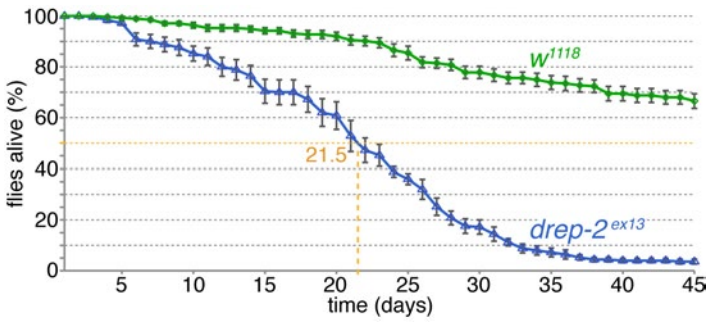

Fig. 61: Reduced life span of *drep-2*^{ex13} mutants.
Comparison to isogenic *w*^{1118} control flies. 50% of mutant flies were dead after 21.5 days. Mutant: n=10 vials (each 25 flies), control: n=11.

2.1.8.4. Drep-2 is not required for basic transmission in the visual system

To examine whether synaptic transmission in *drep-2* mutants might be generally altered in central synapses, we performed electroretinogram recordings (ERGs)[23] (Fig. 62). The level of eye pigmentation influences the response of photoreceptors to light stimulation. *Drep-2*^{ex13} flies have only lightly red eyes (Fig. 59A). In order to create *drep-2* mutant strains with darker eyes, we crossed mutant flies to isogenic lines carrying p-elements with *white*$^{+}$ markers.

We selected two lines with distinctly red eyes that did not confer rescue of *drep-2* mutant phenotypes when combined with *drep-2*^{ex13} (see, for example, Fig. 53B). These two independent mutant strains did not show ERGs that were clearly different from the ones of isogenic *CantonS*[24] flies (Fig. 62). The *CantonS* control flies used here

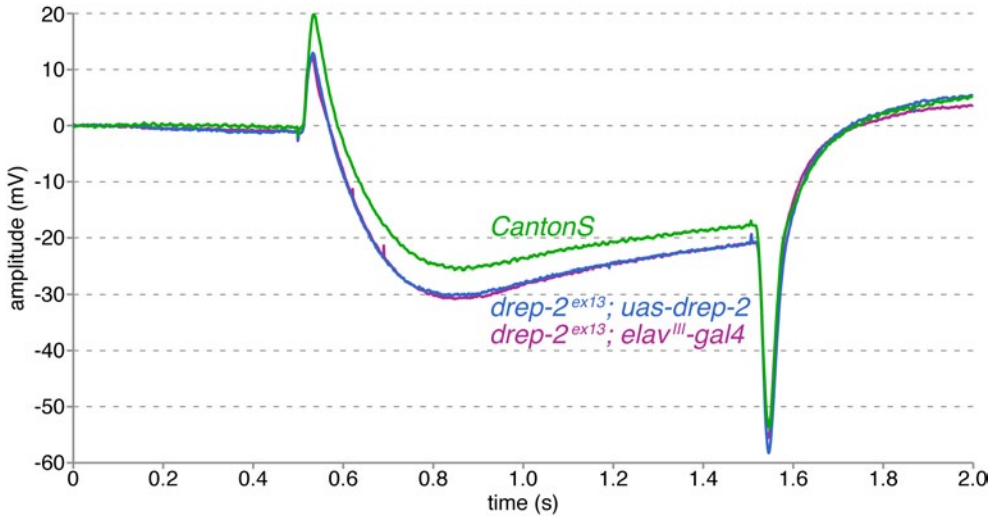

Fig. 62: Drep-2 is not required for basic synaptic transmission in photoreceptors.
Electroretinogram recordings. ERGs of *drep-2* mutants were not different from isogenic *CantonS* controls. The latter strain has a *w*^{1118} genetic background, but was combined with the intact *white* gene from *CantonS* by outcrossing. To create flies with a darker eye colour, *drep-2*^{ex13} mutants were crossed to lines carrying p-elements with *mini-white*$^{+}$ markers.
The graph shows average traces. *CantonS*: n=9 (green), *drep-2*^{ex13}*;uas-drep-2*: n=8 (blue), *drep-2*^{ex13}*;elav*^{III}*-gal4*: n=7 (magenta).

[23] ERGs were measured by Christina Hollmann.

[24] *Canton-S* does not refer to a province of China but is an abbreviation for *Canton, Ohio Standard wild strain* and thus named after a city in the United States (Benzer, 1967).

were outcrossed to w^{1118}, while selecting for red eye colour. Thus, they were isogenic to w^{1118} except for the *white* locus, which they retained from *CantonS*. *CantonS* flies still have darker eyes than the two *drep-2*-mutant lines used here, which is the likely cause for the slightly stronger response of the mutants to light stimuli (Fig. 62). Basic synaptic transmission at peripheral (Fig. 42) and central synapses is thus, by and large, unaltered in *drep-2* mutants.

2.1.8.5. Drep-2 is required for normal olfactory learning

As demonstrated, basic synaptic transmission was not affected in *drep-2* mutants. Hence, we wondered whether Drep-2 might rather play a role in regulating plasticity of central synapses, which is relevant for behavioural control. We therefore turned to investigating a role of Drep-2 in adaptive behaviours.

Drep-2 has a strong presence at Kenyon cell PSDs in the MB calyx (Fig. 49A). MBs are a central structure of the olfactory pathway and essential for olfactory associative learning (see paragraph 2.1.6.1, page 96, as well as the introduction, section 3.1.2, pages 22-24). We therefore examined whether Drep-2 is required for aversive olfactory learning[25]. In this paradigm, flies are trained to distinguish between two odours (for a detailed description see 4.1 (pages 26-28) of the introduction, as well as Tully and Quinn, 1985). One of the odours is paired with electric foot shock and the other remains unpunished. Wildtype flies learn to avoid the punished odour.

As a prerequisite for further experiments, we tested the naïve sensory responses of *drep-2* mutants (Fig. 63A). *Drep-2* mutants sensed odours and electric foot shock normally (Fig. 63A). Of note, the same conditions (e.g. odour concentrations) as used in olfactory conditioning experiments (see below) were used for testing sensory acuity.

We tested the performance of *drep-2* mutants for both short- (STM) and intermediate-term memory (ITM). STM was measured directly following training (three-minute memory) and ITM was assayed three hours after conditioning. ITM is composed of two co-existing memory components, anaesthesia-resistant (ARM) and anaesthesia-sensitive memory (ASM) (Fig. 10B; Quinn and Dudai, 1976; Tully et al., 1994). ARM and ASM can be separated by application of cold amnestic treatment, hence the name. These two forms of memory rely on different molecular and neuronal mechanisms (Folkers et al., 1993; Scheunemann et al., 2012; Tully et al., 1994). They can be distinguished by comparing a group of flies that was cooled, and thus preserved only ARM, to an untreated group, which retains both ARM and ASM.

2.1.8.5.1. Short-term memory

The STM performance of *drep-2* mutants was significantly lower than the performance of isogenic w^{1118} control animals (Fig. 63B). This deficit could be fully rescued by re-expression of *drep-2* cDNA using either the pan-neural driver $elav^{III}$-Gal4 or KC-specific mb247-Gal4 (Fig. 63B).

[25] Sabrina Scholz-Kornehl, lab of Martin Schwärzel at the Freie Universität Berlin, conducted the aversive olfactory conditioning experiments presented here. Previous measurements of *drep-2* mutants were done by Antje Richlitzki and Melanie Gonsior in the same lab and by Michael Cressy, lab of Josh Dubnau at the Cold Spring Harbor Laboratory.

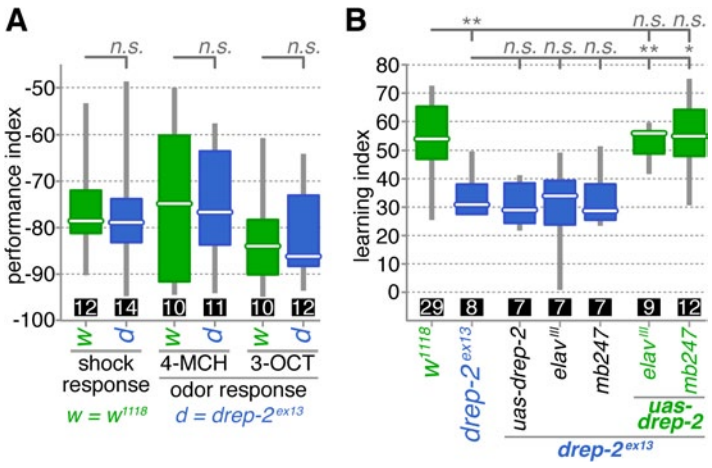

Fig. 63: Sensory acuity and olfactory STM performance of *drep-2* mutants.
The graphs show medians (white bars), interquartile ranges, and min/max values (grey bars). Sample sizes n are indicated in black boxes.
A: *Drep-2*^{ex13} flies sensed electric shock and the odours 4-methyl-cyclohexanol (4-MCH) and 3-octanol (3-OCT) normally; there was no difference in mean performance indices between mutants and isogenic *w*^{1118} control flies (MWU). **B:** *Drep-2*^{ex13} mutants were defective in short-term memory. Re-expression of *drep-2* cDNA with elav^{III}-Gal4 (pan-neural) or mb247-Gal4 (MB KCs) restored the defect to normal levels. MWU for individual comparisons showed a significant difference between these groups (Bonferroni-corrected significance level α=0.0056): *w*^{1118} and *drep-2*^{ex13} (p=0.0004), *drep-2*^{ex13} and *drep-2*^{ex13}*;uas-drep-2/elav*^{III}*-gal4* (p=0.001), *drep-2*^{ex13} and *drep-2*^{ex13}*;uas-drep-2/mb247-gal4* (p=0.002). None of the differences indicated as not significant had a p<0.46.

KCs can be differentiated into three subtypes, αβ, α'β', and γ (Fig. 7C); mb247-Gal4 drives expression in αβ and γ neurons (Aso et al., 2009). Thus, Drep-2 is necessary for short-term memory. Drep-2 probably executes this function in αβ- and/or γ-KCs.

2.1.8.5.2. Intermediate-term memory

Drep-2 mutants were not only deficient in STM, but also in ITM (Fig. 64). The ARM component of ITM remained unaltered, while the animals were almost devoid of ASM. ASM performance can be assessed by subtraction of ARM measurements from ITM (ASM+ARM) scores. Since ARM performance of *drep-2* mutants was not significantly different from ITM performance, ASM had to be missing. As in the case of STM, loss of ASM could be rescued by re-expression of *drep-2* cDNA with either elav^{III}- or mb247-Gal4 (Fig. 64). Hence, Drep-2 is essential for both STM and ASM, but not for ARM. This function of Drep-2 presumably resides within KCs as well.

It is unlikely that these deficiencies in learning and memory are due to gross developmental defects, as the brains of *drep-2* mutants appeared morphologically normal (Fig. 46, Fig. 58). The specificity of the learning phenotypes (only STM and ASM, but not ARM) also supports this notion.

2.1.8.5.3. Stimulation of metabotropic glutamate receptors rescues drep-2 mutant learning deficits

The single functional metabotropic glutamate receptor in *Drosophila*, DmGluRA (Parmentier et al., 1996), shows a broad expression in the CNS that strongly overlaps with that of Drep-2, especially in the calyx (Fig. 57). We therefore wondered whether Drep-2 and DmGluRA are functionally connected. Recently, a role of DmGluRA in olfactory conditioning has been demonstrated (Kanellopoulos et al., 2012): decrease

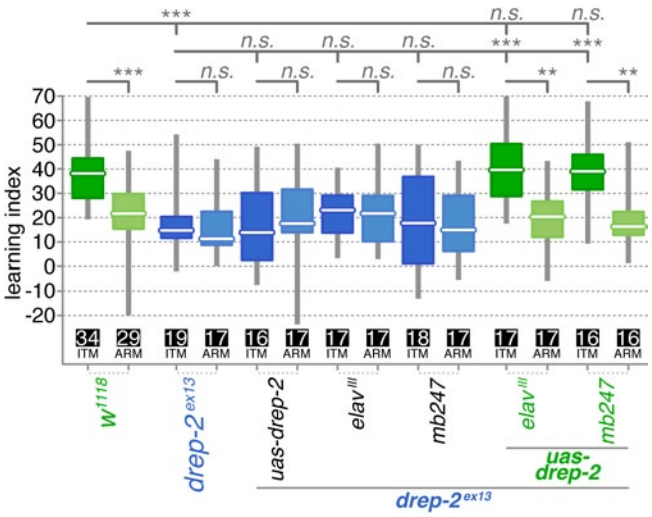

Fig. 64: Intermediate-term memory performance.
ITM = ASM+ARM. *Drep-2*^{ex13} mutants are defective in anaesthesia-sensitive memory (ASM) and not in anaesthesia-resistant memory (ARM). The defect can be restored with elav^{III}- or mb247-Gal4. Statistical tests were run separately for ITM and ARM. For ITM, MWU for individual comparisons showed a significant difference between these groups (α=0.00625): *w*^{1118} and *drep-2*^{ex13} (p<0.0001), *drep-2*^{ex13} and *drep-2*^{ex13}*;uas-drep-2/elav*^{III}*-gal4* (p<0.0001), *drep-2*^{ex13} and *drep-2*^{ex13}*;uas-drep-2/mb247-gal4* (p<0.0001). For assessing differences in ARM, ITM and ARM performance of each genotype was compared separately in pairs with MWUs. The following genotypes showed a significant difference between ITM and ARM (α=0.0071): *w*^{1118} (p<0.0001), *drep-2*^{ex13}*;uas-drep-2/elav*^{III}*-gal4* (p=0.0002), *drep-2*^{ex13}*;uas-drep-2/mb247-gal4* (p=0.0006). None of the differences indicated as not significant had a p<0.11.

of DmGluRA levels by RNA interference modified phenotypes of the olfactory learning mutant *fmr1*. The same effect was observed when decreasing DmGluRA activity by administration of the mGluR antagonist 2-methyl-6-(phenylethynyl)pyridine (MPEP). We therefore assayed the olfactory STM performance of *dmGluRA* mutants and could indeed observe a significant reduction in learning ability (Fig. 65A).

In several previous studies, mGluR activity in flies has been modified effectively by administration of either the mGluR antagonist MPEP or the agonist 1S,3R-1-amino-1,3-cyclopentanedicarboxylate (ACPD) (Bolduc et al., 2008; Hamasaka et al., 2007; Kanellopoulos et al., 2012; McBride et al., 2005; Parmentier et al., 1996; Tauber et al., 2011). We tested the effects of both MPEP and ACPD on olfactory learning of *drep-2* mutants (Fig. 65). To this end, we raised flies on food containing either of the two

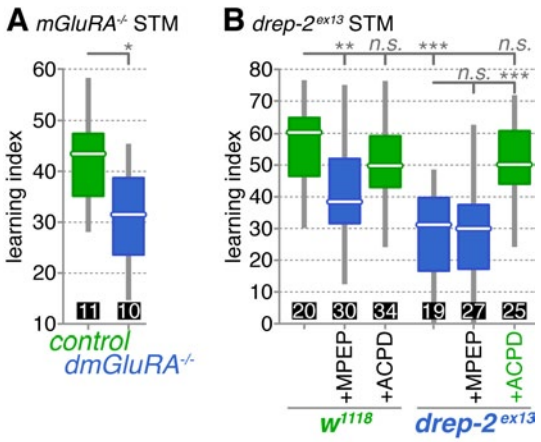

Fig. 65: The learning ability of *drep-2* mutants is influenced by mGluR activity.
A: *DmGluRA*^{112b} mutants are defective in aversive olfactory conditioning STM; MWU: p=0.043, α=0.05.
B: The *drep-2*^{ex13} phenotype in olfactory STM can be rescued by application of the DmGluRA agonist 1S,3R-ACPD.
Food was supplemented with either the DmGluRA receptor antagonist MPEP (9.7 µM) or the agonist 1S,3R-ACPD (72.2 µM).
MPEP lowered *w*^{1118} performance significantly (MWU p=0.0003). MPEP did not alter *drep-2*^{ex13} indices (p=0.8772) and ACPD did not change *w*^{1118} performance (p=0.1145). ACPD rescued the mutant phenotype to control levels (comparison to *drep-2*^{ex13}: p<0.00001; comparison to *w*^{1118}: p=0.0945). The difference between untreated *w*^{1118} and *drep-2*^{ex13} flies was also significant (p<0.00001). Significance level α=0.00833 (6 tests).

components. Already in the earlier studies, MPEP had been fed to flies by adding it to the food; ACPD had, so far, not been used in flies *in vivo*. In agreement with the phenotype observed for *dmGluRA* mutants (Fig. 65A), the antagonist MPEP decreased learning scores of wildtype flies significantly (Fig. 65B). By contrast, MPEP did not modify the learning ability of *drep-2* mutants.

Of note, several earlier studies used a concentration of MPEP 10x higher than we used in our experiments (e.g., Kanellopoulos et al., 2012). We raised flies at a concentration of 9.7 µM, which had been shown to be effective previously (McBride et al., 2005; 2010). At the high concentration used in other laboratories, MPEP might also inhibit NMDA receptors, in addition to mGluR (McBride et al., 2005; Spooren et al., 2001).

While MPEP did not affect *drep-2* mutants, application of the mGluR agonist ACPD caused a rescue of the *drep-2*^{ex13} phenotype (Fig. 65B). At the same time. the agonist did not alter the behaviour of control animals. Thus, artificial activation of mGluR receptors can obviously compensate for the olfactory learning deficits of *drep-2* mutants. This result indicates that DmGluRA-dependent signalling might well be downregulated in *drep-2* mutants.

2.1.8.6. Lowered odour-evoked Ca^{2+} responses in KCs of mutants

Transmission of an odour at PN-KC synapses leads to an increase of intracellular Ca^{2+} levels (Fig. 10A; Busto et al., 2010). In the calyx, this is likely mainly caused by Ca^{2+} influx through nicotinic acetylcholine receptors (Chorna and Hasan, 2012; Gu and O'Dowd, 2006). By contrast, in MB lobes the transient rise of Ca^{2+} levels is mainly induced by voltage-gated Ca^{2+} channels. In olfactory conditioning, the adenylyl cyclase Rutabaga mediates coincidence detection between the conditioned (odour) and the unconditioned stimulus (electric shock) in KC γ-lobes (Fig. 10A; Busto et al., 2010; Qin et al., 2012). Rutabaga is sensitive to both Ca^{2+}/Calmodulin, stimulated by sensation of the odour, and cAMP, stimulated via dopaminergic transmission, which is triggered by the electric shock. Therefore, odour-evoked Ca^{2+} transients are a prerequisite for olfactory learning.

In order to further investigate the function of Drep-2 in olfactory learning, we examined Ca^{2+} responses in KCs of *drep-2* mutants[26]. To this end, we expressed the calcium sensor GCaMP3 in KCs, using mb247-Gal4 (Tian et al., 2009). We measured the GCaMP3 activity in MB α-lobes, which are anatomically easy to access, upon presentation of the same odours used for olfactory conditioning (3-octanol and 4-methyl-cyclohexanol). Odours were also employed at the same concentration as in behavioural assays.

We observed that the maximal amplitude of the evoked change in GCaMP3 intensity was significantly decreased in *drep-2* mutants (Fig. 66). It can thus be concluded that the sensation of an odour likely triggers a lower Ca^{2+} response in *drep-2* mutants than in wildtype animals. This could indeed be the cause for the learning phenotype.

[26] GCaMP3 measurements and the corresponding analysis were conducted with help from Shubham Dipt, lab of André Fiala, Georg-August-Universität Göttingen. Christine Quentin supported the experiments as well.

However, it remained unclear how a lack of Drep-2 might cause lower odour-evoked Ca^{2+} transients.

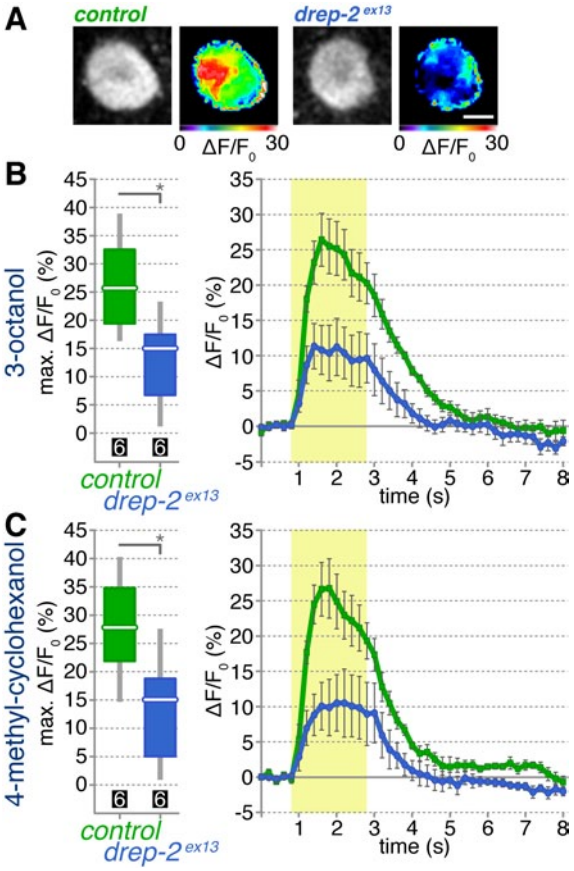

Fig. 66: GCaMP3 imaging in *drep-2* mutants.
Drep-2^{ex13} mutants showed a lower maximal GCaMP3 (calcium) response than controls in MB Kenyon cells (mb247-Gal4), upon presentation of the same odours used for olfactory conditioning. $\Delta F/F_0$ = changes in fluorescence emission.
A: Change in fluorescence intensity (4-MCH). Scale bar: 10 µm.
B-C: Yellow box: time of odour presentation.
B: 3-OCT, p=0.03 (MWU).
C: 4-MCH, p=0.045 (MWU).

2.1.8.7. Ethanol hypersensitivity of *drep-2* mutants

Many genes required for olfactory learning also mediate ethanol sensitivity in *Drosophila* (for examples see section 4.3 of the introduction (pages 29-30), as well as Berger et al., 2008; Laferriere et al., 2008; Morozova et al., 2011). In olfactory conditioning, Drep-2 interferes with mGluR signalling (Fig. 65B); mice mutant for the mammalian mGluR mGlu5 are ethanol hypersensitive (Bird et al., 2008). In flies, the mGluR-associated protein Homer is required in ring cells of the central complex for normal sensitivity towards ethanol (Urizar et al., 2007). Interestingly, Drep-2 is strongly expressed at ring cells postsynapses in the lateral triangle (Fig. 46A, Fig. 48C, Fig. 67).

We therefore examined whether *drep-2* mutants show an altered sensitivity towards ethanol-induced sedation. Indeed, using a *booz-o-mat* setup (Wolf et al., 2002), we could observe that *drep-2* mutants were strongly ethanol hypersensitive[27] (Fig. 68B). Increased sensitivity is not due to altered ethanol pharmacokinetics: during ethanol exposure, the ethanol concentration increased in parallel in mutant and control animals (Fig. 68A).

[27] *Booz-o-mat* and ethanol absorption experiments were conducted by Dana Robertson, Ulrike Heberlein's lab, University of California, San Francisco.

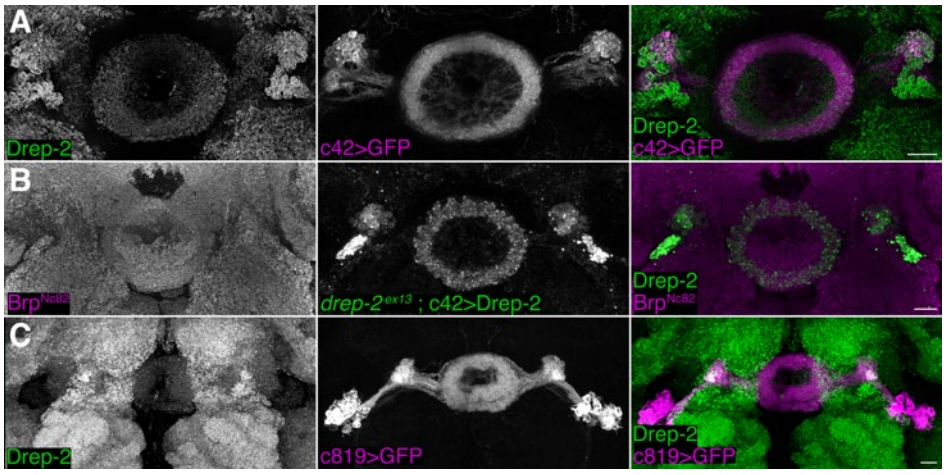

Fig. 67: Drep-2 at ring cell synapses.
C42- (A,B) and c819-Gal4 (C) label R2- and R4m-type ring cells (Renn et al., 1999). Drep-2 colocalized with the ring-shaped synapses, not the cell bodies, which lie distally (C, 3D reconstruction). C42- and c819-Gal4 label different synapse populations in the lateral triangle. Scale bars: 10 µm. **A,C:** GFP expressed by Gal4 drivers, Drep-2$^{C\text{-}Term}$ staining. **B:** *Drep-2^{ex13}* mutant, UAS-drep-2 re-expression by c42-Gal4, Drep-2$^{C\text{-}Term}$ and Brp^{Nc82} staining.

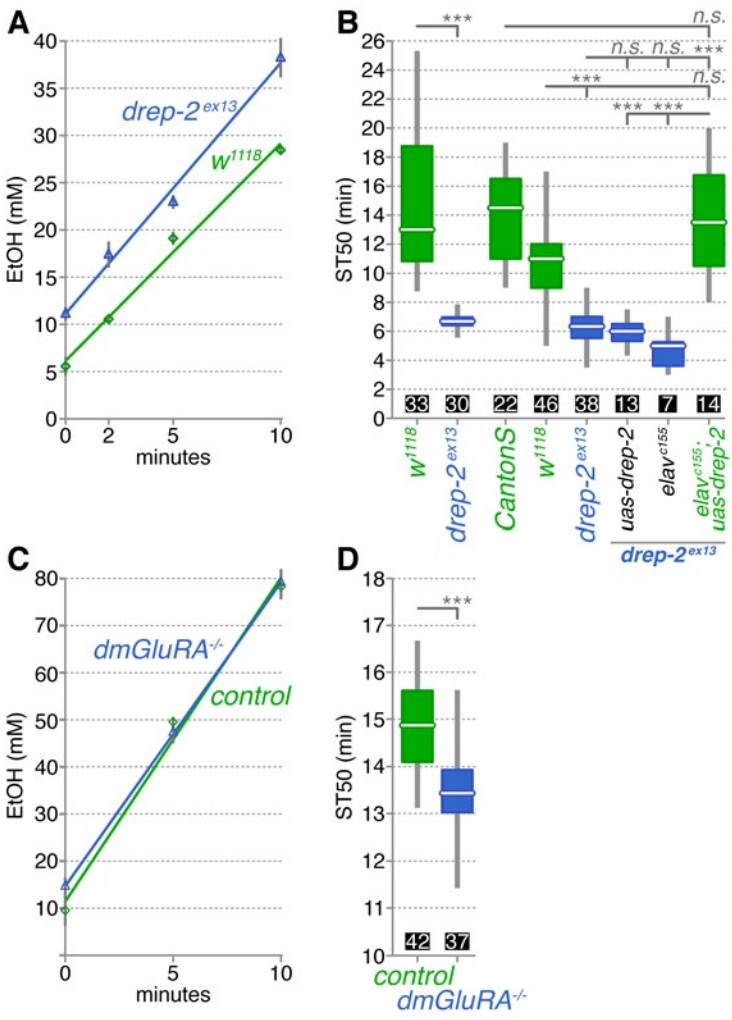

Fig. 68: Ethanol hypersensitivity of *drep-2* and *dmGluRA* mutants.
A,C: Ethanol absorption was measured in an assay for alcohol dehydrogenase activity (Singh and Heberlein, 2000).
B,D: Ethanol sedation measurements; the graphs indicate the time at which 50% of flies were sedated (ST50), outliers have been removed according to Devore, 2011 (see p. 56).
A: *Drep-2* mutants absorbed ethanol normally. The higher baseline of the mutant could be attributed to a slightly lower body size of the mutant flies used for this experiment.
B: *Drep-2* mutants were ethanol hypersensitive. Measurements 1 and 2 were done in a *booz-o-mat* setup, ethanol exposure was 99.5% (Wolf et al., 2002). Measurements 3-8 were done with a simpler assay (Maples and Rothenfluh, 2011). Re-expression of *drep-2* cDNA with *elav^{c155}*-Gal4 (pan-neural) rescued the phenotype. MWU showed a significant difference between these groups (Bonferroni-corrected significance level α=0.00625):
w^{1118} and *drep-2^{ex13}* (p<0.0001) (for both assays), *drep-2^{ex13}* and *drep-2^{ex13};uas-drep-2/elav^{c155}-gal4* (p<0.0001), *drep-2^{ex13};uas-drep-2/+* and *drep-2^{ex13};uas-drep-2/elav^{c155}-gal4* (p<0.0001), *drep-2^{ex13};elav^{c155}-gal4/+* and *drep-2^{ex13};uas-drep-2/elav^{c155}-gal4* (p<0.0001).
C: *DmGluRA* mutants absorbed ethanol normally.
D: *DmGluRA* mutants were ethanol hypersensitive (*booz-o-mat* measurements). MWU (α=0.05): p=0.0021.

We repeated the ethanol sensitivity experiments with a simpler setup (Maples and Rothenfluh, 2011). Here, *drep-2* mutants and isogenic w^{1118} controls showed similar sedation times as in *booz-o-mat* assays (Fig. 68B). With this setup, we could rescue the phenotype: flies in which *drep-2* cDNA was re-expressed with the pan-neural driver elav^{c155}-Gal4 showed normal sensitivity levels (Fig. 68B).

In fact, the sedation time of this genotype was even higher than the one of w^{1118} controls. This can be attributed to the *white* gene, which w^{1118} flies lack: *white* codes for an ABC transporter that regulates levels of biogenic amines, modulates the effects of anaesthetics and influences adaptive behaviours (Anaka et al., 2008; Borycz et al., 2008; Campbell and Nash, 2001; Diegelmann et al., 2006). Accordingly, red-eyed isogenic *CantonS* controls (outcrossed to w^{1118} and thus isogenic to the other strains, except for the *white* locus) showed, compared to w^{1118}, an increased sedation time that was not different from the one of *drep-2* mutants re-expressing *drep-2* cDNA (Fig. 68B).

We also expressed the *drep-2* cDNA with additional Gal4 drivers, in order to reveal in which neurons Drep-2 mediates ethanol sensitivity (Table 5). However, none of the drivers tested could rescue the phenotype, with the exception of pan-neural elav^{c155}. All drivers were backcrossed to w^{1118} to establish an isogenic genetic background, as we had done for the other behavioural experiments. It therefore remains unclear in which cell types Drep-2 is required for normal ethanol sensitivity. To our surprise, also expression with the very broad drivers elav^{appl} (alias appl-Gal4) and elav^{III} did not alter ethanol sensitivity. A comparison revealed that elav^{appl} and, especially, elav^{III} have a more restricted expression pattern than elav^{c155} (Fig. 69). As outlined in the introduction (section 4.3, page 29), several neurons known to regulate ethanol sensitivity reside in the pars intercerebralis and the subesophageal ganglion (SEG) of the CNS. It is possible that the three drivers show a differential expression in the SEG.

Gal4 line	Cell types	Rescue
elav^{c155}	pan-neural	+
elav^{appl}	pan-neural	-
elav^{III}	pan-neural	-
c819	R2-/R4m ring cells (ellipsoid body), large field neurons, pars intercerebralis	-
c42	R2-/R4m ring cells (ellipsoid body), fan shaped neurons, large field neurons, pars intercerebralis, Malpighian tubules	-
c232	R3-/R4d ring cells (ellipsoid body), large field neurons, Malpighian tubules	-
c81	adult: ellipsoid body	-
mb247	Kenyon cells, glia	-
121y	Kenyon cells, pars intercerebralis	-
30y	KCs, tritocerebrum, deuterocerebrum, subesophageal ganglion, superior protocerebrum, pars intercerebralis, lateral horn, optic tubercle, optic lobes	-

Table 5: Gal4 lines used for the rescue of the ethanol hypersensitivity phenotype.
Sources for expression patterns: Aso et al., 2009; McQuilton et al., 2012; Renn et al., 1999; Rodan et al., 2002.

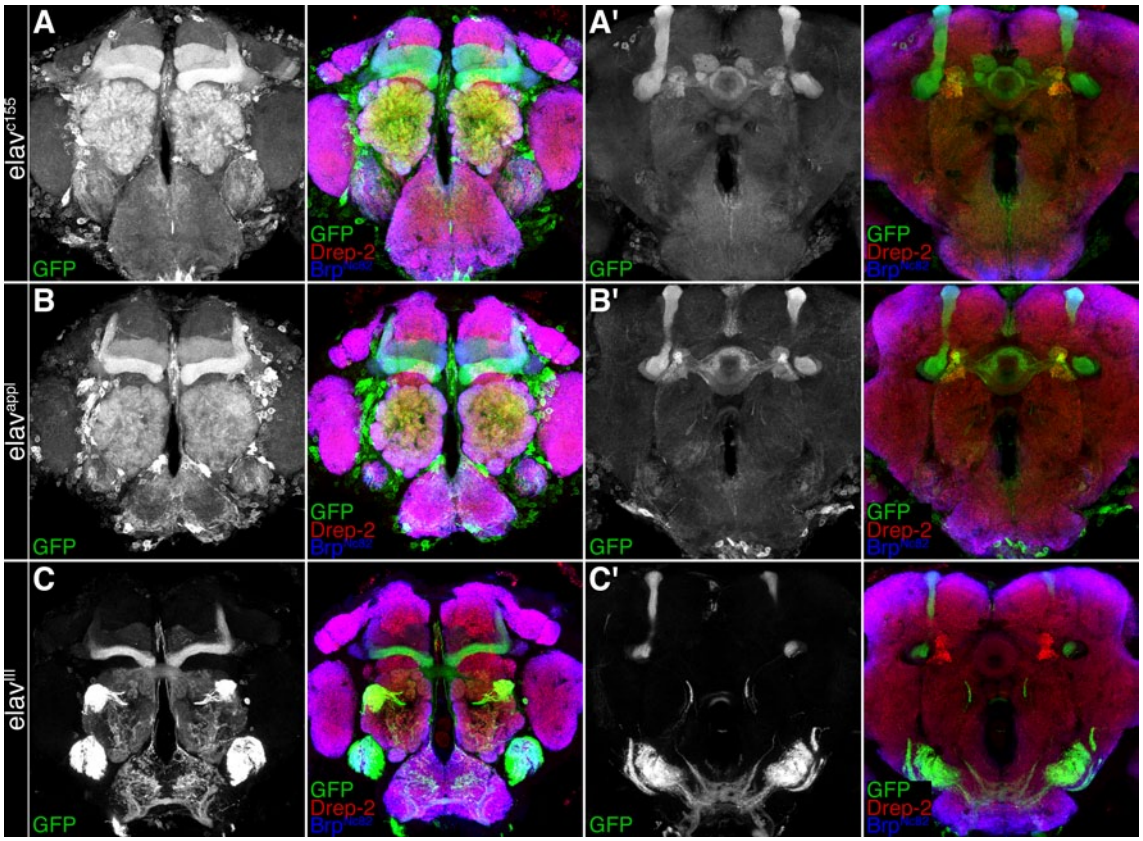

Fig. 69: Expression patterns of different pan-neural drivers.
UAS-GFP is shown in comparison to Drep-2$^{C\text{-}Term}$ and Brp^{Nc82} antibody stainings.
A,B,C: Frontal confocal sections on the level of ALs and MB lobes.
A',B',C': Frontal confocal sections on the level of MB lobes, ellipsoid body and lateral triangle.
A,A': Elav^{c155}-Gal4 shows the broadest expression.
B,B': Elav^{appl}-Gal4 (alias appl-Gal4) shows a slightly weaker expression pattern in most neuropils.
C,C': Elav^{III}-Gal4 shows a much more restricted expression, in part reminiscent of mb247-Gal4.

In addition, we tried to rescue the phenotype by combining the *drep-2^{ex13}* mutant with a *drep-2^{GFP}* construct under control of the endogenous *drep-2* promoter (see paragraph 2.1.4). However, also under this condition, the sensitivity was not restored to normal levels (*not shown*). This could be explained by the observation that expression of this Drep-2^{GFP} construct was much weaker than expression of endogenous Drep-2, possibly due to position-effect variegation (*not shown*). Of note, in general the expression of *drep-2^{GFP}* matched the Drep-2$^{C\text{-}Term}$ label in wildtype brains.

Flies develop tolerance to the sedative effects of ethanol after exposure (see section 4.3 of the introduction and Scholz et al., 2000). We tried to assay whether the establishment of ethanol tolerance was altered in *drep-2* mutants. However, ethanol-induced sedation of *drep-2* mutants was so pronounced that experiments under conditions that allow for the development of tolerance could not be conducted.

2.1.8.7.1. No clear influence of caspases on ethanol sensitivity was found

It has been demonstrated that the Dff-family proteins Drep-1 and Drep-4 are regulated by caspase cleavage (Inohara and Nuñez, 1999; Mukae et al., 2000; Yokoyama et

al., 2000). Drep-3 is predicted to be cleaved by caspases (Park and Park, 2012). Ethanol consumption can induce caspase activation in *Drosophila* and mammals (Chen et al., 2012; Olney et al., 2002). We therefore wondered whether caspases might play a role in mediating ethanol sensitivity in *Drosophila*.

To examine whether ethanol-induced sedation is dependent on caspases in *Drosophila*, we first turned to the protein Ark (Apaf-1). This adaptor protein is required for activation of initiator caspases (Bao and Shi, 2007; Rodriguez et al., 1999). We tested ethanol sedation times of *ark* mutants, which were normal (*not shown*).

Expression of the baculovirus protein p35 inhibits the activity of effector caspases like DrICE (Hay et al., 1994). We expressed UAS-p35 with different Gal4 drivers and assayed ethanol sensitivity. To avoid developmental defects, expression of UAS-p35 was restricted to three days before the experiments by using the temperature-sensitive Gal4-repressor Gal80^{ts}. In this situation, Gal4-mediated expression can be activated by raising the temperature from 18°C to 29°C.

All four Gal4-lines tested (elav^{III}, c42, mb247, and mz19) showed an increased sensitivity at 29°C, when compared to control animals that had remained at 18°C (*not shown*). So far, neither Kenyon cells (mb247) nor projection neurons (mz19) have been implicated in mediating ethanol sensitivity. These two drivers were therefore regarded as negative controls. Our result thus indicated an effect of temperature on ethanol sedation. The difference in sedation time between flies kept at 18°C or 29°C appeared as being the largest for c42-Gal4. However, the differences in experiments with the other three lines were also statistically significant (MWU tests). Due to these ambivalent results, no definite conclusion could be drawn regarding the influence of effector caspases on ethanol-induced sedation. However, it seems unlikely that activation of caspases does play a role in mediating ethanol sensitivity in *Drosophila*.

2.1.8.8. Locomotor hyperactivity of *drep-2* mutants

From our observations, we had the suspicion that *drep-2* mutants show a higher basal locomotor activity than wildtypes. When testing for ethanol sensitivity, we used the *booz-o-mat* assay, an automated locomotor tracking system that monitors the activity of flies (Wolf et al., 2002). With this setup, we could demonstrate that *drep-2* mutants were indeed hyperactive (Fig. 70). Flies continued to show higher activity even two hours after begin of the experiment (*not shown*). Interestingly, ring cells have been implicated in mediating ethanol-induced locomotor hyperactivity (Kong et al., 2010). Moreover, also flies mutant for mGluR-associated Homer show a higher level of spontaneous locomotion (Diagana et al., 2002).

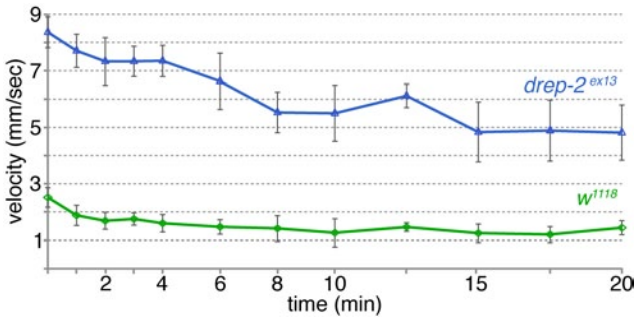

Fig. 70: Locomotion defect of *drep-2*^{ex13} mutants.
During the observation period of 20 min, mutants constantly moved more than isogenic w^{1118} controls. N=4 tubes (each 20 flies) per genotype. The graph shows the mean velocity per point in time and SEMs.

2.1.9. Mass spectrometry: Drep-2 in complexes with translational repressors

So far, we had acquired ample information about the function of Drep-2 on a systems level. In addition, we could demonstrate a physical interaction with the presynaptic protein Bruchpilot (Fig. 38C) and a functional connection with the metabotropic glutamate receptor DmGluRA (Fig. 65B). However, we were still lacking data about the molecular role of Drep-2. We figured that knowledge about Drep-2-interacting proteins could shed light on the molecular function of Drep-2 and explain the phenotypes observed in the mutants. Thus, we aimed at identifying putative Drep-2 *in vivo* interaction partners using quantitative affinity purification and mass spectrometry[28] (Paul et al., 2011; Vermeulen et al., 2008). Unfortunately, the Drep-2$^{C\text{-}Term}$ antibody did not sufficiently precipitate the endogenous Drep-2 protein for such an analysis. Instead, we expressed GFP-tagged Drep-2 using the pan-neural driver line elav^{c155}-Gal4 and subsequently purified the fusion protein from fly heads with anti-GFP beads (Fig. 71). As a control for nonspecific binding, parallel pulldowns were performed, using either plain beads or Drep-2^{GFP}-negative lysates (Fig. 71A). All three pulldowns were conducted in triplicate and processed and analysed by high-resolution shotgun proteomics. Proteins were quantified by label-free quantification; specific interaction partners were extracted using t-test statistics (Hubner et al., 2010).

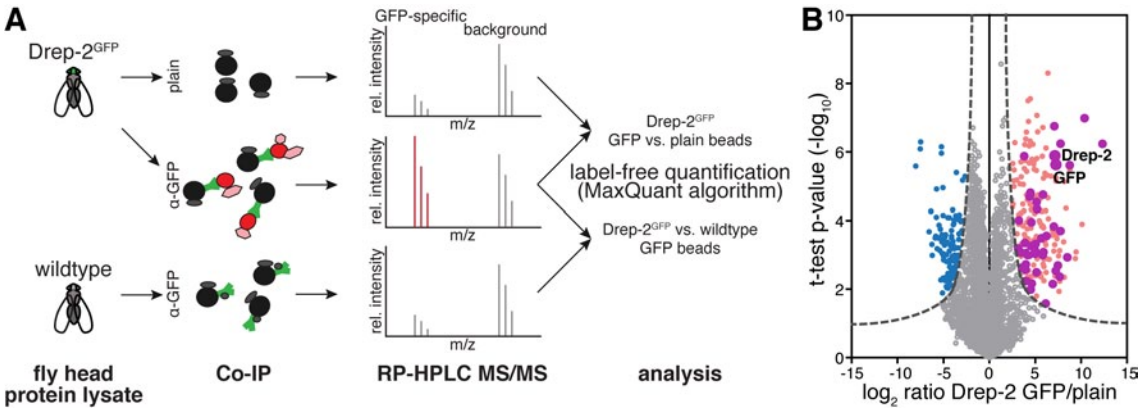

Fig. 71: Quantitative mass spectrometry.
A: Strategy for the identification of Drep-2 interactors by quantitative mass spectrometry.
B: Volcano plot showing proteins from Drep-2^{GFP} flies binding to anti-GFP and/or plain control beads. A hyperbolic curve (set at an FDR of 1%) separates GFP-enriched proteins (light pink) from background (grey). Proteins enriched in the control are shown in blue. Proteins that were significantly enriched, both in Drep-2^{GFP} flies and in independent control experiments with wildtype flies, are coloured magenta (n=35).

With this approach, we identified a total of 3284 proteins in anti-GFP precipitations of Drep-2^{GFP} lysate (Fig. 71B). However, a large number of these proteins were also found in negative controls. 35 proteins plus the bait proteins Drep-2 and GFP were robustly enriched over both controls, at a false-positive discovery rate (FDR) of 1% (Fig. 71B, Table 7, Table 8). An extended protein network was generated, in order to visualize which of these 35 core proteins are part of a larger grid of putative interac-

[28] Husam Babikir generated fly head lysates; Marieluise Kirchner, lab of Matthias Selbach, Max-Delbrück-Centrum für molekulare Medizin, conducted the affinity purification and mass spectrometry. Madeleine Brünner prepared the western blot.

tors (Fig. 72). Proteins that DroID (Murali et al., 2011), Flybase (McQuilton et al., 2012) or other literature lists as (putative) interactors of any of the 35 core proteins (FDR 1%) were added, if they fit the following three conditions: enriched in the pull-downs (*elav^{c155}; uas-drep-2^{GFP}* flies, GFP beads vs. plain beads) at a 10% FDR; not enriched in the control experiment (GFP beads, wildtype flies vs. *elav^{c155}; uas-drep-2^{GFP}* flies) at a 10% FDR (to eliminate false-positives); a (predicted) interaction with at least two of the 35 core proteins (Table 9). Among the proteins that were found to be significantly enriched were Drep-2, GFP, and Drep-3, a cognate binding partner of Drep-2 (Inohara and Nuñez, 1999; Park and Park, 2012). It can thus be concluded that we successfully precipitated proteins interacting with Drep-2 and not merely peptides binding unspecifically.

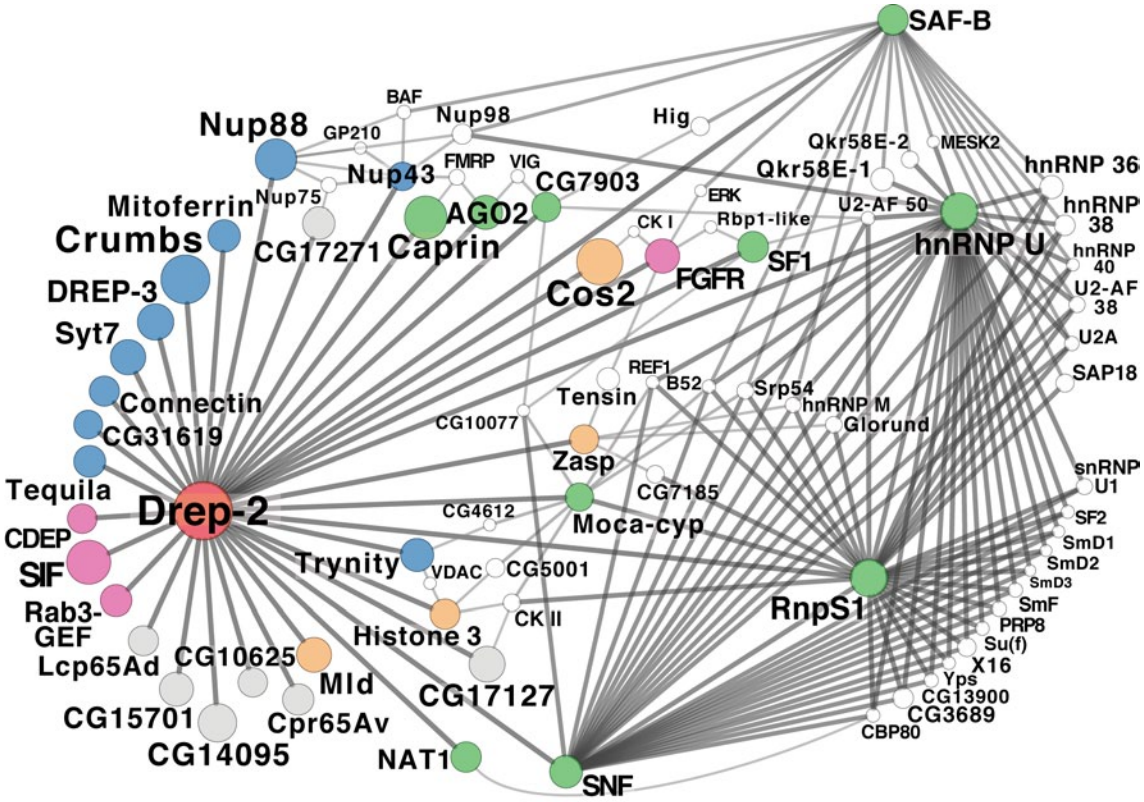

Fig. 72: Protein network based on results from quantitative mass spectrometry.
Network of the 35 core proteins significantly enriched in GFP pulldown experiments (at an FDR of 1%, magenta-coloured dots in Fig. 71B). Additional putative interactors of the core network (FDR set at 10%) are shown in white (Table 9). The circle (node) and font size correspond to the rank within the results. The line (edge) width and shade correspond to the number of interactions each of the significantly enriched proteins has with others. The line/edge length is arbitrary.

	Counts	Percent
Membrane	14	40
RNA	10	29
G-protein	4	11
Cytoskeleton	4	11
Other	4	11
Unknown/Unrelated	7	20
Total	35	

Table 6: Classification of the 35 core network proteins.
Compare Fig. 72; multiple counts were allowed.

Rank	Flybase name	Name in network	Full name	CG number	Flybase ID	Network class I	Network class II
1	crb	Crumbs	Crumbs	CG6383	FBgn0259685	Membrane	Cyto-skeleton
2	cos	Cos2	Costal-2	CG1708	FBgn0000352	Cytoskel-eton	Membrane
3	sif	SIF	Still life	CG34418	FBgn0085447	G-protein	Membrane
4	Capr	Caprin	Caprin	CG18811	FBgn0042134	RNA	
5	mbo	Nup88	Members only	CG6819	FBgn0026207	Membrane	
7	Drep-2	Drep-2	DNA fragmentation factor-related protein 2	CG1975	FBgn0028408	Drep-2	Membrane
8	CG14095	CG14095		CG14095	FBgn0036870	Unrelated	Cuticle
9	RnpS1	RnpS1	RNA-binding protein S1	CG16788	FBgn0037707	RNA	
10	CG30122	hnRNP U	Similar to hnRNP U / SAF-A	CG30122	FBgn0050122	RNA	
11	Drep-3	Drep-3	DNA fragmentation factor-related protein 3	CG8364	FBgn0028407	Membrane	
12	CG17127	CG17127		CG17127	FBgn0032299	Unrelated	Cuticle
13	Syt7	Syt7	Synaptotagmin 7	CG2381	FBgn0039900	Membrane	
14	mld	Mld	Molting defective	CG34100	FBgn0263490	Other	
15	htl	FGFR	Heartless	CG7223	FBgn0010389	G-protein	Membrane
16	CG15701	CG15701	CG15701	CG15701	FBgn0034095	Unknown	
17	AGO2	AGO2	Argonaute 2	CG7439	FBgn0087035	RNA	
18	tyn	Trynity	Trynity	CG17131	FBgn0029128	Membrane	Cyto-skeleton
19	snf	SNF	Sans fille	CG4528	FBgn0003449	RNA	
20	mfrn	Mitoferrin	Mitoferrin	CG4963	FBgn0039561	Membrane	
21	CG17271	CG17271	CG17271	CG17271	FBgn0038829	Unknown	
22	Tequila	Tequila	Tequila	CG4821	FBgn0023479	Membrane	
23	Rab3-GEF	Rab3-GEF	Rab3 GDP-GTP exchange factor	CG5627	FBgn0030613	G-protein	Membrane
24	Cpr65Av	Cpr65Av	Cuticular protein 65Av	CG32405	FBgn0052405	Unrelated	Cuticle
25	SF1	SF1	Splicing factor 1	CG5836	FBgn0025571	RNA	
26	Saf-B	SAF-B	Scaffold attachment factor B	CG6995	FBgn0039229	RNA	
27	NAT1	NAT1	NAT1 / p97 / DAP5	CG3845	FBgn0010488	RNA	
28	Con	Connectin	Connectin	CG7503	FBgn0005775	Membrane	
29	Lcp65Ad	Lcp65Ad	Larval cuticular protein 65Ad	CG6955	FBgn0020641	Unrelated	Cuticle
30	His3: CG31613	Histone 3	His3:CG31613	CG31613	FBgn0051613	Other	
31	Cdep	CDEP	Chondrocyte-derived ezrin-like domain containing protein ortholog	CG44193	FBgn0265082	G-protein	Cyto-skeleton
32	CG10625	CG10625		CG10625	FBgn0035612	Unrelated	Cuticle
33	Zasp52	Zasp	Z band alternatively spliced PDZ-motif protein 52	CG30084	FBgn0083919	Other	
34	CG7903	CG7903	CG7903	CG7903	FBgn0039730	RNA	
35	CG31619	CG31619	CG31619	CG31619	FBgn0051619	Membrane	
36	Nup43	Nup43	Nucleoporin 43kD	CG7671	FBgn0038609	Membrane	
37	Moca-cyp	Moca-cyp	Moca-cyp	CG1866	FBgn0039581	RNA	

Table 7: Core proteins enriched over both controls, at an FDR of 1%. GFP (6) was removed.
The ranks are based on the ratios of Drep-2^{GFP} IPs, GFP beads vs. plain beads (compare Fig. 71).

Rank	Name	Flybase: molecular function	Additional notes
1	Crumbs	protein kinase C binding	polarity, adherens junction, apoptosis
2	Cos2	smoothened binding; microtubule binding; protein binding; protein kinase binding; transcription factor binding	kinesin, hedgehog-signaling, binds microtubules
3	SIF	Rac GEF activity	
4	Caprin	RNA binding	in mRNP complexes, associated with stress granules
5	Nup88	protein binding	regulates transport from/to the nucleus
7	Drep-2	unknown	
8	CG14095	unknown	expressed in trachea and cuticle
9	RnpS1	mRNA binding	splicing, exon junction complex, mRNA decay, nuclear export, apoptosis
10	hnRNP U	mRNA binding	SAF-A, splicing, cleaved by caspase, mRNA transport and metabolism
11	Drep-3	unknown	inhibits Drep-2
12	CG17127	unknown	putative cuticle protein
13	Syt7	calcium-dependent phospholipid binding	in muscles and cell bodies
14	Mld	zinc ion binding; nucleic acid binding	ecdysone biosynthesis, sleep, courtship memory, zinc finger motif
15	FGFR	protein tyrosine kinase activity; fibroblast growth factor-activated receptor activity	in muscles, Ras/MAPK signaling
16	CG15701	unknown	in glands, tubule, gut; WD40 domain
17	AGO2	protein binding; endoribonuclease activity; siRNA binding	RNAi, RISC complex, RNA cleavage, p-bodies, silencing of transposons, olfactory learning
18	Trynity	unknown	binds actin, polarity, zona pellucida, neuronal
19	SNF	U2 snRNA binding; protein binding; snRNA stem-loop binding; U1 snRNA binding	splicing
20	Mitoferrin	iron ion transmembrane transporter activity	in mitochondria
21	CG17271	calcium ion binding	expressed in glands
22	Tequila	serine-type endopeptidase activity	Neurotrypsin-homolog (protease), olfactory ASM & LTM, presynaptic
23	Rab3-GEF	Rab GEF activity	synaptic vesicles, apoptosis
24	Cpr65Av	structural constituent of chitin-based cuticle	larval cuticle and trachea
25	SF1	RNA binding; zinc ion binding	splicing, in U1/U2 snRNPs
26	SAF-B	mRNA binding	splicing, nuclear scaffold, binds to hnRNP A1, transcription factor, apoptosis, mRNA export and translational control?
27	NAT1	translation initiation factor activity	apoptosis
28	Connectin	unknown	cell adhesion, axons and muscles
29	Lcp65Ad	structural constituent of chitin-based cuticle	larval cuticle protein
30	Histone 3	DNA binding	
31	CDEP	actin binding; Rho GEF activity	
32	CG10625	structural constituent of cuticle	
33	Zasp	protein binding	PDZ-LIM domain, muscle attachment, Z-disks
34	CG7903	mRNA binding	
35	CG31619	metalloendopeptidase activity	immunoglobulin, might bind TGF-beta, extracellular or nuclear matrix
36	Nup43	unknown	nuclear pore complex
37	Moca-cyp	peptidyl-prolyl cis-trans isomerase activity	nuclear cyclophilin, putative role in regulation of translation/splicing

Table 8: Putative functions of the core proteins enriched over both controls, at an FDR of 1%.

Rank	Flybase name	Name in network	CG number	FDR 1% (GFP vs. plain)	FDR 5% (GFP vs. plain)	FDR 10% (GFP vs. plain)	FDR 1% (Drep-2^{GFP} vs. wt)	FDR 10% (Drep-2^{GFP} vs. wt)
78	Hrb87F	hnRNP 36	CG12749	+	+	+		
79	qkr58E-1	Qkr58E-1	CG3613	+	+	+		+
87	by	Tensin	CG9379	+	+	+		
113	Hrb98DE	hnRNP 38	CG9983	+	+	+		
115	CG3689	CG3689	CG3689	+	+	+		
122	Nup98-96	Nup98	CG10198		+	+	+	+
149	CG5001	CG5001	CG5001		+	+	+	+
153	x16	X16	CG10203	+	+	+		
155	hig	Hig	CG2040	+	+	+		
165	Bin1	SAP18	CG6046	+	+	+		+
173	CG7185	CG7185	CG7185	+	+	+		+
184	CkIIbeta	CK II	CG15224	+	+	+		
190	qkr58E-2	Qkr58E-2	CG5821			+		
200	Srp54	Srp54	CG4602		+	+		+
202	glo	Glorund	CG6946	+	+	+		+
217	snRNP-U1-70K	snRNP U1	CG8749		+	+		+
219	U2af38	U2-AF 38	CG3582		+	+	+	+
229	Fmr1	FMRP	CG6203		+	+		+
235	rump	hnRNP M	CG9373		+	+		
244	Zasp52	ZasP52	CG30084	+	+	+		
245	Nup75	Nup75	CG5733		+	+		
264	Prp8	PRP8	CG8877			+		
276	U2A	U2A	CG1406		+	+		
280	SmF	SmF	CG16792		+	+	+	+
287	CG13900	CG13900	CG13900		+	+		+
303	su(f)	Su(f)	CG17170		+	+		+
306	baf	BAF	CG7380		+	+		
311	Cbp80	CBP80	CG7035		+	+		
319	B52	B52	CG10851		+	+		
320	vig	VIG	CG4170		+	+		+
324	Ref1	REF1	CG1101		+	+		
331	SF2	SF2	CG6987		+	+		
340	yps	Yps	CG5654		+	+		
363	sqd	hnRNP 40	CG16901		+	+		+
366	Rbp1-like	Rbp1-like	CG1987		+	+		
374	SmD1	SmD1	CG10753		+	+		+
378	CG4612	CG4612	CG4612		+	+	+	+
379	porin	VDAC	CG6647		+	+		
380	CG10077	CG10077	CG10077			+		
388	Gp210	GP210	CG7897		+	+		
389	MESK2	MESK2	CG15669		+	+	+	+
399	rl	ERK	CG12559			+	+	+
404	SmD2	SmD2	CG1249		+	+		
422	SmD3	SmD3	CG8427		+	+		
429	CG17271	CG17271	CG17271		+	+	+	+
439	CkIalpha	CK I	CG2028		+	+		

Table 9: Additional proteins that are part of the extended network (shown in Fig. 72A).
Proteins that are not part of the network have been removed. The level of green indicates whether the protein was significantly enriched in Drep-2^{GFP} IPs, GFP beads vs. plain beads, at an FDR of 1%, 5%, or 10% (compare Fig. 71A). The level of blue indicates enrichment in IPs using GFP beads, Drep-2^{GFP} vs. wildtype head extracts. The ranks are based on the ratios of Drep-2^{GFP} IPs, GFP beads vs. plain beads.

2.1.9.1. Membrane proteins

Characterization of the 35 core interacting proteins found 14 to be associated with membranes (Table 6, Table 7, Table 8). This confirms our observation that Drep-2 localizes to the postsynaptic plasma membrane (Fig. 49, Fig. 53). The protein found to be most highly enriched was the transmembrane protein Crumbs, an apical determinant of epithelia and important for the integrity of adherens junctions (Tepass, 2012).

Two more proteins from a similar context were identified, Trynity, a regulator of apical cell polarity and Connectin, a cell adhesion molecule expressed in axons and muscles (Fernandes et al., 2010; Raghavan and White, 1997). Of note, the significantly enriched adhesion protein Zasp52 plays an important role in muscle development as well (Jani and Schöck, 2007). Moreover, also Synaptotagmin 7 was identified, which is expressed in muscles (Adolfsen et al., 2004).

Four proteins involved in G-protein signalling were among the membrane proteins identified in the mass spectrometry: the three guanyl-nucleotide exchange factors Still life, Rab3-GEF, and CDEP, as well as the fibroblast growth factor receptor Heartless.

Two more interesting proteins that were enriched are Costal-2, a microtubule-binding kinesin that plays a role in hedgehog-signalling (Ranieri et al., 2012) and the Neurotrypsin-homologue Tequila, a protease released from presynaptic terminals and involved in olfactory learning (Didelot et al., 2006; Matsumoto-Miyai et al., 2009). However, it is possible that Tequila constitutes a false-positive hit: the serine protease is mainly contained in intracellular stores until release from synapses and thereafter acts extracellularly.

2.1.9.2. RNA-binding proteins

A large number of the significantly enriched proteins is associated with nucleic acids. Intriguingly, ten of the 35 proteins have been implicated in control of mRNA translation and stability. The network of putative interacting proteins (Fig. 72) underlines a strong connection of Drep-2 with RNA-associated proteins. Most of the significantly enriched RNA-linked proteins were splicing factors: RnpS1 (Lykke-Andersen et al., 2001), which also regulates pro-apoptotic factors and mRNA decay (Michelle et al., 2012; Viegas et al., 2007); CG30122, a sequence homologue of hnRNP U / SAF-A (*homology not shown*), which is a component of the nuclear matrix but also a splicing factor (Xiao et al., 2012) and is cleaved by Caspase-3 during apoptosis (Kipp et al., 2000); the snRNP Sans fille (Mount and Salz, 2000), Splicing Factor 1 (Mount and Salz, 2000), Scaffold attachment factor B (Nayler et al., 1998), and the Cyclophilin Moca-cyp (Cavarec et al., 2002).

The list of RNA-associated proteins also includes the eIF4G-related, cap-independent translation initiation factor NAT1/p97/DAP5 (Hundsdoerfer et al., 2005; Levy-Strumpf et al., 1997). Interestingly, NAT1 mediates translation via internal ribosomal entry sites, is activated by caspase cleavage, and promotes translation of apoptosis-related proteins (Henis-Korenblit et al., 2000; 2002; Nevins et al., 2003).

Furthermore, we found both Caprin, a dendritic translational repressor (Shiina et al., 2005), and Argonaute-2, involved in RNA interference (Ketting, 2011), among the

most highly enriched proteins. Of note, *argonaute-2* mutants show age-dependent impairments in olfactory LTM (Li et al., 2013). Interestingly, both Caprin and Argonaute-2 bind to the fragile X mental retardation protein FMRP (Ishizuka et al., 2002; Papoulas et al., 2010); in fact, FMRP itself was detected in Drep-2 complexes (at an FDR cutoff of 5%; Table 9). We confirmed the consistent presence of FMRP in Drep-2^{GFP} immunoprecipitates by immunoblotting (Fig. 73).

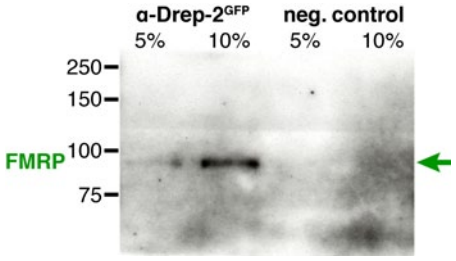

Fig. 73: FMRP in Drep-2 complexes.
Anti-FMRP probing of Drep-2^{GFP} immunoprecipitates confirmed the presence of FMRP in Drep-2^{GFP} complexes.

2.1.9.3. Drep-2 antagonizes FMRP in courtship conditioning

FMRP is an antagonist of mGluR-dependent protein synthesis (Fig. 4). Drep-2, by contrast, appears to stimulate either mGluRs or mGluR-dependent signalling (Fig. 65B). We thus wondered whether the presence of FMRP in Drep-2 complexes had functional implications.

Flies mutant for *fmr1* are hyperactive and deficient in olfactory memory (Bolduc et al., 2008; Kanellopoulos et al., 2012; Tauber et al., 2011; Wan et al., 2000), two phenotypes they share with *drep-2* mutants. However, impaired courtship conditioning constitutes the most characteristic deficiency of *Drosophila fmr1* mutants (Dockendorff et al., 2002; McBride et al., 2005). Interestingly, also *dmGluRA* and *homer* mutants are defective in courtship learning (Diagana et al., 2002; Schoenfeld et al., 2013).

In courtship conditioning, a paradigm for associative learning, it is examined whether male flies can learn from failed courtship (for details see section 4.2 (page 28) of the introduction or the classic publication Siegel and Hall, 1979). Typically, female flies mate with a male after a period of courtship. However, recently mated females repel additional males, both by aversive behaviour and by unattractive pheromones (Ejima et al., 2007).

Wildtype males that have made an unsuccessful courtship attempt with a pre-mated female learn from this experience (Siwicki and Ladewski, 2003). Accordingly, upon the next encounter with a pre-mated female, they spend less time courting in vain. The percentage of time a male spends courting a female during a test period is referred to as courtship index (CI). The difference in CI between naïve males (i.e. without previous experience) and flies previously trained with a pre-mated female, relative to the performance of naïve flies, is referred to as the learning index (LI) (see page 55 for the formula).

In order to investigate whether Drep-2 and FMRP influence each other, we thus turned to courtship conditioning[29], where a deficiency of *fmr1* mutants is firmly established (Dockendorff et al., 2002; McBride et al., 2005). Indeed, we could confirm a severe defect in courtship behaviour of *fmr1* mutants: naïve males spent less time courting (Fig. 74A). Importantly, trained *fmr1*$^{-/-}$ flies also showed a lack of courtship conditioning short-term memory, as published. Their learning index was close to zero, while control flies had a median LI of over 50.

We used the two alleles *fmr1*^{B55} and *fmr1*$^{\Delta 50M}$ *in trans* (Inoue et al., 2002; Zhang et al., 2001). By contrast, in most of the previous publications regarding courtship conditioning of *fmr1* mutants, the allele *fmr1*^{3} had been used homozygously (Dockendorff et al., 2002; McBride et al., 2005; Wan et al., 2000).

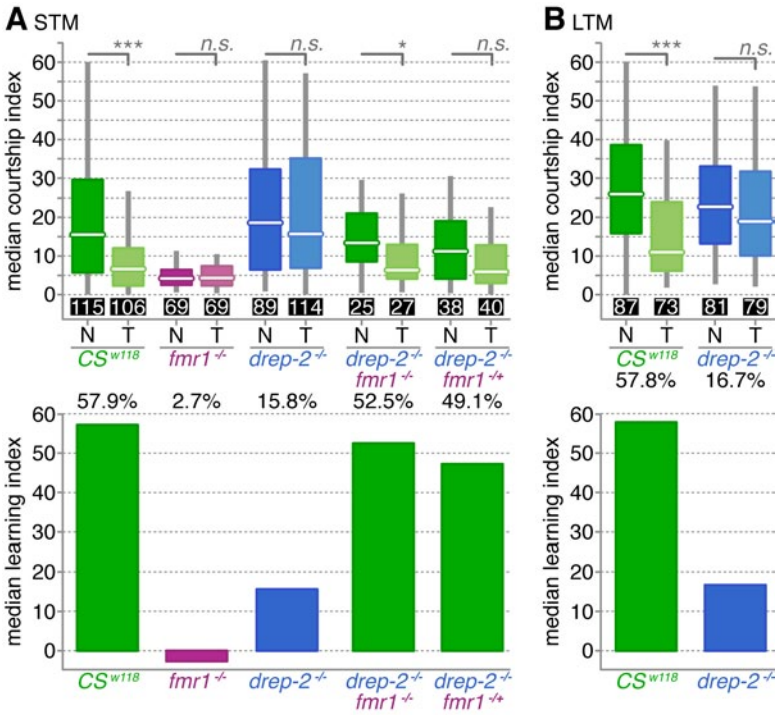

Fig. 74: Drep-2 antagonizes FMRP in courtship conditioning.
Graphs in the upper row show median courtship indices (CIs) between naïve (N) and trained (T) flies. The learning index (LI), i.e. the relative difference between median CIs, is displayed in the lower row. Sample sizes *n* are shown in black boxes.
Learning ability was assayed using a non-parametric permutation (randomization) test (Kamyshev et al., 1999). P-values are indicated for H_0, LI=0 and thus show the probability that flies did not learn – a low p-value signifies that flies did learn.
A: Short-term memory (STM), the significance level α=0.05 was adapted for 5 tests to α=0.05/5=0.01 (Bonferroni correction). P-values were: p<0.0001 for the isogenic *CantonS* control (*CS*^{w1118}; *w*^{1118} genetic background, *CantonS white*$^{+}$ gene); *fmr1*^{B55}/*fmr1*$^{\Delta 50M}$ mutants (*fmr1*$^{-/-}$): p=0.5524; *drep-2*^{ex13} mutants (*drep-2*$^{-/-}$): p=0.1858; *drep-2*^{ex13}/*drep-2*^{ex13} ; *fmr1*^{B55}/*fmr1*$^{\Delta 50M}$ double mutants: p=0.0075; *drep-2*^{ex13}/*drep-2*^{ex13} ; *fmr1*^{B55}/+ heterozygous double mutants: p=0.0452 (and thus not significant at α=0.01).
B: Long-term memory (LTM) performance, α=0.05/2=0.025; p<0.0001 for *CantonS* (*CS*^{w1118}) and p=0.1162 for *drep-2* mutants.

Interestingly, also *drep-2* mutants did not form significant STM in courtship conditioning experiments (Fig. 74A). Their median LI was reduced by about 70%, compared to controls. In contrast to *fmr1* and *dmGluRA* mutants, *drep-2* mutants displayed a normal basic courtship activity level.

As in previous experiments, isogenic *CantonS* flies were used as controls in this assay. These *CantonS* flies were outcrossed to *w*^{1118} but still differed from the other strains

[29] Courtship conditioning experiments were done by Cornelia Oppitz, lab of Krystyna Keleman, Research Institute of Molecular Pathology, Vienna.

at the *white* locus. Red-eyed *CantonS* controls were used instead of white-eyed w^{1118} because the ABC transporter encoded by the *white* gene influences courtship: misexpression of the *white* gene causes increases male-male courtship behaviour (Anaka et al., 2008).

To examine a putative functional interaction of Drep-2 and FMRP, we generated $drep\text{-}2^{ex13}/drep\text{-}2^{ex13}$; $fmr1^{B55}/fmr1^{\Delta 50M}$ double mutants. To our surprise, these animals did show courtship conditioning short-term memory, which both single mutants had not formed (Fig. 74A). This constitutes a strong indication that Drep-2 antagonizes FMRP. It appears that if the animal lacks one of both factors, synaptic plasticity is imbalanced, leading to impaired learning. If, however, flies lacks both Drep-2 and FMRP at the same time, the system is back in balance and the animals can learn. Interestingly, the double mutants also showed a rather normal general courtship activity, unlike *fmr1* single mutants did.

Fmr1-mutant phenotypes are known to be dosage-dependent: the less FMRP the animal has, the more severe are the deficiencies (Bhakar et al., 2012; Kanellopoulos et al., 2012). Hence, we also examined animals still retaining one intact copy of *fmr1*: $drep\text{-}2^{ex13}/drep\text{-}2^{ex13}$; $fmr1^{B55}/+$. Learning ability was, albeit narrowly, not rescued in these animals (Fig. 74A). The observation that heterozygous double mutants behaved in between full double mutants and controls is in agreement with a dosage-dependent effect of FMRP. Furthermore, this experiment supports our hypothesis that the system is only balanced if either both proteins are present or both are completely missing.

While misexpression of the *white* gene causes increased male-male courtship, lack of *white* does not produce a similar phenotype (Anaka et al., 2008). In our experiments, *CantonS* control animals carried the wildtype *white* gene and $drep\text{-}2^{ex13}$ mutants a *mini-white*$^{+}$ gene. The eyes of *drep-2* mutants were not quite as deeply red as the ones of *CantonS* animals, indicating a lower expression level of *white* (Fig. 59A). By contrast, $fmr1^{B55}/fmr1^{\Delta 50M}$ mutants lack the *white* gene completely. While *drep-2* mutants did not show courtship conditioning memory, $drep\text{-}2^{ex13}/drep\text{-}2^{ex13}$; $fmr1^{B55}/fmr1^{\Delta 50M}$ double mutants could learn. These double mutants carry the same *mini-white* gene as *drep-2* mutants and only differ from *drep-2* mutants by a concomitant lack of FMRP. Thus, the presence of White or the strength of *white* expression did likely not influence the outcome of this experiment. Instead, the deficiency of *drep-2* mutants in short-term memory was rescued by elimination of FMRP.

FMRP is a regulator of synaptic protein synthesis and *fmr1* mutants accordingly show deficiencies in long-term memory (LTM) (Banerjee et al., 2010; Bhakar et al., 2012; Bolduc et al., 2008). If Drep-2 interfered with FMRP-mediated synaptic plasticity, LTM of *drep-2* mutants should hence be disturbed. We therefore assayed courtship conditioning LTM formation. Indeed, LTM of *drep-2* mutants was impaired to a similar degree as STM was (Fig. 74B).

Thus, a requirement of Drep-2 for associative learning has been demonstrated in several paradigms. Moreover, we could show that Drep-2 is important not only for short- and intermediate- but also for long-term memory. Mechanistically, Drep-2 likely antagonizes FMRP and promotes mGluR-dependent signalling.

2.2. A brief glance at other Drep family members

Drep-2 is part of a family of related proteins, containing, in addition, Drep-1, -3, and -4. The two pairs Drep-1/-4 and Drep-2/-3, respectively, show sequence homology beyond the characteristic CIDE-N domain (Fig. 39). After discovering Drep-2 as a synaptic protein, we wondered whether the other Drep proteins might also have a non-apoptotic, neuronal function.

2.2.1. Drep-4

Drep-4 is the *Drosophila* homologue of the apoptotic DNase Dff40. The protein is regulated by binding of the inhibitor Drep-1 (Dff45), as well as by activation through caspase-mediated cleavage (Yokoyama et al., 2000). Drep-4 is expressed ubiquitously (Graveley et al., 2011) and its role during apoptosis has been established firmly. Nonetheless, we examined the localization of Drep-4 in the nervous system (Fig. 75).

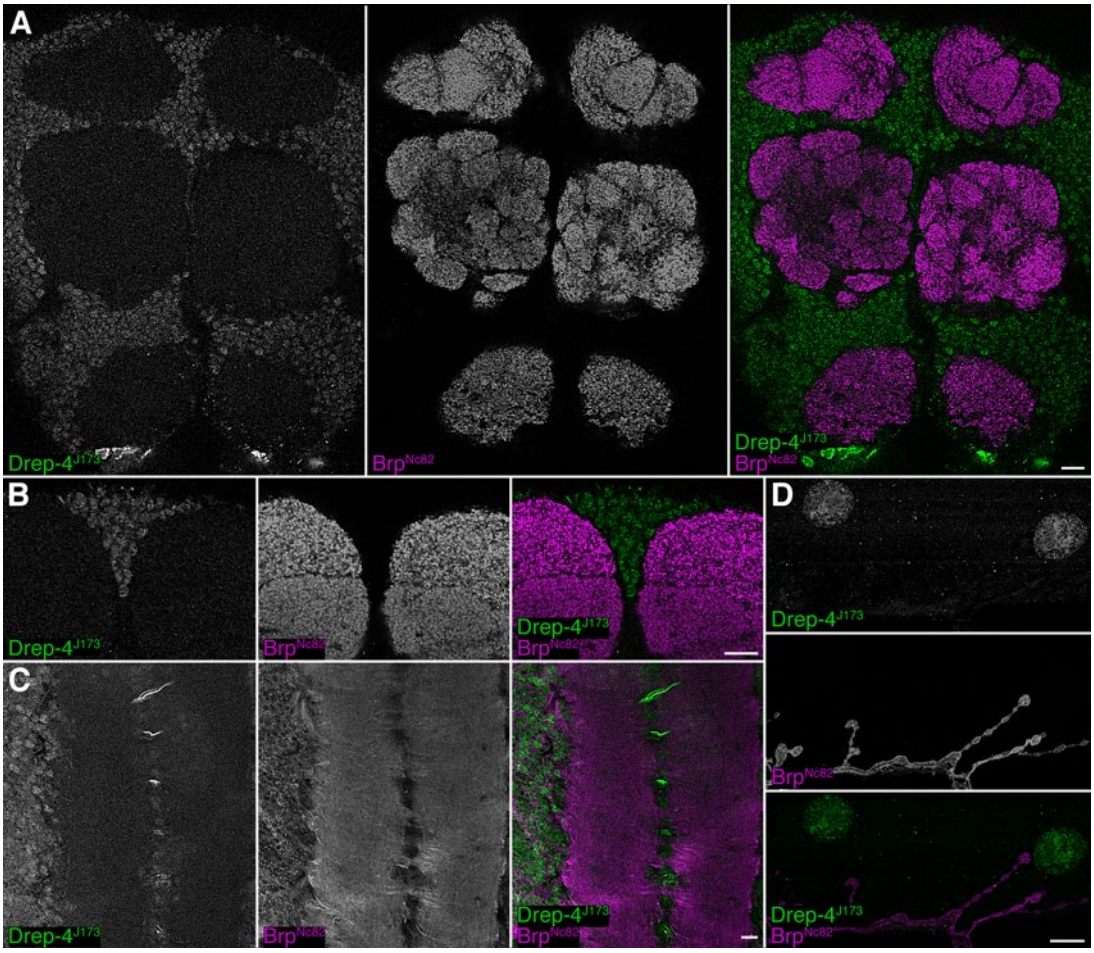

Fig. 75: Expression pattern of Drep-4: no synaptic signal.
Drep-4^{J173} was detected in cell bodies. All Scale bars: 10 µm.
A-B: Frontal confocal sections of Drep-4^{J173} and Brp^{Nc82} antibody stainings in adult w^{1118} brains. This label is especially prominent at the pars intercerebralis (B).
C-D: Drep-4^{J173} and Hrp antibody stainings in w^{1118} stage 3 larvae.
C: Ventral ganglion of the larval brain.
D: Larval neuromuscular junction with an adjacent muscle fibre.

Rui Tian had, in her thesis, reported a potential synaptic staining of the anti-Drep-4 antibody in the peripheral and central nervous system (Tian, 2011). However, this finding could not be confirmed. By contrast, Drep-4 expression appeared to be restricted to cell bodies at larval NMJs (Fig. 75D), in the larval ventral ganglion (Fig. 75C), and in the adult CNS (Fig. 75A,B). While this does not exclude a non-apoptotic function of Drep-4 in neurons, it at least renders a direct contribution of Drep-4 to the synaptic function of Drep-2 unlikely.

2.2.2. Drep-1

Drep-1, the homologue of Dff45, is the caspase-controlled inhibitor of Drep-4 (Mukae et al., 2000). We did not have an anti-Drep-1 antibody available but a *drep-1* mutant (*p(dICAD)*, Mukae et al., 2000). Drep-2 stainings in *drep-1* mutants appeared unaltered (*not shown*). We raised antibodies in rabbit, directed against a central part of Drep-1 (peptide sequence: GRPLCAKRNAEDRLN). The antibody labelled cell bodies in adult wildtypes (Fig. 75A,B). However, this staining was not clearly specific: labelled cell bodies could be observed also in *drep-1* mutants, although the signal was slightly weaker here (Fig. 75C). The anti-Drep-1 staining looked very similar to the anti-Drep-4 staining, including the strong label of cell bodies at the pars intercerebralis (Fig. 76B, Fig. 75B). *Drep-1* mutants were also tested for ethanol sensitivity but had normal sedation times (*not shown*). Therefore, we could not find indications for a non-apoptotic function of Drep-1.

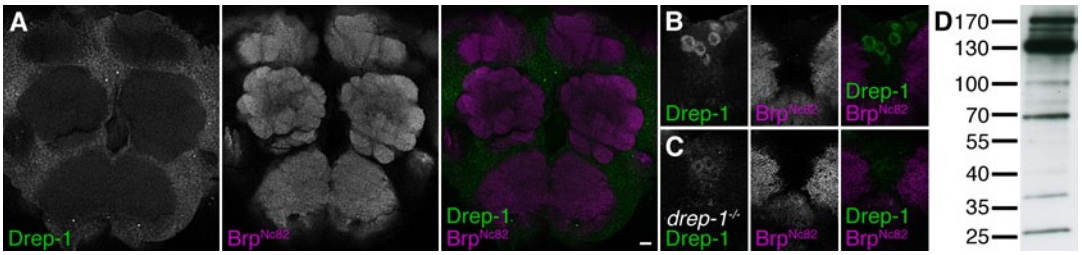

Fig. 76: Staining pattern of the anti-Drep-1 antibody: no synaptic signal.
A-C: Frontal confocal sections of anti-Drep-1^{Pep} and Brp^{Nc82} antibody stainings in adult brains. Scale bars: 10 µm. **A-B:** *W^{1118}* brains. The cell body staining is especially prominent in few cells of the pars intercerebralis (B). **C:** *Drep-1$^{-/-}$* brains. A cell body staining is still present in the mutant.
D: Western blot of Drep-1^{Pep} on *w^{1118}* head extraxt. Drep-1 is predicted to run at 32 and 33 kDa.

2.2.3. Drep-3, a putative interactor of Drep-2

Drep-3 is an unusual family member because it is the only Dff-related protein where the CIDE-N domain resides in the C-terminal half of the protein (Park et al., 2006). Drep-3 binds to Drep-2 (Inohara and Nuñez, 1999; Park and Park, 2012). *Drep-3* transcripts are, like *drep-2* mRNA, highly enriched in the nervous system (Graveley et al., 2011).

In order to study Drep-3, we produced anti-Drep-3 antibodies, directed against either the N-terminal peptide AAGVQCDPDSRIVAPP or the C-terminal peptide YSARSDAARLSTELSC. After comparing the stainings to signals raised by the preimmune serum, we concentrated on the N-terminal antibody; the C-terminal an-

tibody staining did not appear different from the label produced by the respective pre-immune serum. The Drep-3$^{N\text{-}Term}$ antibody produced a staining of both neuropils and cell bodies (Fig. 77), in wildtypes as well as in *drep-2*^{ex13} mutants (*not shown*). Of note, cell bodies in the pars intercerebralis were, once again, strongly labelled.

We could not confirm the specificity of the antibody without a *drep-3* mutant. No p-element insertions exist in the direct vicinity of the genetic locus of *drep-3*, possibly due to the proximity of *rpIII128*, a gene coding for an RNA polymerase. We therefore attempted to produce a *drep-3* mutant with an ends-out homologous recombination knockout approach (Huang et al., 2009; 2008). Unfortunately, we were not able to raise candidate flies in which recombination had occurred at both arms[30]. This indicates that recombination frequencies are very low at the *drep-3* locus. In fact, *drep-3* is predicted to locate within transcriptionally silent heterochromatin (Graveley et al., 2011).

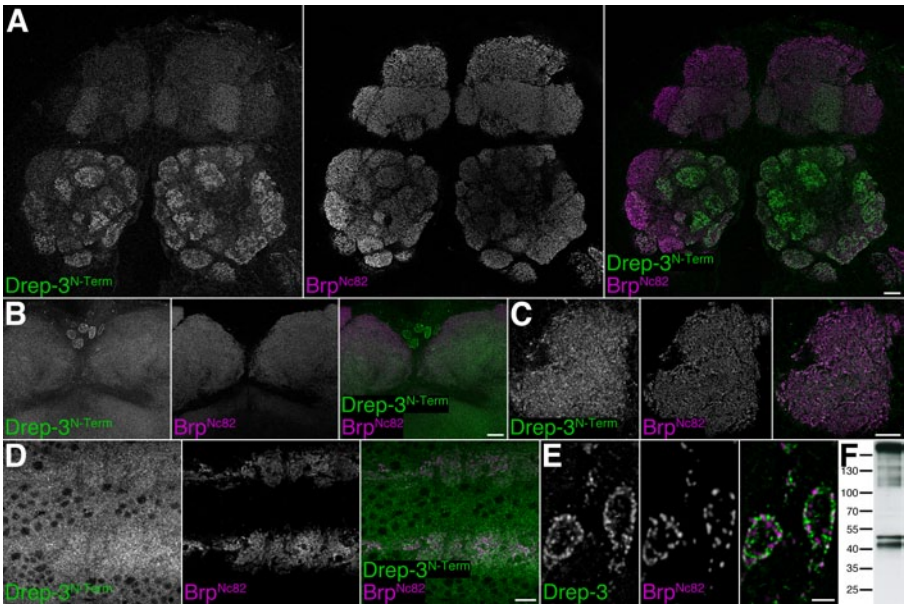

Fig. 77: Staining pattern of the anti-Drep-3$^{N\text{-}Term}$ antibody.
A-C: Frontal confocal sections of anti-Drep-3$^{N\text{-}Term}$ and Brp^{Nc82} antibody stainings in adult brains. Scale bars: 10 µm. **A:** Section showing AL and MB lobe neuropil label, as well as a weak cell body staining. **B:** Maximum intensity projection showing cell body staining at the pars intercerebralis. **C:** Section showing the MB calyx.
D: The larval ventral ganglion; cell bodies are strongly stained. Scale bar: 10 µm.
E: Synaptic boutons at an NMJ; Drep-3$^{N\text{-}Term}$ labels the membrane. Scale bar: 2 µm.
F: Western Blot of Drep-3$^{N\text{-}Term}$ on *w*^{1118} head extract. Drep-3 is predicted to run at 29 kDa. Highest size indicator: 170 kDa.

[30] Ulises Rey and several other supporters did a large share of the fly work for the homologous recombination, i.e. set up crosses and collected candidates, and also tested part of the candidates by PCR and western blots.

2.2.3.1. The localization of Drep-3^{GFP} is highly similar to Drep-2

We were successful in generating flies expressing Drep-3^{GFP} under the endogenous genomic promoter of *drep-3*. To this end, we created *drep-3^{GFP}* P[acman] constructs by recombineering[31]. These flies showed a GFP localization pattern that was remarkably similar to the label produced by the Drep-2$^{C\text{-}Term}$ antibody (Fig. 78). Drep-3^{GFP} also marked cell bodies, but the neuropil label differed from the Drep-3$^{N\text{-}Term}$ staining. Without availability of a *drep-3* mutant, we consider the Drep-3^{GFP} signal as more reliable than the antibody.

Furthermore, we generated flies expressing UAS-Drep-3^{GFP} constructs. We could not observe axonal trafficking of this fusion protein (*not shown*), as was the case for Drep-2 (Fig. 43). Involvement in fast axonal transport could thus constitute a function of Drep-2 that is clearly independent of Drep-3.

In conclusion, Drep-3 appears to be, like Drep-2, a synaptic protein. By contrast, Drep-1 and -4 are ubiquitously expressed and appear to locate to cell bodies. It will therefore likely be rewarding to study the synaptic role of Drep-3 in detail.

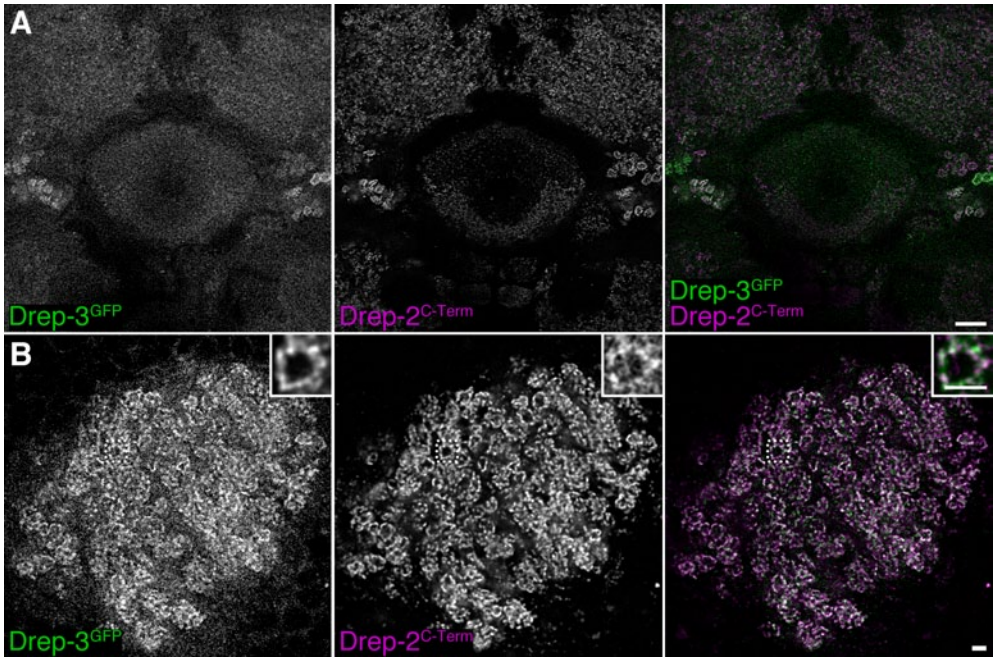

Fig. 78: The Drep-3^{GFP} label is highly similar to an anti-Drep-2$^{C\text{-}Term}$ staining.
Frontal confocal sections showing genomic P[acman] *drep-3^{GFP}* signal as well as Drep-2$^{C\text{-}Term}$ antibody staining in adult brains. Drep-3^{GFP} label was enhanced by anti-GFP antibodies.
A: Frontal section showing the ellipsoid body and the lateral triangle, where ring cell synapses are strongly stained. However, some ring cells show either a stronger Drep-2 or a stronger Drep-3 label. Scale bar: 10 µm.
B: Section showing the MB calyx. The overlap between both signals is remarkable. The inset displays a single microglomerulus. Scale bars: 2 µm.

[31] Tanja Matkovic did the recombineering.

2.2.3.2. Putative cleavage of Drep-3 by caspases

The Drep-3 protein shares sequence similarity with Drep-1 (Fig. 39). Moreover, the genes *drep-1* and *drep-3* locate within 5 kbp of each other (McQuilton et al., 2012). Drep-3 can bind Drep-2 and both proteins colocalize at synapses (Fig. 78). Drep-3 is predicted to be cleaved by caspases (Fig. 79; Park and Park, 2012). It is thus an intriguing idea that Drep-3 might regulate Drep-2, in a similar fashion as Drep-1 inhibits Drep-4. Caspase-mediated cleavage would then be the trigger for Drep-2 activity.

We were not able yet to confirm caspase cleavage experimentally *in vitro*, neither for Drep-2 nor for Drep-3[32]. Nevertheless, cleavage of Drep-3 by *Drosophila* caspases might still take place *in vivo*, with further *in vivo* experiments being necessary to settle this open question. A possible experiment would here be the overexpression of *drep-3* constructs containing mutated putative caspase cleavage sites. It is feasible that such an overexpressed protein would execute a dominant-negative effect over endogenous Drep-3, when binding to Drep-2. Activation of Drep-2 could thus be prevented, resulting in phenotypes comparable to a *drep-2*-mutant situation.

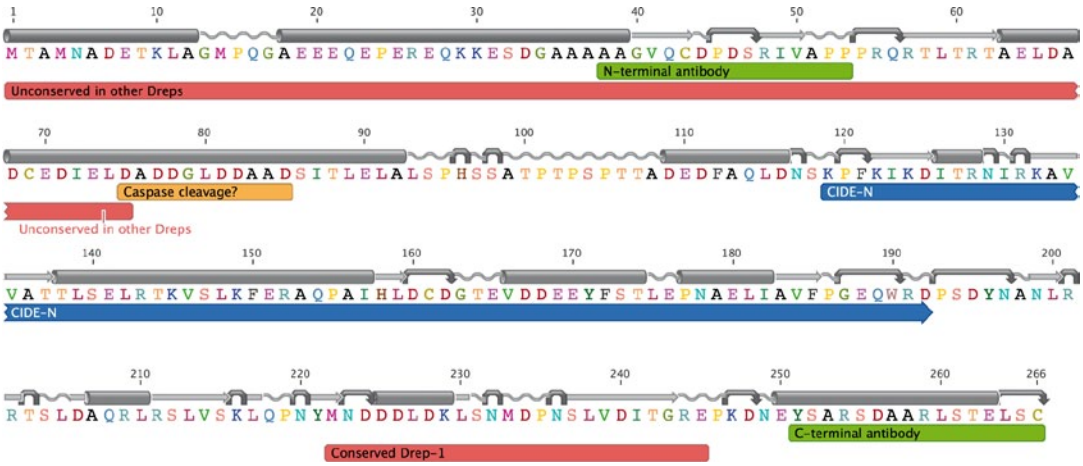

Fig. 79: Drep-3-PA protein sequence: Drep-2 likely is cleaved by caspases.
Above the sequence an EMBOSS garnier structure prediction is displayed. The CIDE-N domain is shown in blue, other regions especially conserved or unconserved in red. The peptides used for antibody generation are indicated in green. A stretch of four strongly predicted caspase cleavage sites (DADD, DGLD, GLDD, DAAD) is shown in orange. The algorithms CASVM, Cascleave, and SitePrediction were used for prediction of cleavage sites (Song et al., 2010; Verspurten et al., 2009; Wee et al., 2006; 2007).

[32] Sabrina Büttner, in Frank Madeo's lab at the University of Graz, as well as Jennifer Lardong, in the lab of Markus Wahl at the FU Berlin, both tried to demonstrate caspase cleavage of Drep-2 and Drep-3, but their efforts unfortunately were of no avail. Their approaches are briefly outlined in Materials and Methods, section 5.2.3, page 50.

Discussion

Kannst du wissen ob von deinem Hauche
Nicht Atome sind am Rosenstrauche?
Ob die Wonnen die dahingezogen,
Nicht als Röslein wieder angeflogen?
ob dein einstig Kindesatemholen
Dich nicht grüßt im Duft der Nachtviolen?

Christian Wagner, Ein Blumenstrauß

1. Characterization of synaptic diversity using ratiometric analyses

ON EXAMINATION OF EXPRESSION LEVELS of presynaptic active zone (AZ) proteins in *D. melanogaster*, marked differences could be observed throughout the adult brain. In stainings using antibodies against such proteins, heterogeneous patterns became visible: subregions within neuropils appeared to show low or high signal intensities for selected antibodies (Fig. 12-Fig. 14, Table 1). These differences did not reflect properties of the antibodies but truly visualized the abundance of protein (Fig. 15). The heterogeneously stained subregions are therefore distinguished by distinct ratios between the amounts of synaptic proteins. Hence, we have developed a method for the quantification of pixel-by-pixel ratios of antibody signal intensities. This approach enabled us to assess whether, at any given position within an image stack, one of the examined proteins was enriched over the others (Fig. 21, Fig. 27).

By labelling synapses with cell-specific driver lines, we were able to assign average pixel ratios to known synapse populations. We could thus identify ratio signatures characteristic for synapse types in the mushroom body (MB) calyx (Fig. 23-Fig. 26, Table 2) as well as in the antennal lobe (AL) (Fig. 28-Fig. 32, Table 3), two relays in the olfactory pathway.

Moreover, we have employed the ratiometric method for the analysis of aberrant situations: We used RNA interference to knock down the presynaptic protein Bruchpilot (Brp) in MB-intrinsic Kenyon cells (KCs). Ratio-based quantification was in agreement with the published results regarding the share of KC presynapses in the MB calyx (Fig. 33). In a more complex challenge, we assessed the change of ratios in *shakB*^{2} mutants, which lack, in addition to gap junctions, several types of chemical synapses in the AL (Fig. 34). Finally, we ablated olfactory receptor neurons by removing antennae of adult flies and examined the subsequent effects on ratio distributions in ALs and calyces (Fig. 35, Fig. 37).

1.1. Advantages of the ratiometric method

1.1.1. Comparison to an analysis of absolute intensity values

Protein cytomatrices at the AZ (CAZs) are characterized by electron-dense specializations that vary in their shape and size among animals as well as between synapse types (Deguchi-Tawarada et al., 2006; Rollenhagen et al., 2007; Südhof, 2012; Zhai and Bellen, 2004). In sensory organs, this specialization has the shape of a large ribbon (Deguchi-Tawarada et al., 2006; Meyer et al., 2009); hippocampal mossy fibre boutons, by contrast, feature only small electron-dense patches (Rollenhagen et al., 2007; Südhof, 2012).

In *Drosophila*, these structures typically have the shape of T-bars (Wichmann and Sigrist, 2010). Both Brp and RBP, proteins examined in the ratiometric analysis, are essential for the formation of proper T-bars (Kittel et al., 2006; Liu et al., 2011). The amount of Brp at synapses influences the size of T-bars and, in consequence, the amount of neurotransmitter vesicles released (i.e. quantal content); eventually, this

regulates the strength of the synapse (Matkovic et al., 2013; Peled and Isacoff, 2011; Wagh et al., 2006; Wichmann and Sigrist, 2010). Therefore, one might argue that an analysis of the signal intensity of Brp stainings should provide sufficient information regarding the strength of synapses.

However, the variegated distribution that we observed for the CAZ proteins RBP and Syd-1 would be uncalled-for, if Brp was the single decisive factor for the properties of presynapses. By contrast, there is ample evidence for the major relevance of other CAZ proteins (Kaeser et al., 2009; Liu et al., 2011; Sigrist and Schmitz, 2011; Südhof, 2012). By quantifying several of these proteins at the same time, a significant amount of information is gained, compared to examining proteins individually. We are therefore convinced that ratios of several antibodies are better suited for the characterization of synapse identities than absolute intensities of individual proteins.

We have demonstrated that the relative intensities of antibody stainings vary within neuropils. Furthermore, we have encountered situations, in which the median ratio was close to 1, even though the respective ratio distribution was characterized by two peaks for high and low ratio values (for example: Fig. 27). This information would likely be missed if ratios were calculated from the intensities averaged over the complete neuropil. Therefore, the calculation of ratios, locally for every pixel within an image, has distinct advantages.

Importantly, absolute intensities recorded from antibody stainings vary: They decrease when penetrating deeper into tissue samples and differ between specimens, microscopy slides and staining batches. Furthermore, protein amounts vary according to the circadian rhythm (Gilestro et al., 2009) and with the age of animals (Juranek et al., 2013). The amount of CAZ proteins can even change within minutes (Matz et al., 2010). Fortunately, most of these variations should affect all proteins we examined to a similar degree. Thus, while a staining of two antibodies might show a lower overall signal intensity in specimen A than in specimen B, the relative difference between the signal intensities of the antibodies is likely similar in both animals. Moreover, typically not absolute ratio values but relative differences between ratios were considered in this study. This added an additional buffer for staining variability.

It was recently shown in mammalian cell culture that even pre- and postsynaptic proteins, though varying considerably in their absolute amounts, kept a constant stoichiometry (ratio) over time at certain synapses (Fisher-Lavie and Ziv, 2013). Interestingly, this ratio appeared to be specific for synapse types. Therefore, the ratiometric method should be more robust than a quantification of absolute intensities. Accordingly, the ratiometric analyses of *shakB*^{2} mutants and of animals lacking antennae found significant differences, where a quantification of absolute intensities did not (Fig. 36). However, depending on the question, quantification of intensities can yield additional information that helps interpreting results from the ratiometric analysis.

1.1.2. Analysis of image stacks

We have chosen to compute ratios for every pixel within image stacks. The recording of image stacks covering complete neuropils requires considerable more time and space than scanning single image planes. Moreover, the computation of a stack-based

analysis is more complex and time-consuming. However, stacks have two advantages over single image planes: First of all, the composition of synapse types within a neuropil varies in three dimensions and a structure like the MB calyx features relatively few landmarks. Therefore, one would likely record slightly different single image planes in different animals. This would, self-evidently, increase the variance of a data set considerably. By recording the complete neuropil, the variability concerning which synapses are included in the analysis is virtually eliminated.

In addition, more pixels imply more data points and, in consequence, ensure a more reliable estimate of average ratios. A masked single image plane typically contained about 300,000 pixels. By contrast, each median ratio value was calculated from 8.4 million pixels on average, when including the complete calyx. A typical mask for an entire AL contained even almost twice as many pixels, about 15 million. Statistics calculated from 15 million values are obviously more dependable than an estimate from only 1/50th this amount of data. Accordingly, median ratios of ALs should be more reliable and show a lower variability than the ones of calyces. In fact, differences between more ratios were significant in the AL than in the calyx (Table 2, Table 3).

1.2. Towards a molecular atlas of synapse types

We believe that we have laid the foundation for a systematic characterization of synaptic diversity in the *Drosophila* brain by our analysis of CAZ protein ratios at synapses of different cell types. To support this claim, we will now examine whether the ratiometric approach is really sufficient for the classification of synapse types.

In order to simplify the amount of information we collected, a three-colour signature fingerprint can be assigned to every situation we examined (Fig. 8o)[33]. For example, green-green-magenta (Fig. 8oB, LN1-Gal4 in the AL) signifies that, at LN1-positive presynapses, the ratios RBP / $Brp^{C\text{-}Term}$ and Syd-1 / $Brp^{C\text{-}Term}$ were elevated, while $Brp^{N\text{-}Term}$ / $Brp^{C\text{-}Term}$ was decreased, relative to all synapses in the AL. All Gal4 drivers examined in the AL (Fig. 8oA-D) as well as in the MB calyx (Fig. 26A) produced distinguishable fingerprints. However, in the case of krasavietz- and mz19-Gal4 in the AL, the differences were only marginal (Fig. 8oC,D).

1.2.1. Mixed synapse populations

A likely reason for the merely subtle differences between krasavietz- and mz19-Gal4 is that both lines include a mixed population of synapses. Krasavietz-Gal4 drives expression in both excitatory and inhibitory local interneurons (LNs) (Acebes et al., 2011; Chou et al., 2010; Huang et al., 2010; Seki et al., 2010; Shang et al., 2007; Yaksi and Wilson, 2010). Moreover, more than two subtypes of LNs exist and the aforementioned reports give very different estimates of the shares of excitatory or inhibitory LNs included in the expression pattern of the line.

The expression pattern of mz19-Gal4 in the AL is limited to projection neurons (PNs). However, PNs form three different kinds of chemical (pre-)synapses in the AL: synapses with other PNs, with excitatory LNs (eLNs), and with inhibitory LNs (iLNs)

[33] For details regarding the generation of fingerprints see page 43.

(Yaksi and Wilson, 2010). For example reciprocal PN-PN synapses might well differ in their configuration from the other two types of PN presynapses. Accordingly, both the median ratios observed for krasavietz- and mz19-gal4 actually constitute a mixed signal, comprising ratios of the different synapse populations included in the respective Gal4 lines.

It is interesting to see that the CAZ protein composition of mz19-Gal4-positive synapses differs between the calyx and the AL (Fig. 23, Fig. 31). This supports our assumption that the signature of AZs is rather specific for synapse types than for neuron types.

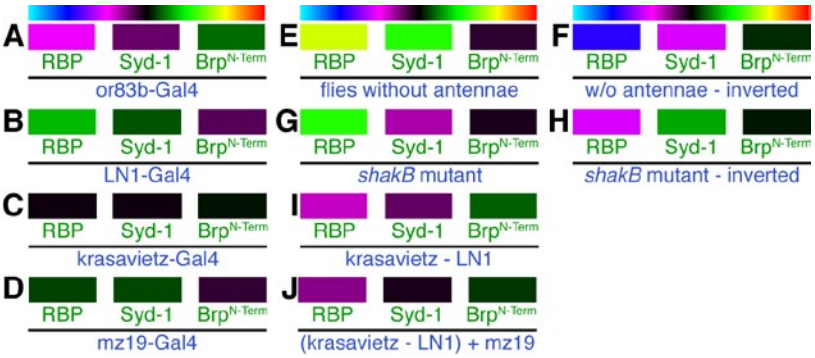

Fig. 80: Colour fingerprints of ratios in the AL.
A-D: Signature fingerprints of Gal4 lines.
E-F: Fingerprints of flies without antennae.
G-H: Fingerprints of the *shakB²* mutant.
F,H: Inverted colour fingerprints: signatures of the synapses missing in the respective situations.
I: The putative fingerprint of excitatory LNs was generated by subtracting B (LN1) from C (krasavietz).
J: The putative fingerprint of all synapses missing in *shakB²* flies was created by adding I (eLNs) to D (mz19).

1.2.1.1. Analysis of the *shakB²* mutant

A similar issue emerged during the analysis of ALs in *shakB²* mutants. In these flies, chemical synapses between eLNs and iLNs as well as reciprocal chemical synapses between PNs are abolished, in addition to gap junctions between several neurons (Yaksi and Wilson, 2010). The RBP / Brp$^{C\text{-}Term}$ ratio of these mutants was significantly increased, compared to wildtype controls (Fig. 34, Fig. 80G). Thus, synapses rich in RBP remained functional in the mutant, rendering the synapses that are abolished likely to be poor in RBP (Fig. 80H). We have shown that PN presynapses are, on average, slightly enriched for RBP (Fig. 31, Fig. 80D). Since PNs feature three kinds of presynapse types in the AL, one of them could differ from the others and be poor in RBP.

However, it is also possible that eLNs form AZs with a low RBP / Brp$^{C\text{-}Term}$ ratio. We could not examine a pure population of eLNs but instead studied krasavietz-Gal4, which also drives expression in iLNs. The latter driver labelled synapses that were, on average, not enriched for RBP (Fig. 30, Fig. 80C). Yet we did calculate ratios for iLNs, which showed a high RBP / Brp$^{C\text{-}Term}$ ratio (Fig. 29, Fig. 80B). Therefore, the excitatory population in krasavietz-Gal4 is likely poor in RBP, so that, together with the inhibitory LNs, the average krasavietz-Gal4 synapse shows a balanced RBP / Brp$^{C\text{-}Term}$ ratio (Fig. 80I).

S*hakB²* mutants have lost two kinds of chemical synapses, involving eLNs and PNs. One or both of these synapse types has to have a very low RBP / Brp$^{C\text{-}Term}$ ratio. In fact, the putative fingerprint of a combined population of both PNs and eLNs looks

much more similar to the synapse population missing in *shakB*^{2} mutants than any other signature (Fig. 80H,J).

1.2.1.2. Analysis of flies lacking antennae

Removal of antennae is a simple way to ablate olfactory receptor neurons (ORNs). In this situation, we observed a clear picture (Fig. 35): the inverted fingerprint of flies without antennae corresponded very well to the or83b-Gal4 signature (Fig. 80A,F). In this experiment, we have removed exactly the same synapse populations that we had previously analysed (or83b), hence the good match. It did thus not matter that ORNs have two different postsynaptic partners, PNs and iLNs (Yaksi and Wilson, 2010).

Accordingly, the ratiometric method is well suited to assess any situation that has been categorized previously, even in case of mixed populations. In consequence, it appears that quantification of a complete set of synapse types in a neuropil is necessary to render the method universally applicable.

1.2.2. Current level of coverage of synapse types

As explained in the previous paragraphs, several known synapse types in the AL could not yet be examined unambiguously. Here, additional Gal4 lines and, potentially, application of the split-Gal4 system would be necessary for improved coverage (Luan et al., 2006; Pfeiffer et al., 2010).

Moreover, we did not yet look at all different synapse types occurring in the MB calyx. For example, we did not consider terminals releasing biogenic amines (Busch et al., 2009; Mao and Davis, 2009; Pech et al., 2013). The ratio RBP / Brp$^{C\text{-}Term}$ was elevated at both KC and PN presynapses (Fig. 23, Fig. 24). By contrast, the same ratio computed over the complete calyx was either balanced or leaning towards Brp$^{C\text{-}Term}$ (Fig. 21). Thus, one or more additional synapse populations should exist in the calyx that feature a low RBP / Brp$^{C\text{-}Term}$ ratio. However, these synapses remain to be identified.

With a more complete coverage of synapse types, a comprehensive molecular atlas of synapses could be assembled. The variety of available cell-type-specific Gal4 driver lines should be sufficient for coverage of all neuron types (Chiang et al., 2011; Jenett et al., 2012). However, in order to assess and distinguish all kinds of synapses, it might be necessary to include additional CAZ proteins, for example UNC-13/Munc13 (Fisher-Lavie and Ziv, 2013; Südhof, 2012).

1.3. Applications of the method

Several possible applications of the ratiometric method exist. For one, the quantification of changes in protein expression at synapses in the central brain is complicated and often requires commercial software (Christiansen et al., 2011; Kremer et al., 2010). The tools developed for the ratiometric quantification can be used for the analysis of antibody intensities in any mutant. In such a case, calculation of ratios with an independent second channel allows for normalization of the data. This decreases variances in staining intensities or in imaging conditions. Application of the ratiometric method is straightforward and easy for the user, once the neuropil of

interest has been segmented. Utilization of automatic, trainable segmentation, implemented for example in the WEKA segmentation algorithm, could further simplify the calculation of ratios (Holmes et al., 2009; Schindelin et al., 2012).

A much larger array of applications emerges once all synapse types in a neuropil are classified. Ratio signatures could constitute a shortcut for the identification of synapses, in the absence of additional anatomic cues. With the help of conditional probabilities, it could be estimated which synapse type likely corresponds to every pixel in an image.

If we understood the function of each examined CAZ protein, it might even be possible to derive some crude physiological characteristics of a synapse type from ratiometric data. Synaptic short-term plasticity is typically mediated by presynaptic mechanisms (Zucker and Regehr, 2002)[34]. Synaptic enhancement, for example, can be caused by elevated presynaptic Ca^{2+} levels, which facilitates the release of neurotransmitters. Depletion of the pool of readily-releasable vesicles, by contrast, causes short-term depression. Thus, CAZ proteins are major factors regulating synaptic short-term plasticity.

It has recently been shown that the amount of Brp at an AZ influences the number of readily-releasable synaptic vesicles (Matkovic et al., 2013). In addition, the C-terminus of Brp tethers a reservoir of synaptic vesicles that can be quickly mobilized to the membrane upon stimulation of sustained neurotransmitter release (Hallermann et al., 2010). The N-terminus of Brp clusters Ca^{2+} channels at the AZ (Kittel et al., 2006). Hence, AZs containing more Brp can release more neurotransmitter per action potential and can support high rates of release over longer periods of time. RBP is, as Brp, an integral component of electron dense T-bars and is important for the recruitment of Ca^{2+} channels to the AZ (Kaeser et al., 2011; Liu et al., 2011). *Drosophila* Syd-1 mediates appropriate localization of Brp to AZs and murine Syd1A has an impact on the number of vesicles docked at AZs (Owald et al., 2010; Wentzel et al., 2013).

Thus, all of the examined presynaptic proteins regulate the localization of Ca^{2+} channels and/or of synaptic vesicles. On the one hand, Syd-1, unlike both Brp and RBP, appears to have a more limited influence on short-term plasticity. On the other hand, Syd-1 does influence localization of Brp and thus, indirectly, also the effects mediated by Brp. Nevertheless, different functions of these presynaptic proteins are beginning to emerge. It is possible that, in the future, limited deductions regarding the basic characteristics of a synapse could be drawn from an analysis of ratiometric CAZ protein data. In such a case, ratiometric images could serve as a rough synaptic road map, of help when trying to get a first idea regarding synapses that should be studied further. But, so far, such an application is still a long way off.

[34] A more detailed description of short-term plasticity and the functions of presynaptic proteins can be found in the introduction, sections 2.1 (page 17) and 1.1 (pp. 12-14), respectively.

1.3.1. The rational approach towards a meaningful connectome

Currently, huge efforts are undertaken to generate the connectome of higher animals, an atlas of all neuronal connections and, eventually, of all synapses in the brain (Alivisatos et al., 2012; Sporns, 2013; Van Essen et al., 2012). Due to a lack of resolution in standard light microscopy, electron microscopy (EM) so far is the method of choice for its generation (Anderson et al., 2011; Briggman and Denk, 2006; Cardona et al., 2010; Kleinfeld et al., 2011; Morgan and Lichtman, 2013).

Although the EM-based, anatomical connectome of *C. elegans* has been deciphered 27 years ago (White et al., 1986), the implications of this achievement have been limited. It can be argued that the nematode's highly specialized nervous system is inherently more difficult to analyse than more redundant networks in higher animals (Morgan and Lichtman, 2013). The enormous complexity and specialization of neurons in the nervous system of worms probably contributes to the difficulties researchers still face in understanding it. Nevertheless, another likely reason for the limited usability of this connectome is that the value of anatomical knowledge without functional data is strongly limited.

Thus, already early proposals for a human connectome have stressed the importance of combining non-invasive mapping techniques with functional imaging (Sporns et al., 2005). Currently, several initiatives focus strongly on mapping brain activity or combine tracking of neurons by EM with functional experiments (Alivisatos et al., 2012; Assaf et al., 2013; Briggman et al., 2011; Hutchison et al., 2013; Van Essen et al., 2012). However, the usability of functional data without molecular information is restricted as well – it is clearly required to link the connectome to the proteome (Arenkiel and Ehlers, 2009; Grant, 2007; Morgan and Lichtman, 2013; O'Rourke et al., 2012)

The analyses of neuronal connectivity and of the molecular composition of synapses are still two separate fields of research. Yet knowledge about molecular differences of synapse populations, for example regarding the abundance of proteins known to mediate short-term plasticity, will be highly relevant for understanding computation within circuits. While a lot of effort is put into the decryption of neuronal circuits, much less work is done regarding a systematic assessment of the molecular configuration of synapse types. Here, the ratiometric method opens a path for the reconciliation of both fields. Of note, evidence for the existence of molecularly diverse synapse identities has also been provided for mammals (O'Rourke et al., 2012; Fisher-Lavie and Ziv, 2013).

Recently, there have been significant advances in the ability to use light microscopy in connectomics (Cai et al., 2013; Osten and Margrie, 2013). Here, one method is particularly interesting: the use of array tomography in combination with ultra-thin slices that can be imaged both by EM and light-based immunohistochemistry (Micheva and Smith, 2007; Micheva et al., 2010; Oberti et al., 2011). In this method, the axial resolution is restricted only by the thickness of sections and the vertical resolution can be optimized by employing high-resolution STED microscopy (O'Rourke et al., 2012). This establishes the possibility to truly unite anatomic with molecular data: if each synapse identified by EM can be labelled with antibodies, the ratiometric meth-

od could be used to determine the respective synapse type. Ratio fingerprints could thus pose a shortcut for the enhancement of anatomical connectomes with molecular information, in neuropils where cell type diversity is not exceedingly high.

On the long run, classification of the synaptic proteome would profit from the establishment of the transcriptome of individual neurons (Grant, 2007). Albeit an intricate task, the single-neuron transcriptome will eventually be indispensable, if only for the unambiguous definition of neuron types. Efforts in this direction are clearly underway (Belgard et al., 2011; Hawrylycz et al., 2012; Lein et al., 2007).

Another application, related to connectomics, could be the use of ratios as a checksum when tracing and reconstructing neurons through image stacks (O'Rourke et al., 2012). If one had determined ratios for both pre- and postsynaptic proteins, the fingerprints could be used to estimate the likelihood of having ended the reconstruction in the same neuron type as one started it in. Image segmentation errors during automatic reconstruction of EM data do occur and can have fatal consequences (O'Rourke et al., 2012). Ratio-based checksums could here serve as a safety net.

So far, we have only begun to establish a catalogue of synaptic diversity using presynaptic proteins. Eventually, a complementary atlas for the postsynapse could be useful as well. However, in *Drosophila*, there is a deplorable lack of universal postsynaptic markers (thus: Nicolaï et al., 2010). In mammals, by contrast, PSD-95 serves as a generic postsynaptic marker that could be used as a reference for the calculation of ratios (Fisher-Lavie and Ziv, 2013), similar to Brp at presynapses of flies.

First studies assessing the postsynaptic proteome of distinct neuron types indicate clear differences between synapse populations (Cheng et al., 2006; Selimi et al., 2009). A challenge will here be to identify postsynaptic proteins that stay constant over time and during plasticity processes. The amounts of non-NMDA glutamate receptors, for example, are flexible (Ashby and Isaac, 2011; Busetto et al., 2008; Schmid et al., 2008). If Drep-2 turns out to be postsynaptic not only in Kenyon cells, this protein has potential for being employed as a postsynaptic label in *Drosophila*.

2. The role of Drep-2 at synapses

In an attempt to identify additional synaptic proteins, we precipitated protein complexes from adult fly head extracts, using antibodies against Brp. To our surprise, we repeatedly identified the protein Drep-2 in such precipitates (Depner, 2013; Owald et al., 2010; Schmidt, 2006; Tian, 2011). Drep-2, related to the DNA fragmentation factor (Dff) 40, has been suggested to be a regulator of apoptosis (Inohara and Nuñez, 1999; Park and Park, 2012; Tan et al., 2012). Of note, a role of other Dff/Drep family members in mediation and regulation of apoptosis has been established firmly (Mukae et al., 2000; Wu et al., 2008; Yokoyama et al., 2000).

We, however, showed that Drep-2 is in fact a neuronal protein, enriched at synaptic membranes (Fig. 38B, Fig. 48, Fig. 52). Since we could not identify a major role of Drep-2 in the peripheral nervous system (Fig. 41-Fig. 45), we examined the function of Drep-2 in the central brain (CNS). Drep-2 is present at most synapses in the adult CNS (Fig. 46-Fig. 48). Interestingly, we found that Drep-2 clustered at postsynaptic

densities (PSDs) of Kenyon cells in the MB calyx (Fig. 49-Fig. 54). Here, as well as at other synapses, Drep-2 consistently colocalized with the metabotropic glutamate receptor (mGluR) DmGluRA as well as with the protein Homer, associated to mGluRs (Fig. 57C).

Drep-2 mutants did not exhibit an obvious misregulation of apoptosis but the animals lived shorter than controls (Fig. 61, Fig. 59). Basic synaptic transmission was unaltered at peripheral and central synapses (Fig. 42, Fig. 62). During behavioural analyses, we discovered that olfactory learning was impaired in *drep-2* mutants (Fig. 63, Fig. 64). The learning performance of mutants could be restored to normal levels by re-expression of *drep-2* cDNA in KCs or by pharmacological stimulation of mGluRs (Fig. 63-Fig. 65). Moreover, *drep-2* mutants were also defective in courtship conditioning STM and long-term memory (LTM) (Fig. 74). In addition, they were found to be ethanol hypersensitive as well as hyperactive in locomotion (Fig. 68, Fig. 70). When investigating possible causes of these phenotypes, we observed that evoked calcium transients were reduced in KCs of *drep-2* mutants (Fig. 66).

In biochemical experiments, Drep-2 was enriched in complexes with RNA-associated proteins, for example the fragile X mental retardation protein FMRP (Table 7, Fig. 72, Fig. 73). In fact, *drep-2* and *fmr1* mutants showed similar phenotypes in several behavioural paradigms. We confirmed that both mutants were impaired in courtship conditioning short-term memory (Fig. 74A). This deficiency was rescued in *drep-2*; *fmr1* double mutants. Thus, Drep-2 appears to antagonize FMRP.
Finally, a brief investigation of other Drep proteins revealed that Drep-3 is present at synapses as well (Fig. 78).

2.1. What is the function of Drep-2 in Kenyon cells?

We and others have demonstrated a role of mGluRs in aversive olfactory learning (Fig. 65; Kanellopoulos et al., 2012). However, it has not been examined yet, in which manner mGluRs influence olfactory conditioning. Moreover, the MB calyx, at which Drep-2 is enriched (Fig. 49), is not regarded as the most relevant site for the formation of olfactory memories (Aso et al., 2012, Wang et al., 2008).

In olfactory conditioning, the conditioned stimulus, an odour, is transmitted at the PN-KC synapse via acetylcholine (ACh) (Fig. 10A; Busto et al., 2010). Activation of ionotropic ACh receptors leads to increased intracellular Ca^{2+} levels, for example via voltage-gated Ca^{2+} channels (Busto et al., 2010; Gu and O'Dowd, 2006). However, also mGluRs are enriched at the PSDs of KCs, where odour information reaches the MB (Fig. 57C; Devaud et al., 2008; Kanellopoulos et al., 2012). Moreover, expression of DmGluRA in KCs has been shown to be important for olfactory learning (Kanellopoulos et al., 2012). In addition, also modulatory neurons releasing biogenic amines target the calyx (Pech et al., 2013); metabotropic GABA, dopamine and octopamine receptors exist here (Busch et al., 2009; Enell et al., 2007; Mao and Davis, 2009).

It is not known whether metabotropic receptors in the calyx play a role during aversive olfactory conditioning. The sensation of electric shock, the unconditioned stimulus in aversive learning, is mediated via dopamine in the MB lobes and not in the calyx (Aso et al., 2012). It is thus unlikely that metabotropic receptors in the calyx

are important for transmission of the unconditioned stimulus. Instead, they might modulate reception of the odour signal (the conditioned stimulus) at KC input synapses. So far, however, how exactly metabotropic G-protein-coupled signalling might contribute to transmission and/or processing of odour information at PN/KC synapses remains elusive.

2.1.1. Putative roles for Drep-2 and G-protein signalling in the calyx

Drosophila has about 10x more Kenyon cells than projection neurons and each KC integrates the signals of several PNs (Butcher et al., 2012; Leiss et al., 2009; Turner et al., 2008). In addition, extrinsic neurons, for example the GABAergic APL neuron (Liu and Davis, 2009), modulate olfactory signalling. In this way, every KC establishes a specialized signature. This allows for the recognition of complex odours, composed of a large mixture of molecules, by a small group of KCs (Campbell et al., 2013; Laurent, 2002). KCs also need to be able to recognize novel odours and discriminate odour concentrations (Laurent, 2002; Masek and Heisenberg, 2008). It is thus necessary for KCs to tune the sensitivity of their input synapses.

Indeed, PN-KC synapses are plastic: among animals, there is no stereotypic response of certain KCs to odours (Murthy et al., 2008) and changes of PN activity can cause structural plasticity at PN-KC synapses (Kremer et al., 2010). KCs fire rarely and a KC action potential has a high information content (Laurent, 2002; Turner et al., 2008); their input synapses therefore need to be tightly balanced and fine-tuned, in order to ensure the appropriate integration of input from different presynaptic partners. Drep-2 might support such plasticity at KC PSDs and thereby warrant the optimal transition from PN signals to calcium responses, a prerequisite for learning.

The observation that evoked calcium transients in KCs are lower in *drep-2* mutants (Fig. 66), argues in favour of this hypothesis. However, in order to be able to interpret the results of our Ca^{2+} imaging unequivocally, additional experiments would be necessary: GCaMP3 imaging of *drep-2* mutants should be repeated, in combination with re-expression of *drep-2* cDNA in KCs. Optimally, similar experiments would also be conducted for *dmGluRA* mutants. Moreover, both imaging and olfactory conditioning experiments should be repeated with additional Gal4 lines, either specific for KCs or not expressing in KCs, in order to substantiate our assumption that Drep-2 is required specifically in KCs for these mechanisms.

Finally, it is possible that the sensitivity towards odours is altered in MBs of *drep-2* mutants. In such a situation, higher odour concentrations would be required for the formation of olfactory memories. This could be the case even though *drep-2* animals can, at the outset of the olfactory pathway, sense odours normally (Fig. 63A). However, we used already very high odour concentrations for all experiments (3-octanol: 1:150 in mineral oil, 4-methyl-cyclohexanol: 1:100), rendering it unlikely that performance would significantly improve at even higher concentrations.

2.1.2. Drep-2 could regulate metabotropic signalling in general

Most proteins involved in olfactory learning also show expression in the calyx. However, to our knowledge, only one other protein is, like Drep-2, more enriched in the calyx than in the MB lobes: the transmembrane receptor tyrosine kinase ALK, primarily activated by the secreted ligand Jelly Belly (Gouzi et al., 2011). Receptor tyrosine kinases stimulate Ras/ERK signalling. Of note, the Ras-GAP Neurofibromin (Nf1), a G-protein-regulated modifier of Ras/ERK signalling, is activated by ALK (Gouzi et al., 2011). Neurofibromin is required for olfactory learning and modulates, in turn, Rutabaga and Synapsin (Cui et al., 2008; Guo et al., 2000), two additional proteins important for learning (Aceves-Piña et al., 1983; Godenschwege et al., 2004). However, ALK is not expressed in KCs but instead likely resides in the GABAergic APL neuron (Gouzi et al., 2011). Neurofibromin, in turn, appears to be required in KCs for the formation of olfactory memories (Buchanan and Davis, 2010).

ALK reduces olfactory learning performance (Gouzi et al., 2011), as does inhibitory output from the APL neuron in general (Liu and Davis, 2009). The $GABA_A$ receptor Rdl, strongly expressed in KCs, inhibits olfactory learning (Liu and Davis, 2009; Liu et al., 2007). Surprisingly, it was recently shown that a group of GABAergic ring cells of the central complex are bidirectionally connected to KCs and specifically inhibit the formation of ASM (Zhang et al., 2013). This form of memory is also affected in *drep-2* mutants (Fig. 64). Ring cell postsynapses in the lateral triangle constitute one of the strongest sites of Drep-2 expression (Fig. 67).

We originally assumed these cells to be responsible for the mediation of ethanol-induced sedation, strongly aggravated in *drep-2* mutants (Fig. 68). However, we could not rescue this phenotype by re-expression of *drep-2* cDNA in ring neurons (Table 5). It could thus be possible that Drep-2 modifies ASM not only in KCs but also at ring cell synapses, which contain a number of different metabotropic receptors, including DmGluRA (Kahsai et al., 2012). But since re-expression of *drep-2* cDNA in KCs fully rescued the deficiency of *drep-2* mutants in ASM (Fig. 64), a major contribution of Drep-2 in ring cells to olfactory learning is unlikely.

Nevertheless, GABAergic signalling plays a major role in the formation of olfactory memories. Metabotropic $GABA_B$ receptors exist at the ring cell synapses in the lateral triangle (Kahsai et al., 2012) and also in the calyx (Fig. 57B; Enell et al., 2007). Moreover, Drep-2 was found to be enriched at synapses that do not contain mGluRs, but metabotropic $GABA_B$ receptors (Fig. 56). Although we have strong indications for Drep-2 being associated with mGluRs, Drep-2 is thus likely not exclusively associated to mGluR signalling, but rather to metabotropic signalling in general. In the calyx, Drep-2 might therefore integrate G-protein signalling from both GABA and glutamate receptors.

2.1.3. Does Drep-2 indirectly regulate cAMP levels?

In *drep-2* mutants, ASM is affected but ARM is not (Fig. 64). Such a specific effect is not surprising *per se*, as many genes are required for only one of the two forms of intermediate-term memory. Examples of proteins expressed in KCs and exclusively involved in ASM but not in ARM are, in addition to the cAMP-dependent

adenylyl cyclase Rutabaga (Aceves-Piña et al., 1983; Dudai et al., 1988; Isabel et al., 2004), the AKAP-binding cAMP-dependent Protein kinase A subunit PKA-RII (Schwaerzel et al., 2007), the PKA-target Synapsin (Knapek et al., 2010), and the PKA-dependent SNARE-binding protein Tomosyn (Chen et al., 2011). The cAMP-stimulating neuropeptide Amnesiac, the first protein identified to be required for ASM but not for ARM, is expressed in DPM neurons and not in KCs (Quinn et al., 1979; Waddell et al., 2000).

All of the aforementioned proteins are either dependent on cAMP levels or regulate them. DmGluRA is coupled to the G protein G_i, which inhibits cAMP (Parmentier et al., 1996); *DmGluRA* mutants thus have too high levels of cAMP. An excess amount of cAMP impairs learning, just as too little cAMP does: mutants of the cAMP-specific phosphodiesterase *dunce* show impaired olfactory memory (Dudai et al., 1976; Kauvar, 1982). Drep-2 could likely play a role in the regulation of cAMP levels: Rutabaga requires calcium for the production of cAMP (Dudai et al., 1988) and *drep-2* mutants show reduced odour-evoked Ca^{2+} levels in KCs (Fig. 66).

It is important to note that we measured calcium levels in KC α-lobes, while the Rutabaga-mediated coincidence detection between Ca^{2+} levels and shock-invoked dopamine takes place in γ-lobes (Aso et al., 2012; Qin et al., 2012). We thus cannot state for sure that, in *drep-2* mutants, the Ca^{2+} levels measured in α-lobes were directly proportional to levels in γ-lobes. However, due to the strong presence of Drep-2 at MB input synapses and the high level of interconnections between KCs (Dubnau and Chiang, 2013), Ca^{2+} transients in α-lobes are very likely related to the ones evoked in γ-lobes. Therefore, *drep-2* mutants might well suffer from decreased cAMP levels, constituting the probable cause of the deficiencies in olfactory learning. However, if this scenario was true, it would be puzzling that application of an agonist of mGluR, which should lead to a further reduction of cAMP levels, can rescue the *drep-2*-mutant phenotype. Thus, it will be necessary to assess cAMP levels in *drep-2* mutants, in order to examine whether cAMP levels stimulated by olfactory conditioning are really reduced in this situation.

Interestingly, a major function of mGluRs is the stimulation of synaptic protein synthesis (Bhakar et al., 2012; Oostra and Willemsen, 2009). A possible explanation for the effects of Drep-2 and DmGluRA on cAMP is thus that the reduction of cAMP levels by mGluRs is insignificant, compared to the effect that chronic stimulation of DmGluRA has on protein translation. Therefore, Drep-2 and DmGluRA might regulate the synthesis of proteins that promote cAMP levels. The impact of these proteins on cAMP could be far greater than the one DmGluRA has directly. For example in *fmr1* mutants, evoked Ca^{2+} signals in KCs are increased, due to misregulation of the translation of Ca^{2+} buffering proteins (Tessier and Broadie, 2011). It should thus be examined whether proteins influencing cAMP levels are chronically misregulated if DmGluRA is stimulated pharmacologically throughout development. To this end, also experiments involving the acute pharmacological activation of DmGluRA, prior to learning tasks, could be performed. It would be interesting to see whether this has a different effect on cAMP levels than chronic stimulation of DmGluRA.

Of note, cAMP levels in KCs have recently been shown to be important mainly for the establishment of ASM (Scheunemann et al., 2012). The formation of ARM, not affected in *drep-2* mutants, depends in part on cAMP levels in inhibitory LNs of the AL. Although we have not examined Drep-2 in the AL, this constitutes a possible explanation of why ARM is not affected by Drep-2.

2.1.4. Drep-2 at mushroom body lobes

Drep-2 can, albeit to a lesser degree, also be observed at MB lobes (Fig. 81A). Here, the Drep-2 staining does, as in the calyx, not overlap with the Brp signal but rather localizes adjacent to it (Fig. 81B,C). Overexpression of *drep-2* cDNA in KCs produces a pattern that appears different and less specific than the staining of endogenous Drep-2 (Fig. 81D). Both observations indicate that Drep-2 likely localizes to postsynaptic elements in MB lobes as well. Yet this line of argument has to be taken with a pinch of salt, because the evidence presented here remains rather thin. The question could be addressed more appropriately with RNA interference directed against *drep-2*. Unfortunately, we were not able to generate an RNAi line that decreases Drep-2 levels, despite lasting efforts.

Our experiments did thus not rule out a contribution of Drep-2 in MB lobes to the defects observed in calcium signalling and olfactory learning. Yet the distinct expression of Drep-2 at PSDs of KCs, the cells in which Drep-2 is essential for olfactory learning, renders the calyx the most likely site of action of Drep-2.

2.2. Presynaptic Drep-2

We have provided several lines of evidence that Drep-2 interferes with postsynaptic, mGluR-regulated signalling and protein translation. The following observations were particularly striking: colocalization of Drep-2 with both mGluR and its associated protein Homer (Fig. 57C), as well as rescue of impaired olfactory learning in *drep-2* mutants by pharmacological stimulation of mGluRs (Fig. 65B). Moreover, FMRP, an inhibitor of mGluR-mediated protein synthesis, was present in Drep-2^{GFP} complexes (Fig. 73). Drep-2 appears to antagonize FMRP functionally, as shown by their mutual influences on courtship conditioning (Fig. 74A).

However, we have indications that Drep-2 can also be present at presynaptic specializations. First of all, Drep-2 was repeatedly identified in immunoprecipitates produced with antibodies directed against presynaptic Brp (Depner, 2013; Owald et al., 2010; Schmidt, 2006; Tian, 2011). Moreover, Drep-2 could, in some experiments, be detected presynaptically at NMJs, in animals containing four genomic copies of *drep-2* (Fig. 41B). The Drep-$2^{C\text{-}Term}$ antibody did not label protein at the NMJs of wildtype larvae (*not shown*). Thus, if present in wildtypes at all, the amount of Drep-2 at NMJs is likely extremely low. In addition, endogenous presynaptic Drep-2 at unidentified central synapses was observed by immuno-EM (Fig. 53D).

The putative presence of Drep-2 at some presynapses does not argue against a link of Drep-2 to metabotropic signalling. By contrast, it rather supports such a connection: DmGluRA, an orthologue of mammalian type II/III mGluRs, is not exclusively postsynaptic, metabotropic signalling also occurs at presynaptic specializations (Bogdanik

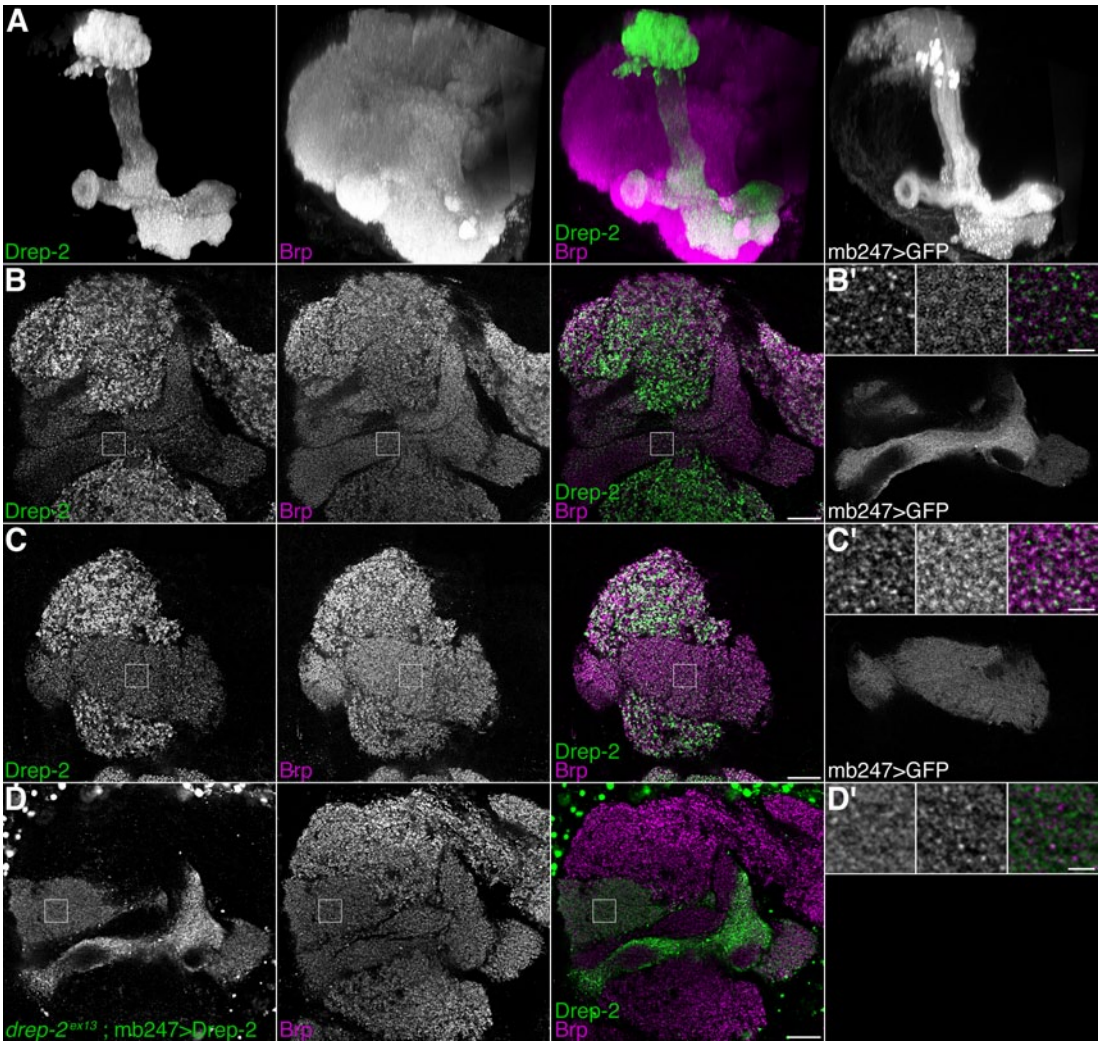

Fig. 81: Drep-2 at mushroom body lobes.
A-D: Scale bars: 10 µm. **A:** Drep-2 expression was stronger in the calyx than in the peduncle or at the lobes. **B-D:** Columns 1-3 show antibody stainings, column 4 shows UAS-GFP expressed by mb247-Gal4 (except for the insets B'-D'). **B-C:** In αβ- (B) and γ-lobes (C), Drep-2 localization was sparse and adjacent to Brp^{Nc82}, not on top of it.
D: When Drep-2 was overexpressed in KCs (*drep-2*^{ex13}/*drep-2*^{ex13} ; *mb247-gal4/uas-drep-2*), the Drep-2 signal in lobes appeared denser and less localized than in the wildtypes. In contrast to wildtypes, Drep-2 also overlapped with Brp^{Nc82} in this situation.
B'-D': Higher magnification images of the boxed areas. Scale bars: 2 µm.

et al., 2004, Parmentier et al., 1996). Drep-2 could therefore localize to either pre- or postsynapses, depending on where metabotropic signalling takes place. Experiments in which *UAS-drep-2* constructs were overexpressed, demonstrated that Drep-2 *per se* can be transported to every compartment of neurons (Fig. 43, Fig. 44, Fig. 50, Fig. 51).

Depending on whether mGluRs are present at pre- or postsynaptic sites, Drep-2 is likely involved in slightly different molecular complexes. In fact, parallels to the phenotypic spectrum of *drep-2* mutants cannot only be found in mutants of *fmr1*, *dmGluRA*, and *homer*, but also in cases where distinctly presynaptic factors are missing: an interesting example is the presynaptic vesicular protein Synapsin. As is the case for *drep-2* mutants, *synapsin* mutants display no deficits in basic synaptic transmission (Godenschwege et al., 2004). However, the size of the reserve pool of synaptic

vesicles is reduced in *synapsin* mutants (Akbergenova and Bykhovskaia, 2010). Both mutants show a normal brain morphology, although the wildtype protein is present at most or all central synapses. Animals mutant for *synapsin* or *drep-2* live shorter. Moreover, altered locomotor activity as well as differences in ethanol-mediated behaviours can be observed in both mutants. In addition, both proteins play a role in mediating courtship conditioning STM. Finally, Synapsin is, like Drep-2, required in KCs for aversive olfactory STM and ASM, but not for ARM (Godenschwege et al., 2004; Knapek et al., 2010). It remains to be seen whether such an overlap of phenotypes is merely coincidental, whether it is due to a direct, physical interaction of both proteins, or whether it is the indirect effect of altered synthesis of synaptic proteins in *drep-2* mutants.

2.3. Connections of Drep-2 to the fragile X protein

We have shown that *drep-2* phenotypes are modulated by mGluR signalling (Fig. 65B). Interestingly, we could identify the fragile X protein FMRP in complexes containing Drep-2^{GFP} (Fig. 73), a major inhibitor of mGluR-induced protein synthesis (Iacoangeli and Tiedge, 2013). Moreover, deficiencies of both *drep-2* and *fmr1* single mutants in courtship conditioning short-term memory were rescued in *drep-2*; *fmr1* double mutants (Fig. 74A).

FMRP binds mRNA and represses synaptic local translation. Several models have been proposed for how FMRP represses translation and it is thus likely that FMRP can block protein synthesis throughout several phases of translation (Bhakar et al., 2012; Iacoangeli and Tiedge, 2013; Willemsen et al., 2011). For one, phosphorylated FMRP can stall polyribosomes during elongation. In addition, FMRP interacts with regulatory RNAs that repress translation and promotes cleavage of transcripts, likely via Argonaute 2 and Dicer. FMRP also appears to play a role in activity-dependent transport of mRNA to dendrites.

Fragile X syndrome (FXS) is a disease caused by the absence of FMRP. It constitutes the most frequent intellectual disorder with a monogenic cause (Bhakar et al., 2012). Patients and animal models of FXS display altered neuronal development, attention deficit hyperactivity and reduced learning and memory performance. The *fmr1* gene codes for the FMRP protein and contains varying numbers of rCGG trinucleotide premutation repeats in its 5' UTR (Hagerman, 2013). An excessive number of these repeats (more than 200) leads to transcriptional silencing of FMRP due to hypermethylation of the *fmr1* promoter region (Fig. 82). In most cases, FXS is not caused by mutated *fmr1* but by such silencing induced through rCGG repeats. The severity of the disease varies, depending on the level of methylation and, thus, on the number of rCGG repeats.

Fragile X associated tremor/ataxia syndrome (FXTAS) is a late-onset, progressive neurodegenerative disorder distinct from FXS (Hagerman, 2013; Oostra and Willemsen, 2009). It occurs in carriers of medium-copy numbers of fragile X premutation repeats (Fig. 82). Conversely to situations with high-copy rCGG numbers, transcription of the *fmr1* mRNA is here *stimulated*, possibly by facilitating access of transcription factors (Li and Jin, 2012). At the same time, the presence of rCGG repeats in the 5'-UTR of *fmr1* mRNA inhibits translation, by impeding migration of ribosomes.

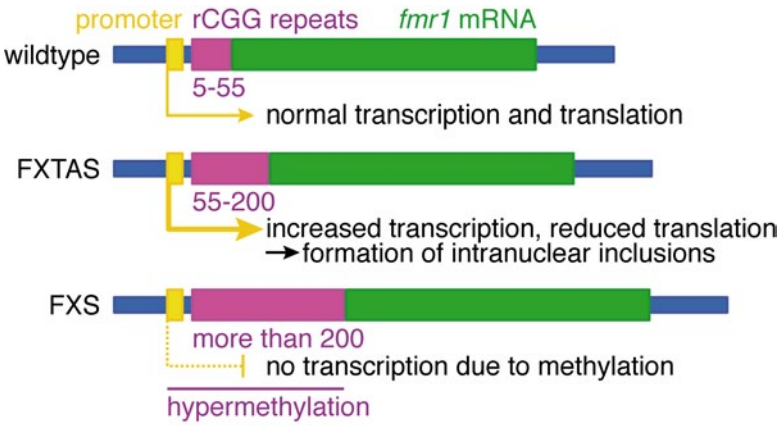

Fig. 82: Genetic causes of fragile X syndrome and FXTAS.
Unaffected patients or animals carry up to 55 rCGG repeats in the 5'UTR of the *fmr1* mRNA.
In FXTAS, rCGG numbers are elevated, leading to increased transcription of the mRNA. Translation of this mRNA, however, is impaired, due to the presence of rCGG repeats. In consequence, intranuclear inclusions are formed that also sequester other important proteins.
In FXS, the high number of rCGG repeats leads to hypermethylation that spreads to the promoter region of *fmr1*. Hence, the gene is transcriptionally silenced.
The scheme is based on information from Oostra and Willemsen, 2009 and from Li and Jin, 2012.

The severity of these effects is, as in the case of FXS, dependent on the number of rCGG repeats. In order to sequester excess untranslated *fmr1* mRNA, intranuclear inclusions are formed, which also seclude other essential nuclear proteins. Importantly, several RNA-binding proteins, e.g. the transcription factor Purα, the miRNA-processing factor DGCR8, and the ribonucleoprotein hnRNP A2/B1, involved for example in mRNA transport, bind directly to rCGG repeats and are thus sequestered (Hagerman, 2013). This, in turn, also leads to altered expression of miRNAs (Tan et al., 2012). Sequestration of these proteins, especially of DGCR8, is believed to be the cause of increased neurodegeneration and, in consequence, of the impairments of FXTAS patients and animal models. However, with increased numbers of rCGG repeats (>120), premutation repeat carriers are also likely to have decreased amounts of FMRP, which might contribute to the symptoms (Hagerman, 2013).

Interestingly, a connection between a phenotype in a *Drosophila* FXTAS model and Drep-2 function was recently established (Tan et al., 2012). Of note, Drep-2 function *per se* was not investigated in this study. However, Drep-2 was shown to modulate the FXTAS neurodegenerative disorder: overexpression or loss-of-function of Drep-2 affected the severity of an FXTAS-evoked rough eye phenotype. Due to this effect of Drep-2 on FXTAS, we did not believe the identification of FMRP in Drep-2 complexes to be a mere coincidence (Fig. 73), even though FXTAS is a disorder independent of FXS.

Indeed, behavioural experiments demonstrated that the presence of both Drep-2 and FMRP in the same complexes also had functional implications. In *Drosophila fmr1* mutants, behavioural phenotypes include abolished courtship conditioning, olfactory memory deficits, and hyperactivity phenotypes (Bolduc et al., 2008; Kanellopoulos et al., 2012; McBride et al., 2005; Tauber et al., 2011; Wan et al., 2000). As demonstrated, *drep-2* mutants showed impairments in all of these behaviours (Fig. 63, Fig. 74, Fig. 70). For olfactory learning, Drep-2 and FMRP are required in the same KC subset (mb247-Gal4, Fig. 63; Kanellopoulos et al., 2012). Most importantly, Drep-2 appeared to antagonize FMRP in courtship conditioning: the *drep-2*; *fmr1* double mutant exhibited normal short-term memory, which both single mutants did not (Fig. 74A).

2.3.1. Interference with mGluR-mediated protein synthesis

G-protein signalling activated by mGluRs stimulates synaptic protein synthesis (Fig. 83; Bhakar et al., 2012; Oostra and Willemsen, 2009). FMRP, in contrast, overall rather antagonizes such synaptic protein translation (Fig. 4, page 20). Therefore, loss of the repressor FMRP leads to an exaggerated response of the translational machinery to mGluR signalling. This, in turn, results in excessive synaptic protein synthesis and increased long-term depression (LTD). In animal models of FXS as well as in FXS patients, pharmacological treatment with allosteric inhibitors of mGluR can attenuate FXS-evoked behavioural deficits (Bhakar et al., 2012; Gross et al., 2012; Krueger and Bear, 2011). In *Drosophila*, learning phenotypes of *fmr1* mutants are rescued by pharmacological *inhibition* of DmGluRA (Bolduc et al., 2008; Kanellopoulos et al., 2012; McBride et al., 2005; Tauber et al., 2011). By contrast, *drep-2* mutants did profit from *stimulation* of mGluRs (Fig. 65). Thus, while FMRP antagonizes effects of mGluR activation, Drep-2 has a positive impact on mGluR signalling.

In consequence, Drep-2 might, in the same pathway, stimulate DmGluRA-signalling, which promotes protein synthesis, and antagonize FMRP, which inhibits translation. It is unclear how Drep-2 could modulate mGluR-induced protein synthesis. One possibility is that Drep-2 interferes with either mGluR-signalling or with FMRP directly. Drep-2$^{C\text{-}Term}$ antibody stainings appeared unaltered in *fmr1*, *dmGluRA*, and *homer* mutants (*not shown*). Thus, it is improbable that expression of Drep-2 is regulated by either FMRP or mGluR signalling. Conversely, also Drep-2 did not appear to play a role in directly regulating DmGluRA or Homer levels (see section 2.1.7.3 of the results, page 105).

We could show a clear colocalization of Drep-2 and DmGluRA at synapses (Fig. 57C). FMRP mainly accumulates in cell bodies and is present at postsynaptic specializations to a lower degree (Morales et al., 2002; Pan et al., 2004). Therefore, it would be much more difficult to observe an immunohistochemical colocalization of Drep-2 and FMRP. Nevertheless, FMRP was biochemically detected in complexes containing Drep-2 (Fig. 73). Neither DmGluRA nor Homer were identified in the quantitative mass spectrometry of Drep-2^{GFP}; however, several other proteins involved in G-protein signalling were found (Fig. 72).

Thus, while Drep-2 appears to functionally promote DmGluRA-mediated signalling and to antagonize FMRP, evidence for a direct, physical interaction of Drep-2 with either FMRP or DmGluRA remains still inconclusive. At present, arguments in favour of Drep-2 being molecularly closely associated with either of the two proteins exist.

2.3.2. A role for Drep-2 in balancing mGluR signalling?

If Drep-2 and FMRP regulated mGluR-mediated translation in an antagonistic manner, it could, at first glance, seem surprising that *drep-2* mutants share several behavioural phenotypes with *fmr1* mutants. However, an optimally balanced level of mGluR-dependent protein translation might be required for normal synaptic function. If this was the case, deviations of the level of translation into any direction could lead to impairments in behaviour and cognitive function.

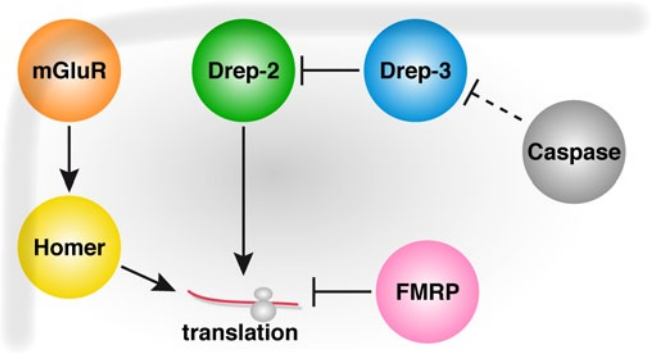

Fig. 83: Model of the putative interactions between Drep-2, mGluR and FMRP.

In fact, evidence exists that suggests such a tightly balanced system: The mammalian gene *tsc2* was initially identified as a tumour suppressor. Mutations in the gene cause tuberous sclerosis, a disease including intellectual disorders in its broad spectrum of symptoms (Auerbach et al., 2011). Tuberous sclerosis is phenotypically similar to FXS: mutations of *tsc2* constitute a monogenic source of autism, as do *fmr1* mutations. Moreover, evidence exists for a direct interaction of TSC1/2 and FMRP pathways (Han and Sahin, 2011). For example, FMRP is phosphorylated by S6 Kinase, which, in turn, is regulated by TSC1/2 via mTOR signalling. Interestingly, impaired LTD in *tsc2*-mutant mice could be rescued by application of mGluR agonists (Auerbach et al., 2011). Moreover, *fmr1* mutants showed exaggerated LTD, while the double mutant exhibited normal LTD. This demonstrated that synaptic proteins, if misregulated by either impaired or excessive mGluR-induced translation, impede appropriate LTD. In this manner, misregulation of opposing effectors can cause similar phenotypes.

Parallels to Drep-2 are obvious: also in *drep-2* mutants, mGluR-signalling appears to be hyperactivated and mGluR-dependent protein synthesis likely is out of balance. Hence, the animal shows similar phenotypes if either Drep-2 or antagonistic FMRP is missing. In courtship conditioning, we have performed a similar experiment as Auerbach and colleagues: single mutants for *dmGluRA* (Schoenfeld et al., 2013), *homer* (Diagana et al., 2002), *fmr1* (Fig. 74A; Dockendorff et al., 2002), and *drep-2* (Fig. 74A) are all deficient in courtship conditioning memory. *Drep-2*; *fmr1* double mutants, however, showed normal memory scores (Fig. 74A).

Drosophila fmr1 mutants display increased Ca^{2+} signals in MB KCs upon KCl-induced membrane depolarization (Tessier and Broadie, 2011). By contrast, *drep-2* mutants exhibited the opposite phenotype in KCs while sensing odours (Fig. 66). Tessier and Broadie demonstrated that, in the case of *fmr1*, misregulation of the translation of Ca^{2+} buffering proteins is the likely cause for the increased Ca^{2+} signals. Along the line of the previous argument, synthesis of the same proteins could be misregulated in the opposite direction in *drep-2* mutants, leading to the antagonistic phenotype. However, Drep-2 is strongly present at PSDs of KC input synapses (Fig. 49). We thus believe that Drep-2 might rather fine-tune the sensitivity of PN-KC synapses in the calyx, as outlined above (section 2.1).

2.4. A direct contribution of Drep-2 to translational regulation?

Considering the large number of RNA-associated proteins identified in the mass spectrometry (Table 6), it is also conceivable that Drep-2 directly modifies local translation regulated by both mGluR and FMRP, instead of interfering with one of the two upstream components. If synthesis of synaptic proteins was disturbed by lack of any of the previously discussed factors (Drep-2, FMRP, DmGluRA, Homer), synaptic plasticity would likely be impaired (Fig. 83).

Interestingly, in quantitative mass spectrometry, we identified not only FMRP, but also many other translational regulators (Table 6-Table 8). Three further well-known examples are Caprin, a translational repressor involved in the regulation of dendritic protein synthesis (Shiina et al., 2005), the translation initiation factor NAT1/p97/DAP5 (Hundsdoerfer et al., 2005; Levy-Strumpf et al., 1997), and Argonaute-2 (Ago2), important for RNA interference as well as for silencing of transposons (Ketting, 2011; Li et al., 2013).

It was recently shown that *ago2* mutants display age-dependent deficits in olfactory LTM (Li et al., 2013). Ago2 putatively exerts this effect by suppression of transposable elements, which are especially active in specific KC subsets (Li et al., 2013; Perrat et al., 2013). Limited and regulated mobilization of these transposons is believed to support the generation of genetic variance between neurons. However, de-repression of the elements, occurring, for example, in various neurodegenerative disorders, causes DNA damage and thus leads to the induction of apoptosis. It is therefore possible that the contribution of Ago2 to olfactory learning is based on the prevention of such DNA damage (Li et al., 2013).

Interestingly, the presence of fragile X rCGG premutation repeats in flies activates the microRNA *miR-277*, which causes neurodegeneration (Tan et al., 2012). One of the targets negatively regulated by *miR-277* is Drep-2. These findings do not argue against an involvement of Drep-2 in protein synthesis. In fact, regulation of translation and of apoptosis can be functions of the same protein, as two examples of proteins enriched in Drep-2^{GFP} complexes demonstrate: NAT1 promotes translation of apoptosis-related proteins (Henis-Korenblit et al., 2000; 2002; Nevins et al., 2003) and RnpS1 controls splicing of pro-apoptotic factors (Michelle et al., 2012). These links between translation and neurodegeneration should be followed up by investigating age-dependent learning performance in *drep-2* mutants.

Recently, a requirement of CREB-independent protein synthesis for olfactory learning has been demonstrated (Pai et al., 2013). Here, ORB-dependent translation was necessary in two MB-extrinsic MB-V3 neurons for LTM, but transcription was not. In fact, already in previous publications, known regulators of local translation like Staufen and Pumilio were found to be involved in mediating olfactory LTM (Bolduc et al., 2008; Dubnau et al., 2003). Interestingly, these factors were required in MB-V3 neurons only after spaced training, the protocol necessary for the formation of LTM, but not after massed training, sufficient for STM.

If Drep-2 directly mediated the regulation of RNA stability or of local protein synthesis at synapses, one could thus expect that Drep-2 has an impact mainly on longer-

term plasticity. On first glance, it might therefore appear contradictory that we have observed several short-term memory phenotypes in *drep-2* mutants (Fig. 63B, Fig. 74A). However, synaptic proteins might be chronically misregulated in *drep-2* mutants, as is the case for *fmr1*: the latter mutant shows deficiencies in STM, likely due to such a chronic misregulation (Bolduc et al., 2008; McBride et al., 2005; Tessier and Broadie, 2011). In this manner, *drep-2*- and *fmr1*-mutant synapses could be shifted to a generally less plastic state, which impedes the formation of STM.

Therefore, we do not believe that Drep-2 regulates translation specifically after the induction of memory formation. In contrast, we argue in favour of a chronic defect in the level of translation of synaptic proteins if Drep-2 is absent. Nevertheless, it supports the view of Drep-2 as a more fundamental regulator of synaptic plasticity that the protein is required in courtship conditioning LTM, which demands for *de novo* protein synthesis (Fig. 74B). It is feasible that Drep-2 mediates both STM and LTM by regulating the basal levels of translation of other factors.

Clearly, further analyses of the interactions of Drep-2 and either FMRP or DmGluRA are required. This could shed light on the question whether Drep-2 directly regulates translation or rather influences upstream factors. These experiments could include double mutants of *drep-2* and *dmGluRA*, as well as reciprocal genetic rescues of *drep-2*, *dmGluRA*, and *fmr1*. Moreover, it should be explored whether it is sufficient to re-express *drep-2* cDNA in adult *drep-2* mutants, or whether Drep-2 is required throughout the development of animals in order to avoid impaired learning.

2.4.1. Caspase-mediated plasticity

Caspases are proteases not only activated during apoptosis but also during learning processes at synapses (see introduction, section 2.2.2.1 (pages 18-19) or Li and Sheng, 2012). In contrast to programmed cell death, caspases are here activated only to a low degree, in a spatially restricted and transient manner. In this way, they can, for example, influence synaptic long-term plasticity (Li and Sheng, 2012).

Both Drep-1 and Drep-4 are for sure regulated by caspases, Drep-3 likely is (Fig. 79; Mukae et al., 2000; Park and Park, 2012; Yokoyama et al., 2000). We could, by contrast, not find any evidence for caspase cleavage of Drep-2 itself. However, Drep-3 tightly colocalizes with Drep-2 and binds to Drep-2 (Fig. 78; Inohara and Nuñez, 1999; Park and Park, 2012). It is thus feasible that Drep-3 regulates Drep-2 in a caspase-dependent manner. Drep-2 could therefore be in the position to integrate RNA-based plasticity with caspase-mediated plasticity. Accordingly, Drep-2 also has the potential to integrate caspase signalling with mGluR signalling and, in consequence, with mGluR-dependent localized synaptic translation.

If Drep-3 was a caspase-dependent regulator of Drep-2, mutation of the putative sites of caspase cleavage in *drep-3* could possibly generate a dominant negative construct. Whether this is the case or not, could be explored by expression of such a construct *in vivo*. Time will tell whether caspases are not the only proteins carrying out a dual role in apoptosis and synaptic plasticity: Dff proteins might show a similar spectrum of functions.

It will be interesting to see whether the synaptic function of Drep-2 is a unique specialization of *Drosophila* Dff proteins. It is promising that the anti-Drep-2 antibody intensely stained the calyces of the honeybee *Apis mellifera* as well (*not shown*). In mammals, Dff-related CIDE proteins have mainly been studied in fat tissue (Yonezawa et al., 2011). However, CIDEc shows a high level of mRNA expression in the mammalian brain (Li et al., 2009). Some Dff family proteins might thus well play non-apoptotic neuronal roles in mammals as well.

APPENDIX

Mikroskope und Fernrohre
verwirren eigentlich den reinen Menschensinn.

Johann Wolfgang von Goethe,
Wilhelm Meisters Wanderjahre,
Teil 2, Betrachtungen im Sinne der Wanderer

REFERENCES

A Washington Doctor Insane (1899). F.C. Kenyon, a Scientist, Is Committed to an Asylum. The New York Times November, 25th.

Abbott, A. (2013). Neuroscience: solving the brain. Nature 499, 272–274.

Aberle, H., Haghighi, A.P., Fetter, R.D., McCabe, B.D., Magalhães, T.R., and Goodman, C.S. (2002). wishful thinking encodes a BMP type II receptor that regulates synaptic growth in *Drosophila*. Neuron 33, 545–558.

Acebes, A., Martín-Peña, A., Chevalier, V., and Ferrús, A. (2011). Synapse loss in olfactory local interneurons modifies perception. J Neurosci 31, 2734–2745.

Aceves-Piña, E.O., Booker, R., Duerr, J.S., Livingstone, M.S., Quinn, W.G., Smith, R.F., Sziber, P.P., Tempel, B.L., and Tully, T. (1983). Learning and memory in *Drosophila*, studied with mutants. Cold Spring Harb. Symp. Quant. Biol. 48 Pt 2, 831–840.

Adolfsen, B., Saraswati, S., Yoshihara, M., and Littleton, J.T. (2004). Synaptotagmins are trafficked to distinct subcellular domains including the postsynaptic compartment. J Cell Biol 166, 249–260.

Akalal, D.-B.G., Yu, D., and Davis, R.L. (2010). A late-phase, long-term memory trace forms in the γ neurons of *Drosophila* mushroom bodies after olfactory classical conditioning. J Neurosci 30, 16699–16708.

Akbergenova, Y., and Bykhovskaia, M. (2010). Synapsin regulates vesicle organization and activity-dependent recycling at *Drosophila* motor boutons. Neuroscience 170, 441–452.

Albus, J.S., Bekey, G.A., Holland, J.H., Kanwisher, N.G., Krichmar, J.L., Mishkin, M., Modha, D.S., Raichle, M.E., Shepherd, G.M., and Tononi, G. (2007). A proposal for a Decade of the Mind initiative. Science 317, 1321.

Alivisatos, A.P., Chun, M., Church, G.M., Greenspan, R.J., Roukes, M.L., and Yuste, R. (2012). The brain activity map project and the challenge of functional connectomics. Neuron 74, 970–974.

Anaka, M., MacDonald, C.D., Barkova, E., Simon, K., Rostom, R., Godoy, R.A., Haigh, A.J., Meinertzhagen, I.A., and Lloyd, V. (2008). The white gene of *Drosophila melanogaster* encodes a protein with a role in courtship behavior. J. of Neurogenetics 22, 243–276.

Anderson, J.R., Jones, B.W., Watt, C.B., Shaw, M.V., Yang, J.-H., Demill, D., Lauritzen, J.S., Lin, Y., Rapp, K.D., Mastronarde, D., et al. (2011). Exploring the retinal connectome. Mol. Vis. 17, 355–379.

Andlauer, T.F.M., and Sigrist, S.J. (2010). In Vivo Imaging of *Drosophila* Larval Neuromuscular Junctions to Study Synapse Assembly. Chapter 21 in *Drosophila* Neurobiology, B. Zhang, M.R. Freeman, and S. Waddell, eds. (Cold Spring Harbor Press).

Andlauer, T.F.M., and Sigrist, S.J. (2012). In vivo imaging of *Drosophila* larval neuromuscular junctions to study synapse assembly. Cold Spring Harbor Protocols 2012, 407–413.

Anwyl, R. (2009). Metabotropic glutamate receptor-dependent long-term potentiation. Neuropharmacology 56, 735–740.

Arenkiel, B.R., and Ehlers, M.D. (2009). Molecular genetics and imaging technologies for circuit-based neuroanatomy. Nature 461, 900–907.

Ashby, M.C., and Isaac, J.T.R. (2011). Maturation of a recurrent excitatory neocortical circuit by experience-dependent unsilencing of newly formed dendritic spines. Neuron 70, 510–521.

Aso, Y., Grübel, K., Busch, S., Friedrich, A.B., Siwanowicz, I., and Tanimoto, H. (2009). The mushroom body of adult *Drosophila* characterized by GAL4 drivers. J. of Neurogenetics 23, 156–172.

Aso, Y., Herb, A., Ogueta, M., Siwanowicz, I., Templier, T., Friedrich, A.B., Ito, K., Scholz, H., and Tanimoto, H. (2012). Three dopamine pathways induce aversive odor memories with different stability. PLoS Genet 8, e1002768.

Assaf, Y., Alexander, D.C., Jones, D.K., Bizzi, A., Behrens, T.E.J., Clark, C.A., Cohen, Y., Dyrby, T.B., Huppi, P.S., Knoesche, T.R., et al. (2013). The CONNECT project: Combining macro- and micro-structure. Neuroimage 80, 273–282.

Atwood, H.L., Govind, C.K., and Wu, C.F. (1993). Differential ultrastructure of synaptic terminals on ventral longitudinal abdominal muscles in *Drosophila* larvae. J Neurobiol 24, 1008–1024.

Auerbach, B.D., Osterweil, E.K., and Bear, M.F. (2011). Mutations causing syndromic autism define an axis of synaptic pathophysiology. Nature 480, 63–68.

Bakker, C.E., Verheij, C., Willemsen, R., van der Helm, R., Oerlemans, F., Vermey, M., Bygrave, A., Hoogeveen, A.T., Oostra, B.A., Reyniers, E., et al. (1994). Fmr1 knockout mice: a model to study fragile X mental retardation. Cell 78, 23–33.

Banerjee, P., Schoenfeld, B.P., Bell, A.J., Choi, C.H., Bradley, M.P., Hinchey, P., Kollaros, M., Park, J.H., McBride, S.M.J., and Dockendorff, T.C. (2010). Short- and Long-Term Memory Are Modulated by Multiple Isoforms of the Fragile X Mental Retardation Protein. J Neurosci 30, 6782–6792.

Banovic, D., Khorramshahi, O., Owald, D., Wichmann, C., Riedt, T., Fouquet, W., Tian, R., Sigrist, S.J., and Aberle, H. (2010). *Drosophila* neuroligin 1 promotes growth and postsynaptic differentiation at glutamatergic neuromuscular junctions. Neuron 66, 724–738.

Bao, Q., and Shi, Y. (2007). Apoptosome: a platform for the activation of initiator caspases. Cell Death Differ 14, 56–65.

Bardin, J. (2012). Neuroscience: Making connections. Nature 483, 394–396.

Bear, M.F., Huber, K.M., and Warren, S.T. (2004). The mGluR theory of fragile X mental retardation. Trends in Neurosciences 27, 370–377.

Belgard, T.G., Marques, A.C., Oliver, P.L., Abaan, H.O., Sirey, T.M., Hoerder-Suabedissen, A., García-Moreno, F., Molnár, Z., Margulies, E.H., and Ponting, C.P. (2011). A transcriptomic atlas of mouse neocortical layers. Neuron 71, 605–616.

Benito, E., and Barco, A. (2010). CREB's control of intrinsic and synaptic plasticity: implications for CREB-dependent memory models. Trends Neurosci 33, 230–240.

Benzer, S. (1967). Behavioral mutants of *Drosophila* isolated by countercurrent distribution. Proc Natl Acad Sci USA 58, 1112–1119.

Berger, K.H., Heberlein, U., and Moore, M.S. (2004). Rapid and chronic: two distinct forms of ethanol tolerance in *Drosophila*. Alcohol Clin Exp Res 28, 1469–1480.

Berger, K.H., Kong, E.C., Dubnau, J., Tully, T., Moore, M.S., and Heberlein, U. (2008). Ethanol sensitivity and tolerance in long-term memory mutants of *Drosophila melanogaster*. Alcohol Clin Exp Res 32, 895–908.

Bhakar, A.L., Dölen, G., and Bear, M.F. (2012). The pathophysiology of fragile X (and what it teaches us about synapses). Annu Rev Neurosci 35, 417–443.

Bird, M.K., Kirchhoff, J., Djouma, E., and Lawrence, A.J. (2008). Metabotropic glutamate 5 receptors regulate sensitivity to ethanol in mice. Int J Neuropsychopharmacol 11, 765–774.

Blum, A.L., Li, W., Cressy, M., and Dubnau, J. (2009). Short- and long-term memory in *Drosophila* require cAMP signaling in distinct neuron types. Curr Biol 19, 1341–1350.

Bogdanik, L., Mohrmann, R., Ramaekers, A., Bockaert, J., Grau, Y., Broadie, K.S., and Parmentier, M.-L. (2004). The *Drosophila* metabotropic glutamate receptor DmGluRA regulates activity-dependent synaptic facilitation and fine synaptic morphology. J Neurosci 24, 9105–9116.

Bolduc, F.V., Bell, K., Cox, H., Broadie, K.S., and Tully, T. (2008). Excess protein synthesis in *Drosophila* Fragile X mutants impairs long-term memory. Nat Neurosci 11, 1143–1145.

Borycz, J., Borycz, J.A., Kubów, A., Lloyd, V., and Meinertzhagen, I.A. (2008). *Drosophila* ABC transporter mutants white, brown and scarlet have altered contents and distribution of biogenic amines in the brain. J Exp Biol 211, 3454–3466.

Bosch, M., and Hayashi, Y. (2012). Structural plasticity of dendritic spines. Curr Opin Neurobiol 22, 383–388.

Bramham, C.R. (2008). Local protein synthesis, actin dynamics, and LTP consolidation. Curr Opin Neurobiol 18, 524–531.

Brand, A.H., and Perrimon, N. (1993). Targeted gene expression as a means of altering cell fates and generating dominant phenotypes. Development 118, 401–415.

Briggman, K.L., and Denk, W. (2006). Towards neural circuit reconstruction with volume electron microscopy techniques. Curr Opin Neurobiol 16, 562–570.

Briggman, K.L., Helmstaedter, M., and Denk, W. (2011). Wiring specificity in the direction-selectivity circuit of the retina. Nature 471, 183–188.

Bruckner, J.J., Gratz, S.J., Slind, J.K., Geske, R.R., Cummings, A.M., Galindo, S.E., Donohue, L.K., and O'Connor-Giles, K.M. (2012). Fife, a *Drosophila* Piccolo-RIM homolog, promotes active zone organization and neurotransmitter release. J Neurosci 32, 17048–17058.

Buchanan, M.E., and Davis, R.L. (2010). A distinct set of *Drosophila* brain neurons required for neurofibromatosis type 1-dependent learning and memory. J Neurosci 30, 10135–10143.

Burg, M.G., Sarthy, P.V., Koliantz, G., and Pak, W.L. (1993). Genetic and molecular identification of a *Drosophila* histidine decarboxylase gene required in photoreceptor transmitter synthesis. Embo J 12, 911–919.

Burke, N.V., Han, W., Li, D., Takimoto, K., Watkins, S.C., and Levitan, E.S. (1997). Neuronal peptide release is limited by secretory granule mobility. Neuron 19, 1095–1102.

Busch, S., Selcho, M., Ito, K., and Tanimoto, H. (2009). A map of octopaminergic neurons in the *Drosophila* brain. J Comp Neurol 513, 643–667.

Busetto, G., Higley, M.J., and Sabatini, B.L. (2008). Developmental presence and disappearance of postsynaptically silent synapses on dendritic spines of rat layer 2/3 pyramidal neurons. J Physiol (Lond) 586, 1519–1527.

Busto, G.U., Cervantes-Sandoval, I., and Davis, R.L. (2010). Olfactory learning in *Drosophila*. Physiology (Bethesda, Md) 25, 338–346.

Butcher, N.J., Friedrich, A.B., Lu, Z., Tanimoto, H., and Meinertzhagen, I.A. (2012). Different classes of input and output neurons reveal new features in microglomeruli of the adult *Drosophila* mushroom body calyx. J Comp Neurol 520, 2185–2201.

Cai, D., Cohen, K.B., Luo, T., Lichtman, J.W., and Sanes, J.R. (2013). Improved tools for the Brainbow toolbox. Nature Methods 10, 540–547.

Campbell, J.L., and Nash, H.A. (2001). Volatile general anesthetics reveal a neurobiological role for the white and brown genes of *Drosophila melanogaster*. J Neurobiol 49, 339–349.

Campbell, R.A.A., Honegger, K.S., Qin, H., Li, W., Demir, E., and Turner, G.C. (2013). Imaging a Population Code for Odor Identity in the *Drosophila* Mushroom Body. J Neurosci 33, 10568–10581.

Cardona, A., Saalfeld, S., Preibisch, S., Schmid, B., Cheng, A., Pulokas, J., Tomancak, P., and Hartenstein, V. (2010). An integrated micro- and macroarchitectural analysis of the *Drosophila* brain by computer-assisted serial section electron microscopy. PLoS Biol 8(10): e1000502.

Carpenter, F.W. (1905). The reactions of the pomace fly (*Drosophila* ampelophila Loew) to light, gravity, and mechanical stimulation. The American Naturalist 39, 157–171.

Cassenaer, S., and Laurent, G. (2007). Hebbian STDP in mushroom bodies facilitates the synchronous flow of olfactory information in locusts. Nature 448, 709–713.

Castellanos, F.X., Di Martino, A., Craddock, R.C., Mehta, A.D., and Milham, M.P. (2013). Clinical applications of the functional connectome. Neuroimage 80, 527–540.

Cavarec, L., Kamphausen, T., Dubourg, B., Callebaut, I., Lemeunier, F., Métivier, D., Feunteun, J., Fischer, G., and Modjtahedi, N. (2002). Identification and characterization of Moca-cyp. A *Drosophila melanogaster* nuclear cyclophilin. J Biol Chem 277, 41171–41182.

Celebrating a decade of progress (1999). Editorial. Nat Neurosci 2, 487.

Chamaon, K., Schulz, R., Smalla, K.H., Seidel, B., and Gundelfinger, E.D. (2000). Neuronal nicotinic acetylcholine receptors of *Drosophila melanogaster*: the alpha-subunit dalpha3 and the beta-type subunit ARD co-assemble within the same receptor complex. FEBS Lett 482, 189–192.

Chen, K., Richlitzki, A., Featherstone, D.E., Schwärzel, M., and Richmond, J.E. (2011). Tomosyn-dependent regulation of synaptic transmission is required for a late phase of associative odor memory. Proc Natl Acad Sci USA 108, 18482–18487.

Chen, P., Tu, X., Akdemir, F., Chew, S.K., Rothenfluh, A., and Abrams, J.M. (2012). Effectors of alcohol-induced cell killing in *Drosophila*. Cell Death Differ 19, 1655–1663.

Cheng, D., Hoogenraad, C.C., Rush, J., Ramm, E., Schlager, M.A., Duong, D.M., Xu, P., Wijayawardana, S.R., Hanfelt, J., Nakagawa, T., et al. (2006). Relative and absolute quantification of postsynaptic density proteome isolated from rat forebrain and cerebellum. Mol. Cell Proteomics 5, 1158–1170.

Chiang, A.-S.S., Lin, C.-Y., Chuang, C.-C., Chang, H.-M., Hsieh, C.-H., Yeh, C.-W., Shih, C.-T., Wu, J.-J., Wang, G.-T., Chen, Y.-C., et al. (2011). Three-dimensional reconstruction of brain-wide wiring networks in *Drosophila* at single-cell resolution. Curr Biol 21, 1–11.

Cho, K.O., Hunt, C.A., and Kennedy, M.B. (1992). The rat brain postsynaptic density fraction contains a homolog of the *Drosophila* discs-large tumor suppressor protein. Neuron 9, 929–942.

Chorna, T., and Hasan, G. (2012). The genetics of calcium signaling in *Drosophila melanogaster*. Biochim. Biophys. Acta 1820, 1269–1282.

Chou, Y.-H., Spletter, M.L., Yaksi, E., Leong, J.C.S., Wilson, R.I., and Luo, L. (2010). Diversity and wiring variability of olfactory local interneurons in the *Drosophila* antennal lobe. Nat Neurosci 13, 439–449.

Christiansen, F., Zube, C., Andlauer, T.F.M., Wichmann, C., Fouquet, W., Owald, D., Mertel, S., Leiss, F., Tavosanis, G., Farca Luna, A.J., et al. (2011). Presynapses in Kenyon Cell Dendrites in the Mushroom Body Calyx of *Drosophila*. J Neurosci 31, 9696–9707.

Cohan, F.M., and Graf, J.-D. (1985). Latitudinal Cline in *Drosophila melanogaster* for Knockdown Resistance to Ethanol Fumes and for Rates of Response to Selection for Further Resistance. Evolution 39, 278–293.

Collingridge, G.L., Peineau, S., Howland, J.G., and Wang, Y.-T. (2010). Long-term depression in the CNS. Nat Rev Neurosci 11, 459–473.

Connolly, J., Roberts, I., Armstrong, J.D., Kaiser, K., Forte, M., Tully, T., and O'Kane, C.J. (1996). Associative learning disrupted by impaired Gs signaling in *Drosophila* mushroom bodies. Science 274, 2104–2107.

Corl, A.B., Berger, K.H., Ophir-Shohat, G., Gesch, J., Simms, J.A., Bartlett, S.E., and Heberlein, U. (2009). Happyhour, a Ste20 family kinase, implicates EGFR signaling in ethanol-induced behaviors. Cell 137, 949–960.

Corl, A.B., Rodan, A.R., and Heberlein, U. (2005). Insulin signaling in the nervous system regulates ethanol intoxication in *Drosophila melanogaster*. Nat Neurosci 8, 18–19.

Couturier, S., Bertrand, D., Matter, J.M., Hernandez, M.C., Bertrand, S., Millar, N., Valera, S., Barkas, T., and Ballivet, M. (1990). A neuronal nicotinic acetylcholine receptor subunit (alpha 7) is developmentally regulated and forms a homo-oligomeric channel blocked by alpha-BTX. Neuron 5, 847–856.

Cowan, W.M., and Kandel, E.R. (2001). A brief history of synapses and synaptic transmission. In Synapses, W.M. Cowan, T.C. Südhof, and C.F. Stevens, eds. (Baltimore: The John Hopkins University Press), pp. 1–87.

Cox, J., Neuhauser, N., Michalski, A., Scheltema, R.A., Olsen, J.V., and Mann, M. (2011). Andromeda: a peptide search engine integrated into the MaxQuant environment. J. Proteome Res. 10, 1794–1805.

Crawford, E.D., and Wells, J.A. (2011). Caspase substrates and cellular remodeling. Annu. Rev. Biochem. 80, 1055–1087.

Cui, Y., Costa, R.M., Murphy, G.G., Elgersma, Y., Zhu, Y., Gutmann, D.H., Parada, L.F., Mody, I., and Silva, A.J. (2008). Neurofibromin regulation of ERK signaling modulates GABA release and learning. Cell 135, 549–560.

D'Amelio, M., Cavallucci, V., and Cecconi, F. (2010). Neuronal caspase-3 signaling: not only cell death. Cell Death Differ 17, 1104–1114.

D'Amelio, M., Cavallucci, V., Middei, S., Marchetti, C., Pacioni, S., Ferri, A., Diamantini, A., De Zio, D., Carrara, P., Battistini, L., et al. (2011). Caspase-3 triggers early synaptic dysfunction in a mouse model of Alzheimer's disease. Nat Neurosci 14, 69–76.

Dale, H.H. (1914). The action of certain esters and ethers of choline and their relation to muscarine. J. Pharmacol. Exp. Ther. 6, 147–190.

Das, A., Sen, S., Lichtneckert, R., Okada, R., Ito, K., Rodrigues, V., and Reichert, H. (2008). *Drosophila* olfactory local interneurons and projection neurons derive from a common neuroblast lineage specified by the empty spiracles gene. Neural Dev 3, 33.

Davis, R.L. (2011). Traces of *Drosophila* memory. Neuron 70, 8–19.

Deguchi-Tawarada, M., Inoue, E., Takao-Rikitsu, E., Inoue, M., Kitajima, I., Ohtsuka, T., and Takai, Y. (2006). Active zone protein CAST is a component of conventional and ribbon synapses in mouse retina. J Comp Neurol 495, 480–496.

Depner, H. (2013). Molecular scaffolds of the Active Zone. Doctoral Thesis. Freie Universität Berlin.

Devaud, J.-M., Clouet-Redt, C., Bockaert, J., Grau, Y., and Parmentier, M.-L. (2008). Widespread brain distribution of the *Drosophila* metabotropic glutamate receptor. Neuroreport 19, 367–371.

Devineni, A.V., and Heberlein, U. (2009). Preferential ethanol consumption in *Drosophila* models features of addiction. Curr Biol 19, 2126–2132.

Devineni, A.V., and Heberlein, U. (2013). The evolution of *Drosophila melanogaster* as a model for alcohol research. Annu Rev Neurosci 36, 121–138.

Devore, J.L. (2011). Overview and Descriptive Statistics, 1.4: Measures of Variability. In Probability and Statistics for Engineering and the Sciences, (Boston: Brooks/Cole, Cengage Learning), pp. 39–41.

Diagana, T.T., Thomas, U., Prokopenko, S.N., Xiao, B., Worley, P.F., and Thomas, J.B. (2002). Mutation of *Drosophila* homer disrupts control of locomotor activity and behavioral plasticity. J Neurosci 22, 428–436.

Didelot, G., Molinari, F., Tchenio, P., Comas, D., Milhiet, E., Munnich, A., Colleaux, L., and Preat, T. (2006). Tequila, a neurotrypsin ortholog, regulates long-term memory formation in *Drosophila*. Science 313, 851–853.

Diegelmann, S., Zars, M., and Zars, T.D. (2006). Genetic dissociation of acquisition and memory strength in the heat-box spatial learning paradigm in *Drosophila*. Learn Mem 13, 72–83.

Dockendorff, T.C., Su, H.S., McBride, S.M.J., Yang, Z., Choi, C.H., Siwicki, K.K., Sehgal, A., and Jongens, T.A. (2002). *Drosophila* lacking dfmr1 activity show defects in circadian output and fail to maintain courtship interest. Neuron 34, 973–984.

Dorsey, E.R., Constantinescu, R., Thompson, J.P., Biglan, K.M., Holloway, R.G., Kieburtz, K., Marshall, F.J., Ravina, B.M., Schifitto, G., Siderowf, A., et al. (2007). Projected number of people with Parkinson disease in the most populous nations, 2005 through 2030. Neurology 68, 384–386.

Doyle, W. (1962). Operations useful for similarity-invariant pattern recognition. Journal of the ACM 9, 259–267.

Dubnau, J., and Chiang, A.-S.S. (2013). Systems memory consolidation in *Drosophila*. Curr Opin Neurobiol 23, 84–91.

Dubnau, J., Chiang, A.-S.S., Grady, L., Barditch, J., Gossweiler, S., McNeil, J., Smith, P., Buldoc, F., Scott, R., Certa, U., et al. (2003). The staufen/pumilio pathway is involved in *Drosophila* long-term memory. Curr Biol 13, 286–296.

Dudai, Y., Corfas, G., and Hazvi, S. (1988). What is the possible contribution of Ca2+-stimulated adenylate cyclase to acquisition, consolidation and retention of an associative olfactory memory in *Drosophila*. J. Comp. Physiol. A 162, 101–109.

Dudai, Y., Jan, Y.N., Byers, D., Quinn, W.G., and Benzer, S. (1976). dunce, a mutant of *Drosophila* deficient in learning. Proc Natl Acad Sci USA 73, 1684–1688.

Dudai, Y., Uzzan, A., and Zvi, S. (1983). Abnormal activity of adenylate cyclase in the *Drosophila* memory mutant rutabaga. Neuroscience Letters 42, 207–212.

Dujardin, F. (1850). Mémoire sur le système nerveux des insectes. Ann. Sci. Nat. Zool. 14, 195–206.

Eisenstein, M. (2009). Neural circuits: Putting neurons on the map. Nature 461, 1149–1152.

Ejima, A., Smith, B.P.C., Lucas, C., van der Goes van Naters, W., Miller, C.J., Carlson, J.R., Levine, J.D., and Griffith, L.C. (2007). Generalization of courtship learning in *Drosophila* is mediated by cis-vaccenyl acetate. Curr Biol 17, 599–605.

Enari, M., Sakahira, H., Yokoyama, H., Okawa, K., Iwamatsu, A., and Nagata, S. (1998). A caspase-activated DNase that degrades DNA during apoptosis, and its inhibitor ICAD. Nature 391, 43–50.

Endersby, J. (2007). A Guinea Pig's History Of Biology (London: William Heinemann).

Enell, L.E., Hamasaka, Y., Kolodziejczyk, A., and Nässel, D.R. (2007). gamma-Aminobutyric acid (GABA) signaling components in *Drosophila*: immunocytochemical localization of GABA(B) receptors in relation to the GABA(A) receptor subunit RDL and a vesicular GABA transporter. J Comp Neurol 505, 18–31.

Enell, L.E., Kapan, N., Söderberg, J.A.E., Kahsai, L., and Nässel, D.R. (2010). Insulin signaling, lifespan and stress resistance are modulated by metabotropic GABA receptors on insulin producing cells in the brain of *Drosophila*. PLoS ONE 5, e15780.

Fayyazuddin, A., Zaheer, M.A., Hiesinger, P.R., and Bellen, H.J. (2006). The nicotinic acetylcholine receptor Dalpha7 is required for an escape behavior in *Drosophila*. PLoS Biol 4, e63.

Feinstein-Rotkopf, Y., and Arama, E. (2009). Can't live without them, can live with them: roles of caspases during vital cellular processes. Apoptosis 14, 980–995.

Fejtova, A., Davydova, D., Bischof, F., Lazarevic, V., Altrock, W.D., Romorini, S., Schöne, C., Zuschratter, W., Kreutz, M.R., Garner, C.C., et al. (2009). Dynein light chain regulates axonal trafficking and synaptic levels of Bassoon. J Cell Biol 185, 341–355.

Fernandes, I., Chanut-Delalande, H., Ferrer, P., Latapie, Y., Waltzer, L., Affolter, M., Payre, F., and Plaza, S. (2010). Zona pellucida domain proteins remodel the apical compartment for localized cell shape changes. Dev Cell 18, 64–76.

Fischbach, K.F., and Dittrich, A. (1989). The optic lobe of *Drosophila melanogaster*. I: A. Golgi analysis of wild-type structure. Cell Tissue Res 258, 441–475.

Fischer, J.A., Giniger, E., Maniatis, T., and Ptashne, M. (1988). GAL4 activates transcription in *Drosophila*. Nature 332, 853–856.

Fisher-Lavie, A., and Ziv, N.E. (2013). Matching dynamics of presynaptic and postsynaptic scaffolds. J Neurosci 33, 13094–13100.

Folkers, E., Drain, P., and Quinn, W.G. (1993). Radish, a *Drosophila* mutant deficient in consolidated memory. Proc Natl Acad Sci USA 90, 8123–8127.

Fouquet, W., Owald, D., Wichmann, C., Mertel, S., Depner, H., Dyba, M., Hallermann, S., Kittel, R.J., Eimer, S., and Sigrist, S.J. (2009). Maturation of active zone assembly by *Drosophila* Bruchpilot. J Cell Biol 186, 129–145.

Frank, T., Rutherford, M.A., Strenzke, N., Neef, A., Pangršič, T., Khimich, D., Fejtova, A., Fetjova, A., Gundelfinger, E.D., Liberman, M.C., et al. (2010). Bassoon and the synaptic ribbon organize Ca^2+ channels and vesicles to add release sites and promote refilling. Neuron 68, 724–738.

Fuhrmann, J.C., Kins, S., Rostaing, P., Far, El, O., Kirsch, J., Sheng, M., Triller, A., Betz, H., and Kneussel, M. (2002). Gephyrin interacts with Dynein light chains 1 and 2, components of motor protein complexes. J Neurosci 22, 5393–5402.

Furshpan, E.J., and Potter, D.D. (1957). Mechanism of nerve-impulse transmission at a crayfish synapse. Nature 180, 342–343.

Gailey, D.A., Jackson, F.R., and Siegel, R.W. (1984). Conditioning Mutations in *Drosophila Melanogaster* Affect an Experience-Dependent Behavioral Modification in Courting Males. Genetics 106, 613–623.

Ghezzi, A., Krishnan, H.R., and Atkinson, N.S. (2012). Susceptibility to ethanol withdrawal seizures is produced by BK channel gene expression. Addict Biol., DOI: 10.1111/j.1369-1600.2012.00465.x

Gilestro, G.F., Tononi, G., and Cirelli, C. (2009). Widespread changes in synaptic markers as a function of sleep and wakefulness in *Drosophila*. Science 324, 109–112.

Giot, L., Bader, J.S., Brouwer, C., Chaudhuri, A., Kuang, B., Li, Y., Hao, Y.L., Ooi, C.E., Godwin, B., Vitols, E., et al. (2003). A protein interaction map of *Drosophila melanogaster*. Science 302, 1727–1736.

Godenschwege, T.A., Reisch, D., Diegelmann, S., Eberle, K., Funk, N., Heisenberg, M., Hoppe, V., Hoppe, J., Klagges, B.R.E., Martin, J.-R., et al. (2004). Flies lacking all synapsins are unexpectedly healthy but are impaired in complex behaviour. Eur J Neurosci 20, 611–622.

Gouzi, J.Y., Moressis, A., Walker, J.A., Apostolopoulou, A.A., Palmer, R.H., Bernards, A., and Skoulakis, E.M.C. (2011). The receptor tyrosine kinase Alk controls neurofibromin functions in *Drosophila* growth and learning. PLoS Genet 7, e1002281.

Graf, E.R., Valakh, V., Wright, C.M., Wu, C., Liu, Z., Zhang, Y.Q., and Diantonio, A. (2012). RIM promotes calcium channel accumulation at active zones of the *Drosophila* neuromuscular junction. J Neurosci 32, 16586–16596.

Grant, S.G.N. (2007). Toward a molecular catalogue of synapses. Brain Research Reviews 55, 445–449.

Grauso, M., Reenan, R.A., Culetto, E., and Sattelle, D.B. (2002). Novel putative nicotinic acetylcholine receptor subunit genes, Dalpha5, Dalpha6 and Dalpha7, in *Drosophila melanogaster* identify a new and highly conserved target of adenosine deaminase acting on RNA-mediated A-to-I pre-mRNA editing. Genetics 160, 1519–1533.

Graveley, B.R., Brooks, A.N., Carlson, J.W., Duff, M.O., Landolin, J.M., Yang, L., Artieri, C.G., van Baren, M.J., Boley, N., Booth, B.W., et al. (2011). The developmental transcriptome of *Drosophila melanogaster*. Nature 471, 473–479.

Gross, C., Berry-Kravis, E.M., and Bassell, G.J. (2012). Therapeutic strategies in fragile X syndrome: dysregulated mGluR signaling and beyond. Neuropsychopharmacology 37, 178–195.

Gu, H., and O'Dowd, D.K. (2006). Cholinergic synaptic transmission in adult *Drosophila* Kenyon cells in situ. J Neurosci 26, 265–272.

Gundelfinger, E.D., and Fejtova, A. (2012). Molecular organization and plasticity of the cytomatrix at the active zone. Curr Opin Neurobiol 22, 423–430.

Gundelfinger, E.D., and Hess, N. (1992). Nicotinic acetylcholine receptors of the central nervous system of *Drosophila*. Biochim. Biophys. Acta 1137, 299–308.

Guo, A., Li, L., Xia, S.Z., Feng, C.H., Wolf, R., and Heisenberg, M. (1996). Conditioned visual flight orientation in *Drosophila*: dependence on age, practice, and diet. Learn Mem 3, 49–59.

Guo, H.F., Tong, J., Hannan, F., Luo, L., and Zhong, Y. (2000). A neurofibromatosis-1-regulated pathway is required for learning in *Drosophila*. Nature 403, 895–898.

Hagerman, P. (2013). Fragile X-associated tremor/ataxia syndrome (FXTAS): pathology and mechanisms. Acta Neuropathol. 126, 1–19.

Hallermann, S., Kittel, R.J., Wichmann, C., Weyhersmüller, A., Fouquet, W., Mertel, S., Owald, D., Eimer, S., Depner, H., Schwärzel, M., et al. (2010). Naked Dense Bodies Provoke Depression. J Neurosci 30, 14340–14345.

Hamasaka, Y., Rieger, D., Parmentier, M.-L., Grau, Y., Helfrich-Förster, C., and Nässel, D.R. (2007). Glutamate and its metabotropic receptor in *Drosophila*clock neuron circuits. J Comp Neurol 505, 32–45.

Hampel, S., Chung, P., Mckellar, C.E., Hall, D., Looger, L.L., and Simpson, J.H. (2011). *Drosophila* Brainbow: a recombinase-based fluorescence labeling technique to subdivide neural expression patterns. Nature Methods 8, 253–259.

Han, J.M., and Sahin, M. (2011). TSC1/TSC2 signaling in the CNS. FEBS Lett 585, 973–980.

Hanesch, U., Fischbach, K.-F., and Heisenberg, M. (1989). Neuronal architecture of the central complex in *Drosophila melanogaster*. Cell Tissue Res 257, 343–366.

Harris, R.A., Trudell, J.R., and Mihic, S.J. (2008). Ethanol's molecular targets. Science Signaling 1, re7.

Haucke, V., Neher, E., and Sigrist, S.J. (2011). Protein scaffolds in the coupling of synaptic exocytosis and endocytosis. Nat Rev Neurosci 125–136.

Hawrylycz, M.J., Lein, E.S., Guillozet-Bongaarts, A.L., Shen, E.H., Ng, L., Miller, J.A., van de Lagemaat, L.N., Smith, K.A., Ebbert, A., Riley, Z.L., et al. (2012). An anatomically comprehensive atlas of the adult human brain transcriptome. Nature 489, 391–399.

Hay, B.A., Wolff, T., and Rubin, G.M. (1994). Expression of baculovirus P35 prevents cell death in *Drosophila*. Development 120, 2121–2129.

Hay, B.A., and Guo, M. (2006). Caspase-dependent cell death in *Drosophila*. Annu Rev Cell Dev Biol 22, 623–650.

Hazelrigg, T., Levis, R., and Rubin, G.M. (1984). Transformation of white locus DNA in *drosophila*: dosage compensation, zeste interaction, and position effects. Cell 36, 469–481.

Hebb, D.O. (1949). The Organization of Behavior (New York: John Wiley & Sons).

Hebert, L.E., Scherr, P.A., Bienias, J.L., Bennett, D.A., and Evans, D.A. (2003). Alzheimer disease in the US population: prevalence estimates using the 2000 census. Arch. Neurol. 60, 1119–1122.

Heisenberg, M. (1971). Separation of receptor and lamina potentials in the electroretinogram of normal and mutant *Drosophila*. J Exp Biol 55, 85–100.

Heisenberg, M. (2003). Mushroom body memoir: from maps to models. Nat Rev Neurosci 4, 266–275.

Henis-Korenblit, S., Strumpf, N.L., Goldstaub, D., and Kimchi, A. (2000). A novel form of DAP5 protein accumulates in apoptotic cells as a result of caspase cleavage and internal ribosome entry site-mediated translation. Molecular and Cellular Biology 20, 496–506.

Henis-Korenblit, S., Shani, G., Sines, T., Marash, L., Shohat, G., and Kimchi, A. (2002). The caspase-cleaved DAP5 protein supports internal ribosome entry site-mediated translation of death proteins. Proc Natl Acad Sci USA 99, 5400–5405.

Holmes, G., Pfahringer, B., and Reutemann, P. (2009). The WEKA data mining software. ACM SIGKDD Explorations 11, 10–18.

Holtzman, D.M., Mandelkow, E., and Selkoe, D.J. (2012). Alzheimer Disease in 2020. Cold Spring Harbor Perspectives in Medicine 2, a011585–a011585.

Huang, J., Zhang, W., Qiao, W., Hu, A., and Wang, Z. (2010). Functional connectivity and selective odor responses of excitatory local interneurons in *Drosophila* antennal lobe. Neuron 67, 1021–1033.

Huang, J., Zhou, W., Dong, W., Watson, A.M., and Hong, Y. (2009). Directed, efficient, and versatile modifications of the *Drosophila* genome by genomic engineering. Proc Natl Acad Sci USA 106, 8284–8289.

Huang, J., Zhou, W., Watson, A.M., Jan, Y.N., and Hong, Y. (2008). Efficient ends-out gene targeting in *Drosophila*. Genetics 180, 703–707.

Huber, K.M., Kayser, M.S., and Bear, M.F. (2000). Role for rapid dendritic protein synthesis in hippocampal mGluR-dependent long-term depression. Science 288, 1254–1257.

Hubner, N.C., Bird, A.W., Cox, J., Splettstoesser, B., Bandilla, P., Poser, I., Hyman, A., and Mann, M. (2010). Quantitative proteomics combined with BAC TransgeneOmics reveals in vivo protein interactions. J Cell Biol 189, 739–754.

Hundsdoerfer, P., Thoma, C., and Hentze, M.W. (2005). Eukaryotic translation initiation factor 4GI and p97 promote cellular internal ribosome entry sequence-driven translation. Proc Natl Acad Sci USA 102, 13421–13426.

Hunt, D.L., and Castillo, P.E. (2012). Synaptic plasticity of NMDA receptors: mechanisms and functional implications. Curr Opin Neurobiol 22, 496–508.

Hutchison, R.M., Womelsdorf, T., Allen, E.A., Bandettini, P.A., Calhoun, V.D., Corbetta, M., Penna, Della, S., Duyn, J.H., Glover, G.H., Gonzalez-Castillo, J., et al. (2013). Dynamic functional connectivity: Promise, issues, and interpretations. Neuroimage 80, 360–378.

Iacoangeli, A., and Tiedge, H. (2013). Translational control at the synapse: role of RNA regulators. Trends Biochem Sci 38, 47–55.

Iasevoli, F., Tomasetti, C., and de Bartolomeis, A. (2013). Scaffolding proteins of the post-synaptic density contribute to synaptic plasticity by regulating receptor localization and distribution: relevance for neuropsychiatric diseases. Neurochem Res 38, 1–22.

Inohara, N., and Nuñez, G. (1999). Genes with homology to DFF/CIDEs found in *Drosophila melanogaster*. Cell Death Differ 6, 823–824.

Inoue, S., Shimoda, M., Nishinokubi, I., Siomi, M.C., Okamura, M., Nakamura, A., Kobayashi, S., Ishida, N., and Siomi, H. (2002). A role for the *Drosophila* fragile X-related gene in circadian output. Curr Biol 12, 1331–1335.

Inoué, S. (2006). Foundations of Confocal Scanned Imaging in Light Microscopy. In Handbook of Biological Confocal Microscopy, J.B. Pawley, ed. (New York: Springer), pp. 1–19.

Isabel, G., Pascual, A., and Preat, T. (2004). Exclusive consolidated memory phases in *Drosophila*. Science 304, 1024–1027.

Ishizuka, A., Siomi, M.C., and Siomi, H. (2002). A *Drosophila* fragile X protein interacts with components of RNAi and ribosomal proteins. Genes Dev 16, 2497–2508.

Ito, K., Suzuki, K., Estes, P., Ramaswami, M., Yamamoto, D., and Strausfeld, N.J. (1998). The organization of extrinsic neurons and their implications in the functional roles of the mushroom bodies in *Drosophila melanogaster* Meigen. Learn Mem 5, 52–77.

Ito, M., Masuda, N., Shinomiya, K., Endo, K., and Ito, K. (2013). Systematic analysis of neural projections reveals clonal composition of the *Drosophila* brain. Curr Biol 23, 644–655.

Jani, K., and Schöck, F. (2007). Zasp is required for the assembly of functional integrin adhesion sites. J Cell Biol 179, 1583–1597.

Jefferis, G.S.X.E., Vyas, R.M., Berdnik, D., Ramaekers, A., Stocker, R.F., Tanaka, N.K., Ito, K., and Luo, L. (2004). Developmental origin of wiring specificity in the olfactory system of *Drosophila*. Development 131, 117–130.

Jenett, A., Rubin, G.M., Ngo, T.-T.B., Shepherd, D., Murphy, C., Dionne, H., Pfeiffer, B.D., Cavallaro, A., Hall, D., Jeter, J., et al. (2012). A GAL4-driver line resource for *Drosophila* neurobiology. Cell Rep 2, 991–1001.

Jia, X.X., Gorczyca, M., and Budnik, V. (1993). Ultrastructure of neuromuscular junctions in *Drosophila*: comparison of wild type and mutants with increased excitability. J Neurobiol 24, 1025–1044.

Jiang, T. (2013). Brainnetome: A new -ome to understand the brain and its disorders. Neuroimage 80C, 263–272.

Jiao, S., and Li, Z. (2011). Nonapoptotic function of BAD and BAX in long-term depression of synaptic transmission. Neuron 70, 758–772.

Joiner, M.A., and Griffith, L.C. (2000). Visual input regulates circuit configuration in courtship conditioning of *Drosophila melanogaster*. Learn Mem 7, 32–42.

Juranek, J.K., Mukherjee, K., Siddiqui, T.J., Kaplan, B.J., Li, J.Y., Ahnert-Hilger, G., Jahn, R., and Calka, J. (2013). Active zone protein expression changes at the key stages of cerebellar cortex neurogenesis in the rat. Acta Histochem. 115, 616–625.

Kaeser, P.S., Deng, L., Chávez, A.E., Liu, X., Castillo, P.E., and Südhof, T.C. (2009). ELKS2alpha/CAST deletion selectively increases neurotransmitter release at inhibitory synapses. Neuron 64, 227–239.

Kaeser, P.S., Deng, L., Wang, Y., Dulubova, I., Liu, X., Rizo, J., and Südhof, T.C. (2011). RIM proteins tether Ca2+ channels to presynaptic active zones via a direct PDZ-domain interaction. Cell 144, 282–295.

Kahsai, L., Carlsson, M.A., Winther, A.M.E., and Nässel, D.R. (2012). Distribution of metabotropic receptors of serotonin, dopamine, GABA, glutamate, and short neuropeptide F in the central complex of *Drosophila*. Neuroscience 208, 11–26.

Kaiser, K. (1993). Second generation enhancer traps. Curr Biol 3, 560–562.

Kamyshev, N.G., Iliadi, K.G., and Bragina, J.V. (1999). *Drosophila* conditioned courtship: two ways of testing memory. Learn Mem 6, 1–20.

Kanellopoulos, A.K., Semelidou, O., Kotini, A.G., Anezaki, M., and Skoulakis, E.M.C. (2012). Learning and memory deficits consequent to reduction of the fragile X mental retardation protein result from metabotropic glutamate receptor-mediated inhibition of cAMP signaling in *Drosophila*. J Neurosci 32, 13111–13124.

Kang, H., and Schuman, E.M. (1996). A requirement for local protein synthesis in neurotrophin-induced hippocampal synaptic plasticity. Science 273, 1402–1406.

Karunanithi, S., Marin, L., Wong, K., and Atwood, H.L. (2002). Quantal size and variation determined by vesicle size in normal and mutant *Drosophila* glutamatergic synapses. J Neurosci 22, 10267–10276.

Kaufmann, N., DeProto, J., Ranjan, R., Wan, H., and Van Vactor, D. (2002). *Drosophila* liprin-alpha and the receptor phosphatase Dlar control synapse morphogenesis. Neuron 34, 27–38.

Kaun, K.R., Azanchi, R., Maung, Z., Hirsh, J., and Heberlein, U. (2011). A *Drosophila* model for alcohol reward. Nat Neurosci 14, 612–619.

Kauvar, L.M. (1982). Defective cyclic adenosine 3':5'-monophosphate phosphodiesterase in the *Drosophila* memory mutant dunce. J Neurosci 2, 1347–1358.

Keene, A.C., and Waddell, S. (2007). *Drosophila* olfactory memory: single genes to complex neural circuits. Nat Rev Neurosci 8, 341–354.

Keleman, K., Vrontou, E., Krüttner, S., Yu, J.Y., Kurtovic-Kozaric, A., and Dickson, B.J. (2012). Dopamine neurons modulate pheromone responses in *Drosophila* courtship learning. Nature 489, 145–149.

Kenyon, F.C. (1896). The brain of the bee. A preliminary contribution to the morphology of the nervous system of the arthropoda. J Comp Neurol 6, 133–210.

Ketting, R.F. (2011). The many faces of RNAi. Dev Cell 20, 148–161.

Kim, Y.-C., Lee, H.-G., and Han, K.-A. (2007). D1 dopamine receptor dDA1 is required in the mushroom body neurons for aversive and appetitive learning in *Drosophila*. J Neurosci 27, 7640–7647.

Kipp, M., Schwab, B.L., Przybylski, M., Nicotera, P., and Fackelmayer, F.O. (2000). Apoptotic cleavage of scaffold attachment factor A (SAF-A) by caspase-3 occurs at a noncanonical cleavage site. J Biol Chem 275, 5031–5036.

Kirby, W., and Spence, W. (1816). An Introduction to Entomology: Or Elements of the Natural History of Insects. (London: Logman, Hurst, Rees, Orme, And Brown).

Kistner, U., Wenzel, B.M., Veh, R.W., Cases-Langhoff, C., Garner, A.M., Appeltauer, U., Voss, B., Gundelfinger, E.D., and Garner, C.C. (1993). SAP90, a rat presynaptic protein related to the product of the *Drosophila* tumor suppressor gene dlg-A. J Biol Chem 268, 4580–4583.

Kittel, R.J., Wichmann, C., Rasse, T.M., Fouquet, W., Schmidt, M., Schmid, A., Wagh, D.A., Pawlu, C., Kellner, R.R., Willig, K.I., et al. (2006). Bruchpilot promotes active zone assembly, Ca^{2+} channel clustering, and vesicle release. Science 312, 1051–1054.

Kleinfeld, D., Bharioke, A., Blinder, P., Bock, D.D., Briggman, K.L., Chklovskii, D.B., Denk, W., Helmstaedter, M., Kaufhold, J.P., Lee, W.-C.A., et al. (2011). Large-scale automated histology in the pursuit of connectomes. J Neurosci 31, 16125–16138.

Knapek, S., Gerber, B., and Tanimoto, H. (2010). Synapsin is selectively required for anesthesia-sensitive memory. Learning & Memory 17, 76–79.

Knapek, S., Sigrist, S.J., and Tanimoto, H. (2011). Bruchpilot, a synaptic active zone protein for anesthesia-resistant memory. J Neurosci 31, 3453–3458.

Kolodziejczyk, A., Sun, X., Meinertzhagen, I.A., and Nässel, D.R. (2008). Glutamate, GABA and acetylcholine signaling components in the lamina of the *Drosophila* visual system. PLoS ONE 3, e2110.

Kong, E.C., Woo, K., Li, H., Lebestky, T., Mayer, N., Sniffen, M.R., Heberlein, U., Bainton, R.J., Hirsh, J., and Wolf, F.W. (2010). A pair of dopamine neurons target the D1-like dopamine receptor DopR in the central complex to promote ethanol-stimulated locomotion in *Drosophila*. PLoS ONE 5, e9954.

Koon, A.C., Ashley, J., Barria, R., DasGupta, S., Brain, R., Waddell, S., Alkema, M.J., and Budnik, V. (2011). Autoregulatory and paracrine control of synaptic and behavioral plasticity by octopaminergic signaling. Nat Neurosci 14, 190–199.

Krashes, M.J., and Waddell, S. (2011). *Drosophila* aversive olfactory conditioning. Cold Spring Harbor Protocols 2011, 5, pdb.prot5608.

Kremer, M.C., Christiansen, F., Leiss, F., Paehler, M., Knapek, S., Andlauer, T.F.M., Förstner, F., Kloppenburg, P., Sigrist, S.J., and Tavosanis, G. (2010). Structural long-term changes at mushroom body input synapses. Curr Biol 20, 1938–1944.

Krueger, D.D., and Bear, M.F. (2011). Toward fulfilling the promise of molecular medicine in fragile X syndrome. Annu. Rev. Med. 62, 411–429.

Kumar, S. (2007). Caspase function in programmed cell death. Cell Death Differ 14, 32–43.

Kumar, S. (2004). Migrate, differentiate, proliferate, or die: pleiotropic functions of an apical "apoptotic caspase." Sci STKE 2004, pe49.

Laemmli, U.K. (1970). Cleavage of structural proteins during the assembly of the head of bacteriophage T4. Nature 227, 680–685.

Laferriere, H., Guarnieri, D.J., Sitaraman, D., Diegelmann, S., Heberlein, U., and Zars, T.D. (2008). Genetic dissociation of ethanol sensitivity and memory formation in *Drosophila melanogaster*. Genetics 178, 1895–1902.

Lahey, T., Gorczyca, M., Jia, X.X., and Budnik, V. (1994). The *Drosophila* tumor suppressor gene dlg is required for normal synaptic bouton structure. Neuron 13, 823–835.

Lane, M.E., and Kalderon, D. (1993). Genetic investigation of cAMP-dependent protein kinase function in *Drosophila* development. Genes Dev 7, 1229–1243.

Laurent, G. (2002). Olfactory network dynamics and the coding of multidimensional signals. Nat Rev Neurosci 3, 884–895.

Lee, T., and Luo, L. (1999). Mosaic analysis with a repressible cell marker for studies of gene function in neuronal morphogenesis. Neuron 22, 451–461.

Lein, E.S., Hawrylycz, M.J., Ao, N., Ayres, M., Bensinger, A., Bernard, A., Boe, A.F., Boguski, M.S., Brockway, K.S., Byrnes, E.J., et al. (2007). Genome-wide atlas of gene expression in the adult mouse brain. Nature 445, 168–176.

Leiss, F., Groh, C., Butcher, N.J., Meinertzhagen, I.A., and Tavosanis, G. (2009a). Synaptic organization in the adult *Drosophila* mushroom body calyx. J Comp Neurol 517, 808–824.

Leiss, F., Koper, E., Hein, I., Fouquet, W., Lindner, J., Sigrist, S.J., and Tavosanis, G. (2009b). Characterization of dendritic spines in the *Drosophila* central nervous system. Dev Neurobiol 69, 221–234.

Levy-Strumpf, N., Deiss, L.P., Berissi, H., and Kimchi, A. (1997). DAP-5, a novel homolog of eukaryotic translation initiation factor 4G isolated as a putative modulator of gamma interferon-induced programmed cell death. Molecular and Cellular Biology 17, 1615–1625.

Li, W., Prazak, L., Chatterjee, N., Grüninger, S., Krug, L., Theodorou, D., and Dubnau, J. (2013). Activation of transposable elements during aging and neuronal decline in *Drosophila*. Nat Neurosci 16, 529–531.

Li, Y.H., Lei, T., Chen, X.D., Xia, T., Peng, Y., Long, Q.Q., Zhang, J., Feng, S.Q., Zhou, L., and Yang, Z.Q. (2009). Molecular cloning, chromosomal location and expression pattern of porcine CIDEa and CIDEc. Mol. Biol. Rep. 36, 575–582.

Li, Y., and Jin, P. (2012). RNA-mediated neurodegeneration in fragile X-associated tremor/ataxia syndrome. Brain Res. 1462, 112–117.

Li, Z., and Sheng, M. (2012). Caspases in synaptic plasticity. Mol Brain 5, 15.

Li, Z., Jo, J., Jia, J.-M., Lo, S.-C., Whitcomb, D.J., Jiao, S., Cho, K., and Sheng, M. (2010). Caspase-3 activation via mitochondria is required for long-term depression and AMPA receptor internalization. Cell 141, 859–871.

Lin, D.M., and Goodman, C.S. (1994). Ectopic and increased expression of Fasciclin II alters motoneuron growth cone guidance. Neuron 13, 507–523.

Liu, K.S.Y. (2012). Genetic Dissections of Active Zone Proteins. Doctoral Thesis. Freie Universität Berlin.

Liu, K.S.Y., Siebert, M., Mertel, S., Knoche, E., Wegener, S., Wichmann, C., Matkovic, T., Muhammad, K., Depner, H., Mettke, C., et al. (2011). RIM-binding protein, a central part of the active zone, is essential for neurotransmitter release. Science 334, 1565–1569.

Liu, X., and Davis, R.L. (2009). The GABAergic anterior paired lateral neuron suppresses and is suppressed by olfactory learning. Nat Neurosci 12, 53–59.

Liu, X., Krause, W.C., and Davis, R.L. (2007). GABAA receptor RDL inhibits *Drosophila* olfactory associative learning. Neuron 56, 1090–1102.

Ljaschenko, D., Ehmann, N., and Kittel, R.J. (2013). Hebbian plasticity guides maturation of glutamate receptor fields in vivo. Cell Rep 3, 1407–1413.

Luan, H., Peabody, N.C., Vinson, C.R., and White, B.H. (2006). Refined spatial manipulation of neuronal function by combinatorial restriction of transgene expression. Neuron 52, 425–436.

Luo, L., Liao, Y.J., Jan, L.Y., and Jan, Y.N. (1994). Distinct morphogenetic functions of similar small GTPases: *Drosophila* Drac1 is involved in axonal outgrowth and myoblast fusion. Genes Dev 8, 1787–1802.

Lykke-Andersen, J., Shu, M.D., and Steitz, J.A. (2001). Communication of the position of exon-exon junctions to the mRNA surveillance machinery by the protein RNPS1. Science 293, 1836–1839.

Maglione, M., and Sigrist, S.J. (2013). Seeing the forest tree by tree: super-resolution light microscopy meets the neurosciences. Nat Neurosci 16, 790–797.

Malenka, R.C., and Siegelbaum, S.A. (2001). Synaptic plasticity: diverse targets and mechanisms for regulating synaptic efficacy. In Synapses, W.M. Cowan, T.C. Südhof, and C.F. Stevens, eds. (Baltimore: The John Hopkins University Press), pp. 393–454.

Manseau, L., Baradaran, A., Brower, D., Budhu, A., Elefant, F., Phan, H., Philp, A.V., Yang, M., Glover, D., Kaiser, K., et al. (1997). GAL4 enhancer traps expressed in the embryo, larval brain, imaginal discs, and ovary of *Drosophila*. Dev. Dyn. 209, 310–322.

Mao, Z., and Davis, R.L. (2009). Eight different types of dopaminergic neurons innervate the *Drosophila* mushroom body neuropil: anatomical and physiological heterogeneity. Front. Neural Circuits 3, 5.

Maples, T., and Rothenfluh, A. (2011). A simple way to measure ethanol sensitivity in flies. JoVE e2541.

Markoff, J., and Gorman, J. (2013). Obama to Unveil Initiative To Map the Human Brain. The New York Times February, 4th, A12.

Masek, P., and Heisenberg, M. (2008). Distinct memories of odor intensity and quality in *Drosophila*. Proc Natl Acad Sci USA 105, 15985–15990.

Matkovic, T., Siebert, M., Knoche, E., Depner, H., Mertel, S., Owald, D., Schmidt, M., Thomas, U., Sickmann, A., Kamin, D., et al. (2013). The Bruchpilot cytomatrix determines the size of the readily releasable pool of synaptic vesicles. J Cell Biol 202, 667–683.

Matsumoto-Miyai, K., Sokolowska, E., Zurlinden, A., Gee, C.E., Lüscher, D., Hettwer, S., Wölfel, J., Ladner, A.P., Ster, J., Gerber, U., et al. (2009). Coincident pre- and postsynaptic activation induces dendritic filopodia via neurotrypsin-dependent agrin cleavage. Cell 136, 1161–1171.

Matz, J., Gilyan, A., Kolar, A., McCarvill, T., and Krueger, S.R. (2010). Rapid structural alterations of the active zone lead to sustained changes in neurotransmitter release. Proc Natl Acad Sci USA 107, 8836–8841.

McBride, S.M., Giuliani, G., Choi, C., Krause, P., Correale, D., Watson, K., Baker, G., and Siwicki, K.K. (1999). Mushroom body ablation impairs short-term memory and long-term memory of courtship conditioning in *Drosophila melanogaster*. Neuron 24, 967–977.

McBride, S.M.J., Choi, C.H., Schoenfeld, B.P., Bell, A.J., Liebelt, D.A., Ferreiro, D., Choi, R.J., Hinchey, P., Kollaros, M., Terlizzi, A.M., et al. (2010). Pharmacological and genetic reversal of age-dependent cognitive deficits attributable to decreased presenilin function. J Neurosci 30, 9510–9522.

McBride, S.M.J., Choi, C.H., Wang, Y., Liebelt, D., Braunstein, E., Ferreiro, D., Sehgal, A., Siwicki, K.K., Dockendorff, T.C., Nguyen, H.T., et al. (2005). Pharmacological Rescue of Synaptic Plasticity, Courtship Behavior, and Mushroom Body Defects in a *Drosophila* Model of Fragile X Syndrome. Neuron 45, 753–764.

McGuire, S.E., Le, P.T., Osborn, A.J., Matsumoto, K., and Davis, R.L. (2003). Spatiotemporal rescue of memory dysfunction in *Drosophila*. Science 302, 1765–1768.

McQuilton, P., St Pierre, S.E., Thurmond, J., FlyBase Consortium (2012). FlyBase 101--the basics of navigating FlyBase. Nucleic Acids Res 40, D706–D714.

Melzig, J., Rein, K.H., Schäfer, U., Pfister, H., Jäckle, H., Heisenberg, M., and Raabe, T. (1998). A protein related to p21-activated kinase (PAK) that is involved in neurogenesis in the *Drosophila* adult central nervous system. Curr Biol 8, 1223–1226.

Meyer, A.C., Frank, T., Khimich, D., Hoch, G., Riedel, D., Chapochnikov, N.M., Yarin, Y.M., Harke, B., Hell, S.W., Egner, A., et al. (2009). Tuning of synapse number, structure and function in the cochlea. Nat Neurosci 12, 444–453.

Mezler, M., Müller, T., and Raming, K. (2001). Cloning and functional expression of GABA(B) receptors from *Drosophila*. Eur J Neurosci 13, 477–486.

Michel, C.I., Kraft, R., and Restifo, L.L. (2004). Defective neuronal development in the mushroom bodies of *Drosophila* fragile X mental retardation 1 mutants. J Neurosci 24, 5798–5809.

Michelle, L., Cloutier, A., Toutant, J., Shkreta, L., Thibault, P., Durand, M., Garneau, D., Gendron, D., Lapointe, E., Couture, S., et al. (2012). Proteins associated with the exon junction complex also control the alternative splicing of apoptotic regulators. Molecular and Cellular Biology 32, 954–967.

Micheva, K.D., and Smith, S.J. (2007). Array tomography: a new tool for imaging the molecular architecture and ultrastructure of neural circuits. Neuron 55, 25–36.

Micheva, K.D., Busse, B., Weiler, N.C., O'Rourke, N., and Smith, S.J. (2010). Single-synapse analysis of a diverse synapse population: proteomic imaging methods and markers. Neuron 68, 639–653.

Miller, K.E., DeProto, J., Kaufmann, N., Patel, B.N., Duckworth, A., and Van Vactor, D. (2005). Direct observation demonstrates that Liprin-alpha is required for trafficking of synaptic vesicles. Curr Biol 15, 684–689.

Molnár, E. (2011). Long-term potentiation in cultured hippocampal neurons. Semin Cell Dev Biol 22, 506–513.

Moore, M.S., DeZazzo, J., Luk, A.Y., Tully, T., Singh, C.M., and Heberlein, U. (1998). Ethanol intoxication in *Drosophila*: Genetic and pharmacological evidence for regulation by the cAMP signaling pathway. Cell 93, 997–1007.

Morales, J., Hiesinger, P.R., Schroeder, A.J., Kume, K., Verstreken, P., Jackson, F.R., Nelson, D.L., and Hassan, B.A. (2002). *Drosophila* fragile X protein, DFXR, regulates neuronal morphology and function in the brain. Neuron 34, 961–972.

Morgan, J.L., and Lichtman, J.W. (2013). Why not connectomics? Nature Methods 10, 494–500.

Morozova, T.V., Mackay, T.F.C., and Anholt, R.R.H. (2011). Transcriptional networks for alcohol sensitivity in *Drosophila melanogaster*. Genetics 187, 1193–1205.

Mount, S.M., and Salz, H.K. (2000). Pre-messenger RNA processing factors in the *Drosophila* genome. J Cell Biol 150, F37–F44.

Mukae, N., Yokoyama, H., Yokokura, T., Sakoyama, Y., Sakahira, H., and Nagata, S. (2000). Identification and developmental expression of inhibitor of caspase-activated DNase (ICAD) in *Drosophila melanogaster*. J Biol Chem 275, 21402–21408.

Mukae, N., Yokoyama, H., Yokokura, T., Sakoyama, Y., and Nagata, S. (2002). Activation of the innate immunity in *Drosophila* by endogenous chromosomal DNA that escaped apoptotic degradation. Genes Dev 16, 2662–2671.

Muller, H.J. (1927). Artificial transmutation of the gene. Science 66, 84–87.

Murali, T., Pacifico, S., Yu, J., Guest, S., Roberts, G.G., and Finley, R.L. (2011). DroID 2011: a comprehensive, integrated resource for protein, transcription factor, RNA and gene interactions for *Drosophila*. Nucleic Acids Res 39, D736–D743.

Murthy, M., Fiete, I., and Laurent, G. (2008). Testing Odor Response Stereotypy in the *Drosophila* Mushroom Body. Neuron 59, 1009–1023.

Müller, M., Liu, K.S.Y., Sigrist, S.J., and Davis, G.W. (2012). RIM controls homeostatic plasticity through modulation of the readily-releasable vesicle pool. J Neurosci 32, 16574–16585.

Nayler, O., Strätling, W., Bourquin, J.P., Stagljar, I., Lindemann, L., Jasper, H., Hartmann, A.M., Fackelmayer, F.O., Ullrich, A., and Stamm, S. (1998). SAF-B protein couples transcription and pre-mRNA splicing to SAR/MAR elements. Nucleic Acids Res 26, 3542–3549.

Neuser, K., Triphan, T., Mronz, M., Poeck, B., and Strauss, R. (2008). Analysis of a spatial orientation memory in *Drosophila*. Nature 453, 1244–1247.

Nevins, T.A., Harder, Z.M., Korneluk, R.G., and Holcík, M. (2003). Distinct regulation of internal ribosome entry site-mediated translation following cellular stress is mediated by apoptotic fragments of eIF4G translation initiation factor family members eIF4GI and p97/DAP5/NAT1. J Biol Chem 278, 3572–3579.

Ng, M., Roorda, R.D., Lima, S.Q., Zemelman, B.V., Morcillo, P., and Miesenböck, G. (2002). Transmission of olfactory information between three populations of neurons in the antennal lobe of the fly. Neuron 36, 463–474.

Nicholls, J.G., Martin, A.R., Wallace, B.G., and Fuchs, P.A. (2001). Indirect Mechanisms of Synaptic Transmission. In From Neuron to Brain, (Sunderland, MA: Sinauer Associates), pp. 177–197.

Nicolaï, L.J.J., Ramaekers, A., Raemaekers, T., Drozdzecki, A., Mauss, A.S., Yan, J., Landgraf, M., Annaert, W., and Hassan, B.A. (2010). Genetically encoded dendritic marker sheds light on neuronal connectivity in *Drosophila*. Proc Natl Acad Sci USA 107, 20553–20558.

O'Dell, K., Armstrong, J.D., Yang, M., and Kaiser, K. (1995). Functional dissection of the *Drosophila* mushroom bodies by selective feminization of genetically defined subcompartments. Neuron 15, 55–61.

O'Rourke, N.A., Weiler, N.C., Micheva, K.D., and Smith, S.J. (2012). Deep molecular diversity of mammalian synapses: why it matters and how to measure it. Nat Rev Neurosci 13, 365–379.

Oberti, D., Kirschmann, M.A., and Hahnloser, R.H.R. (2011). Projection neuron circuits resolved using correlative array tomography. Front Neurosci 5, 50.

Ohtsuka, T. (2013). CAST: functional scaffold for the integrity of the presynaptic active zone. Neurosci. Res. 76, 10–15.

Okamura, K., Ishizuka, A., Siomi, H., and Siomi, M.C. (2004). Distinct roles for Argonaute proteins in small RNA-directed RNA cleavage pathways. Genes Dev 18, 1655–1666.

Olney, J.W., Tenkova, T., Dikranian, K., Muglia, L.J., Jermakowicz, W.J., D'Sa, C., and Roth, K.A. (2002). Ethanol-induced caspase-3 activation in the in vivo developing mouse brain. Neurobiol Dis 9, 205–219.

Oostra, B.A., and Willemsen, R. (2009). FMR1: a gene with three faces. Biochim. Biophys. Acta 1790, 467–477.

Osten, P., and Margrie, T.W. (2013). Mapping brain circuitry with a light microscope. Nature Methods 10, 515–523.

Owald, D., Fouquet, W., Schmidt, M., Wichmann, C., Mertel, S., Depner, H., Christiansen, F., Zube, C., Quentin, C., Körner, J., et al. (2010). A Syd-1 homologue regulates pre- and postsynaptic maturation in *Drosophila*. J Cell Biol 188, 565–579.

Owald, D., Khorramshahi, O., Gupta, V.K., Banovic, D., Depner, H., Fouquet, W., Wichmann, C., Mertel, S., Eimer, S., Reynolds, E., et al. (2012). Cooperation of Syd-1 with Neurexin synchronizes pre- with postsynaptic assembly. Nat Neurosci 15, 1219–1226.

Pai, T.-P., Chen, C.-C., Lin, H.-H., Chin, A.-L., Lai, J.S.-Y., Lee, P.-T., Tully, T., and Chiang, A.-S.S. (2013). *Drosophila* ORB protein in two mushroom body output neurons is necessary for long-term memory formation. Proc Natl Acad Sci USA 110, 7898–7903.

Palma, E., Mileo, A.M., Martinez-Torres, A., Eusebi, F., and Miledi, R. (2002). Some properties of human neuronal alpha 7 nicotinic acetylcholine receptors fused to the green fluorescent protein. Proc Natl Acad Sci USA 99, 3950–3955.

Pan, L., and Broadie, K.S. (2007). *Drosophila* fragile X mental retardation protein and metabotropic glutamate receptor A convergently regulate the synaptic ratio of ionotropic glutamate receptor subclasses. J Neurosci 27, 12378–12389.

Pan, L., Zhang, Y.Q., Woodruff, E., and Broadie, K.S. (2004). The *Drosophila* Fragile X Gene Negatively Regulates Neuronal Elaboration and Synaptic Differentiation. Curr Biol 14, 1863–1870.

Panneels, V., Eroglu, C., Cronet, P., and Sinning, I. (2003). Pharmacological characterization and immunoaffinity purification of metabotropic glutamate receptor from *Drosophila* overexpressed in Sf9 cells. Protein Expr Purif 30, 275–282.

Papoulas, O., Monzo, K.F., Cantin, G.T., Ruse, C., Yates, J.R., Ryu, Y.H., and Sisson, J.C. (2010). dFMRP and Caprin, translational regulators of synaptic plasticity, control the cell cycle at the *Drosophila* mid-blastula transition. Development 137, 4201–4209.

Papula, L. (2008). Gaußsches Fehlerfortpflanzungsgesetz (Varianzfortpflanzungsgesetz). In Mathematik Für Ingenieure Und Naturwissenschaftler Band 3, (Vieweg+Teubner), pp. 678–681.

Park, H.H., Tookes, H.E., and Wu, H. (2006). Crystallization and preliminary X-ray crystallographic studies of Drep-3, a DFF-related protein from *Drosophila melanogaster*. Acta Crystallogr Sect F Struct Biol Cryst Commun 62, 597–599.

Park, O.K., and Park, H.H. (2012). Dual apoptotic DNA fragmentation system in the fly: Drep2 is a novel nuclease of which activity is inhibited by Drep3. FEBS Lett 586, 3085–3089.

Park, S.K., Sedore, S.A., Cronmiller, C., and Hirsh, J. (2000). Type II cAMP-dependent protein kinase-deficient *Drosophila* are viable but show developmental, circadian, and drug response phenotypes. J Biol Chem 275, 20588–20596.

Parmentier, M.L., Pin, J.P., Bockaert, J., and Grau, Y. (1996). Cloning and functional expression of a *Drosophila* metabotropic glutamate receptor expressed in the embryonic CNS. J Neurosci 16, 6687–6694.

Parnas, D., Haghighi, A.P., Fetter, R.D., Kim, S.W., and Goodman, C.S. (2001). Regulation of postsynaptic structure and protein localization by the Rho-type guanine nucleotide exchange factor dPix. Neuron 32, 415–424.

Patel, M.R., Lehrman, E.K., Poon, V.Y., Crump, J.G., Zhen, M., Bargmann, C.I., and Shen, K. (2006). Hierarchical assembly of presynaptic components in defined C. elegans synapses. Nat Neurosci 9, 1488–1498.

Paul, F.E., Hosp, F., and Selbach, M. (2011). Analyzing protein-protein interactions by quantitative mass spectrometry. Methods 54, 387–395.

Pech, U., Pooryasin, A., Birman, S., and Fiala, A. (2013). Localization of the contacts between Kenyon cells and aminergic neurons in the *Drosophila melanogaster* brain using splitGFP reconstitution. J Comp Neurol ahead of print, DOI:10.1002–cne.23388.

Peled, E.S., and Isacoff, E.Y. (2011). Optical quantal analysis of synaptic transmission in wild-type and rab3-mutant *Drosophila* motor axons. Nat Neurosci 14, 519–526.

Perrat, P.N., DasGupta, S., Wang, J., Theurkauf, W., Weng, Z., Rosbash, M., and Waddell, S. (2013). Transposition-driven genomic heterogeneity in the *Drosophila* brain. Science 340, 91–95.

Pfeiffer, B.D., Ngo, T.-T.B., Hibbard, K.L., Murphy, C., Jenett, A., Truman, J.W., and Rubin, G.M. (2010). Refinement of tools for targeted gene expression in *Drosophila*. Genetics 186, 735–755.

Phelan, P., and Starich, T.A. (2001). Innexins get into the gap. Bioessays 23, 388–396.

Phelan, P., Nakagawa, M., Wilkin, M.B., Moffat, K.G., O'Kane, C.J., Davies, J.A., and Bacon, J.P. (1996). Mutations in shaking-B prevent electrical synapse formation in the *Drosophila* giant fiber system. J Neurosci 16, 1101–1113.

Phelan, P., Stebbings, L.A., Baines, R.A., Bacon, J.P., Davies, J.A., and Ford, C. (1998). *Drosophila* Shaking-B protein forms gap junctions in paired Xenopus oocytes. Nature 391, 181–184.

Pilling, A.D., Horiuchi, D., Lively, C.M., and Saxton, W.M. (2006). Kinesin-1 and Dynein are the primary motors for fast transport of mitochondria in *Drosophila* motor axons. Mol Biol Cell 17, 2057–2068.

Pitman, J.L., Huetteroth, W., Burke, C.J., Krashes, M.J., Lai, S.-L., Lee, T., and Waddell, S. (2011). A pair of inhibitory neurons are required to sustain labile memory in the *Drosophila* mushroom body. Curr Biol 21, 855–861.

Pohorecky, L.A. (1977). Biphasic action of ethanol. Biobehavioral Reviews 1, 231–240.

Proctor, D.T., Coulson, E.J., and Dodd, P.R. (2011). Post-synaptic scaffolding protein interactions with glutamate receptors in synaptic dysfunction and Alzheimer's disease. Prog Neurobiol 93, 509–521.

Ptashne, M., and Gann, A. (2002). Yeast: a single-celled eukaryote. In Genes and Signals, (CSHL Press), pp. 63–87.

Qin, G., Schwarz, T., Kittel, R.J., Schmid, A., Rasse, T.M., Kappei, D., Ponimaskin, E., Heckmann, M., and Sigrist, S.J. (2005). Four different subunits are essential for expressing the synaptic glutamate receptor at neuromuscular junctions of *Drosophila*. J Neurosci 25, 3209–3218.

Qin, H., Cressy, M., Li, W., Coravos, J.S., Izzi, S.A., and Dubnau, J. (2012). Gamma neurons mediate dopaminergic input during aversive olfactory memory formation in *Drosophila*. Curr Biol 22, 608–614.

Qin, M., Entezam, A., Usdin, K., Huang, T., Liu, Z.-H., Hoffman, G.E., and Smith, C.B. (2011). A mouse model of the fragile X premutation: effects on behavior, dendrite morphology, and regional rates of cerebral protein synthesis. Neurobiol Dis 42, 85–98.

Qu, L., Akbergenova, Y., Hu, Y., and Schikorski, T. (2009). Synapse-to-synapse variation in mean synaptic vesicle size and its relationship with synaptic morphology and function. J Comp Neurol 514, 343–352.

Quinn, W.G., and Dudai, Y. (1976). Memory phases in *Drosophila*. Nature 262, 576–577.

Quinn, W.G., Harris, W.A., and Benzer, S. (1974). Conditioned behavior in *Drosophila melanogaster*. Proc Natl Acad Sci USA 71, 708–712.

Quinn, W.G., Sziber, P.P., and Booker, R. (1979). The *Drosophila* memory mutant amnesiac. Nature 277, 212–214.

Raghavan, S., and White, R.A. (1997). Connectin mediates adhesion in *Drosophila*. Neuron 18, 873–880.

Rajashekhar, K.P., and Singh, R.N. (1994). Neuroarchitecture of the tritocerebrum of *Drosophila melanogaster*. J Comp Neurol 349, 633–645.

Ramaekers, A., Parmentier, M.L., Lasnier, C., Bockaert, J., and Grau, Y. (2001). Distribution of metabotropic glutamate receptor DmGlu-A in *Drosophila melanogaster* central nervous system. J Comp Neurol 438, 213–225.

Ranieri, N., Ruel, L., Gallet, A., Raisin, S., and Thérond, P.P. (2012). Distinct phosphorylations on kinesin costal-2 mediate differential hedgehog signaling strength. Dev Cell 22, 279–294.

Rao, S., Lang, C., Levitan, E.S., and Deitcher, D.L. (2001). Visualization of neuropeptide expression, transport, and exocytosis in *Drosophila melanogaster*. J Neurobiol 49, 159–172.

Rappsilber, J., Ishihama, Y., and Mann, M. (2003). Stop and go extraction tips for matrix-assisted laser desorption/ionization, nanoelectrospray, and LC/MS sample pretreatment in proteomics. Anal. Chem. 75, 663–670.

Renn, S.C., Armstrong, J.D., Yang, M., Wang, Z., An, X., Kaiser, K., and Taghert, P.H. (1999). Genetic analysis of the *Drosophila* ellipsoid body neuropil: organization and development of the central complex. J Neurobiol 41, 189–207.

Rizzoli, S.O., and Betz, W.J. (2005). Synaptic vesicle pools. Nat Rev Neurosci 6, 57–69.

Robinson, B.G., Khurana, S., Kuperman, A., and Atkinson, N.S. (2012). Neural Adaptation Leads to Cognitive Ethanol Dependence. Curr Biol 22, 2338–2341.

Rodan, A.R., Kiger, J.A., and Heberlein, U. (2002). Functional dissection of neuroanatomical loci regulating ethanol sensitivity in *Drosophila*. J Neurosci 22, 9490–9501.

Rodriguez, A., Oliver, H., Zou, H., Chen, P., Wang, X., and Abrams, J.M. (1999). Dark is a *Drosophila* homologue of Apaf-1/CED-4 and functions in an evolutionarily conserved death pathway. Nat Cell Biol 1, 272–279.

Rollenhagen, A., Sätzler, K., Rodríguez, E.P., Jonas, P., Frotscher, M., and Lübke, J.H.R. (2007). Structural determinants of transmission at large hippocampal mossy fiber synapses. J Neurosci 27, 10434–10444.

Root, C.M., Masuyama, K., Green, D.S., Enell, L.E., Nässel, D.R., Lee, C.-H., and Wang, J.W. (2008). A Presynaptic Gain Control Mechanism Fine-Tunes Olfactory Behavior. Neuron 59, 311–321.

Rothenfluh, A., Threlkeld, R.J., Bainton, R.J., Tsai, L.T.-Y., Lasek, A.W., and Heberlein, U. (2006). Distinct behavioral responses to ethanol are regulated by alternate RhoGAP18B isoforms. Cell 127, 199–211.

Rubin, G.M., and Spradling, A.C. (1982). Genetic transformation of *Drosophila* with transposable element vectors. Science 218, 348–353.

Sachs, L. (2003). Der Standardfehler des arithmetischen Mittels und des Medianwertes. In Angewandte Statistik, (Berlin Heidelberg: Springer), p. 160.

Sambrook, J., and Russell, D.W. (2000). Molecular Cloning (Cold Spring Harbor Press).

Scheunemann, L., Jost, E., Richlitzki, A., Day, J.P., Sebastian, S., Thum, A.S., Efetova, M., Davies, S.-A., and Schwärzel, M. (2012). Consolidated and Labile Odor Memory Are Separately Encoded within the *Drosophila* Brain. J Neurosci 32, 17163–17171.

Schindelin, J., Arganda-Carreras, I., Frise, E., Kaynig, V., Longair, M., Pietzsch, T., Preibisch, S., Rueden, C., Saalfeld, S., Schmid, B., et al. (2012). Fiji: an open-source platform for biological-image analysis. Nature Methods 9, 676–682.

Schmid, A., Hallermann, S., Kittel, R.J., Khorramshahi, O., Frölich, A., Quentin, C., Rasse, T.M., Mertel, S., Heckmann, M., and Sigrist, S.J. (2008). Activity-dependent site-specific changes of glutamate receptor composition in vivo. Nat Neurosci 11, 659–666.

Schmid, B. (2010). Computational tools for the segmentation and registration of confocal brain images of *Drosophila melanogaster*. Doctoral Thesis. Julius-Maximilians-Universität Würzburg.

Schmidt, M. (2006). Characterization of synaptic protein complexes in *Drosophila melanogaster*. Doctoral Thesis. Georg-August-Universität Göttingen.

Schoenfeld, B.P., Choi, R.J., Choi, C.H., Terlizzi, A.M., Hinchey, P., Kollaros, M., Ferrick, N.J., Koenigsberg, E., Ferreiro, D., Leibelt, D.A., et al. (2013). The *Drosophila* DmGluRA is required for social interaction and memory. Front Pharmacol 4, 64.

Scholz, H., Ramond, J., Singh, C.M., and Heberlein, U. (2000). Functional ethanol tolerance in *Drosophila*. Neuron 28, 261–271.

Schulz, R., Chromey, C., Lu, M., Zhao, B., and Olson, E. (1996). Expression of the D-MEF2 transcription in the *Drosophila* brain suggests a role in neuronal cell differentiation. Oncogene 12, 1827–1831.

Schuster, R., Phannavong, B., Schröder, C., and Gundelfinger, E.D. (1993). Immunohistochemical localization of a ligand-binding and a structural subunit of nicotinic acetylcholine receptors in the central nervous system of *Drosophila melanogaster*. J Comp Neurol 335, 149–162.

Schwaerzel, M., Heisenberg, M., and Zars, T.D. (2002). Extinction antagonizes olfactory memory at the subcellular level. Neuron 35, 951–960.

Schwaerzel, M., Jaeckel, A., and Mueller, U. (2007). Signaling at A-kinase anchoring proteins organizes anesthesia-sensitive memory in *Drosophila*. J Neurosci 27, 1229–1233.

Schwaerzel, M., Monastirioti, M., Scholz, H., Friggi-Grelin, F., Birman, S., and Heisenberg, M. (2003). Dopamine and octopamine differentiate between aversive and appetitive olfactory memories in *Drosophila*. J Neurosci 23, 10495–10502.

Seki, Y., Rybak, J., Wicher, D., Sachse, S., and Hansson, B.S. (2010). Physiological and morphological characterization of local interneurons in the *Drosophila* antennal lobe. J Neurophysiol 104, 1007–1019.

Selimi, F., Cristea, I.M., Heller, E., Chait, B.T., and Heintz, N. (2009). Proteomic studies of a single CNS synapse type: the parallel fiber/purkinje cell synapse. PLoS Biol 7, e83.

Shang, Y., Claridge-Chang, A., Sjulson, L., Pypaert, M., and Miesenböck, G. (2007). Excitatory local circuits and their implications for olfactory processing in the fly antennal lobe. Cell 128, 601–612.

Sheng, M. (2001). The postsynaptic specialization. In Synapses, W.M. Cowan, T.C. Südhof, and C.F. Stevens, eds. (Baltimore: The John Hopkins University Press), pp. 315–355.

Sherrington, C.S. (1897). The central nervous system. In A Textbook of Physiology, M. Foster, ed. (London: Macmillan).

Shiina, N., Shinkura, K., and Tokunaga, M. (2005). A novel RNA-binding protein in neuronal RNA granules: regulatory machinery for local translation. J Neurosci 25, 4420–4434.

Sidorov, M.S., Auerbach, B.D., and Bear, M.F. (2013). Fragile X mental retardation protein and synaptic plasticity. Mol Brain 6, 15.

Siegel, R.W., and Hall, J.C. (1979). Conditioned responses in courtship behavior of normal and mutant *Drosophila*. Proc Natl Acad Sci USA 76, 3430–3434.

Sigrist, S.J., and Schmitz, D. (2011). Structural and functional plasticity of the cytoplasmic active zone. Curr Opin Neurobiol 21, 144–150.

Sigrist, S.J., Reiff, D.F., Thiel, P.R., Steinert, J.R., and Schuster, C.M. (2003). Experience-dependent strengthening of *Drosophila* neuromuscular junctions. J Neurosci 23, 6546–6556.

Sigrist, S.J., Thiel, P.R., Reiff, D.F., Lachance, P., Lasko, P., and Schuster, C.M. (2000). Postsynaptic translation affects the efficacy and morphology of neuromuscular junctions. Nature 405, 1062–1065.

Singh, C.M., and Heberlein, U. (2000). Genetic control of acute ethanol-induced behaviors in *Drosophila*. Alcohol Clin Exp Res 24, 1127–1136.

Sinnamon, J.R., and Czaplinski, K. (2011). mRNA trafficking and local translation: the Yin and Yang of regulating mRNA localization in neurons. Acta Biochim. Biophys. Sin. (Shanghai) 43, 663–670.

Siwicki, K.K., and Ladewski, L. (2003). Associative learning and memory in *Drosophila*: beyond olfactory conditioning. Behav. Processes 64, 225–238.

Skoulakis, E.M., Kalderon, D., and Davis, R.L. (1993). Preferential expression in mushroom bodies of the catalytic subunit of protein kinase A and its role in learning and memory. Neuron 11, 197–208.

Song, J., Tan, H., Shen, H., Mahmood, K., Boyd, S.E., Webb, G.I., Akutsu, T., and Whisstock, J.C. (2010). Cascleave: towards more accurate prediction of caspase substrate cleavage sites. Bioinformatics 26, 752–760.

Song, J., and Tanouye, M.A. (2006). Seizure suppression by shakB2, a gap junction mutation in *Drosophila*. J Neurophysiol 95, 627–635.

Song, Z., Guan, B., Bergman, A., Nicholson, D.W., Thornberry, N.A., Peterson, E.P., and Steller, H. (2000). Biochemical and genetic interactions between *Drosophila* caspases and the proapoptotic genes rpr, hid, and grim. Molecular and Cellular Biology 20, 2907–2914.

Spangler, S.A., and Hoogenraad, C.C. (2007). Liprin-alpha proteins: scaffold molecules for synapse maturation. Biochem Soc Trans 35, 1278–1282.

Spangler, S.A., Schmitz, S.K., Kevenaar, J.T., de Graaff, E., de Wit, H., Demmers, J., Toonen, R.F., and Hoogenraad, C.C. (2013). Liprin-α2 promotes the presynaptic recruitment and turnover of RIM1/CASK to facilitate synaptic transmission. J Cell Biol 201, 915–928.

Spieth, H.T. (1974). Courtship behavior in *Drosophila*. Annu Rev Entomol 19, 385–405.

Spooren, W.P., Gasparini, F., Salt, T.E., and Kuhn, R. (2001). Novel allosteric antagonists shed light on mglu(5) receptors and CNS disorders. Trends Pharmacol. Sci. 22, 331–337.

Sporns, O. (2013). The human connectome: Origins and challenges. Neuroimage 80, 53–61.

Sporns, O., Tononi, G., and Kötter, R. (2005). The Human Connectome: A Structural Description of the Human Brain. PLoS Comput Biol 1, e42.

Stewart, B.A., Atwood, H.L., Renger, J.J., Wang, J., and Wu, C.F. (1994). Improved stability of *Drosophila* larval neuromuscular preparations in haemolymph-like physiological solutions. J. Comp. Physiol. A 175, 179–191.

Stocker, R.F., Heimbeck, G., Gendre, N., and de Belle, J.S. (1997). Neuroblast ablation in *Drosophila* P[GAL4] lines reveals origins of olfactory interneurons. J Neurobiol 32, 443–456.

Strausfeld, N.J., Hansen, L., Li, Y., Gomez, R.S., and Ito, K. (1998). Evolution, discovery, and interpretations of arthropod mushroom bodies. Learn Mem 5, 11–37.

Strausfeld, N.J. (1976). Atlas of an Insect Brain (Springer Berlin Heidelberg).

Strauss, R. (2002). The central complex and the genetic dissection of locomotor behaviour. Curr Opin Neurobiol 12, 633–638.

Sun, Y.A., and Wyman, R.J. (1996). Passover eliminates gap junctional communication between neurons of the giant fiber system in *Drosophila*. off. J Neurobiol 30, 340–348.

Südhof, T.C. (2012). The presynaptic active zone. Neuron 75, 11–25.

Tamayev, R., Akpan, N., Arancio, O., Troy, C.M., and D Adamio, L. (2012). Caspase-9 mediates synaptic plasticity and memory deficits of Danish dementia knock-in mice: caspase-9 inhibition provides therapeutic protection. Mol Neurodegener 7, 60.

Tan, H., Poidevin, M., Li, H., Chen, D., and Jin, P. (2012). MicroRNA-277 modulates the neurodegeneration caused by Fragile X premutation rCGG repeats. PLoS Genet 8, e1002681.

Tanaka, N.K., Endo, K., and Ito, K. (2012). Organization of antennal lobe-associated neurons in adult *Drosophila melanogaster* brain. J Comp Neurol 520, 4067–4130.

Tanaka, N.K., Tanimoto, H., and Ito, K. (2008). Neuronal assemblies of the *Drosophila* mushroom body. J Comp Neurol 508, 711–755.

Tauber, J.M., Vanlandingham, P.A., and Zhang, B. (2011). Elevated levels of the vesicular monoamine transporter and a novel repetitive behavior in the *Drosophila* model of fragile X syndrome. PLoS ONE 6, e27100.

Tepass, U. (2012). The apical polarity protein network in *Drosophila* epithelial cells: regulation of polarity, junctions, morphogenesis, cell growth, and survival. Annu Rev Cell Dev Biol 28, 655–685.

Tessier, C.R., and Broadie, K.S. (2011). The fragile X mental retardation protein developmentally regulates the strength and fidelity of calcium signaling in *Drosophila* mushroom body neurons. Neurobiol Dis 41, 147–159.

The benefits of brain mapping (2013). Editorial. Nature 499, 253.

Thévenaz, P., Ruttimann, U.E., and Unser, M. (1998). A pyramid approach to subpixel registration based on intensity. IEEE Trans Image Process 7, 27–41.

Thomas, J.B., and Wyman, R.J. (1984). Mutations altering synaptic connectivity between identified neurons in *Drosophila*. J Neurosci 4, 530–538.

Thompson, V. (1977). Recombination and response to selection in *Drosophila melanogaster*. Genetics 85, 125–140.

Tian, L., Hires, S.A., Mao, T., Huber, D., Chiappe, M.E., Chalasani, S.H., Petreanu, L., Akerboom, J., McKinney, S.A., Schreiter, E.R., et al. (2009). Imaging neural activity in worms, flies and mice with improved GCaMP calcium indicators. Nature Methods 6, 875–881.

Tian, R. (2011). Structural and Functional Organization of Synaptic Proteins in D. *melanogaster*. Doctoral Thesis. Julius-Maximilians-Universität Würzburg.

tom Dieck, S., Altrock, W.D., Kessels, M.M., Qualmann, B., Regus, H., Brauner, D., Fejtova, A., Bracko, O., Gundelfinger, E.D., and Brandstätter, J.H. (2005). Molecular dissection of the photoreceptor ribbon synapse: physical interaction of Bassoon and RIBEYE is essential for the assembly of the ribbon complex. J Cell Biol 168, 825–836.

tom Dieck, S., Specht, D., Strenzke, N., Hida, Y., Krishnamoorthy, V., Schmidt, K.-F., Inoue, E., Ishizaki, H., Tanaka-Okamoto, M., Miyoshi, J., et al. (2012). Deletion of the presynaptic scaffold CAST reduces active zone size in rod photoreceptors and impairs visual processing. J Neurosci 32, 12192–12203.

Torroja, L., Chu, H., Kotovsky, I., and White, K. (1999). Neuronal overexpression of APPL, the *Drosophila* homologue of the amyloid precursor protein (APP), disrupts axonal transport. Curr Biol 9, 489–492.

Tully, T., and Quinn, W.G. (1985). Classical conditioning and retention in normal and mutant *Drosophila melanogaster*. J. Comp. Physiol. A 157, 263–277.

Tully, T., Preat, T., Boynton, S., and Del Vecchio, M. (1994). Genetic dissection of consolidated memory in *Drosophila*. Cell 79, 35–47.

Turner, G., Bazhenov, M., and Laurent, G. (2008). Olfactory representations by *Drosophila* mushroom body neurons. J Neurophysiol 99, 734–746.

Tusher, V.G., Tibshirani, R., and Chu, G. (2001). Significance analysis of microarrays applied to the ionizing radiation response. Proc Natl Acad Sci USA 98, 5116–5121.

Urizar, N.L., Yang, Z., Edenberg, H.J., and Davis, R.L. (2007). *Drosophila* homer is required in a small set of neurons including the ellipsoid body for normal ethanol sensitivity and tolerance. J Neurosci 27, 4541–4551.

Van Essen, D.C., and Ugurbil, K. (2012). The future of the human connectome. Neuroimage 62, 1299–1310.

Van Essen, D.C., Ugurbil, K., Auerbach, E., Barch, D., Behrens, T.E.J., Bucholz, R., Chang, A., Chen, L., Corbetta, M., Curtiss, S.W., et al. (2012). The Human Connectome Project: a data acquisition perspective. Neuroimage 62, 2222–2231.

Van Harreveld, A., and Fifkova, E. (1975). Swelling of dendritic spines in the fascia dentata after stimulation of the perforant fibers as a mechanism of post-tetanic potentiation. Exp Neurol 49, 736–749.

Venken, K.J.T., Carlson, J.W., Schulze, K., Pan, H., He, Y., Spokony, R., Wan, K., Koriabine, M., de Jong, P.J., White, B.H., et al. (2009). Versatile P[acman] BAC libraries for transgenesis studies in *Drosophila melanogaster*. Nature Methods 6, –434.

Venken, K.J.T., He, Y., Hoskins, R.A., and Bellen, H.J. (2006). P[acman]: a BAC transgenic platform for targeted insertion of large DNA fragments in D. *melanogaster*. Science 314, 1747–1751.

Venken, K.J.T., Kasprowicz, J., Kuenen, S., Yan, J., Hassan, B.A., and Verstreken, P. (2008). Recombineering-mediated tagging of *Drosophila* genomic constructs for in vivo localization and acute protein inactivation. Nucleic Acids Res 36, e114.

Vermeulen, M., Hubner, N.C., and Mann, M. (2008). High confidence determination of specific protein-protein interactions using quantitative mass spectrometry. Curr. Opin. Biotechnol. 19, 331–337.

Verspurten, J., Gevaert, K., Declercq, W., and Vandenabeele, P. (2009). SitePredicting the cleavage of proteinase substrates. Trends Biochem Sci 34, 319–323.

Vessey, J.P., and Karra, D. (2007). More than just synaptic building blocks: scaffolding proteins of the post-synaptic density regulate dendritic patterning. J Neurochem 102, 324–332.

Viegas, M.H., Gehring, N.H., Breit, S., Hentze, M.W., and Kulozik, A.E. (2007). The abundance of RNPS1, a protein component of the exon junction complex, can determine the variability in efficiency of the Nonsense Mediated Decay pathway. Nucleic Acids Res 35, 4542–4551.

Vosshall, L.B., Amrein, H., Morozov, P.S., Rzhetsky, A., and Axel, R. (1999). A spatial map of olfactory receptor expression in the *Drosophila* antenna. Cell 96, 725–736.

Vosshall, L.B., and Stocker, R.F. (2007). Molecular Architecture of Smell and Taste in *Drosophila*. Annu Rev Neurosci 30, 505–533.

Vu, N.T., Park, M.A., Shultz, J.C., Goehe, R.W., Hoeferlin, L.A., Shultz, M.D., Smith, S.A., Lynch, K.W., and Chalfant, C.E. (2013). hnRNP U enhances caspase-9 splicing and is modulated by AKT-dependent phosphorylation of hnRNP L. Journal of Biological Chemistry 288, 8575–8584.

Waddell, S., Armstrong, J.D., Kitamoto, T., Kaiser, K., and Quinn, W.G. (2000). The amnesiac gene product is expressed in two neurons in the *Drosophila* brain that are critical for memory. Cell 103, 805–813.

Wagh, D.A., Rasse, T.M., Asan, E., Hofbauer, A., Schwenkert, I., Dürrbeck, H., Buchner, S., Dabauvalle, M.-C., Schmidt, M., Qin, G., et al. (2006). Bruchpilot, a protein with homology to ELKS/CAST, is required for structural integrity and function of synaptic active zones in *Drosophila*. Neuron 49, 833–844.

Waites, C.L., Leal-Ortiz, S.A., Andlauer, T.F.M., Sigrist, S.J., and Garner, C.C. (2011). Piccolo regulates the dynamic assembly of presynaptic f-actin. J Neurosci 31, 14250–14263.

Waldeyer, W. (1891). Ueber einige neuere Forschungen im Gebiete der Anatomie des Centralnervensystems. Dtsch Med Wochenschr 17, 1213–1218.

Wan, L., Dockendorff, T.C., Jongens, T.A., and Dreyfuss, G. (2000). Characterization of dFMR1, a *Drosophila melanogaster* Homolog of the Fragile X Mental Retardation Protein. Molecular and Cellular Biology 20, 8536–8547.

Wang, J.W., Wong, A.M., Flores, J., Vosshall, L.B., and Axel, R. (2003). Two-photon calcium imaging reveals an odor-evoked map of activity in the fly brain. Cell 112, 271–282.

Wang, Y., Mamiya, A., Chiang, A.-S.S., and Zhong, Y. (2008). Imaging of an early memory trace in the *Drosophila* mushroom body. J Neurosci 28, 4368–4376.

Wee, L.J.K., Tan, T.W., and Ranganathan, S. (2006). SVM-based prediction of caspase substrate cleavage sites. BMC Bioinformatics 7 Suppl 5, S14.

Wee, L.J.K., Tan, T.W., and Ranganathan, S. (2007). CASVM: web server for SVM-based prediction of caspase substrates cleavage sites. Bioinformatics 23, 3241–3243.

Wentzel, C., Sommer, J.E., Nair, R., Stiefvater, A., Sibarita, J.-B., and Scheiffele, P. (2013). mSYD1A, a mammalian synapse-defective-1 protein, regulates synaptogenic signaling and vesicle docking. Neuron 78, 1012–1023.

White, J.G., Southgate, E., Thomson, J.N., and Brenner, S. (1986). The structure of the nervous system of the nematode Caenorhabditis elegans. Philos. Trans. R. Soc. Lond., B, Biol. Sci. 314, 1–340.

Wichmann, C., and Sigrist, S.J. (2010). The active zone T-bar--a plasticity module? J. of Neurogenetics 24, 133–145.

Willemsen, R., Levenga, J., and Oostra, B.A. (2011). CGG repeat in the FMR1 gene: size matters. Clin. Genet. 80, 214–225.

Wilson, R.I. (2013). Early Olfactory Processing in *Drosophila*: Mechanisms and Principles. Annu Rev Neurosci 36, 217–241.

Wolf, F.W., Rodan, A.R., Tsai, L.T.-Y., and Heberlein, U. (2002). High-resolution analysis of ethanol-induced locomotor stimulation in *Drosophila*. J Neurosci 22, 11035–11044.

Wolff, T., and Ready, D.F. (1991). Cell death in normal and rough eye mutants of *Drosophila*. Development 113, 825–839.

Wu, C.-L., Shih, M.-F.M., Lai, J.S.-Y., Yang, H.-T., Turner, G.C., Chen, L., and Chiang, A.-S.S. (2011). Heterotypic gap junctions between two neurons in the *drosophila* brain are critical for memory. Curr Biol 21, 848–854.

Wu, C.-L., Xia, S., Fu, T.-F., Wang, H., Chen, Y.-H., Leong, D., Chiang, A.-S.S., and Tully, T. (2007). Specific requirement of NMDA receptors for long-term memory consolidation in *Drosophila* ellipsoid body. Nat Neurosci 10, 1578–1586.

Wu, C., Zhang, Y., Sun, Z., and Li, P. (2008). Molecular evolution of Cide family proteins: novel domain formation in early vertebrates and the subsequent divergence. BMC Evol Biol 8, 159.

Xia, S., Miyashita, T., Fu, T.-F., Lin, W.-Y., Wu, C.-L., Pyzocha, L., Lin, I.-R., Saitoe, M., Tully, T., and Chiang, A.-S.S. (2005). NMDA receptors mediate olfactory learning and memory in *Drosophila*. Curr Biol 15, 603–615.

Xiao, R., Tang, P., Yang, B., Huang, J., Zhou, Y., Shao, C., Li, H., Sun, H., Zhang, Y., and Fu, X.-D. (2012). Nuclear matrix factor hnRNP U/SAF-A exerts a global control of alternative splicing by regulating U2 snRNP maturation. Molecular Cell 45, 656–668.

Yaksi, E., and Wilson, R.I. (2010). Electrical Coupling between Olfactory Glomeruli. Neuron 67, 1034–1047.

Yang, M., Armstrong, J.D., Vilinsky, I., Strausfeld, N., and Kaiser, K. (1995). Subdivision of the *Drosophila* mushroom bodies by enhancer-trap expression patterns. Neuron 15, 45–54.

Yasuyama, K., and Salvaterra, P.M. (1999). Localization of choline acetyltransferase-expressing neurons in *Drosophila* nervous system. Microsc Res Tech 45, 65–79.

Yasuyama, K., Meinertzhagen, I.A., and Schürmann, F.-W. (2002). Synaptic organization of the mushroom body calyx in *Drosophila melanogaster*. J Comp Neurol 445, 211–226.

Yeh, E., Gustafson, K., and Boulianne, G.L. (1995). Green fluorescent protein as a vital marker and reporter of gene expression in *Drosophila*. Proc Natl Acad Sci USA 92, 7036–7040.

Yin, J.C., Wallach, J.S., Del Vecchio, M., Wilder, E.L., Zhou, H., Quinn, W.G., and Tully, T. (1994). Induction of a dominant negative CREB transgene specifically blocks long-term memory in *Drosophila*. Cell 79, 49–58.

Yokoyama, H., Mukae, N., Sakahira, H., Okawa, K., Iwamatsu, A., and Nagata, S. (2000). A novel activation mechanism of caspase-activated DNase from *Drosophila melanogaster*. J Biol Chem 275, 12978–12986.

Yonezawa, T., Kurata, R., Kimura, M., and Inoko, H. (2011). Which CIDE are you on? Apoptosis and energy metabolism. Mol Biosyst 7, 91–100.

Young, J.M., and Armstrong, J.D. (2010). Structure of the adult central complex in *Drosophila*: organization of distinct neuronal subsets. J Comp Neurol 518, 1500–1524.

Zador, A.M., Dubnau, J., Oyibo, H.K., Zhan, H., Cao, G., and Peikon, I.D. (2012). Sequencing the Connectome. PLoS Biol 10, e1001411.

Zars, T.D., Fischer, M., Schulz, R., and Heisenberg, M. (2000). Localization of a short-term memory in *Drosophila*. Science 288, 672–675.

Zhai, R.G., and Bellen, H.J. (2004). The architecture of the active zone in the presynaptic nerve terminal. Physiology (Bethesda, Md) 19, 262–270.

Zhang, Y.Q., Bailey, A.M., Matthies, H.J., Renden, R.B., Smith, M.A., Speese, S.D., Rubin, G.M., and Broadie, K.S. (2001). *Drosophila* fragile X-related gene regulates the MAP1B homolog Futsch to control synaptic structure and function. Cell 107, 591–603.

Zhang, Y.Q., Rodesch, C.K., and Broadie, K.S. (2002). Living synaptic vesicle marker: synaptotagmin-GFP. Genesis 34, 142–145.

Zhang, Z., Li, X., Guo, J., Li, Y., and Guo, A. (2013). Two clusters of GABAergic ellipsoid body neurons modulate olfactory labile memory in *Drosophila*. J Neurosci 33, 5175–5181.

Zhou, L., Schnitzler, A., Agapite, J., Schwartz, L.M., Steller, H., and Nambu, J.R. (1997). Cooperative functions of the reaper and head involution defective genes in the programmed cell death of *Drosophila* central nervous system midline cells. Proc Natl Acad Sci USA 94, 5131–5136.

Zinsmaier, K.E., Eberle, K.K., Buchner, E., Walter, N., and Benzer, S. (1994). Paralysis and early death in cysteine string protein mutants of *Drosophila*. Science 263, 977–980.

Zucker, R.S., and Regehr, W.G. (2002). Short-term synaptic plasticity. Annu. Rev. Physiol. 64, 355–405.

INDEX OF FIGURES

INDEX OF TABLES

INDEX OF ABBREVIATIONS

°C	Degrees Celsius
4-MCH	4-Methyl-cyclohexanol
3-OCT	3-Octanol
α	Significance level
ACh	Acetylcholine
ACPD	1S,3R-1-Amino-1,3-cyclopentanedicarboxylate
Ago2	Argonaute-2
AKAP	A-kinase anchoring protein
AL	Antennal lobe
ALK	Anaplastic lymphoma kinase
AMPA	α-Amino-3-hydroxy-5-methyl-4-isoxazole propionic acid
ANF	Pre-pro-atrial natriuretic factor
APL	Anterior paired lateral (neuron)
ARM	Anaesthesia-resistant memory
ASM	Anaesthesia-sensitive memory
AZ	Active zone
BAC	Bacterial artificial chromosome
bp	Base pairs
Brp	Bruchpilot
CamKII	Ca^{2+}/Calmodulin-depend. kinase II
C.	*Caenorhabditis*
c.	control
cont.	control
ca	Calyx
Ca^{2+}	Calcium
CAD	Caspase-activated DNase
cAMP	Cyclic adenosine monophosphate
CAZ	Cytomatrix at the AZ
cDlc-2	Cytoplastic Dynein light chain 2
cDNA	Complementary DNA
CG	Computed gene
ChAT	Choline acetyltransferase
CI	Courtship index
CIDE	Cell-death inducing Dff-like effector
CIDE-N	N-terminal CIDE domain
CNS	Central nervous system
CREB	cAMP response element-binding protein
CSP	Cysteine string protein
D.	*Drosophila*
Da	Dalton
Dcp-1	Death caspase-1
Dff	DNA fragmentation factor
Dlg	Discs large
DPM	Dorsal paired medial (neuron)
DrICE	*Drosophila* Interleukin-1β-converting enzyme
$\Delta F/F_0$	Changes in fluorescence emission
DNA	Deoxyribonucleic acid
DNase	Deoxyribonuclease
Drep	Dff-related protein
eEJC	evoked excitatory junctional current
EM	Electron microscopy
EMS	Ethyl methane sulfonate
ERG	Electroretinogram
ERK	Extracellular signal regulated kinase
e,g,	*exempli gratia*
et al.	*et alii*
FDR	False-positive discovery rate
Fig.	Figure
FLP	FLP recombinase
FMRP	Fragile X mental retardation protein
freq.	frequency
FRT	FLP recombination target
FXS	Fragile X syndrome
FXTAS	Fragile X associated tremor/ataxia syndrome
GABA	γ-Aminobutyric acid
GAP	GTPase activating protein
GCaMP	GFP-Calmodulin probe
GEF	Guanyl-nucleotide exchange factor
GFP	Green fluorescent protein
GTP	Guanosine triphosphate
HL3	Hemolymph-like saline

hnRNP	Heterogeneous nuclear RNP
Hz	Hertz
ICAD	Inhibitor of CAD
i.e.	*id est*
IP	Immunoprecipitation
ISI	inter-stimulus interval
ITM	Intermediate-term memory
k	Kilo
KC	Kenyon cell
KCAC	KC-derived AZs in the calyx
LI	Learning index
LN	Local interneuron
LTM	Long-term memory
MARCM	mosaic analysis with a repressible cell marker
max	Maximum
MB	Mushroom body
mGluR	Metabotropic glutamate receptor
min	Minute or minimum, depending on the context
mM	Millimolar
µm	Micrometer
µM	Micromolar
ms	Millisecond
MPEP	2-Methyl-6-(phenylethynyl)pyridine
MS/MS	Tandem mass spectrometry
Munc13	Mammalian Uncoordinated movement 13
mV	Millivolt
MWU	Mann-Whitney U-test
n	Number of replicates in a sample set
NGS	Normal goat serum
NMDA	N-Methyl-D-aspartate
NMJ	Neuromuscular junction
n.s.	Not significant
NSF	N-ethylmaleimide-sensitive factor
OR	Odourant receptor
ORN	Olfactory receptor neuron
p	Probability value
P[acman]	P/ϕC31 artificial chromosome for manipulation
PAGE	Polyacrylamide gel electrophoresis
PBS	Phosphate-buffered saline
PCR	Polymerase chain reaction
PKA	cAMP-dependent protein kinase A
PKC	Protein kinase C
PLC	Phospholipase C
PN	Projection neuron
PSD	Post-synaptic density
Rab	Products of *ras genes from rat brain*
Ras	Rat sarcoma virus oncogene
RBP	RIM-Binding Protein
RNA	Ribonucleic acid
RNAi	RNA interference
RNP	Ribonucleoprotein
RT-PCR	Reverse transcription PCR
RIM	Rab3-Interacting Module/Molecule
s	Second
S.	*Saccharomyces*
Scampi	Scampolo
SDS	Sodium dodecyl sulfate
SEM	Standard error of the mean
ShakB	Shaking-B
siRNA	short interference RNA
SNAP	Soluble NSF attachment protein
SNARE	SNAP receptor
snRNA	small nuclear RNA
ST50	Sedation time 50%
STED	Stimulated emission depletion
STM	Short-term memory
Syd-1	Synapse-defective 1
Term	Terminal
TRP	Transient receptor potential
UAS	Upstream activating sequence
UTR	Untranslated region
vs.	*versus*
W	White
w/o	without
ZNS	Zentrales Nervensystem

ACKNOWLEDGEMENTS

Having conducted most of this work in a place distant from my actual lab, I have, probably more than the average, been dependent on the support and helpfulness of others. Therefore, while thinking about whom I should thank for their help, myriads of names keep on streaming through my head. Since I don't have Homer's talent for transforming endless rows of names into poetry, I needed to cut off the list somewhere. Of course, I'll notice rather sooner than later that I have forgotten to thank important people and, consequently, want to start with an apology to these. But without further ado I'll now begin in a somewhat chronological order:

Although he probably never realised that I actually greatly appreciated his lessons, I would have never developed a deeper interest in biology without the inspiration by Konrad Jäger. And of course, my mother's passion for nature (the environment, not the journal) has probably played a role as well. Staying with her, I can just state that I find it the most difficult to express apt gratitude to the people that deserve it the most. Needless to say, her huge support played a very decisive role in getting me where I'm standing now. Unfortunately, I can thank my father only for his genes and for his clairvoyant insistence on providing me with middle name(s) for a potential future academic life. However, not only the work presented here shows that genes are, in fact, quite important. Andreas showed all his support and influence at a later stage, when experience rather than genes shapes the mind. As if further proof for this was still needed, he demonstrated the importance of non-genetic influences on behaviour. To just pick out one thing, he was so kind to introduce me to the world of computers while my mother preferred to groom flowers in the garden.

Since it's high time for progress, I'll jump forward and want to thank Karl Fischbach, who introduced me to flies, genetics, microscopy, and proper scientific conduct. Which is a lot, actually. I would also like to thank Jan Wijnholds for his support and for his understanding.

After all these lines, I finally come to the most important person I'd like to express my gratitude to, and that is of course Stephan Sigrist. It is self-evident that his support and influence are the key pillars of this thesis. However, I not only want to stress the importance of the scientific aspects of his supervision: I am very aware that it cannot be taken for granted that he let me conduct my work in the city and under the circumstances that I chose. And not only did he allow me to do so, but he also supported me in that choice in every manner. I also want to thank him for always and unconditionally standing by my side in difficult situations. I'm very grateful as well to my two other supervisors, Erich Buchner and Thomas Raabe. Again, not only for their scientific input, but also very much for their personal support and for always being there, as soon as I needed any help.

I would like to thank every past and present member of our lab, for all their support as well as for the entertainment they provided. The following people, however, deserve a special mention: Frauke Christiansen (now Engelhardt) not only taught me a lot about the olfactory system but is actually also the one who developed the initial methods for quantifying central brain AZs in Imaris, together with Omid Khorramshahi. She and her family hosted me during most of my trips to Berlin, and Frauke is one of the most helpful and kind persons I've ever met. Omid also hosted me several times and with him I've spent numerous days and nights discussing life and science. Especially his input on microscopy and *in vivo* imaging was and is invaluable. David Owald is the third person I would like to thank for his hospitality, his countless scientific contributions, and, last but not least, for his company in many bars. He was so kind to remind me of my preference for box-whisker plots, which I had articulated on several occasions but then miraculously forgotten about when beginning to assemble this thesis. All three of them, Omid, David, and Frauke, also helped me with questions that came up while writing this thesis and proofread parts of the text.

In addition, within the realm of our lab, I'd like to thank Christine Quentin for her constant support in every aspect of my work and especially for her enthusiasm regarding EM. Wernher Fouquet taught me much about microscopy. Franziska Zehe and Anastasia Stawrakakis deserve gratitude mainly, but not exclusively, for their support in molecular biology. Madeleine Brünner purified several antibodies for me and has an admirable passion for the aesthetics of western blots. Rui Tian started the Drep-2 project and it is needless to say that her many contributions are the basis of all my Drep-related work. In the context of this project, I also want to thank Caro Wichmann for EM and entertaining phone calls, Elena Knoche for electrophysiology, Christina Hollmann for ERGs; Husam Babikir and Harald Depner for the biochemistry; Tanja Matkovic for performing the recombineering, supervising homologous recombinations and for many PCRs; Sara Mertel for numerous acts of support. In the ratio project, Karen Liu, Christina Zube and Nico Steckhan made outstanding contributions. Many people cooked great fly food for me, which I, fortunately, had to do only once myself during all these years.

Reaching beyond our lab, I'd first of all like to thank the Rudolf-Virchow-Zentrum for hosting me during all of my work. Next, I'd like to thank Martin Heisenberg, Reinhard Wolf and all the members of the Heisenberg lab for their hospitality, scientific support and insightful discussions. The structural biology and microscopy groups of the RVZ were also often very helpful. I thank Michael Sendtner and Albrecht Müller for lending me equipment and Gunther Tietsch for great technical support. Although usually acting in the background, many administrative people were very supportive as well.

The last major group of people I really want and need to thank are collaborators that supported this work. I'd like to thank Adrian Rothenfluh for giving me the idea to test for ethanol sensitivity. Dana Robertson was extremely helpful and very enthusiastic in performing detailed and proper ethanol experiments, I want to thank her very much for her help. I'm also grateful to Ulrike Heberlein for letting her do this work for me. Mike Cressy readily agreed to do the first olfactory conditioning experiments, which was very kind of him. His supervisor Josh Dubnau provided advice for the design of these experiments. Later on, Sabrina Scholz-Kornehl and Martin Schwärzel did and supervised, respectively, the olfactory conditioning experiments actually presented here. Melanie Gonsior added some measurements as well, which unfortunately didn't make it into the final data set. Sabrina Büttner tried her best at caspase assays and I'm very grateful for her insistence. Jennifer Lardong, Nicole Holton and Bernhard Loll did additional work in the same direction. Konstantin Lehmann was a huge help in Matlab programming. Cornelia Oppitz, in the lab of Krystyna Keleman, was so friendly to do all the courtship conditioning experiments without ever complaining. André Fiala allowed me to do the GCaMP3 measurements in his lab and Shubham Dipt helped me a lot in getting them done. Marieluise Kirchner, of Matthias Selbach's lab, conducted the mass spectrometry and didn't get tired by all my ideas for analysis of the data. I'd also like to thank Dave Featherstone for his help and advice. Moreover, he and Dana had to proofread numerous of my texts. Last but not least, I want to thank Johannes Hain for help with statistics.

Outside the world of flies and work, Maren was of course the decisive factor that kept my life running. Not only need I to thank her for making me move to Würzburg and thus setting in motion the events that lead to the completion of this thesis, but also for her constant and universal support that made this work possible. She, Puma and Scampolo had to go through many difficult and many happy days until this work was completed. Of note, any repetitive letters and random deletions in the text can likely be attributed to Scampi, who enjoyed lying on the keyboard. However, I refrained from adding her as a co-author, since her helpful contributions were as marginal as Puma's.

LIST OF PUBLICATIONS

Andlauer TFM, Liu KSY, Sigrist SJ: *A ratiometric approach to synaptic diversity.* In preparation.

Andlauer TFM, Scholz-Kornehl S, Tian R, Oppitz C, Kirchner ML, Robertson DK, Babikir H, Depner H, Loll B, Quentin C, Dipt S, Cressy M, Fiala A, Selbach M, Keleman K, Schwärzel M, Sigrist SJ: *The Dff-family protein Drep-2 is a novel synaptic protein important for learning and memory.* Submitted.

Andlauer TFM, Sigrist SJ (2012): *In vivo imaging of Drosophila larval neuromuscular junctions to study synapse assembly.* Cold Spring Harbor Protocols 2012(4):407-13

Andlauer TFM, Sigrist SJ (2012): *Building an imaging chamber for in vivo imaging of Drosophila larvae.* Cold Spring Harbor Protocols 2012(4):476-80

Andlauer TFM, Sigrist SJ (2012): *In vivo imaging of the Drosophila larval neuromuscular junction.* Cold Spring Harbor Protocols 2012(4):481-9

Andlauer TFM, Sigrist SJ (2012): *Quantitative analysis of Drosophila larval neuromuscular junction morphology.* Cold Spring Harbor Protocols 2012(4):490-3

Park B, Alves CH, Lundvig DM, Tanimoto N, Beck SC, Huber G, Richard F, Klooster J, **Andlauer TFM**, Swindell EC, Jamrich M, Le Bivic A, Seeliger MW, Wijnholds J. (2011): *PALS1 is essential for retinal pigment epithelium structure and neural retina stratification.* Journal of Neuroscience 31(47):17230-41

Waites CL, Leal-Ortiz SA, **Andlauer TFM**, Sigrist SJ, Garner CC (2011): *Piccolo regulates the dynamic assembly of presynaptic f-actin.* Journal of Neuroscience 31(40):14250-63

Christiansen F, Zube C, **Andlauer TFM**, Wichmann C, Fouquet W, Owald D, Mertel S, Leiss F, Tavosanis G, Farca Luna AJ, Fiala A, Sigrist SJ (2011): *Presynapses in Kenyon Cell Dendrites in the Mushroom Body Calyx of Drosophila.* Journal of Neuroscience 31(26):9696-707

Sigrist SJ, **Andlauer TFM** (2011): *Fighting the famine with an amine: synaptic strategies for smart search.* Nature Neuroscience 14(2):124-6

Kremer MC, Christiansen F, Leiss F, Paehler M, Knapek S, **Andlauer TFM**, Förstner F, Kloppenburg P, Sigrist SJ, Tavosanis G (2010): *Structural Long-Term Changes at Mushroom Body Input Synapses.* Current Biology 20(21):1938-44

Andlauer, TFM, Sigrist, SJ (2010): *In Vivo Imaging of Drosophila Larval Neuromuscular Junctions to Study Synapse Assembly.* Chapter 21 in *Drosophila* Neurobiology, B. Zhang, M.R. Freeman, and S. Waddell, eds. (Cold Spring Harbor Press)

Andlauer TFM, Sigrist SJ (2009): *Intravitale Bildgebung in Drosophila-Larven.* Biospektrum 6/2009:632-635

Fischbach KF, Linneweber GA, **Andlauer TFM**, Hertenstein A, Bonengel B, Chaudhary K (2009): *The irre cell recognition module (IRM) proteins.* Journal of Neurogenetics 23(1-2):48-67

CURRICULUM VITAE

Fig. 84: Three rabbits on fire.
High magnification view of a larval *Drosophila melanogaster* neuromuscular junction bouton in a transgenic background. Stained using antibodies against acetylated Tubulin (STED), representing the burning cytoskeleton, and Synaptotagmin, outlining the rabbits.
Because even a high-resolution microscope obviously constitutes an inappropriate environment for rabbits, the animals were embedded in a natural scenery, consisting of cheerful plastic fern, as well as a cardboard frame decorated with a wooden sun, both affectionately coloured with acrylic paint.
September, 2009.